Effects of tidal bores on turbulent mixing : a numerical and physical study in positive surges

Bruno Simon

N° d'ordre:

THE UNIVERSITY OF QUEENSLAND
AUSTRALIA

UNIVERSITÉ BORDEAUX 1
Sciences Technologies

THÈSE

PRÉSENTÉE Á

L'UNIVERSITÉ BORDEAUX 1
ET
THE UNIVERSITY OF QUEENSLAND

ÉCOLE DOCTORALE DES SCIENCES PHYSIQUES ET DE L'INGÉNIEUR
SCHOOL OF CIVIL ENGINEERING

Par Bruno SIMON

POUR OBTENIR LE GRADE DE

DOCTEUR

SPÉCIALITÉ : Mécanique

Effects of tidal bores on turbulent mixing:
a numerical and physical study in positive surges

Soutenue le : 24/10/2013

Devant la commission d'examen formée de :

Dr BRANGER, Hubert	Chargé de recherche CNRS, IRPHE, IOA, Marseille	Examinateur
Pr CHANSON, Hubert	Professeur, School of Civil Engineering, UQ, Brisbane	Directeur
Pr HUBERSON, Serge	Professeur, PPrime, Université de Poitiers	Président
Pr LARRARTE, Frédérique	Directrice de recherche MEDDE, IFFSTAR, Nantes	Rapporteur
Dr LUBIN, Pierre	Maitre de Conférences, I2M, Université Bordeaux 1	Directeur
Pr REEVE, Dominic	Professeur, College of Engineering, Swansea University	Rapporteur

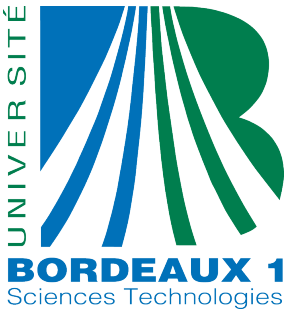

Effects of tidal bores on turbulent mixing:

a numerical and physical study in positive surges

Bruno SIMON

PhD thesis

Supervisors:

Dr Pierre LUBIN

Prof Hubert CHANSON

A thesis submitted for the degree of Doctor of Philosophy at

The University of Queensland in 2013

School of Civil Engineering

and

L'Université de Bordeaux 1 en 2013

École Doctorale des Sciences Physiques et de l'Ingénieur

Résumé

Un mascaret est une onde positive se formant lorsque la marée montante se propage contre le courant dans un estuaire. Bien que ressemblant à des vagues observables près des côtes, les mascarets ont des propriétés physiques différentes. Les mascarets sont des phénomènes fascinants ayant un impact sur l'environnement estuarien et fluvial tel que la faune et la flore, la dispersion et la resuspension de particules, sur les constructions (ponton, pont) ou encore le tourisme. Peu d'étude détaillée sur le terrain existe et l'étude des modèles de mascaret ne permet pas toujours une étude approfondie des processus turbulents. De plus, les mesures de terrain demeurent difficiles à entreprendre à cause de la nature violente du phénomène. Pour cette thèse, l'hydrodynamique des mascarets est étudiée par des mesures en canal expérimental ainsi que des simulations numériques en utilisant un modèle idéalisé d'onde positive. Alors que les expériences en canal offrent une méthode rapide et précise pour accéder à certaines propriétés de l'écoulement, les simulations numériques donnent des informations détaillées sur la structure de l'écoulement. Néanmoins, les simulations numériques ont besoin de données expérimentales détaillées pour reproduire les expériences ainsi que pour valider les méthodes numériques. Dans cette étude, les deux aspects numérique et expérimental sont traités et leur complémentarité est mise en avant

L'étude en laboratoire a été réalisée à The University of Queensland dans un canal rectangulaire partiellement recouvert par des graviers collés sur le fond. Une étude détaillée des propriétés de l'écoulement avant et après génération de l'onde fut réalisée. Les propriétés de l'écoulement permanent ont été mesurées avec un tube de Pitot et des vélocimètres acoustiques Doppler (ADVs). Pour la génération de l'écoulement instationnaire, la fermeture rapide d'une porte située en aval du canal créait une onde positive se propageant contre le courant. L'écoulement instationnaire fut systématiquement étudié en répétant les expériences jusqu'à 25 fois afin de réaliser des moyennes d'ensemble. Les propriétés de surface libre ont été étudiées pour plusieurs types d'ondes allant de vagues lisses et ondulées à des ondes déferlantes. Ces mesures ont montré des fluctuations importantes de la surface libre durant le passage de l'onde en accord avec des mesures antérieures. Des mesures de vitesses ont été réalisées avec un ADV mesurant à 200 Hz. L'étude d'ondes positives déferlantes a montré que pendant et après le passage de l'onde, une forte diminution de la vitesse de l'écoulement initial avait lieu, associé à une inversion de la vitesse près du fond, tandis que les ondes ondulées induisaient une diminution plus faible de la vitesse de l'écoulement. Pour les modèles de mascaret ondulé et déferlant, la vitesse verticale suivait l'évolution de la dérivée temporelle de la surface libre. Les mesures de vitesses montraient aussi des fluctuations plus importantes au passage de l'onde. Ces fluctuations induiraient un fort mélange turbulent. La turbulence dans l'écoulement a aussi été étudiée par des corrélations doubles en deux points afin de calculer des échelles intégrales temporelles et spatiales de la turbulence. Les échelles spatiales avaient des longueurs similaires dans l'écoulement stationnaire et instationnaire, cependant les échelles temporelles étaient plus grandes dans l'écoulement instationnaire. Les expériences ont aussi été limitées par l'instrumentation puisque des interactions entre les sondes diminuant la précision des mesures avaient lieu lorsque les deux ADVs étaient proches l'un de l'autre.

L'étude numérique a été réalisée en utilisant le code de mécanique des fluides numériques (CFD)

Thétis développé au laboratoire I2M de l'Université de Bordeaux. Les configurations des simulations numériques étaient basées sur des expériences d'onde positive ondulée réalisées en canal indépendamment de la présente étude (Chanson, 2010a,b). Les simulations numériques ont été réalisées par la résolution des équations de Navier-Stokes incluant un modèle de turbulence pour des écoulements diphasiques donnant ainsi accès à la description complète du phénomène. La turbulence était modélisée par un modèle de simulation des grandes échelles. La surface libre était suivie par une méthode de volume de fluide. Des simulations en deux et trois dimensions ont été réalisées afin d'étudier l'évolution détaillée de l'écoulement lors de la propagation d'ondes positives ondulées dans différentes configurations initiales. Plusieurs configurations en deux et trois dimensions ont été utilisées pour valider et vérifier les capacités du code de CFD. Les résultats des simulations bidimensionnels ont confirmé certains résultats expérimentaux. Des zones de forte inversion de la vitesse près du fond ont pu être observées. Les simulations en trois dimensions ont été réalisées avec et sans turbulence dans l'écoulement initial. Une méthode de génération synthétique de la turbulence (Jarrin, 2008) a été ajoutée au code afin de recréer une turbulence réaliste se propageant dans l'écoulement initial. Les différents effets de la propagation d'une onde positive sur un écoulement initial turbulent et non turbulent furent comparés avec une attention particulière portée sur le fond du domaine et les parois latérales. Les simulations ont montré l'apparition d'une forte inversion de la vitesse près du fond et des parois latérales, créant un fort cisaillement et générant de la turbulence dans certaines configurations initiales. De plus, il fut observé que la présence d'une turbulence initiale dans l'écoulement, bien que changeant peu l'apparence de la surface libre, avait un effet important sur les vitesses dans l'écoulement. Ces simulations numériques sont les premières simulations d'onde positive ondulée avec un écoulement initial turbulent.

Les résultats expérimentaux et numériques offrent des méthodes précises et complémentaires pour quantifier les informations sur l'écoulement et analyser la structure de l'écoulement durant la propagation d'onde positive. Dans un mascaret ondulé, le fort cisaillement observé

près des parois et amplifier par les ondulations pourrait induire un affouillement du fond et des berges lors du passage des ondes. Les résultats obtenus sont un pas vers une meilleure compréhension des processus prenant place durant les mascarets et pourrait, par exemple, être utilisé pour suivre le morphodynamisme des estuaires soumis au mascaret. Une meilleure compréhension des mascarets pourrait améliorer la gestion de l'environnent estuarien. Par exemple, les opérations de dragage et les constructions (digue, pont, ponton) pourraient être réalisées à des emplacements qui amélioreraient la sécurité pour le trafic fluvial tout en préservant le phénomène, contrairement au mascaret de la Seine qui a presque disparu après des travaux d'emménagement de l'estuaire. Le résultat obtenu sur la turbulence et le mélange observé pourraient être utilisés pour aider à la préservation d'espèces qui dépendent de la turbulence générée par le mascaret pour se nourrir et se reproduire.

Abstract

Tidal bores are positive surges created by the flooding of tides inside estuaries and rivers. They propagate upstream in an estuary sometimes as several metre high waves. Tidal bores are fascinating phenomenon with some impact on the wildlife, the mixing and re-suspension of sediments, and river constructions. Field studies remain challenging due to the violent nature of some bores. Herein, the hydrodynamics of tidal bores was investigated in a complementary study with experimental measurements and numerical simulations of idealised models of tidal bores. While laboratory experiments offer an accurate way to measure the flow properties, numerical simulations provide rather detailed information on the hydrodynamics of bores. These simulations require detailed experimental data to accurately replicate the experiments and validate the numerical methods.

Investigations were conducted at the University of Queensland in a large rectangular channel partially covered by a fixed gravel bed. The steady flow condition properties were investigated using a Pitot tube and acoustic Doppler velocimeters (ADVs). The unsteady flow conditions were obtained by the fast closure of a downstream gate, which led to an upstream propagating bore. Free surface characteristics were studied for several types of bores, from undular to breaking. Those measurements showed large free surface fluctuations during the bore passage in agreement with earlier findings. Velocity measurements were conducted at high frequency

(200 Hz). In breaking bores, the ensemble averaged data exhibited large velocity reversals near the bed beneath the bore front and in its wake, whereas, in undular bores, a lesser deceleration was observed. The vertical velocity data trend closely followed the water depth time derivative for both breaking and undular bores. Overall, the velocity measurements displayed large velocity fluctuations during the passage of the bore which were believed to induce strong turbulent mixing. The turbulence was further investigated by a two point correlation technique to estimate both turbulent integral time and length scales. The turbulent integral length scales values were similar in the steady and unsteady flows, whereas the turbulent time scales were larger in the unsteady flow. The experiments were limited by the instrumentation since the ADV systems interacted with each other and lacked accuracy for measurements performed in the near vicinity of physical boundaries.

A numerical investigation was then performed using the computational fluid dynamics (CFD) code Thétis developed in the I2M laboratory of the Université de Bordeaux. Numerical simulations reproduced experiments performed in laboratory prior to this study (Chanson, 2010a,b). The fluid was modelled by the Navier-Stokes equations in their incompressible two-phase form. The turbulence model used a large eddy simulation and the interface air-water was tracked by using a volume of fluid model. Two dimensional and three dimensional simulations were performed to study the complete flow evolution beneath undular bores for different bore configurations. Two and three dimensional simulations were used to validate the capacity of the CFD code. The analysis of the two dimensional simulations confirmed some previous experimental findings, detailing data unreachable by ADV units and showed the strong effects of the bore on the flow velocity, including intense flow reversals very close to the bed. Three dimensional simulations were conducted with and without initial steady turbulent conditions. A synthetic eddy method (Jarrin, 2008) was implemented to recreate realistic turbulent steady flow conditions. The different effects of turbulent and non-turbulent flows were analysed with a particular

focus on the lateral walls and channel bed effects. The simulations showed a strong flow reversal very close to the bed and the lateral walls, inducing a strong shear and turbulence generation.

The findings of both experimental and numerical studies offered accurate and complementary methods to quantify information on the flow evolution and to analyse the flow structure during positive surge propagation. The strong shear next to the wall would induce some scouring in rivers with a movable bed, associated with sediment re-suspension. These results are a step toward a better understanding of tidal bores and could be used to explain pollutant dispersion in rivers affected by tidal bores. A better understanding of the bore hydrodynamics would improve the management of estuarine systems. For example, dredging operations or river constructions (pontoon, dyke or bridge) could be performed at selected sites to ensure the safety of navigation and infrastructure as well as to preserve the phenomenon, unlike the Seine River bore which nearly disappeared after estuarine settlements. These findings might also help with the preservation of wildlife for which feeding and breeding depend on tidal bore turbulent mixing.

Declaration by author

This thesis is composed of my original work, and contains no material previously published or written by another person except where due reference has been made in the text. I have clearly stated the contribution by others to jointly-authored works that I have included in my thesis.

I have clearly stated the contribution of others to my thesis as a whole, including statistical assistance, survey design, data analysis, significant technical procedures, professional editorial advice, and any other original research work used or reported in my thesis. The content of my thesis is the result of work I have carried out since the commencement of my research higher degree candidature and does not include a substantial part of work that has been submitted to qualify for the award of any other degree or diploma in any university or other tertiary institution. I have clearly stated which parts of my thesis, if any, have been submitted to qualify for another award.

I acknowledge that an electronic copy of my thesis must be lodged with the University Library and, subject to the General Award Rules of The University of Queensland, immediately made available for research and study in accordance with the Copyright Act 1968.

I acknowledge that copyright of all material contained in my thesis resides with the copyright holder(s) of that material. Where appropriate I have obtained copyright permission from the copyright holder to reproduce material in this thesis.

Publications during candidature

Chanson, H., P. Lubin, B. Simon, and D. Reungoat (2010). *Turbulence and sediment processes in the tidal bore of the Garonne River: First observations*. Department Technical Report CH 79/10. Brisbane, Australia: School of Civil Engineering, The University of Queensland, p. 99.

Mouazé, D., H. Chanson, and B. Simon (2010). *Field measurements in the tidal bore of the Sélune River in the bay of Mont Saint Michel (September 2010)*. Department Technical Report CH81/10. Brisbane, Australia: School of Civil Engineering, The University of Queensland, p. 72.

Chanson, H., D. Reungoat, B. Simon, and P. Lubin (2011). "High-frequency turbulence and suspended sediment concentration measurements in the Garonne River tidal bore". In: *Estuarine, Coastal and Shelf Science* 95.2–3, pp. 298–306.

Simon, B., P. Lubin, S. Glockner, and H. Chanson (2011a). "Three-dimensional numerical simulation of the hydrodynamics generated by a weak breaking tidal bore". In: *34th IAHR World Congress, 33rd Hydrology and Water Resources Symposium and 10th Conference on Hydraulics in Water Engineering*. Brisbane, Australia: Eric Valentine, Colin Apelt, James Ball, Hubert Chanson, Ron Cox, Robert Ettema, George Kuczera, Martin Lambert, Bruce Melville and Jane Sargison, pp. 1133–1140.

Simon, B., P. Lubin, D. Reungoat, and H. Chanson (2011b). "Turbulence measurements in the Garonne River tidal bore: First observations". In: *34th IAHR World Congress, 33rd Hydrology and Water Resources Symposium and 10th Conference on Hydraulics in Water Engineering*. Brisbane, Australia: Eric Valentine, Colin Apelt, James Ball, Hubert Chanson, Ron Cox, Robert Ettema, George Kuczera, Martin Lambert, Bruce Melville and Jane Sargison, pp. 1141–1148.

Berchet, A., A. Beaudoin, A. Huberson, G. Rousseaux, B. Simon, and P. Lubin (2013). "Une vision naïve du transport sédimentaire induit par un mascaret ondulant". French. In: *21ème Congrés Français de Mécanique*. Bordeaux, France: AFM, Maison de la Mécanique, 39/41 rue Louis Blanc - 92400 Courbevoie.

Simon, B. and H. Chanson (2013). *Turbulence measurements in tidal bore-like positive surges over a rough bed*. Hydraulic Model Report CH90/12. Brisbane, Australia: School of Civil Engineering, The University of Queensland, p. 176.

Simon, B. and P. Lubin (2013). "Simulation de l'écoulement sous une onde positive ondulée". French. In: *21ème Congrés Français de Mécanique*. Bordeaux, France: AFM, Maison de la Mécanique, 39/41 rue Louis Blanc - 92400 Courbevoie.

Publications included in this thesis

No publications included

Contributions by others to the thesis

None

Statement of parts of the thesis submitted to qualify for the award of another degree

The whole thesis is submitted for the degree of Docteur, specialité: Mécanique, as part of a joint agreement between the University of Queensland and l'Université de Bordeaux 1, France.

Acknowledgements

This study was possible thank to a joint agreement between the Université de Bordeaux 1 and The University of Queensland. I wish to thank both universities, as well as the Institut de Mécanique et d'Ingénierie and the School of Civil Engineering for welcoming me in their facilities.

I acknowledge the funding of my PhD by the Région Aquitaine and the Institut Polytechnique de Bordeaux, as well as a travel grant from the Université de Bordeaux 1. I also acknowledge the ANR project MASCARET for the financial support.

I greatly thank my two supervisors. Hubert Chanson, professor at the University of Queensland, for his patience, support and assistance. He was always available to provide helpful advice. Pierre Lubin, professor at the University of Bordeaux, for trusting in my capacity, letting me perform my research independently and being always available. More than a supervisor, he became a friend.

I also acknowledge the reviewers of my manuscript, Frédérique Larrarte and Dominic Reeve for accepting to review my manuscript, as well as Huber Branger and Serge Huberson for accepting to be part of my jury at my thesis defence with my reviewers.

I thank Valerie Thouard and Jeannette Watson for helping me through the administrative jungle of being a student in two universities on two opposite side of the Earth.

I wish to thank my multiple office mates: Stéphane Glockner for making and keeping the CFD code thètis run smoothly and sharing is office with me. I also thank Nazanin Khezri for sharing the office in UQ with me, sharing her interest for tidal bores and feeding me with cake and Iranian food. I also thank my current office mate Ludovic Osmar.

I also wish to thank all my colleague in France and Australia, in particular, Lucille Furgerot,

Dominique Mouazé, Stefan Felder, Philipp Günther and last but not least Nina Welti.

I thanks my friends for their continuous support and understanding, Élodie, Rémi, Arnax, Christelle, Matatini, Pauline, Suzon, Darren, Helena, Lisa. Thanks a lot.

I thank my housemates from Australia for sharing a year of their life with me and making the stay really fun. An extra thanks goes to Geoff for sharing his wine and taste in music with me and believing I would be a good housemate.

I deeply thank Christelle for her unconditional support, understanding, help and caring, as well as my family.

Mots clefs

Mascaret, onde positive, modélisation physique, simulation numérique, turbulence, écoulement à surface libre, structures cohérentes, simulation des grandes échelles, corrélation double

Keywords

Tidal bore, positive surge, physical modelling, numerical simulation, unsteady open channel flow, turbulence, coherent structures, large eddy simulation, two-point correlation

Australian and New Zealand Standard Research Classifications (ANZSRC)

ANZSRC code: 040608, Surface-water Hydrology, 60%
ANZSRC code: 090509, Water Resources Engineering, 20%
ANZSRC code: 090599, Civil Engineering not elsewhere classified, 20%

Fields of Research (FoR) Classification

FoR code: 0406, Physical Geography and Environmental Geoscience, 60%
FoR code: 0905, Civil Engineering, 40%

Table of Contents

List of Figures

List of Tables

List of Symbols

List of Symbols

Symbol	Description	Units
$\bar{\cdot}$	Average of a variable	
$\langle ., . \rangle$	Turbulent fluctuation operator	
a_w	First wave amplitude	m
$\mathbf{A}$	Cholesky decomposition of the stress tensor matrix	
$\mathbf{B_u}$	Function modelling the boundary condition for the Navier–Stokes equations	
C	Phase function	
C_i	Dimensionless constant in Equation (IV.3) for the i-direction	
C_M	Mixed scale model constant for large eddy simulation	
C_s	Smagorinsky model constant for large eddy simulation	
C_{TKE}	Turbulent kinetic energy model constant for large eddy simulation	
d	Water depth	m
d_0	Initial water depth or low dam reservoir water depth	m
d_1	High dam reservoir water depth	m
d_b	Conjugate water depth in the unsteady flow	m
d_c	Critical flow depth. $d_c = \sqrt[3]{Q^2/(gW^2)}$ for a rectangular open channel	m
$d_{\max}$	Bore water depth beneath the first wave crest	m
$d_{\min}$	Bore water depth beneath the first wave trough	m
d_{EA}	Ensemble averaged water depth	m
d_{PVC}	Elevation above the PVC bed	m
D	Water vein diameter $D = 0.1$ m	m
D_i	Dimensionless constant in Equation (IV.3) for the i-direction	

E	Specific energy defined as: $E = H - z_0$	m
f	Darcy-Weisbach friction factor	
f_{vort}	Frequency of ejection of vortical structure	Hz
$\boldsymbol{f_\sigma}$	Shape function with support $\boldsymbol{\sigma}$	
Fr	Froude number of the unsteady flow, $Fr = (U_b + V_0)/\sqrt{gd_0}$	
g	Gravity acceleration	$\mathrm{m.s^{-2}}$
$\mathbf{g}$	Gravity vector, $\|\mathbf{g}\| = 9.80$ $\mathrm{m.s^{-2}}$ in Brisbane Australia	$\mathrm{m.s^{-2}}$
h_g	Gate opening after closure	m
H_1	Total head read with the Pitot tube	m
H_2	Static head, or piezometric head of Pitot tube	m
$\mathbf{Id}$	Identity matrix	
k_s	Equivalent sand height of bed roughness	m
K	Permeability coefficient	$\mathrm{m^2}$
L	Channel length	m
L_i	Integral turbulent length scale for the velocity component u_i	m
L_w	First wave length measured from first wave crest to the second wave crest	m
M	Size of the mesh for the grid generating turbulence	m
n	Number of iteration	
$\mathbf{n}$	Exterior normal unit vector	
N	Number of eddies for the synthetic eddy method	
p	Pressure	Pa
q	Water discharge per unit width	m
q_{SGS}	Kinetic energy of the subgrid modes for large eddy simulation	$\mathrm{m^2.s^{-2}}$
Q	Second invariant of the velocity gradient tensor, used for visualisation of coherent structures	$\mathrm{s^{-2}}$
Q	Volume flow rate or discharge	$\mathrm{m^3.s^{-1}}$
Re	Reynolds number, $Re = V_0 d_0/\nu$	
Re_b	Reynolds number of the unsteady flow, $Re_b = (U_b + V_0)d_0/\nu$	
$R_{i,j}$	Reynolds stress tensor, $R_{i,j} = \overline{u_i' u_j'}$ of the i and j velocity components	$\mathrm{m^2.s^{-2}}$
R_{ij}^+	Normalised cross-correlation function for the velocity components u_i and u_j	
$\mathbf{S}$	Strain rate tensor, $\mathbf{S} = 1/2\left(\nabla\mathbf{u} + \nabla^T\mathbf{u}\right)$	$\mathrm{s^{-1}}$
S_0	Channel slope. For the experiments, $S_0 = \sin\theta = 0.0077$, for the numerical simulations $S_0 = 0$	

S_f	Friction slope or slope of the total head line	
St	Strouhal number calculated by a quasi-steady flow analogy, $St = f_{vort} d_0/(U_b + V_0)$	
St_2	Strouhal number calculated in the bore, $St = f_{vort} d_b/(V_b)$	
t	Time	s
T	Averaging time for the correlation function	s
T_i	Integral turbulent time scale for the velocity component u_i	s
T_{ii}	Integral cross-correlation time scale for the velocity component u_i	s
$\mathbf{Tr}$	Trace operator of matrix	
T_w	Period of the first wave length	s
u_*	Shear velocity	$\mathrm{m.s}^{-1}$
u_c	Critical flow velocity. $u_c = \sqrt{g d_c}$ for a rectangular channel	$\mathrm{m.s}^{-1}$
$\mathbf{u}$	Flow velocity as a vector with components u_x, u_y and u_z	$\mathrm{m.s}^{-1}$
$\mathbf{u}'$	Velocity fluctuation with components u'_x, u'_y and u'_z	$\mathrm{m.s}^{-1}$
$\mathbf{u}_*^n$	Predicted velocity at iteration n	$\mathrm{m.s}^{-1}$
$\mathbf{u}_\infty$	Velocity set at the boundary condition	$\mathrm{m.s}^{-1}$
$\mathbf{u}_{EA}$	Ensemble averaged flow velocity	$\mathrm{m.s}^{-1}$
U_b	Bore celerity	$\mathrm{m.s}^{-1}$
U_r	Ursell number, $Ur = 2a_w L_w^2/d_b$	
V_0	Initial longitudinal flow velocity	$\mathrm{m.s}^{-1}$
V_1	Flow velocity in the high dam, $V_1 = 0$	$\mathrm{m.s}^{-1}$
V_b	Flow velocity after the bore	$\mathrm{m.s}^{-1}$
W	Channel width, $W = 0.5$ m in the present study	m
x	Longitudinal component	m
x_{inlet}	Location of the channel upstream end	m
$\mathbf{X}$	Point with coordinates (x, y, z)	m
y	Transversal component	m
z	Vertical component	m
z_0	Bed elevation	m
α	Large eddy simulation parameter for the mixed scale model constant	
α_g	Gate angle with the channel bed: $\alpha_g = \pi/2$ when the gate is fully closed	
β_0	Momentum correction coefficient in the steady flow	
β_b	Momentum correction coefficient after the bore passage	

$\boldsymbol{\gamma}$	Friction function	$\mathrm{kg.m^{-3}.s^{-1}}$
δ	Boundary layer thickness	m
δ_0	Distance between correlation points where $R_{ij}^{+}(\delta_{0,}\tau) = 0$	m
$\boldsymbol{\delta}$	Distance between correlations points with components δ_x, δ_y and δ_z	m
Δ	Mesh grid space step with components Δ_x, Δ_y and Δ_z	m
Δt	Time step	s
$\bar{\Delta}$	Large eddy simulation filter width	m
ϵ	Distribution of the eddies intensity for the synthetic eddy method	
θ	Angle between the channel bed and the horizontal positive downwards	
κ	Von Karman constant. $\kappa = 0.4$	
μ	Fluid viscosity	Pa.s
$\mu_t = \nu_t$	Turbulent viscosity for the large eddy simulation	Pa.s
ρ	Fluid density	$\mathrm{kg.m^{-3}}$
σ	Surface tension between air and water	N.m^{-}1
$\boldsymbol{\sigma}$	Eddies size for the synthetic eddy method	m
τ	Correlation time shift	s
τ_0	Correlation time shift such as $R_{ij}^{+}(\delta, \tau_0) = 0$	s
τ_m	Correlation time shift such as $R_{ij}^{+}(\delta, \tau_m) = \max_{\tau} R_{ij}^{+}(\delta, \tau)$	s
$\boldsymbol{\tau}$	Subgrid tensor	$\mathrm{m^2.s^{-2}}$
φ	Pressure increment	Pa
ω	Flow vorticity	$\mathrm{s^{-1}}$
$\boldsymbol{\Omega}$	Vorticity tensor	$\mathrm{s^{-1}}$

List of Abbreviations

ADCP	Acoustic Doppler current profiler
ADM	Acoustic displacement meter
ADV	Acoustic Doppler velocimeter
BDF	Backward differential formulae
CFD	Computational fluid dynamic
CTD	Conductivity, temperature and depth
EA	Ensemble average
KdV	Korteweg & de Vries

LDV	Laser Doppler velocimetry
LES	Large eddy simulation
MAC	Marker and cell
max	Maximum
min	Minimum
MPI	Message passing interface
MS	Mixed scale
PIV	Particles image velocimetry
PLIC	Piecewise linear interface construction
PMMA	Polymethyl methacrylate
PT	Pitot tube
PVC	Polyvinyl chloride
RANS	Reynolds-averaged Navier–Stokes
RMS	Root mean square
SEM	Synthetic eddy method
SGS	Subgrid-scale
SLIC	Simple linear interface calculation
SNR	Signal to noise ratio
SSC	Suspended sediment concentration
TKE	Turbulent kynetic energy
TVD	Total variation diminishing
VITA	Variable-interval time average
VOF	Volume of fluid

I

Introduction

When the sun, moon and earth form a line, the tidal forces are reinforced and the tidal range is at its maximum forming what is called a spring tide. Spring tides are the best moments to observe, in rivers or estuaries, a unique natural phenomenon: a tidal bore. Spring tides are also for some surfers the season they decide to abandon the coast and its waves, to migrate inland and surf the unique natural phenomenon that is a tidal bore. Surfers post on internet videos of their uncommon surf sessions in rivers; looking for videos with keywords such as, tidal bore, mascaret, seven ghost bore, pororoca or silver dragon bore, will provide many examples of surfers riding the unusual waves that are tidal bores. Figure I.1 presents three photos of tidal bores with and without surfers.

Tidal bores can be explained by looking through the typical journey of tidal bore surfers. Firstly, surfers wait for the bore with an Eulerian view of the initial flow. Secondly, they ride the bore with a pseudo-Lagrangian view of the flow. And lastly, they paddle back to the bank experiencing the effect of the bore passage. Therefore, riding a tidal bore could be decomposed in three stages as follow.

The first step is to prepare and wait for the bore. Surfers have to arrive early enough not to miss the bore. They estimate the time of bore passage using tide table since a tidal bore is a wave created by the upstream propagation of the leading edge of the rising tide upstream the river (Bartsch-Winkler and Lynch, 1988; Chanson, 2004c; Lynch, 1982). But how does

(a) Undular tidal bore of the Dordogne river at Saint-Pardon (France), estimated height: 60-70 cm

(b) Tidal bore partially breaking and partially undular of the See River (France)

(c) Breaking tidal bore near the bank of the Garonne River, Arcins (France)

Figure I.1: Photographs of tidal bores looking downstream at the approaching bore (Photos: Bruno Simon)

the tide creates tidal bores? Consider a symmetrical tide, as it progresses against the river flow in a slowly converging estuary, the tidal wave loses its symmetry resulting in a flood tide shorter than the ebb tide. The large and rapid flood generated by the tide creates a situation of hydrodynamic shock between the low water depth in the river and the incoming flood tide from the ocean. Figure I.2 illustrates the change happening to a tidal cycle as the tide enters an estuary and propagates upstream a river ultimately leading to the formation of a tidal bore. (Figure I.2b). It is the case, for example, in the Bay of Mont Saint-Michel, where the semi-diurnal tide loses its symmetry after propagating in the estuary. This results in a flood tide lasting only 30 min where a 0.5 m high tidal bore is observed (Furgerot et al., 2013). In the meantime, the tidal range drops from 14 m at the estuary mouth to 1.5 to 2 m at the observation point of the study, 15 km upstream the estuary mouth (Furgerot et al., 2013). The shape of the estuary can also induce an amplification of the tidal range as observed in the Garonne River (Chanson et al., 2011) or the Qiantang Estuary (Fan et al., 2012). In summary, a tidal bore might appear when the tidal flood range and the period of flood are respectively

large and short enough, and its passage can be predicted by tide table.

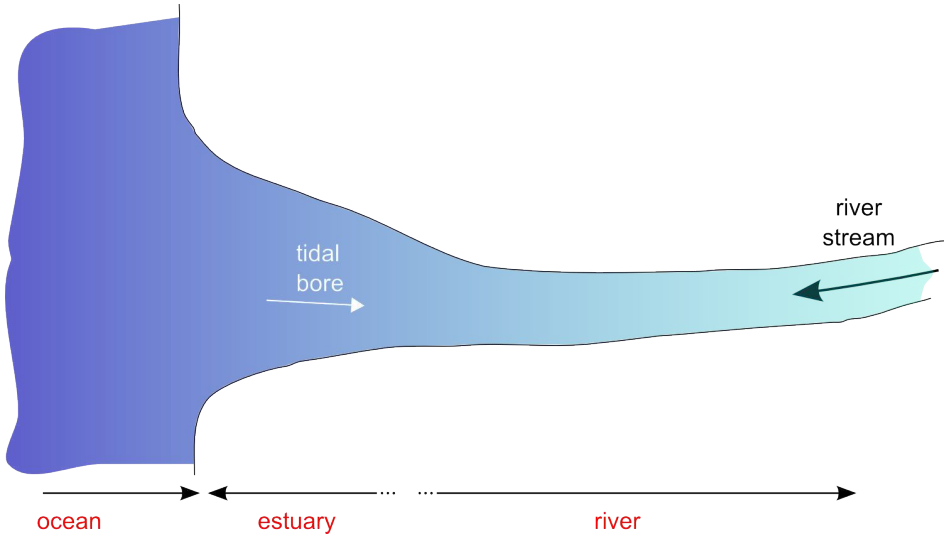

(a) Simplified form of a convergent estuary with a tidal bore

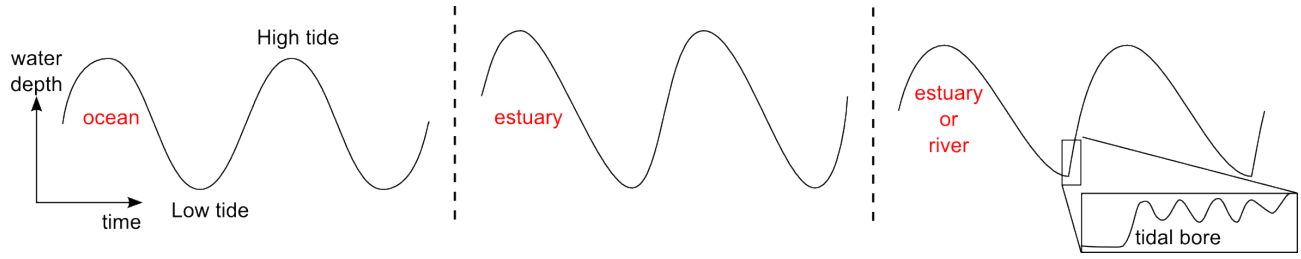

(b) Typical tidal cycle evolution as the tide propagate from the ocean to the river leading to the appearance of a tidal bore, with zoom on a tidal bore

Figure I.2: Typical evolution of the tidal wave as it enters in an estuary leading to the formation of a tidal bores

For their preparation, surfers also need to choose the ideal spot where the wave can be caught. Tidal bores do not propagate as a uniform front. Wave breaking takes place on the bank and the bore might disappear on the deepest part of the river (Figure I.1b). The location is usually chosen after sightseeing. Surfers also use the stream of the river to get to their spot using the current to avoid paddling and to be carried downstream. Even when surfers come for the right tidal conditions, at the right time and found the good spot, a moment of anxiety always surges during the wait of the bore, "Will the bore appear today? Is it the right spot? Will the bore be strong enough to give me a ride?" are questions in surfer minds. This anxiety is amplified by the silence preceding the bore. There is almost no sound prior to the arrival of the bore, contrarily to ocean waves, where a constant rumbling noise of the wave breaking can be heard, the river is a quiet environment. Moreover, the wave only appears as many times a day as there are low tides in the river. For surfers, this means they have a chance to catch the bore

at best every 12 hours. The apparition of tidal bores is also sensitive to external phenomenon; some weather disturbances such as wind and waves for example have an impact on the bore characteristics and particularly its height (Gordon, 1924). Ultimately, after long minutes of waiting, the sound of the bore is finally heard. The breaking of the bore on the river banks makes a surprisingly loud noise in contrast with the silence of the river (Chanson, 2011a, Chap. 4; Moore, 1888). With the bore approaching, surfers start paddling.

The second step for surfers is to surf the tidal bore, for those who caught the wave... The wave can be a breaking wave or an undular wave followed or not by a wave train (Figures I.1 and I.3) with an increase of the mean water level of the river. The shape of the bore also varies toward the river width by being breaking or undular (Figure I.1b). Surfers try to stay on the bore front where the undular wave is steep in order to enjoy the gliding sensation of the smooth curvature provided by the undular front. Needless to say it is not an easy task to stay on the tidal bore for it changes its shape with the local bathymetry, breaking in the shallower part and eventually disappearing in the deepest part of the river. In the Petitcodiac River, Canada, surfers have managed to stay on the wave for more than 30 minutes, over a distance of 20 km. In the Amazon River, tidal bores were observed to form as far as 150 km inland (Bartsch-Winkler and Lynch, 1988) with successive disappearance and reappearance of the wave. For surfers, the ride is long, whereas, for observers on the bank, the show only lasts about 1 or 2 minutes as the bore can propagate at a celerity generally close to 4-5 $m.s^{-1}$ (15-18 $km.h^{-1}$) and sometimes up to 9 $m.s^{-1}$ (Bartsch-Winkler and Lynch, 1988). The observers are thus left on the spot, only being able to witness the water level increases after the bore passage (Figures I.3).

One difference between coastal waves and tidal bores is that surfers get to "share" the wave. For coastal waves, “surfing rules” limit the number of surfers to one per wave, whereas for tidal bores, as many surfers as spatially possible can surf the wave. Sometimes hundreds of surfers can be seen sharing the same wave making this a unique performance for observers on the river bank (Figure I.4). Figure I.4 only shows about 40 surfers on the wave, as many others were left behind, either fallen early or simply unable to catch the wave. Another difference is that surfers have to remain careful to avoid the river debris or hazard hidden by the murky water. Surprisingly, surfers are not the only one waiting for the wave. As a matter of fact, other animals, such as swans were seen to ride on tidal bores (Chanson, 2011a, Fig. 6-2(E-F), p. 130).

The third and last step comes with the end of the ride. The ride usually ends because either the surfer falls or because the river is locally too deep and the bore disappears. Once finished, the surfer has to paddle back to the bank against the river flow since the flow generally changes direction after the bore passage. The increase of the water level together with the flooding of

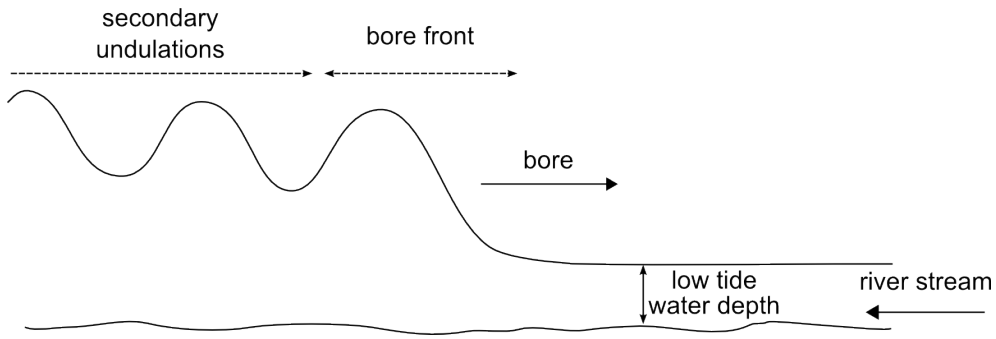

(a) Undular bore

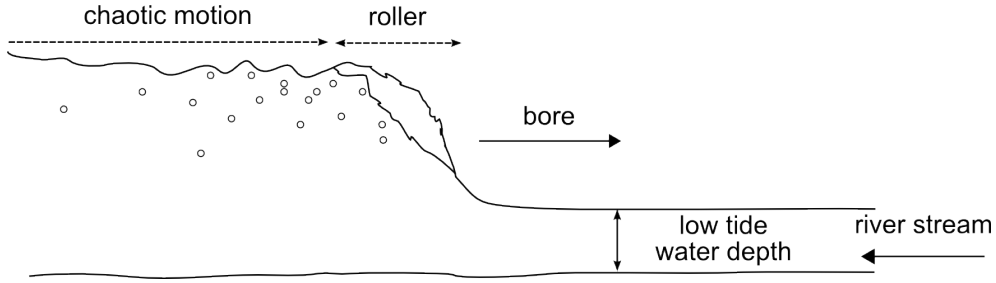

(b) Breaking bore

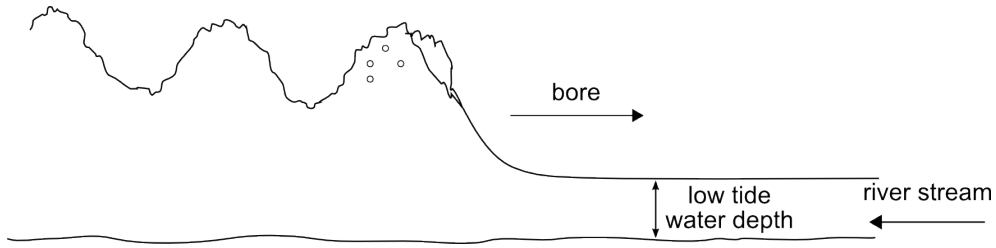

(c) Transitory bore, breaking bore with undulations

Figure I.3: Typical shape of tidal bores propagating upstream rivers

the estuary by the tide induces an intense change in the river flow. The normal course of the river resumes before the high tide with the water flowing downstream again (Dyer, 1997). For surfers, the paddling to the bank is made even more difficult by the increase of turbulence of the water. The turbulence is induced by the sudden flow change combined with the undulations or the breaking of the bore. Both the turbulence and mixing are visible by large turbulent patches or 'clouds' of sediment reaching the surface (Chanson, 2011a). The river is also made more dangerous by the presence of large debris for bores have the power to uproot trees (La Condamine, 1778). Note that the power of tidal bores has been known for hundred of years. Along the Qiantang River, banks were even reinforced by constructing strong seawall as early as A.D. 1540 in order to protect the land (Jiang et al., 2014).

The turbulence and the sediment mixing, which can be a burden for surfers, are in fact an asset for animals (fish, bird, marine mammal) since it facilitates the search for food and enables the

Figure I.4: Tourists watching and surfers riding the tidal bore in the Dordogne River, Saint-Pardon (France) (Photo: Bruno Simon)

proliferation of certain species through the scattering of their eggs (Rulifson and Tull, 1999). Fish, whales and seals can be observed following tidal bores (Ezer et al., 2008; Mouazé et al., 2010) looking for resuspension of food in the water. Beluga whales, for example, were observed in the Cook Inlet, Alaska, an estuary with tidal bores. The whales were not seen surfing the wave but they do take advantage of the large tides in order to reach areas that are not accessible during low tide and to feed on fish present in those areas (Ezer et al., 2008).

Through the previous examples, it was seen that tidal bores are not only significant for surfers. Bores have consequence on the wildlife and also cities development: for example, in cities along the Dordogne River, France, and along the Qiantang River, China, special facilities were built in order to welcome surfers and observers. For spring tide conditions in summer, festivals are sometimes organised around the tidal bore (Saint Pardon, France, or in China). Overall, the phenomenons have an impact on tourism, economy, the ecosystem, navigation and river constructions. Considering the impact of the bore on the estuarine system, there are rather few studies on the phenomenon as detailed in Chapter II.

Herein, a detailed scientific study was conducted on tidal bores. The objectives of this work were to get a better understanding of tidal bore hydrodynamics by the study of positive surges using numerical and experimental modelling. The experimental measurements gave detailed information on the velocity field beneath bores in reproducible configurations. The unsteady

turbulent flow field, including turbulent intensities and turbulent scales, were measured experimentally for a range of flow conditions based on a Froude similitude. The study provided the first measurements of evolution of the turbulent integral scales during bores. However, the experimental methods gave detailed information only at the measurements points. Numerical simulations gave access to the complete bores hydrodynamic, albeit the methods must be validated with various configurations including undular bores. For the first time, numerical simulations of undular bores were realised by solving the Navier-Stokes equations in both two and three dimensions. The analysis of the numerical data showed detailed effects of undular positive surge passage on both turbulent and non turbulent steady flow in two and three dimensions. Some findings of this study, such as the changes of turbulent scales, the generation of turbulence from the channel bed and the strong shear created during bore propagation, have direct applications on estuarine systems.

The manuscript is composed of seven chapters including this introduction. Chapter II presents a bibliographic review about tidal bores. Major findings of scientific observations and field studies on tidal bores are detailed, as well as experimental and numerical studies. Chapter III presents the methodology used to conduct the experimental and numerical studies in this work. Chapter IV presents detailed analysis of the data collected during the experimental study. This study of positive surges presents the results of experimental investigations with a focus on free surface properties and unsteady turbulent velocity characteristics under controlled flow conditions using ensemble-averaged data sets. The measurement data were performed over a fixed gravel bed and conducted at two different scales to test the Froude number dynamic similarity in terms of potential viscous scale effects. In Chapter V, the accuracy of the numerical methods was tested on two dimensional and three dimensional cases. A case of two dimensional undular dam break wave propagation was simulated. The code was thoroughly validated with experimental data of undular bores propagating against a steady flow. The model used to generate a turbulent inflow condition was validated with experimental data of grid generated turbulence. Chapter VI concerns the study of undular bores generated by numerical simulation. A detailed description of the effect of the propagation of undular bore was performed. The three dimensional simulations was performed with bores propagating on initially non-turbulent and turbulent steady flows by using a synthetic inflow turbulence. A detailed analysis of the bore effects on the steady flow was performed. Finally, the conclusion (Chapter VII) resumes the findings and proposes possible work for future studies. In addition, four appendices (A, B, C and D) contain further complementary data of both experimental and numerical studies.

II

Literature review

II.1 Chapter overview

To date, the detailed effects of tidal bores on estuaries and rivers remains poorly known. The flow changes and other effects induced by the passage of tidal bores have not been studied in detail, although, recent researches brought lots of information on the tidal bore dynamics.
This chapter starts by describing scientific observations and field studies performed during tidal bores. Theories estimating the generation and propagation of bores are detailed and compared with theories on similar phenomenon. The physical modelling of bores in the laboratory is summarised with an accent put on the flow changes. Then, the numerical works on tidal bores are detailed. Finally, the areas requiring further investigations are identified.

II.2 Field studies: observations and detailed measurements

II.2.1 Observations

Tidal bores are observed in many countries. A catalogue on the worldwide locations of reported tidal bores can be found in Bartsch-Winkler and Lynch (1988) and Chanson (2011a, p. 155).

Reported observations of tidal bores mainly present the basic free surface characteristics of bores, such as water depth, bore celerity and other free surface properties. Some observations and field studies are reported in Table II.1 with some bore details and measurements. Some other information obtained with observations of tidal bores can be the location where a bore forms, how it propagates and what noticeable effects it has on the river. All reported observations show that bores happen in a vast diversity of conditions and have different effects on the estuary dynamics (Table II.1). It is not always easy to differentiate which conditions are coincidental and which are necessary for the bore existence.

Some literature reports that tidal bores require a large tidal range, superior to 4-6 m, to appear (Chanson, 2011a). In some estuaries, the tidal range leading to the development of a bore can be higher than 15 m. Two famous examples are found in the Bay of Fundy, Canada and the Bay of Mont-Saint Michel, France (Archer, 2013). But smaller tidal ranges can also generate tidal bores. In the Qiantang River, the tidal range at the open sea is 2-3 m high (Fan et al., 2012). In the estuary, the range increases to 5-6 m high under the constraint of the specific estuary shape and the river flow. As a result, a several metre high tidal bore appears (Fan et al., 2012). Usually, the strongest and largest tidal bores appear for spring tide conditions when the moon, the sun and the earth are close to alignment. But bores can also be seen for smaller tide conditions as reported in the Garonne River, France (Bonneton et al., 2011) or flood conditions (Reungoat et al., 2012). However, bores always appear when the tidal wave is strongly asymmetrical with a short flood tide and a long ebb. For example, Furgerot et al. (2012) studied tidal bores where the flood tide lasted $\approx$ 30min with an ebb tide lasting $\approx$ 11h45min. Similarly, the study by Fan et al. (2012) was conducted at a site where the flood lasted $\approx$ 1h30min and the ebb $\approx$ 10h45min. Only one study tried to link the tidal asymmetry to the tidal bore apparition (Mazumder and Bose, 1995, see section II.3).

The bore celerity and shape will be different depending upon the estuary but also depending on the distance of propagation. Some bores can occur as far as 150 km inland or be 6 m high (Bartsch-Winkler and Lynch, 1988). Such bores were even observed in recent scientific investigations (Pan and Lu, 2011). Studies reported 3 m high bores in the Amazon River, Brazil (Branner, 1884; La Condamine, 1778) and in the Qiantang River, China (Moore, 1893). These bores are sometimes the topic of TV documentaries and surf videos. Smaller bores are seen in the Severn River, UK (Cornish, 1900, 1934), the Petitcodiac River, Canada (Brownlie, 1901), the Hooghly River, India (Chugh, 1961), or the Changjiang Estuary (Chen et al., 2003). Measurements on small bores, 10-20 cm high, were also conducted (Uncles et al., 2006).

The celerity of bores varies greatly (Table II.1). A celerity of 9 $m.s^{-1}$ was measured for a bore in the Hooghly River (Chugh, 1961) and 3.8 $m.s^{-1}$ for a bore with the same size in the Petitcodiac River (Brownlie, 1901). Nonetheless, several bores were reported to propagate with a celerity

close to 3 to 4 m.s^{-1} (Bartsch-Winkler and Lynch, 1988).
Despite all those variations, bores always have marked effects on the river. The river banks are washed by the passage of the bore. The largest bores can even uproot trees close to the banks (Branner, 1884). The water gets murky after the passage of the bore due to the large turbulence and mixing in the flow. Studies not directly focused on bores have shown this tendency. Some fish species were observed to use the strong mixing properties of tidal bores to spawn (Paramore and Rulifson, 2001; Rulifson and Tull, 1999). Tidal bores also impact the transport and deposition of pollen and other palynomorphs (organic microfossils) in the estuary and river system (Gastaldo, 2012; Laut et al., 2010). Those effects can even be seen in the sediment of the estuaries. In the Bay of Mont-Saint Michel, the sediment deposits in layer forming specific patterns under the tidal dynamics and the bore passage deforms the layer shapes (Tessier and Terwindt, 1994). Ancient bores from the Jurassic that have disappeared nowadays could even be rediscovered by analysing the sediment deposits (Martinius and Gowland, 2011).
The dynamics inducing the tidal bore is basically the tide, but the formation and propagation of bore is also sensitive to the estuary conditions such as the flow and the bathymetry. Shallower water will contribute in the formation of a larger bore. Studies conducted in the Garonne River (Chanson et al., 2011; Reungoat et al., 2012) were performed for two different flow conditions with one study taking place shortly after a flood. It resulted in the observation of a smaller bore, almost not visible, after the flood (Reungoat et al., 2012). External conditions, such as wind, wind wave, rain and atmospheric pressure can also impact the celerity or the height of the bore. In the USA, a 1 m high bore was observed in the Colorado River (Gordon, 1924). The expedition learned from local fishermen that the bore could reach 3 m high. Because of particular weather and river conditions, the bore was significantly smaller than expected despite the large tidal range during that expedition (Gordon, 1924). This is an example showing that the phenomenon is fragile and very sensitive to river changes and local conditions. Bores have appeared and disappeared after river management works. For example, the tidal bore in the Ord River, Australia (Wolanski et al., 2001) appeared after the construction of a dam upstream the river. Some others have nearly disappeared, like the bore in the Seine River after river management works (Musset, 1955).
The previous studies mainly reported visual observations of tidal bores. They gave qualitative information of tidal bores properties and presented some effects of the phenomenon on rivers and estuaries. Nonetheless, some basic details of the flow are missing for a more 'in depth' analysis of the phenomenon. More detailed field studies, as presented in the following section, gave precious information on the change happening to the flow during the passage of the bore.

Table II.1: Observations and field studies on tidal bores

Location and reference	Bore elevation m	Bore celerity m/s	d_0 m	Shape and Froude	Velocity measurements	Free surface measurements	Remarks
				Observations			
Amazon River, Brazil (La Condamine, 1778)	3	/	/	U – B	/	/	Visual observations
Qiantang River, China (Moore, 1893)	1 – 4	5 – 12	4	B	/	/	Visual observation + photographs
Severn River, UK (Cornish, 1900, 1934)	1 – 1.5	3 – 4.5	/	U – B	/	/	Visual observations, $L_w \approx 9$ m, $a_w \approx 0.6$ m
Petit Codiac river, Canada (Brownlie, 1901)	1	3.8	/	B	/	/	Visual observations
Colorado River, Mexico (Gordon, 1924)	1*	3.5	/	U	/	/	Visual observations, $L_w = 6$ m
Seine River, France (Musset, 1955)	4 – 5	7 – 8	/	U – B	/	/	Visual observations
Hooghly River, India (Chugh, 1961)	0 – 1.5	7 – 13	3 – 8	U – B	Yes, but instrumentation not detailed		Tide tables and tidal bore observations
Shubenacadie Estuary, Canada, (Rulifson and Tull, 1999)	0.2 – 0.5	/	/	/	/	/	Study of fish spawning, visual observations
Changjiang Estuary, China (Chen et al., 2003)	0 – 1	2 – 4.5	2 – 4	U – B < 1.4**	/	/	Visual observations, SSC from 15.9 to 2.5 kg^2/m^3 2h after bore
				Field studies			
Seine River, France (Partiot in Darcy and Bazin, 1865)	2 – 2.5	/	1 – 7	/	Immersed buoys	/	$a_w \approx 0.8$ to 1 m, delay of flow reversal: up to 145 s
Mearim river, Brazil (Kjerfve and Ferreira, 1993)	0.8	7.2	1 – 3	U – B 3.5 and 4.5 ***	InterOcean S4 current meter equipped with CTD + depth measurement (sampling 2 Hz)		Salinity, temperature

Continued on next page

Table II.1 – *Continued from previous page*

Location and reference	Bore elevation m	Bore celerity m/s	d_0 m	Shape and Froude	Velocity measurements	Free surface measurements	Remarks
Dordogne River, France (Navarre, 1995)	1.1 – 1.5	4	1 – 1.15	U – B	Current meters (sampling 10 Hz)	Filmed gauges	Water samplings
Dee River, UK (Simpson et al., 2004)	0 – 0.6	4.1	1	U – B < 1.8	ADCP	Tide gauges	TKE analysis
Daly Estuary, Australia (Wolanski et al., 2004)	0.2 – 0.6	4.7	3	U 1.22	InterOcean S4 current meter and ADCP	Rigo and Aqualab Diver	SSC, salinity and temperature
Humber Estuary, UK (Uncles et al., 2006)	0.1 – 0.2	/	1.6	U	Vertical profile	Instrument not detailed	Study not focused on the tidal bore passage
Sélune river, France (Mouazé et al., 2010)	0.4	2	0.3 – 0.4	B 2.3 – 2.5	Vector ADV (sampling 64 Hz)	Filmed gauge	Analysis of the backscatter intensity
Garonne River, France (Chanson et al., 2011)	0.4 – 0.5	4.2 – 4.5	1.7 – 1.8	U 1.2 – 1.3	Vector ADV (sampling 64 Hz)	Filmed gauge	SSC measurements with ADV
Garonne River, France (Bonneton et al., 2011)	0.7 – 1.3	4.3 – 5.4	1.5 – 5.2	U – B 1.2	/	Pressure and altimeters	Not presented: velocity and turbidity data
Qiantang river, China (Fan et al., 2012)	2	/	/	B	ADCP (sampling 0.1 Hz)	Optical backscatter sensor	SSC, grain-size, conductivity, temperature
Sée River, France (Furgerot et al., 2012)	0.5	3 – 4.5	0.7 – 1.3	U – B 1 – 1.8	Vector ADV (sampling 64 Hz)	Filmed gauge, pressure	Vertical SSC profiles, turbidity
Garonne River, France (Reungoat et al., 2012)	0.5	3.9 – 4.6	2.7	U 1 – 1.2	microADV (sampling 50 Hz)	Filmed gauge	SSC, salinity, temperature

Notes: * 3 m bores seen by locals on other days (Gordon, 1924), ** Froude number calculated as $V_0/(\sqrt{gd_0} - U_b)$ (Chen et al., 2003), *** Froude number calculated as $U_b/\sqrt{gd_0}$ (Kjerfve and Ferreira, 1993), ADCP: Acoustic Doppler current profiler, d_0: initial water depth, g: gravity acceleration, V_0: flow velocity before the bore, U_b: bore celerity, $Fr = (U_b + V_0)/\sqrt{gd_0}$: Froude number, a_w: wave amplitude, L_w: wave length, U: undular bore, B: breaking bore, /: information not available

II.2.2 Fields measurements

Some of the first bore study of the flow within a tidal bore were probably realised in the Seine River when the phenomenon was still several meter high (Babinet, 1855; Darcy and Bazin, 1865). Flow velocity measurements were conducted using a system of buoys and a flow reversal was observed to happen one minute after the passage of the bore front next to the bottom and one more minute later next to the free surface (Partiot in Darcy and Bazin, 1865).
Recently, with the generalisation of electronic instrumentation, more detailed studies took place, even if their number is still limited. Kjerfve and Ferreira (1993) performed measurements in the Rio Mearim, Brazil, with current meters and conductivity, temperature and depth (CTD) probes. They observed a 0.8 m bore with a flow reversal beneath the bore. The salinity increased and the water temperature dropped suddenly 18 min after the passage of the bore. Moreover, they experienced some difficulties during the measurements as their instruments got tumbled away for 1.4 km due to the strong current. Note that the bore was studied in a meander and it was not a unique front but two consecutive bores probably as a response to the meander (Kjerfve and Ferreira, 1993).
Wolanski et al. (2004) performed measurements in the Daly Estuary, Northern Australia. A small 0.3 m undular bore propagated over the measurement site. Large eddies rotating around a vertical axis were observed after the bore. The suspended sediment concentration (SSC) increased two minutes after the bore front passage. Wolanski et al. (2004) proposed that the 2 min delay was due to the time the sediment took to diffuse in the water column since two probes were used at 0.45 m and the other at 1.26 m above the bed. The probe at 1.26 m from the bed showed a small delay compared to the one at 0.45 m. In this study (Wolanski et al., 2004), a comparison was proposed with undular hydraulic jump generated in rectangular channel, but large unexplained discrepancies were observed for both the free surface and the flow velocity evolution.
Simpson et al. (2004) installed an acoustic Doppler current profiler and tidal gauges in the Dee River, UK, for long period measurements. They analysed the turbulent kinetic energy (TKE) and measured a TKE peak during the passage of the tidal bore front. They concluded that the intensity of bores, in term of TKE, was independent of the tidal range. However, the study could not determine if a bore was breaking or undular (Simpson et al., 2004). The intensity could not be studied based on the type of bore.
The height of the bore may have an impact on the turbulent mixing. During the study of Uncles et al. (2006), a small tidal bore of 0.1 to 0.15 m was observed and had small consequences on the fine sediment resuspension of the Humber Estuary, UK. However, little more details are given in the study since they focused their investigation on the estuary and not directly on the tidal bore.

The study performed by Fan et al. (2012) measured the sediment processes taking place in the Qiantang River during a breaking tidal bore. The bore caused a large resuspension of the sediments for 30 min after its passage. During the decelerated flooding stage of the tide, a poorly sorted sedimentation occurred. The sedimentation associated to tidal bore was different than regular tidal deposit. The grain size of deposit associated to tide with tidal bore was larger than the muddy or sandy deposit created for regular tide. The sedimentary structure of deposit was also different during tidal bores with formation of a thick bedding contrarily to a more structured and layered beddings for tidal cycles without bores. This specific deposition of sediment could be used to identify estuaries with tidal bores similarly to observations made by Tessier and Terwindt (1994).

As part of the ANR project MASCARET[1], several field studies were performed on both the Garonne River, France and the Bay of Mont Saint Michel (Chanson et al., 2011; Mouazé et al., 2010; Reungoat et al., 2012; Simon et al., 2011b). The studies used an acoustic Doppler velocimeter (ADV) to measure the flow velocity. Using the ADV signal, the SSC could also be deduced. It was highlighted that the bore induced a strong mixing as well as large and rapid fluctuations of the SSC whether the bore was breaking (Mouazé et al., 2010) or undular (Chanson et al., 2011; Reungoat et al., 2012).

Detailed studies were performed in the Bay of Mont-Saint Michel and upstream in the Sée River, France, as part of the ANR project MASCARET (Furgerot et al., 2012, 2013). The repeated field studies led to a better understanding of the sediment flux. During the passage of the bore and secondary undulations, the bed was scoured and the SSC greatly increased near the bed as the velocity and pressure suddenly changed within highly sheared flow inducing a diffusion of sediments in the water column.

The field studies gave direct information on tidal bores. However, the studies are challenging as many studies reported damages on the instrumentation (Chanson et al., 2011; Kjerfve and Ferreira, 1993; Mouazé et al., 2010; Reungoat et al., 2012). Most studies showed that the bore passage induces an increase of the turbulence also affecting the river sediments, but the measurements are punctual in both space and time with each bore being different. The comprehension of the phenomenon from field studies is made difficult by several aspects: measurements on the complete water column or on several points of a river section are rare, each study is unique in term of bore dynamics, river shape, river properties and sediment properties, moreover each bore for a same study is different from the previous one. Numerical and experimental studies of the modelled and controlled phenomenon can thus offer complementary information to field studies which are limited in numbers.

[1] `http://mascaret.enscbp.fr/`

II.3 Tidal bore theory and parallel with other positive surge theories

II.3.1 Theoretical aspects of tidal bores

Tidal bores are unsteady flows for a person watching the bore from the river bank. Figure II.1 shows an idealised bore presented as a discontinuity of the water surface propagating against an adverse flow. The first analytical development linked to tidal bore was proposed by Barré de Saint Venant (1871) based on a quasi-steady flow analogy. During its propagation, a bore must satisfy the momentum and continuity principles (Chanson, 2001; Henderson, 1966; Rayleigh, 1908). In a quasy-steady system of reference, neglecting friction losses and assuming a hydrostatic pressure distribution, the integral form of the equations for the conservation of mass and momentum gives a series of relationships between flow properties during the bore propagation:

$$\begin{cases} (V_0 + U_b)\, d_0 = (V_b + U_b)\, d_b \\ \rho g\, (d_b^2 - d_0^2) = 2\rho d_0\, (V_0 + U_b)\, (\beta_0\, (V_0 + U_b) - \beta_b\, (V_b + U_b)) \end{cases} \tag{II.1}$$

where V_0 is the initial flow velocity positive downstream, V_b is the flow velocity after the bore passage, U_b is the bore velocity positive upstream for a stationary observer, d_0 is the initial steady water depth, d_b is the water depth after the bore passage, g is the gravity acceleration, ρ is the water density, and β_0 and β_b are momentum correction coefficients. Neglecting the effects of the correction coefficients ($\beta_0 = \beta_b = 1$), equations II.1 yield:

$$\frac{d_b}{d_0} = \frac{1}{2} \left(\sqrt{1 + 8Fr^2} - 1 \right) \tag{II.2}$$

where Fr is the bore Froude number defined as:

$$Fr = \frac{V_0 + U_b}{\sqrt{g d_0}}. \tag{II.3}$$

Equation II.2 implies that the Froude number determines the height of the bore d_b for a selected water depth d_0. Moreover, the bore Froude number is always greater than unity and is linked to the type of bore, breaking or undular (Chanson, 2011a). The Froude number is often used to indicate the bore strength. The effects of bed friction and cross sectional shape can also be taken into consideration as investigated by Chanson (2012).

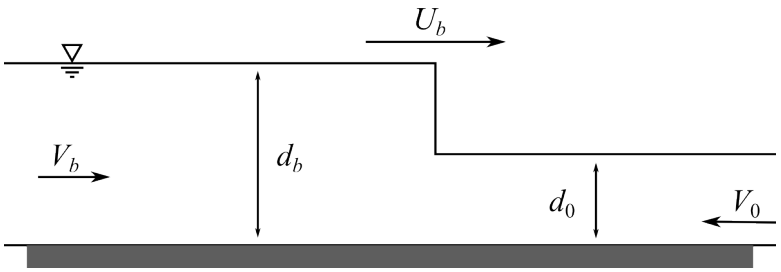

Figure II.1: Definition sketch of tidal bore propagation from left to right for an observer standing still within the hypotheses of equations II.1

The propagation of tidal bore was studied by Abbott and Lighthill (1956) without using a quasi-steady flow analogy. The shallow water theory was applied to find the height and the velocity of the bore by taking into account the tidal range, the river geometry and the bed friction. The results of the simulation of their model were found in agreement with observations of bore but lacking accuracy due to an approximation of the bed friction which value was not known (Abbott and Lighthill, 1956).

Concerning the formation of the bore, Mazumder and Bose (1995) proposed a theory linking the appearance of tidal bores and the tidal asymmetry. They verified their theory by applying it successfully to tidal bores in the Hooghly River. They showed that tidal bore appears only when the tidal wave is strongly asymmetrical with a rapid flood tide and a long ebb tide. A large dissymmetry is found in every estuary with tidal bores (section II.2.1). In most studies, the impact of the tidal dissymmetry was marginalised in favour of the tidal range to explain the apparition of tidal bores stating that a bore might appear in a river with a 4 to 6 m tide.

In rivers and estuaries, the tide is the motor for the apparition of tidal bore; however for a study in channel, it is complicated to recreate the dynamic of the tide propagating in a river. The study of bores in hydraulic channels is therefore based on the equation II.1 to model bores or positive surges, in a more general terminology. Using a quasi-steady flow analogy and based on a Froude similitude, bores can be compared to hydraulic jumps (Donnelly and Chanson, 2005), surges generated by a dam failure (Hornung et al., 1995; Marche et al., 1995; Yeh and Mok, 1990) or surges generated by the reflection of a stream against a wall fully or partially closed (Koch and Chanson, 2008; Stoker, 1957). The case of the hydraulic jump will not be developed as the generated surge is stationary, contrarily to the two other cases for which the surge propagates in the channel.

II.3.2 Positive surges generated by a dam break

Bores generated by dam breaks are often used to draw parallel with tidal bores. Since the initial conditions are simple, an analytical formula can be obtain to estimate some flow properties assuming a hydrostatic pressure and a frictionless boundary condition. The complete detail

of the calculus can be found in (Stoker, 1957, p. 334) by solving a Riemann problem, a variation of the Bélanger equations (eq. II.1). Figure II.2 presents the initial condition of a dam break and the surge propagating after the dam breaks. Before the dam break, consider two reservoirs of still water ($V_0 = V_1 = 0$ m.s^{-1}) with infinite length and a depth d_0 and d_1 with $d_1 > d_0$ (Figure II.2a). When the dam is instantaneously removed, four zones are observed (Figure II.2b). One zone with a bore propagating with a constant celerity U_b, a constant flow velocity V_b and a constant water depth d_b. The bore propagates over the constant zone of low water height $d_0 = cst$ and $V_0 = 0$. And the bore is connected to the other constant zone with $d_1 = cst$ and $V_1 = 0$ by a rarefaction wave with a non constant velocity and non constant water depth. The conjugate depth of the bore is given by:

$$d_b = \frac{\left(d_b - d_0\right)^2 \left(d_b + d_0\right)}{8 d_0 \left(\sqrt{d_1} - \sqrt{d_b}\right)^2} \tag{II.4}$$

where d_b is the bore water depth deduced with a root-finding method (e.g. secant method). Once the bore height is known, the flow velocity in the bore zone and the bore celerity are given by the formula $V_b = 2\left(\sqrt{g d_1} - \sqrt{g d_b}\right)$ and $U_b = d_b V_b / \left(d_b - d_0\right)$ respectively (Stoker, 1957).

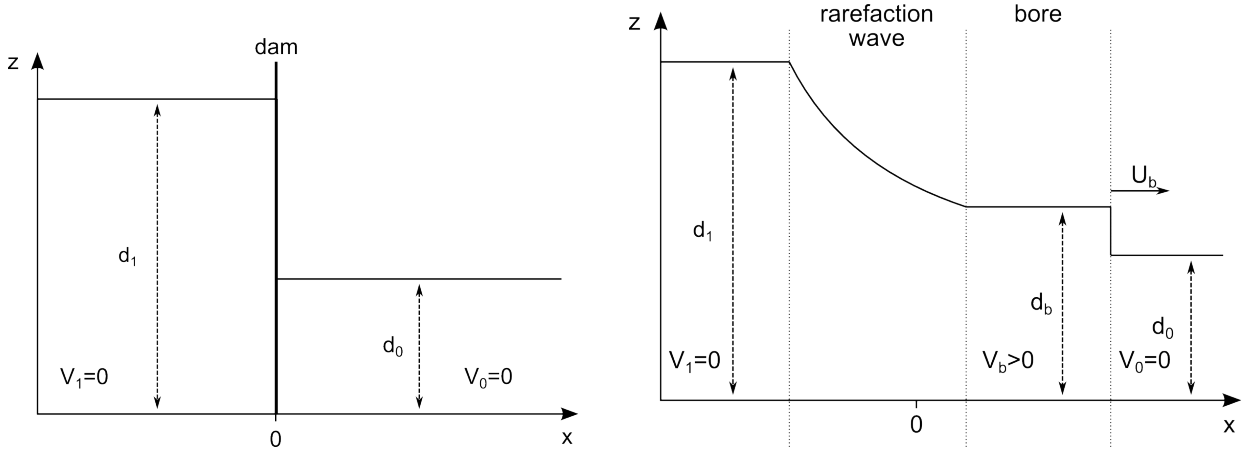

(a) Initial condition, $t = 0$ (b) After dam removal, $t > 0$

Figure II.2: Positive surge generation from a dam break configuration

II.3.3 Positive surges generated from the reflection of a stream against a wall

Another model used to study positive surge is the reflection of a horizontal stream against a closed vertical wall. The problem can be simplified to obtain an analytical formula of the bore properties. The configuration is the following, an initial free stream flow (Figure II.3a)

impacts a wall, the reflection of the flow creates a bore propagating usptream (Figure II.3b). An analytical formula can be determined when the wall is fully closed (Stoker, 1957, p. 330). Assuming a hydrostatic pressure, with d_0 the initial steady flow depth and $V_0 = cst$ the flow velocity, the bore celerity U_b and water depth after the bore d_b are deduced from the following equations:

$$- U_b \left(V_0 - U_b\right) = g \frac{d_0}{2} \left(1 - \frac{V_0 - U_b}{U_b}\right) \tag{II.5}$$

$$d_b = d_0 \frac{\left(U_b - V_0\right)}{U_b} \tag{II.6}$$

The flow velocity in the region of depth d_b is $V_b = 0$ (Stoker, 1957).

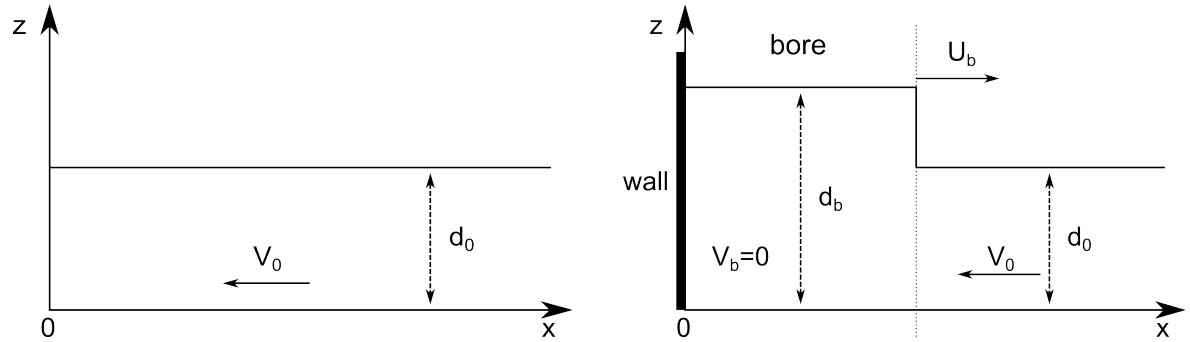

(a) Initial condition without wall, $t = 0$ (b) Bore propagation, $t > 0$

Figure II.3: Positive surge generation from the reflection of a stream against a wall

II.3.4 Flow dynamic comparison in full scale tidal bores and laboratory models

Previous models of dam break wave and reflection of the flow against a wall give a one-dimensional approximation of the unsteady flow conditions. The water depth and celerity of the bore are estimated assuming a hydrostatic pressure distribution, a homogeneous flow velocity and a frictionless bed. Therefore the free surface evolution, the turbulence and the boundary layer are not represented. Nonetheless, those analytical models give correct approximations of the celerity and the conjugate depth of the surge generated in similar experimental conditions with the difference that the pressure is not hydrostatic and that there is a turbulent boundary layer.

The full scale tidal bore differs in term of flow dynamics with the presented models. Table II.3 shows the theoretical value of the flow velocity upstream and downstream the bore in the situation of Figure II.1. In most cases of tidal bores, the flow completely reverses after the

bore passage whereas in a dam break, the surge propagates over a still water and in the case of stream reflection, the flow only decelerate or stop after the surge (Table II.3). These discrepancies might induce differences in the flow hydrodynamic of positive surges even when they have a similar free surface evolution. There is no study that detail the difference in flow dynamic with full scale tidal bores: field studies do not give access to the same level of detail as experiments, plus, there is no experiment reproducing conditions with a complete flow reversal ($V_b > 0$). Nonetheless, the models based on analytical condition presented in section II.3.2 and II.3.3 showed the same free surface profiles than a tidal bore (section V). The model of positive surges generated by reflection against a wall is even closer to tidal bores in river as the surge propagates against an adverse flow.

Table II.3: Comparison of the theoretical flow velocity before and after positive surge fronts

Type of positive surge	V_0	V_b	U_b
Full scale tidal bore	≤ 0	$\geq 0^*$	> 0
Dam break wave	$= 0$	> 0	> 0
Fully closed gate reflection	< 0	$= 0$	> 0
Partially closed gate reflection	< 0	< 0	> 0
Hydraulic jump	< 0	< 0	$= 0$

Notes: For an horizontal channel with the hypothesis of equation II.1, * flow inversion measured in most full scale tidal bores

II.4 Experimental studies of positive surges

Laboratory studies provide a controlled environment where the modelled phenomenon can be repeated under various conditions and configurations. This allows the data to be acquired easily and at various locations. For some laboratory studies of positive surges, parallel can be drawn with tidal bores. It is the case with dam break configuration over a tailwater (Hornung et al., 1995; Marche et al., 1995; Soares Frazao and Zech, 2002; Yeh and Mok, 1990), reflection of a stream against a completely or partially closed wall (Benet and Cunge, 1971; Chanson, 2004b; Favre, 1935; Treske, 1994), by moving an underwater weir (Wilkinson and Banner, 1977) or with hydraulic jumps using a quasi-steady flow analogy (Chanson, 2005).

In the whole literature on translating positive surges, the studies measuring the flow turbulence are rare, the majority of studies were focused on the free surface evolution. Those studies gave details on the unsteady free surface characteristics based on the Froude number (II.3) or the dimensionless water elevation (for example, the ratio of water elevation d_b/d_0). The characteristics include the bore celerity, the conjugated depth, the wave length and the amplitude of the secondary undulations (Benet and Cunge, 1971; Chanson, 2010a; Favre, 1935; Gualtieri

and Chanson, 2012; Jánosi et al., 2004; Marche et al., 1995; Treske, 1994). Most studies tested several flow configurations, ranging from undular to breaking bores, thus giving an indication on the flow conditions leading to the formation of a breaking roller on the first undulations. For a bore propagating over a still water (dam break cases), there will be a transition of an undular bore into a breaking bore for a $Fr > 1.28$ (Benet and Cunge, 1971; Favre, 1935; Soares Frazao and Zech, 2002). In the case of a dam break surge, the bore is breaking for a ratio $d_0/d_1 \leq 0.55$. However, if a bore propagates over a steady flow, the Froude number for the transition can change depending on the initially steady flow condition and the generation method. Undular bores with a Froude number $Fr > 2$ are reported in Ryabenko (1998) (with reference to papers in Russian). As the breaking roller becomes stronger, the size of secondary undulations decreases and eventually disappears and a chaotic flow motion follows their disappearance. This observation is similar to what can be seen on the field (Chanson, 2011a). The threshold value inducing the appearance of a breaking roller has not been found yet (Cunge, 2003).

For undular bores, the shape of the secondary undulations was compared successfully with the second order Stokes wave theory (Wilkinson and Banner, 1977), with cnoïdal theory (Benjamin and Lighthill, 1954; Keulegan and Patterson, 1940; Sturtevant, 1965) or with linear wave theory (Chanson, 2010a; Lemoine, 1948). Even if the theories are different, the best fit for the secondary oscillations seems to depend on the laboratory case.

The pressure in translating positive surges has rarely been measured. In dam break cases, the pressure was non-hydrostatic (Marche et al., 1995). Measurements in stationnary undular hydraulic jump also showed that the pressure was non hydrostatic in unsteady flow (Montes and Chanson, 1998). The non hydrostatic pressure in bores is expected from ideal fluid flow theory (Chanson, 2005).

Concerning the flow velocity, few experimental studies can be found in the literature. During the passage of a positive surge, the longitudinal flow velocity suddenly changes as the water depth increases. After the bore front, the flow velocity evolution is synchronised with the water free surface. For a dam break case over quiescent water, the turbulence generated by a breaking roller was studied by Yeh and Mok (1990) and Hornung et al. (1995). The turbulence extended almost horizontally to the roller toe wake and propagated deeper in the flow slower than for a stationary hydraulic jump. The propagation into deeper parts of the flow was linked with the three dimensional properties of eddies. For positive surge propagating over a stream, early observations of a "bottom roll" (Ryabenko, 1998), i.e. transient flow reversal just above the channel bed usually beneath the bore front, were measured under undular bores with large Froude numbers. This was also observed in detail for breaking bore (Koch and Chanson, 2008). Some pictures of breaking bores were taken with aluminium powder inserted in the flow

(Bukreev, 2000). They showed a stratification of the flow beneath the bore front with formation of vortices near the roller and a zone of detachment near the bed (Bukreev, 2000). However, only two pictures are presented and the analysis is limited.
Several studies on positive surges propagating against an initially steady flow took place in the University of Queensland. They were mostly based on Froude number comparison, using high frequency ADV systems to record the flow velocity and non-intrusive acoustic probes to record the free surface evolution (section III.3). The flow evolution beneath bores was detailed in Koch and Chanson (2005, 2008, 2009). A transient velocity recirculation was observed beneath breaking bores, but not for undular bores. This has been confirmed in some other studies (Chanson, 2010b; Docherty and Chanson, 2012; Khezri and Chanson, 2012c). After the bore passage, the turbulence in terms of Reynolds stress was shown to be larger than in the initial steady flow, and different between breaking and undular bores (Koch and Chanson, 2005, 2008, 2009). The effects of bed roughness and adverse slope on the bore propagation were also studied (Chanson, 2008, 2010b; Docherty and Chanson, 2010, 2012). The rough screen contributed to the wave dispersion and attenuation according to gravity wave theory. Larger turbulent stresses were recorded with the rough screen experiments than without. With an adverse slope, the bore was slowing down, and eventually stopping, turning into a hydraulic jump (Chanson, 2011b). Another series of measurements studied the effect of channel constriction on tidal bore to model the propagation of a bore beneath a bridge (Chanson, 2009a, 2011c). The constriction had a major effect on the wave free surface, leading to some three dimensional motions. The velocity measurements on the middle of the constriction were close to the measurements without constriction. The modelling of fish egg dispersions under bores was investigated in the channel (Chanson and Tan, 2010). Light weight particles were introduced in the steady flow. The particles were strongly influenced by the flow deceleration associated to the bore passage. The particles close to the bed followed the direction of the bore for both undular and breaking bores with a different repartition depending on the depth before the passage of the leading front. Undular bores induced larger vertical mixing than the breaking bore. In the previous study, the turbulence in the unsteady flow velocity was studied by using a time filtering. A comparison with ensemble averaging measurements showed that the time filtering had some non-neglible differences with ensemble average during the bore passage (Chanson and Docherty, 2012; Docherty and Chanson, 2010, 2012). The effect of the positive surge over moveable gravel was investigated (Khezri and Chanson, 2012a,b,c). For the selected size of gravel and flow condition, no motion of the gravel bed happened under undular bores, but happened beneath bores with a breaking front. The longitudinal gradient pressure together with the transient flow recirculation contributed to the sediment inception. It was also shown that the turbulent stress beneath the bore was stronger with a moveable gravel bed than with a fixed gravel bed.

II.5 Numerical studies of tidal bores and positive surges

Modelling a tidal bore can also be performed by numerical simulations. One can choose to study the complete three dimensional flow by solving the Navier-Stokes equations or just represent the two dimensional evolution of the free surface with particular hypothesis on the flow velocity and pressure, for example by solving the Saint-Venant equations or the Boussinesq equations. The studies modelling the complete flow evolution using the Navier-Stokes equations are rare (only three, Furuyama and Chanson, 2010; Lubin et al., 2010a; Simon et al., 2011a), and most studies only simulated the free surface evolution.

Two dimensional depth averaged simulations of tidal bore in estuary, using the Saint Venant equations, were performed in several studies (Caputo and Stepanyants, 1999; Lu et al., 2009; Madsen et al., 2005; Pan and Lu, 2011; Su et al., 2001). They offer a fast method to predict the celerity and averaged height of a bore propagating in an estuary. They can also produce interesting rendering visualisation of the bore propagation in an estuary (Wang et al., 2009). The numerical methods used to model the free surface evolution of a tidal bore are often tested on simpler configurations. Simulations of positive surges in a rectangular channel offer a simple test case to validate free surface models in numerical simulation. The free surface is solved assuming an average flow velocity on the water column by the Saint Venant equations (Madsen et al., 2005; Mitchell, 2010; Su et al., 2001), the Boussinesq equations (Abbott and Rodenhuis, 1972; Devkota and Imberger, 2009; Marche et al., 1995) or the Korteweg-de Vries (KdV) equation (Grujić and Kalisch, 2009; Peregrine, 1966). But they only predict an averaged flow velocity evolution.

The formation and propagation of an undular bore was simulated by Peregrine (1966) for a propagation over a still water. The simulation was based on the Boussinesq equations. The shape of the bore front was found in agreement with experimental studies considering a uniform flow. Similar simulations were performed by Soares Frazao and Zech (2002) with a different method to initialise the pressure gradient. A good agreement was also found with dam break positive surge.

There are some limitations with "depth-averaged" simulations. Only a continuous free surface can be modelled and the flow structure is never known in details. Therefore, it is impossible to study breaking bores or turbulent flows. For example, the "depth-averaged" numerical simulation cannot reproduce the "bottom roll" beneath a breaking bore and its effect on the flow cannot be investigated.

The simulation of the complete flow evolution requires the use of the Navier-Stokes equations with a method to identify the water free surface. Such methods were not yet applied to three dimensional simulations of the geophysical phenomenon. However, it is possible to simulate bore in simpler configurations. Simulations of positive surges in channel were performed to test

some free surface interface methods: the Marker-and-Cell method (Hirt and Shannon, 1968) and the volume of fluid method (VOF) (Hirt and Nichols, 1981) were applied to simulate a stream impacting a wall. The simulations were performed to present the possibility offered by the VOF method for conserving a two-fluid interface. The flow evolution was not studied in details (Hirt and Nichols, 1981).

A two dimensional simulation of the flow beneath a breaking positive surge based on an experimental configuration (Koch and Chanson, 2008) was performed using a large eddy simulation (LES) and for a two-phase flow (Furuyama and Chanson, 2008, 2010). The results were in agreement with the laboratory data and a transient flow inversion was also observed close to the channel bed similarly to the experimental study (Koch and Chanson, 2008). However, there model was only two dimensional and lacked a fine mesh grid resolution to model the complete flow dynamic and turbulence. The mesh sizes were $\Delta_x = \Delta_y = 0.0125$ m and Furuyama and Chanson (2010) acknowledged the necessity to use mesh sizes of millimetre order for accurate solution.

Another two dimensional simulation of the same flow configuration was performed with LES and a VOF method (Lubin et al., 2010a,b). The simulation was run in parallel using 128 processors for a domain of 2000×1000 constant Cartesian cells. The main features of the flow were in agreement with the experiment. A breaking bore propagated with a sudden flow deceleration beneath the bore. Large velocity fluctuations were observed after the bore passage as well as the presence of transient recirculation structures. Figure II.4 shows a sketch based on the simulation performed (Lubin et al., 2010a). The streamlines show the macro-structures created by a breaking bore and propagating with the bore front in a two dimensional simulation with no turbulence or boundary layer flow in the steady flow. Nonetheless, the simulation was only two dimensional and omitted the representation of a three dimensional flow with lateral walls and three dimensional turbulent effects.

The simulation of a three dimensional breaking positive surge was tested for breaking bore using a realistic turbulent inflow conditions (Chanson et al., 2012; Simon et al., 2011a). Some flow characteristics of the simulated bore were in agreement with the experiments. The sudden rise of the free surface with the presence of a breaking roller was reproduced and the strong flow deceleration beneath the bore was simulated. However, the study lacked accuracy due to a coarse mesh grid ($600 \times 400 \times 100$ regular Cartesian cells for a $7 \times 1 \times 0.5$ m domain) and numerical limitations on the domain size. One of the missing feature of the simulation was the presence of a flow reversal near the bed that was observed in the experiment (Koch and Chanson, 2009) as well as in the two dimensional simulation (Lubin et al., 2010a) which used finer meshes in the longitudinal and vertical directions.

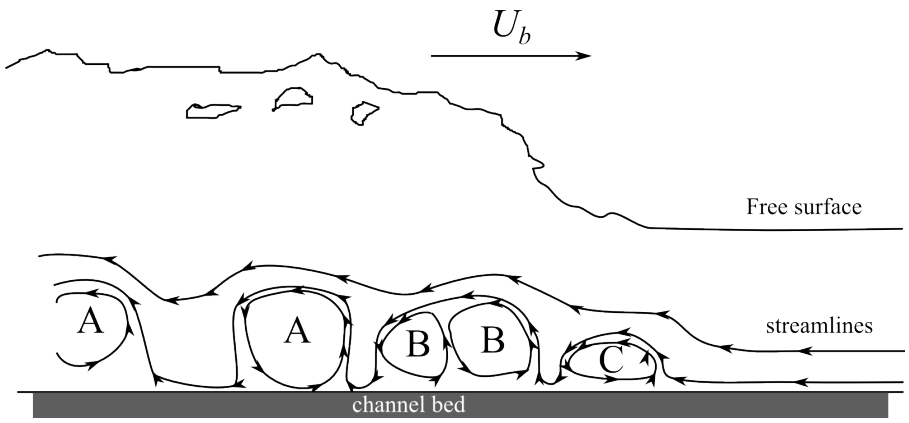

Figure II.4: Sketch of streamlines indicating recirculation structures under a propagating breaking tidal bore. (A) indicates macro-structures propagating downstream, (B) shows separating structures, shedding and propagating downstream and (C) is the main recirculation structure propagating upstream with the bore. Based on Lubin et al. (2010a)

II.6 Summary

A great variability of shape and effects of tidal bores is observed during field studies depending upon many parameters, such as the estuary shape, the river flow properties, the tide characteristics, etc. The phenomenon is known to have unique effects on the flow with large turbulent levels observed after the bore. The river sediments are also impacted by the bore passage with large resuspension and scour measured after the bore. Those observations remain punctual and it is unknown if one effect observed in an estuary will be reproduced in a similar way in another estuary with a different shape, different flow conditions or different sediments. The dominant forces inducing the sediment resuspension are not completely defined. The flow hydrodynamic of bores is investigated with models of tidal bores to offset the lack of details given by field studies. The studies in hydraulic channel gave access to the flow information at several positions and allowed to reproduce the bores with the same flow conditions. To model tidal bores, a Froude similitude is used since the bore effects are studied as function of the type of bores: undular or breaking.

The literature on experimental studies showed that the leading front of a bore induced important changes of the flow velocity near the channel bed with apparition of flow recirculation near the bed in some cases. An intense mixing was observed after the bore passage for the various configurations tested in previous studies. Configurations with various roughness, obstacles or different slopes were used showing their effects on bores. Concerning the numerical studies, most simulations of bores were mainly two dimensional. Therefore many studies were performed only to predict the free surface evolution during a bore passage. Those simulations were also limited to undular bores since a breaking roller cannot be modelled with depth averaged methods. Simulations on the detailed flow changes are less abundant. The preliminary detailed two

dimensional works on breaking bores were performed by solving the Navier-Stokes equations. They provided a detailed description of the flow. In particular, those simulations showed transient recirculations propagating with the bore front. But two dimensional and depth averaged simulations do not describe the complete three dimensional dynamic (turbulence, effects of bed and sidewalls) appearing in estuary and in hydraulic channel.
The presented numerical study was performed in both two and three dimensions to highlight the limit of two dimensional simulations. The three dimensional simulations of undular bores showed, for the first time, the impact of bore propagation on a turbulent and non turbulent initial steady flow. Note that simulation of undular bores were possible because the experimental study helped finding the possible flow configurations to simulate an undular bore. The present experimental study was performed to obtain information of the size of turbulence in bores. In rivers, large vortical structures were reported to be seen after bore propagation but the field measurements could not measure these structures and their effects are unknown. Another interest of the experimental study was to provide a detailed set of measurements for numerical simulation that would provide the currently missing data for initialisation and detailed validation of simulations. However, the experiments could not measure the flow properties close to the bed and the sidewalls, three dimensional numerical simulations gave data in the complete domain that, so far, were missing in both laboratory and field studies.

III

Methodology

III.1 Chapter overview

The present work includes two aspects of the study of positive surges. One part is focused on the numerical simulation of positive surges using the computational fluid dynamic (CFD) code Thétis developed in the Université de Bordeaux, France. The other part consists of experimental works in the hydraulic laboratory of the University of Queensland, Australia. The detailed instrumentations and methods used for the study of both numerical and experimental studies are presented introducing first dimensional considerations.

III.2 Dimensional analysis of tidal bores

Physical and numerical model of tidal bores are studied considering the geometrical similarities between the prototype (geophysical tidal bores) and the model through a geometric scaling ratio of the prototype over the model dimension. In this study as well as in previous study (sections II.4 and II.5), the scaling ratio is generally larger than one, but can also be close to one if the bore propagates, for example, in rills or rivulets, the size of an experimental channel, adjacent to the river.

In study of tidal bores, the study of flow turbulence includes the effects of various parameters. The most pertinent parameters are the fluid properties, the channel geometry, the physical constants, the boundary conditions and the air-water interface (Chanson et al., 2012; Docherty and Chanson, 2012). Other parameters such as the biochemical properties of the water solution or the compressibility of air bubbles can eventually be considered. A simplified dimensional analysis yields:

$$\mathbf{u}, P = F\left(\mathbf{X}, t, U_b, d_0, V_0, \delta, W, \mathbf{g}, \rho, \mu, \sigma, k_s, \cdots\right) \tag{III.1}$$

where $\mathbf{u}$ is the flow velocity, P the pressure, $\mathbf{X}$ the position (x, y, z), t the time, U_b the bore celerity, d_0 the steady flow water depth, V_0 the steady flow velocity, δ the boundary layer thickness, W the channel width, $\mathbf{g}$ the gravity vector, ρ the density, μ the viscosity, σ the air-water surface tension and k_s a roughness height.

Scale effects may exist when one or more terms have different values between the model and prototype. In dimensionless term, equation III.1 can be written as:

$$\frac{\mathbf{u}}{V_0}, \frac{P}{\rho g d_0} = F\left(\frac{\mathbf{X}}{d_0}, t\sqrt{\frac{g}{d_0}}, \frac{V_0 + U_b}{\sqrt{g d_0}}, \rho\frac{(V_0 + U_b)d_0}{\mu}, \frac{\delta}{d_0}, \frac{W}{d_0}, \frac{g\mu^4}{\rho\sigma^3}, \frac{k_s}{d_0}, \theta, \cdots\right) \tag{III.2}$$

where θ is the bed slope.

At a location $\mathbf{X} = (x, y, z)$ and a time t, the flow properties depend on the bore Froude number $Fr = (V_0 + U_b)/\sqrt{g d_0}$, the bore Reynolds number $\rho(V_0 + U_b)d_0/\mu$ and the Morton number $g\mu^4/(\rho\sigma^3)$. The shape of bore is linked with the Froude number, therefore modelling undular or breaking bore will directly select a range of usable Froude number, between 1 to 1.3 for undular bores and larger than 1.3 for breaking bores. The viscous effects in hydraulic channel are smaller than in rivers. In rivers, typical bore Reynolds numbers varies from 10^6 to 10^7 (Chanson et al., 2011; Mouazé et al., 2010) whereas in channel, due to the water depth limitation and the study of bore propagating against the steady flow, the Reynolds number varies from 10^4 to 10^5 (Chanson and Toi, 2013; Koch and Chanson, 2009). The Morton number becomes a constant because both model and prototype use the same fluids. In practice, model studies use a Froude similitude, the scales effect affecting the turbulent mixing in tidal bores were not investigated to date (Chanson et al., 2012; Docherty and Chanson, 2012).

Herein, the experimental study was conducted for two steady flow Reynolds numbers and two types of bores, undular and breaking (Chapter IV). The numerical study was conducted for undular bores since no numerical work was conducted to study the turbulence for this type of bores (Chapter VI).

III.3 Experimental study

III.3.1 Facility

The physical experiments were carried out in a flume located at the University of Queensland. The channel was 0.50 m wide and 12 m long, made with 0.30 m high glass walls and a smooth PVC bed (Figure III.1). The bed slope was set with $S_0 = \sin\theta = 0.0077$ for all experiments[1]. A constant head tank supplied the water into a large basin leading to the channel through a bed and sidewall convergent. The same channel with a similar set up was used previously by Docherty and Chanson (2012) and Khezri and Chanson (2012b). The tainter gate used to generate the unsteady flow was located next to the downstream channel end at $x = 0$ when fully-closed and vertical as sketched in Figure III.2a. Herein, x is positive in the direction of propagation of the bore, y is the distance from the channel centreline positive toward the right wall and z is the distance from the bed positive upward. The channel inlet was located at $x = 11.13$ m from the closed gate. The channel ended with a free overfall.

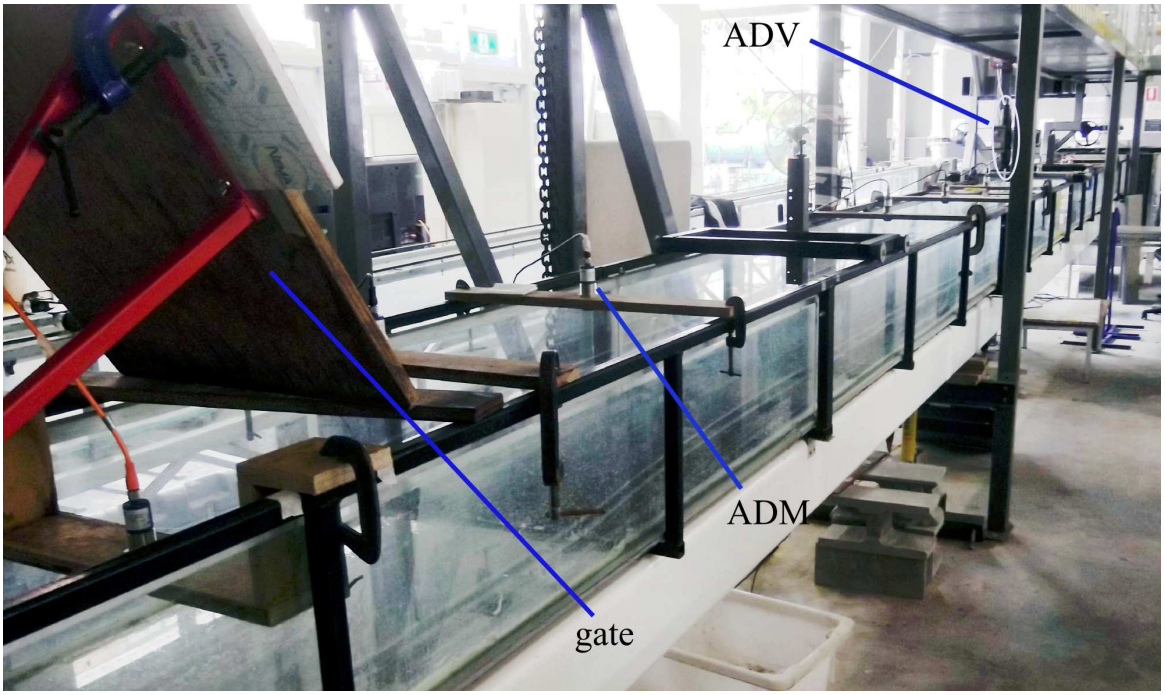

Figure III.1: Experimental channel, picture from the downstream end (Photo: Bruno Simon)

The PVC bed was covered by a rough bed made out of a layer of blue granite gravels sieved between 4.75 mm and 6.70 mm glued on plywood sheets. Figure III.2a shows the general channel arrangement. Figure III.2b details the bed transitions on both ends of the fixed gravel

[1] A slope was used to increase the range of bore Froude numbers usable for the unsteady flow study presented in section IV.

bed section[2]. The overall thickness of the gravel bed (plywood sheet and glued gravels) was on average 15 mm and it was installed between $x = 0.59$ m and $x = 9.15$ m from the gate. The fixed gravel bed configuration was selected to continue experiments with the same set up as Docherty and Chanson (2012) and Khezri and Chanson (2012b) who used the same gravel bed. The hydraulic roughness of the fixed gravel bed yielded a Darcy-Weisbach friction factor $f = 0.031$ to 0.045, corresponding to an equivalent sand bed roughness height $k_s = 3.4$ mm (Docherty and Chanson, 2010).

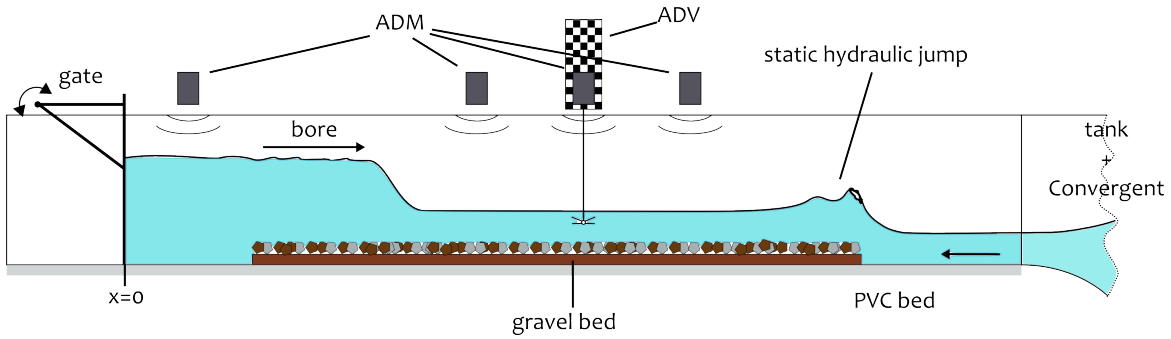

(a) Definition sketch with the initially steady flow direction from right to left and the bore propagation from left to right

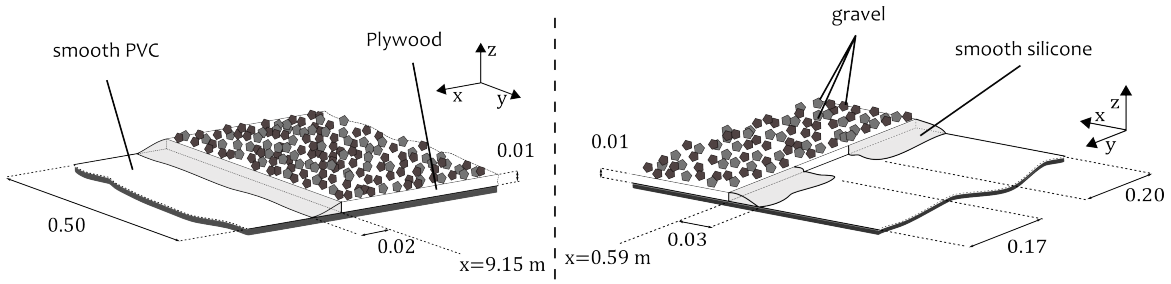

(b) Details of the gravel bed transition regions. Left: upstream transition at $x = 9.15$ m - Right downstream transition at $x = 0.59$ m

Figure III.2: Experimental channel

III.3.2 Instrumentation

Several instruments were used during the experiments. The water discharge was measured with an orifice meter designed upon the British Standards (1951) and calibrated on site with a V-notch weir. The error was expected to be less than 2%. In steady flows, the water depth was measured using rail mounted pointer gauges and a ruler with a semi-circular footing with

[2]The bed transition at the downstream end was open in the middle to avoid having air being trapped between the PVC bed and the gravel bed when the water filled the channel. The opening also allowed the channel to dry faster with water leaving more easily by the joint opening.

a 27.2 cm^2 area (Figure III.3a). Figure III.3 shows the semi-circular footing used to zero the probe elevations above the irregular fixed gravel bed.

III.3.2.1 Prandtl-Pitot tube

The pressure and velocity were measured using a Prandtl-Pitot tube seen in Figure III.3b. The Prandtl-Pitot tube had an external diameter of 3.05 mm. The total head was measured through a 1.2 mm diameter tapping and the piezometric head was measured with eight 0.5 mm diameter holes spaced around the Pitot tube circumference. The dynamic and static tappings were separated by a longitudinal distance of 24.5 mm. The vertical position of the Pitot tube was controlled by a traverse mechanism coupled with a Mitutoyo^{TM} digimatic scale unit (accuracy 0.025 mm).

(a) Ruler with the semi-circular footing

(b) Prantdl-Pitot tube set over the semi circular footing

Figure III.3: Details of the semi-circular footing used to define $z = 0$ over the gravel bed (Photos: Bruno Simon)

III.3.2.2 Unsteady free surface measurements

In the unsteady flow, the time-variation of free surface elevations was recorded using a series of acoustic displacement meters (ADMs) Microsonic^{TM} MIC+25 (Table III.1). The probes are non-intrusive sensors. They were positioned above the channel free-surface. The ADM probes were calibrated in steady flow conditions using the pointer gauge readings. In a first series of experiments, four ADM sensors were located at $x = 0.33,\ 5.13,\ 6.13$ and 7.13 m from the gate.

During a second series of experiments, six ADM sensors were added to the previous probes in the channel and located at x = 0.93, 3.13, 4.13, 8.38, 8.93 and -0.1 m. Note that the last sensor was located downstream of the tainter gate. All ADM sensors were connected to a high speed data acquisition system NI^{TM} DAQ Card 6024E with a maximum sampling capacity of 200 000 samples per second. The ADMs data were sampled at 200 Hz when coupled with flow velocity measurements.

Table III.1: Characteristics of Microsonic^{TM} Mic+25/IU/TC sensor (Microsonic, 2004)

Accuracy	0.18 mm
Response time	32 ms
Ultrasonic frequency	320 kHz
Wave length (at 20 °C)	1.1 mm
Detection zone radius at operating range	22 mm
Blind zone (from emitter)	30 mm
Operating range	250 mm
Maximum range	350 mm

III.3.2.3 Unsteady velocity measurements

The turbulent velocity measurements were performed with one or two acoustic Doppler velocimeters (ADVs) Nortek^{TM} Vectrino+ (Serial No. VNO 0436 and VNO 0802, Table III.2). Both units were equipped with a side looking head[3] (Figure III.4). An ADV unit uses the Doppler Effect, emitting short acoustic pulses which reflect on very small particles crossing a remote sampling volume located approximately 50 mm from the emitter. The instantaneous velocity is measured using the Doppler shift principle (McLelland and Nicholas, 2000; Nortek AS, 2009; Voulgaris and Trowbridge, 1998). Figure III.4 illustrates details of the ADV head. The ADV settings were a transmit length of 0.3 mm, a sampling volume height of 1 mm and a velocity range of 1 or 2.5 m.s^{-1}, while the maximal sampling frequency was 200 Hz. The vertical elevation of the ADV was controlled by a Mitutoyo^{TM} digimatic scale unit mounted on a trolley. The ADV velocity signal outputs were sampled with the Vectrino software and the longitudinal velocity u_x output was simultaneously recorded with the ADM sensors by the NI^{TM} DAQ Card to synchronise the velocity and free surface measurements. Details of the synchronisation method are presented in Simon and Chanson (2013).

[3]The shape of side looking heads allows to get measurements of the longitudinal and transversal velocity closer to the free surface than down looking probes.

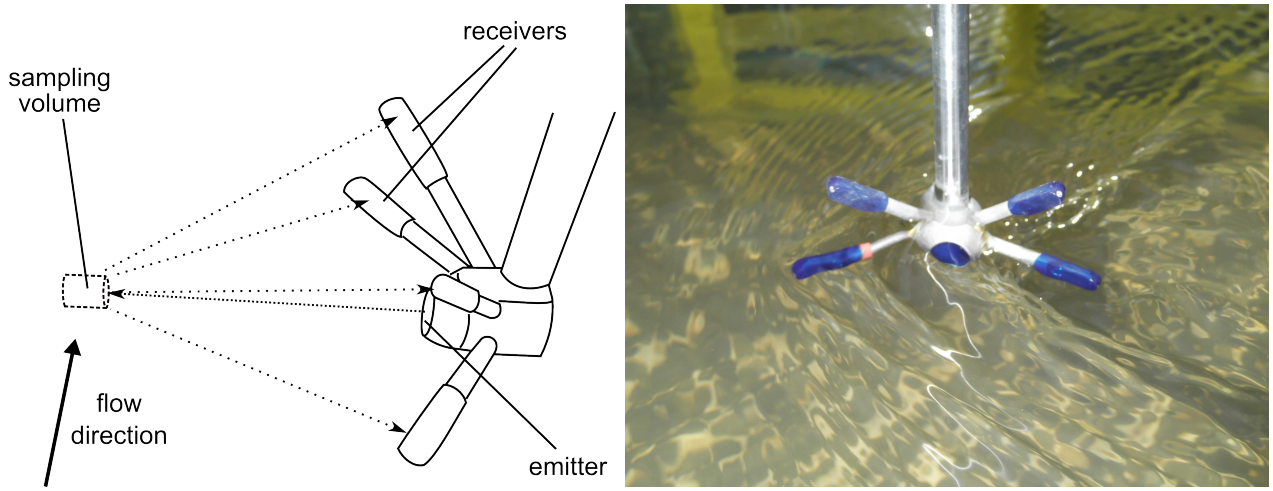

Figure III.4: Nortek^{TM} Vectrino+ ADV side looking head details

Table III.2: Characteristics of Nortek^{TM} Vectrino+ ADV (Nortek AS, 2009)

Accuracy	1% of vel. range
Acoustic frequency	10 MHz
Sampling volume, diameter×length	6×1 mm
Distance from probe	5 cm
Velocity range used	1 and 2.5 m.s^{-1}
Firmware used	1.31

III.3.2.4 Unsteady flow generation

The bore was generated by the rapid manual closure of a tainter gate located at the downstream end of the channel ($x = 0$) (Figure III.5). A similar method was used by Koch and Chanson (2005), Docherty and Chanson (2010) and Khezri and Chanson (2012b). After rapid closure, the water initially accumulated against the gate, thus increasing the water depth and creating a surge propagating upstream into the channel. The gate closure was estimated to take less than 0.2 s (Figure III.6). The rapid closure time was critical to eliminate any effect on the bore generation process. For a partial closure, $h_g > 0$, only the gate interfered with the water where h_g is the gate opening after closure (Figure III.6). For a partial gate closure, the gate formed an angle α_g with the horizontal, the values of α_g are reported in Simon and Chanson (2013). An estimate of the contraction effect of the gate is presented in Koch and Chanson (2005). Note that the time of closure of the gate was not reported in the recorded data, although two ADMs were located on each side of the gate. The exact time of closure was not necessary to study and to synchronise bores since the synchronisation of bore was based on their shape at $x = 6.13$ m (Simon and Chanson, 2013).

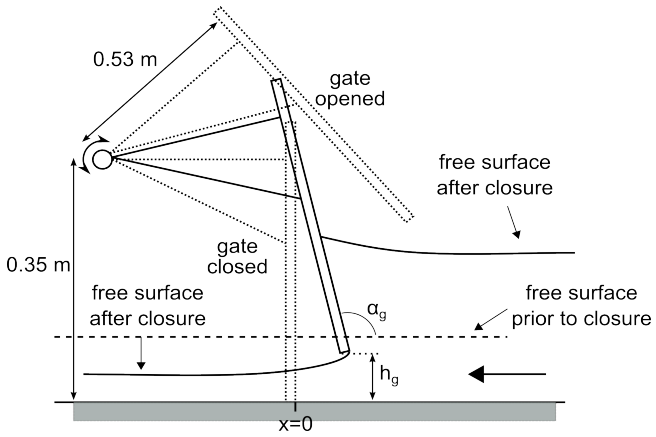

Figure III.5: Tainter gate at the downstream end of the channel

III.3.3 Data acquisition and processing

III.3.3.1 Pitot tube operation

The pressure and velocity were measured in steady flow using a Prandtl-Pitot tube connected to an inclined manometer. The dynamic and static readings gave respectively the total head H_1 and the piezometric head H_2. At a distance z above the bed, the pressure p, the time-averaged velocity $\bar{u}_x$ and the specific energy E were calculated as:

$$\frac{p}{g\rho} = H_2 - z_0 - z\cos\theta \tag{III.3}$$

$$|\bar{u}_x| = \sqrt{2g\left(H_1 - H_2\right)} \tag{III.4}$$

$$E = H_1 - z_0 \tag{III.5}$$

where ρ is the water density, g is the gravity acceleration, z_0 is the bed elevation, z is the distance to the bed, and θ is the angle between the channel invert and horizontal. In each case, the bed elevation z_0 was checked to satisfy $p = 0$ at the free-surface ($z = d$).

III.3.3.2 Free surface treatments

The free surface elevation was recorded with ADM sensors. The signal outputs included some erroneous points when the emitted signal was reflected away from the receiver, inducing out of range or non-physical data. The erroneous data were removed and replaced by a linear interpolation between the two nearest valid points.

The unsteady free surface data were analysed by reproducing N times a bore with a same set of flow conditions. The free surface signals of each bore were superposed based on the bore

(a) Frame -5/30, $t = -0.167$ s, contact gate-water

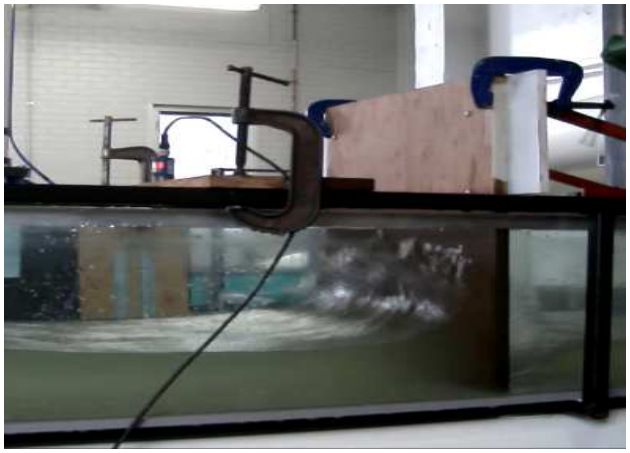

(b) Frame 0/30, $t = 0$ s, gate fully closed

(c) Frame 6/30, $t = 0.2$ s, run up

(d) Frame 17/30, $t = 0.566$ s, splash

Figure III.6: Gate closure sequence generating a breaking bore, $h_g = 0$ and $Q = 0.55$ L.s^{-1} (Photos: Bruno Simon)

front passage beneath an ADM used as reference (Simon and Chanson, 2013). The unsteady ensemble averaged water depth was calculated using a median of each superposed bore, $\overline{d}_{EA} = \text{median}_{k=1,...,N}(d_{run\ k})$.

III.3.3.3 Velocity signal processing

The instantaneous velocity components were recorded using an ADV system (firmware version 1.31) controlled with the software Vectrino+ version 1.20. The longitudinal velocity output was also sampled by the NI^{TM} DAQ Card data acquisition system to synchronise free surface and velocity measurements. Additionally, the ADV signal outputs included the level of signal strength, signal correlation and signal to noise ratio (SNR) for each beam. These parameters were used to assess the quality of the signal which could be adversely affected by the proximity

of solid boundary near the ADV control volume or by a lack of particle in the flow (Chanson et al., 2007; Docherty and Chanson, 2010). During the present study, kaolin powder was added to the flow as seeding material only to improve the signal quality, similarly to Docherty and Chanson (2012) who used Clay powder as seeding material. The kaolin powder was diluted in water for a quantity of 25 g.L^{-1}. The solution was progressively introduced upstream the channel convergent by a 15 cL reservoir approximately 20 s before a bore generation. The reservoir was empty in 30 to 40 s. The impact of seeding on the signal is illustrated in Figure III.7. The seeding solution reached the ADV control volume at $t = 58$ s when the noise in the velocity signal diminishes and the SNR increases significantly (Figure III.7).

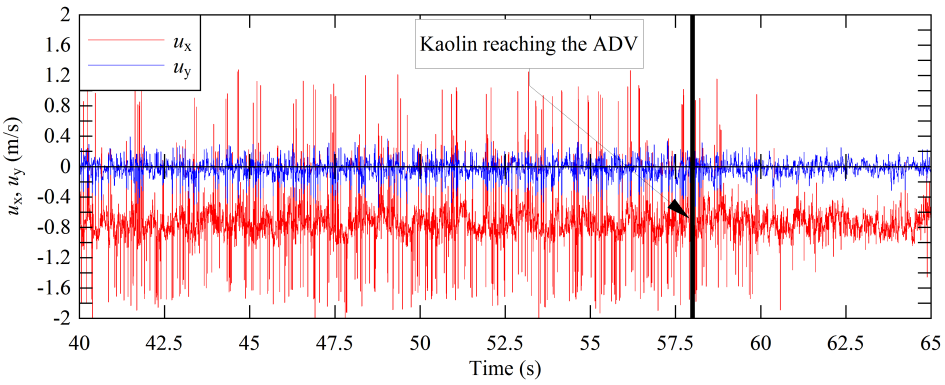

(a) Longitudinal and transversal velocity

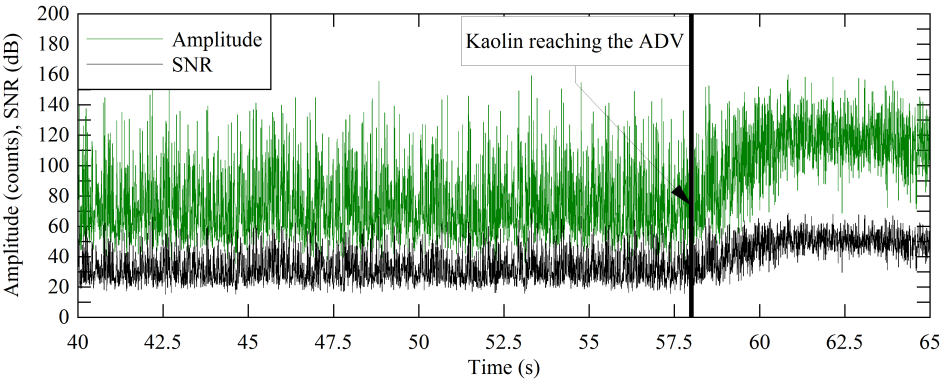

(b) Signal amplitude and SNR

Figure III.7: Typical ADV signal time evolution in a steady flow after seeding the water with kaolin at the channel inflow

In steady flows, the basic post processing of ADV signal was conducted using the software WinADV^{TM} v2.028. The signal filtering included the removal of communication errors, the removal of average signal to noise ratio data less than 5 dB and the removal of average correlation less than 0.6 (McLelland and Nicholas, 2000). In addition spikes were removed using the phase-space thresholding technique developed by Goring and Nikora (2002) and modified

by Wahl (2003). In unsteady flow, the mentioned post processing technique was not applicable (Chanson, 2010b; Koch and Chanson, 2009). Only the removal of communication errors was performed in the unsteady flow using a home-made software[4]. Finally, the velocity data were rotated in the xy-plane to yield a zero time averaged transversal velocity ($\bar{u}_y = 0$) on the channel centreline in the initially steady flow.

As for the free surface measurements, an ensemble average was performed on the velocity signal with all the experiments, it yields $\overline{\mathbf{u}}_{EA} = \text{median}_{k=1,...,N}(\mathbf{u}_{run\ k})$. For both free surface and velocity measurements, bores were generated every 5 min to achieve the same water depth, velocity and turbulent level for each bore. For each depth of the ADV measurements, 25 runs were performed. A number of bores superior to 15 had to be realised to get a meaningful average (Simon and Chanson, 2013). It took a minimum of 2h05min to record each complete data set of 25 runs for one configuration at one depth (see Chapter IV for the detail of all configurations).

III.3.3.4 Integral turbulent length and time scales

Turbulent integral length and time scales were calculated using a two-point measurement technique (Cousteix, 1989; Favre, 1965; Favre et al., 1957). The flow velocity was measured with two ADVs facing each other's with their control volume separated by a spacing $\boldsymbol{\delta}$. The velocity was cross-correlated for a time lag τ at a position $\mathbf{X}$:

$$R_{ij}^{+}(\boldsymbol{\delta}, \tau) = R^{+}\left(u_i'(\mathbf{X}, t), u_j'(\mathbf{X} + \boldsymbol{\delta}, t + \tau)\right) = \frac{\overline{u_i'(\mathbf{X}, t)\, u_j'(\mathbf{X} + \boldsymbol{\delta}, t + \tau)}}{\sqrt{\overline{u_i'(\mathbf{X}, t) u_j'(\mathbf{X}, t)}}} \tag{III.6}$$

where R^{+} is the normalised correlation function, $\boldsymbol{\delta} = (\delta_x, \delta_y, \delta_z)$ is the separation between sampling volumes, u_i' is the velocity fluctuation around the mean calculated over a period T (i.e. $u_i' = u_i - \bar{u}_i$), and the subscript i and j refer to the velocity component direction (x, y, z). Figure III.8 illustrates the calculation of the cross-correlation time scale. The time average is calculated as:

$$\overline{u_i(\mathbf{X}, t)} = \frac{1}{T} \int_{t-T/2}^{t+T/2} u_i(\mathbf{X}, t') dt \tag{III.7}$$

Using formula (III.6), an auto-correlation time scale may be estimated from single-point measurements, i.e. for $\boldsymbol{\delta} = 0$ (Chanson and Carosi, 2007; Cousteix, 1989):

$$T_{ii}(0) = \int_0^{\tau_0} R_{ii}^{+}(0, \tau) d\tau \tag{III.8}$$

[4] I coded the software from scratch in C++. It reads the data files, did some basic signal error filtering, synchronised all data together, computed all steady and unsteady characteristic quantities, and wrote the data. Some methods are detailed in Simon and Chanson (2013)

with the integration process being stopped at the time where the correlation is zero, called τ_0 (Figure III.8). Similarly a cross-correlation time scale may be calculated for two-point measurements with the sampling volumes separated by a distance $\boldsymbol{\delta}$:

$$T_{ii}(\boldsymbol{\delta}) = \int_{\tau_m}^{\tau_0} R_{ii}^{+}(\boldsymbol{\delta}, \tau) d\tau \tag{III.9}$$

where τ_m is the shift giving the best correlation and verifies:

$$|R_{ii}^{+}(\boldsymbol{\delta}, \tau_m)| = \max\left(R_{ii}^{+}(\boldsymbol{\delta}, \tau); |\tau| < T/2\right). \tag{III.10}$$

If the spacing $\boldsymbol{\delta}$ varies, the integral turbulent length L_i and time T_i scales are defined as:

$$\mathrm{L}_i = \int_0^{\boldsymbol{\delta}_0} R_{ii}^{+}\left(\boldsymbol{\delta}', \tau_m\right) d\boldsymbol{\delta}' \tag{III.11}$$

$$\mathrm{T}_i = \frac{1}{\mathrm{L}_i} \int_0^{\boldsymbol{\delta}_0} T_{ii}\left(\boldsymbol{\delta}'\right) R_{ii}\left(\boldsymbol{\delta}', \tau_m\right) d\boldsymbol{\delta}' \tag{III.12}$$

where $\boldsymbol{\delta}_0$ is the spacing such as u_i' are still correlated. It is defined by $\boldsymbol{\delta}_0 = \min\left(\boldsymbol{\delta}; R_{ii}^{+}(\boldsymbol{\delta}, \tau_m) = 0\right)$. The correlation time scale $T_{ii}(\boldsymbol{\delta})$ is a time scale of a structure of size $\boldsymbol{\delta}$ advected by the u_i velocity. The integral turbulent time scale T_i characterise a typical 'lifetime' of the flow coherence, while the integral length scale L_i represents an average size of the advected eddies.

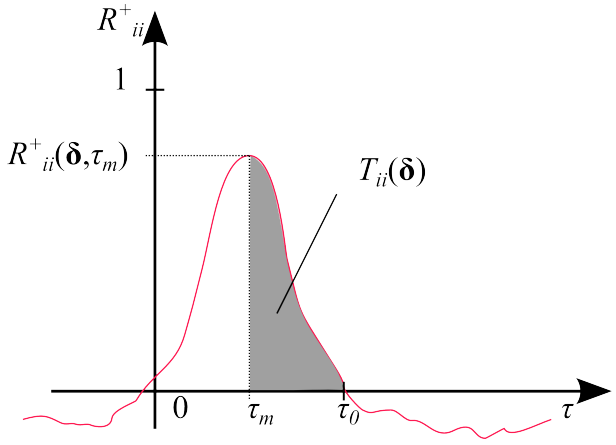

Figure III.8: Definition sketch of cross correlation function and correlation time scale

In the present study, the two-point velocity measurements were obtained using two ADV units located at $x = 6.13$ m from the gate (i.e. 5 m downstream of the channel inflow). One ADV control volume was located on the channel centreline and the other was adjusted away from the channel centreline in the transverse direction. The control volume of the ADVs was separated by a distance δ_y (Figure III.9). The measurements were performed at four vertical elevations

z for six transversal spacing δ_y. Each experiment was repeated 5 times and the correlation functions were averaged.

Note that some practical difficulties were experienced for $\delta_y < 6$ mm and $20 < \delta_y < 25$ mm. The two ADV units were interfering with each other, thus producing meaningless signals. For the vertical velocity component measured by the ADV, interference constantly occurred at each transverse separation distance δ_y giving a meaningless signal. For completeness, some unsuccessful tests were performed with longitudinal separation distance δ_x as well as vertical separation distances δ_z. The ADV units were interfering with each other and produced meaningless velocity signals. Therefore only the u_x and u_y components measured with a transverse spacing δ_y could be used for correlation analysis.

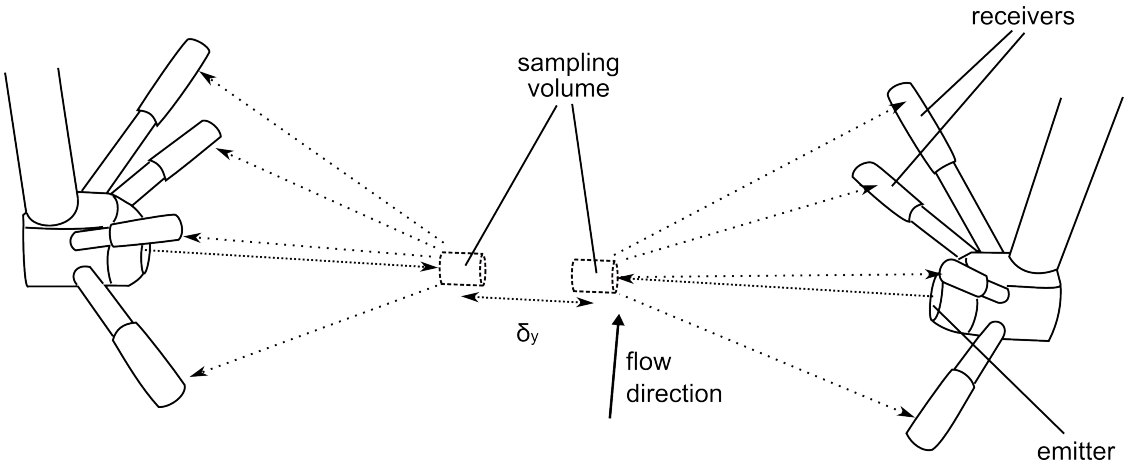

Figure III.9: Sketch of the two ADV units with their sampling volumes separated by a transverse distance δ_y

III.4 Numerical study

Positive surges were modelled in a simplified version of the channel presented in section III.3.1. The simulations aim at reproducing the flow free surface and the detailed flow structure. The principal difficulties lie in the accurate reproduction of the turbulence of the initial flow, in the transient free surface evolution and in the reproduction of the turbulence induced by the unsteady flow.

The hypotheses used to model the phenomenon are as follow. The flow is considered to be an incompressible non-miscible two-phase flow, considering air and water. The domain is bounded in time and space. It is a simplified version of the physical channel modelled as a perfect rectangle or parallelepiped, for two or three dimensional simulations, respectively. Figure III.10 present a sketch of the domain used to model undular bores. The initial configurations of the

simulations are reconstructed from experimental data by specifying the steady flow conditions and reproducing the method of generation of the unsteady flow (complete or partial gate closure). The methods were selected for their successful use in coastal applications using the CFD code Thètis (Helluy et al., 2005; Lubin et al., 2010a, 2006).

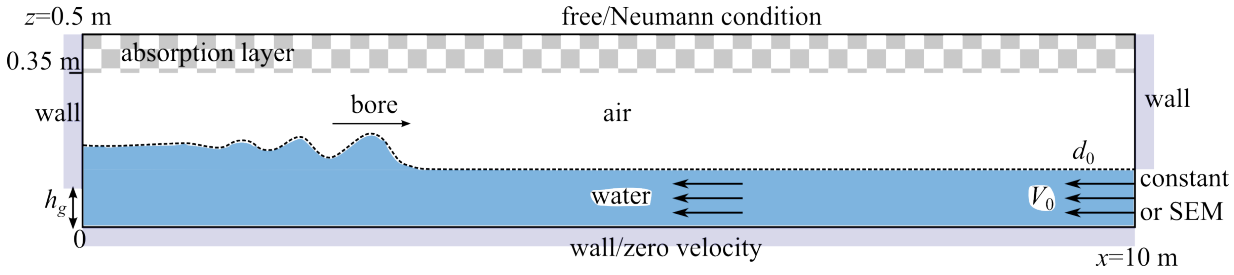

Figure III.10: Definition sketch of the numerical domain used for bore simulations

III.4.1 Equations for fluid motion

The flow is modelled using the Navier-Stokes equations in their single fluid formulation (Kataoka, 1986). The objective is to model the domain presented in Figure III.10. The steps to obtain the final set of equations will be detailed in the following sections. The final formulation of the equations is:

$$\begin{cases} \nabla \cdot \mathbf{u} = 0 \\ \rho \left(\dfrac{\partial \mathbf{u}}{\partial t} + (\mathbf{u} \cdot \nabla)\, \mathbf{u} \right) + \underbrace{\mathbf{B}_\mathbf{u} (\mathbf{u} - \mathbf{u}_\infty)}_{\text{Boundary condition}} \\ = \rho \mathbf{g} - \nabla p + \nabla \cdot \left[(\mu + \underbrace{\mu_t}_{\text{Turbulence}}) \left(\nabla \mathbf{u} + \nabla^T \mathbf{u} \right) \right] - \underbrace{\dfrac{\mu}{K} \mathbf{u}}_{\text{Brinkman}} \\ \underbrace{\dfrac{\partial C}{\partial t} + \mathbf{u} \cdot \nabla C = 0}_{\text{Phase interface}} \end{cases} \tag{III.13}$$

Each term will be detailed in the corresponding section.

III.4.1.1 Navier-Stokes Equations

The complete structure of a water flow can be completely detailed by the Navier-Stokes equations under the hypothesis of an incompressible flow. Assuming $\mathbf{u}$ is the velocity, p is the pressure, t is the time, $\mathbf{g}$ is the gravity vector, ρ is the density and μ the viscosity, the Eulerian system of equations for an incompressible flow is written as follow considering mass and momentum conservations:

$$\begin{cases} \nabla \cdot \mathbf{u} = 0 \\ \rho \left(\dfrac{\partial \mathbf{u}}{\partial t} + (\mathbf{u} \cdot \nabla)\, \mathbf{u} \right) = \rho \mathbf{g} - \nabla p + \nabla \cdot \left[\mu \left(\nabla \mathbf{u} + \nabla^T \mathbf{u} \right) \right] \end{cases} \tag{III.14}$$

III.4.1.2 Boundary conditions

The equations require specific boundary conditions to fully determine the system and obtain a mathematically well posed problem. Here a unique system of equations is solved in the whole domain. The boundary conditions are modelled by adding a penalisation term in the Navier-Stokes equations (III.14). This method is based on the work of Angot (1989) and Khadra (1994). The boundary conditions are treated as a surface flux with:

$$- \left. \frac{\partial \mathbf{u}}{\partial \mathbf{n}} \right|_S = \mathbf{B_u} \left(\mathbf{u} - \mathbf{u}_\infty \right) \tag{III.15}$$

where $\mathbf{B_u}$ is matrix penalising the velocity components, $\mathbf{n}$ is the exterior normal unit vector of the boundary S and $\mathbf{u}_\infty$ is a user set velocity. The values of the coefficient $\mathbf{B_u}$ give the type of boundary condition. For example, if $\mathbf{B_u} = 0$, a Neumann condition is modelled but if $\mathbf{B_u} = +\infty$ a Dirichlet condition is set by inducing $\mathbf{u} = \mathbf{u}_\infty$.
After adding the new term (in blue), the Navier-Stokes equations become:

$$\begin{cases} \nabla \cdot \mathbf{u} = 0 \\ \rho \left(\dfrac{\partial \mathbf{u}}{\partial t} + (\mathbf{u} \cdot \nabla)\, \mathbf{u} \right) \textcolor{blue}{+ \mathbf{B_u} \left(\mathbf{u} - \mathbf{u}_\infty \right)} = \rho \mathbf{g} - \nabla p + \nabla \cdot \left[\mu \left(\nabla \mathbf{u} + \nabla^T \mathbf{u} \right) \right] \end{cases} \tag{III.16}$$

III.4.1.3 Permeable obstacles and Brinkman term

To model obstacles or absorption layers, the equations are modified to take into account variation of permeability in the domain. A similar method of penalisation as the previous section III.4.1.2 is used to model obstacle. A penalisation term is added to the system of equations (Angot et al., 1999; Arquis and Caltagirone, 1984; Khadra et al., 2000). The domain is considered as a porous medium based on the Brinkman theory. A permeability coefficient K defines the capacity of a porous medium to let pass the fluids more or less freely. If the coefficient K is set to zero, then the medium is an impermeable solid. The larger the coefficient is set, the more the medium is equivalent to a fluid. Herein, the permeability was only used to set an absorption layer on the top of the domain (Figure III.10).
The momentum equation is modified by the addition of an extra term taking into account the

permeability coefficient, called Brinkman term, $(\mu/K)\mathbf{u}$. The Navier-stokes equations become:

$$\begin{cases} \nabla \cdot \mathbf{u} = 0 \\ \rho\left(\dfrac{\partial \mathbf{u}}{\partial t} + (\mathbf{u}\cdot\nabla)\,\mathbf{u}\right) + \mathbf{B_u}\,(\mathbf{u}-\mathbf{u}_\infty) = \rho\mathbf{g} - \nabla p + \nabla\cdot\left[\mu\left(\nabla\mathbf{u} + \nabla^T\mathbf{u}\right)\right] - \dfrac{\mu}{K}\mathbf{u} \end{cases} \tag{III.17}$$

Tangential velocity damping layer

In order to reduce numerical interferences with an open boundary, a zone dissipating the tangential velocities can be added near the domain boundary (Hafsia et al., 2009). On the damping zone, a friction term $-\boldsymbol{\gamma}\circ u = -\left(\gamma_i u_i\right)_i$ is added to the momentum equation. Hafsia et al. (2009) used a linear function $\boldsymbol{\gamma}$ to damp the tangential velocities in two dimensional simulations. The absorption layer was implemented in Thétis for three dimensional simulations. Considering an open boundary defined on the yz-plan at x_e with $x_s < x_e$, the function $\boldsymbol{\gamma}$ is defined as:

$$\boldsymbol{\gamma} = (\gamma_i)_i \begin{cases} \gamma_i = \gamma_m \dfrac{x - x_s}{(x_e - x_s)} & \text{for } x \in [x_s; x_e] \text{ and } i \in \{y, z\} \\ 0 & \text{otherwise} \end{cases} \tag{III.18}$$

where x_s is the start of the damping zone and γ_m is the maximal value of the damping zone. The damping zone is defined such that $\boldsymbol{\gamma}(x_s) = 0$ and $\gamma_i(x_e) = \gamma_m$ for $i = y$ or z. The damping function is calibrated only by the coefficient γ_m (Hafsia et al., 2009). The linear increase of the friction coefficient forces the tangential velocities to decrease.

III.4.1.4 Turbulence modelling

The turbulence is modelled using a large eddy simulation (LES) approach. It was chosen over other methods for its relatively affordable computational cost with an accurate description of the turbulence. The LES method simulates only the large scales of the turbulence, while the smaller scales are modelled by a subgrid-scale model (SGS). The separation of large and small scales found its justification in the Kolmogorov theory which suggests a cascade of eddies from large to small structures. The inertial and dissipative effects of small scales are considered to have a universal behaviour and can be parameterised solely by the energy transfer rate entering the cascade (Sagaut, 2006).

The separation of scale is accomplished by applying a convolution product to the Navier-Stokes equations acting as a low-pass filter. A convolution filter is defined as:

$$\bar{\mathbf{u}}(x) = (\mathbf{u} * G)(x) = \int_{-\infty}^{+\infty} \mathbf{u}\,(x - x')\,G\,(x')\,dx' \tag{III.19}$$

where G is a kernel function usually compactly supported, i.e. G is non zero over an interval of finite length Δ. As a consequence, the size of the filter is inferior to Δ.

The convolution is applied to the complete system of equations (III.17). It results in the appearance of the term $-\nabla \cdot \tau$ with $\tau = \bar{\mathbf{u}} \otimes \bar{\mathbf{u}} - \overline{\mathbf{u} \otimes \mathbf{u}}$ called the subgrid tensor. Moreover, the velocity and pressure variables, $\mathbf{u}$ and p, are also filtered and replaced by $\bar{\mathbf{u}}$ and $\bar{p}$.
To close the equation, the term τ is modelled by known quantities using an eddy viscosity model:

$$\tau = \frac{1}{3}\mathbf{Tr}(\tau)\mathbf{Id} - 2\mu_t \bar{\mathbf{S}} \tag{III.20}$$

with $\mathbf{Id}$ the identity matrix, $\mathbf{Tr}$ the matrix trace operator and $\bar{\mathbf{S}} = 1/2\left(\nabla\bar{\mathbf{u}} + \nabla^T\bar{\mathbf{u}}\right)$. The term μ_t is the eddy viscosity also called turbulent viscosity. The equation (III.20) is based on the hypothesis that "The energy transfer mechanism from the resolved to the subgrid scales is analogous to the molecular mechanisms represented by the diffusion term, in which the viscosity ν appears" (Sagaut, 2006, p. 109). The SGS models used to calculate μ_t are discussed in section III.4.1.5. Finally, the model for the stress tensor is re-injected in the filtered Navier-Stokes equations yielding:

$$\begin{cases} \nabla \cdot \bar{\mathbf{u}} = 0 \\ \rho\left(\dfrac{\partial \bar{\mathbf{u}}}{\partial t} + (\bar{\mathbf{u}} \cdot \nabla)\,\bar{\mathbf{u}}\right) + \mathbf{B_u}\,(\bar{\mathbf{u}} - \mathbf{u}_\infty) \\ = \rho\mathbf{g} - \nabla\bar{p^*} + \nabla \cdot \left[(\mu{+}\mu_t)\left(\nabla\bar{\mathbf{u}} + \nabla^T\bar{\mathbf{u}}\right)\right] - \dfrac{\mu}{K}\bar{\mathbf{u}} \end{cases} \tag{III.21}$$

where $\bar{p}^* = \bar{p} + 1/3\tau_{kk}$.
Note that in the following, the notation with the over-bar $\bar{\mathbf{u}}$ and $\bar{p}^*$ will be replaced by the original notation $\mathbf{u}$ and p respectively unless clarifications are needed.

III.4.1.5 Subgrid scale models for LES

The convolution filter applied to the Navier-Stokes is implicitly applied by the domain discretisation (section III.4.2.2). The cut-off length $\bar{\Delta}$ of the filter depends on the mesh grid size and is generally evaluated as follow:

$$\bar{\Delta} = (\Delta_x \Delta_y \Delta_z)^{1/3} \tag{III.22}$$

where Δ_i is the size of the mesh grid in the i-direction (Deardorff, 1970).
The subgrid tensor was simplified by the use of a turbulent viscosity ν_t. This turbulent viscosity can be modelled by several methods (Sagaut, 2006, p. 132). Some methods implemented in Thétis are presented hereafter:

Smagorinsky model

The simplest SGS model is probably the Smagorinsky model (Smagorinsky, 1963). The turbulent viscosity is replaced by

$$\frac{\mu_t}{\rho} = \nu_t = \left(C_s\bar{\Delta}\right)^2 \tilde{S} \tag{III.23}$$

where $\tilde{S} = \sqrt{2\bar{S}\bar{S}}$ and C_s is the Smagorinsky constant. The constant usually take values between 0.18 and 0.23 for homogeneous isotropic turbulence. As a drawback of the simplicity, the constant value of the Smagorinsky model makes it unconditionally dissipative and makes it unable to describe the transition between laminar to turbulent flow. Moreover in the case of wall flow, the turbulence cannot be properly modelled. To improve the method, the Smagorinsky constant can be reduced near the walls (Deardorff, 1970) or a damping law can be applied such as the Van Driest damping law (Van Driest, 1956).

Turbulent kinetic energy model

Another method to estimate the eddy viscosity is the Turbulent kinetic energy (TKE) model (Bardina et al., 1980). The eddy viscosity is determined as a function of $\bar{\Delta}$ and q_{SGS} the kinetic energy of the subgrid modes. The eddy viscosity is modelled by

$$\mu_t = \rho C_{TKE}\bar{\Delta}\sqrt{q_{SGS}} \tag{III.24}$$

The constant C_{TKE} is generally chosen to be equal to 0.2 and $q_{SGS} = 1/2\overline{(\bar{u}_i - \bar{u}_i)}^2$.

Mixed scale model

The mixed scale (MS) model is derived from a weighed geometric average of the Smagorinsky model and the TKE model (Sagaut, 2006). The model has a triple dependency on the large and small structures of the resolved field as a function of the cut-off length. The eddy viscosity is defined as

$$\nu_t = (\nu_{t,\text{smago}})^\alpha - (\nu_{t,\text{TKE}})^{1-\alpha} = C_M\bar{\Delta}^{1+\alpha}\tilde{S}^{\frac{\alpha}{2}}\left(q_{SGS}\right)^{\frac{1-\alpha}{2}} \tag{III.25}$$

The parameter α varies between 0 and 1. If $\alpha = 0$, the TKE model is used and if $\alpha = 1$, the Smagorinsky model is used. The constant C_M is evaluated from the constant C_s and C_{TKE}. In the following, the constant is evaluated as $C_M = 0.06$ using $\alpha = 0.5$. As an advantage, the MS model does not require a complementary wall model. The correct disappearance of the eddy viscosity is correctly reproduced near the wall as the kinetic energy tends to zero.

III.4.1.6 Two-phase interface modelling

The interface modelling method is a volume of fluid method (VOF) developed by Hirt and Nichols (1981). The method is relatively simple and offers a good accuracy to describe a flow interface with rupture and reconnection. The basic idea is to locate the two media by a colour function C indicating the phase rate of presence. For a two-phase flow, one medium will be identified by the value $C = 0$ and the other by $C = 1$. The function C is dependent of the fluid velocity and its evolution is described by a advection equation:

$$\frac{\partial C}{\partial t} + \mathbf{u} \cdot \nabla C = 0 \tag{III.26}$$

The magnitude of the physical characteristics of the fluids depends on the local phase. They are defined according to C by:

$$\begin{cases} \mu = C\mu_0 + (1 - C)\,\mu_1 \\ \rho = C\rho_0 + (1 - C)\,\rho_1 \end{cases} \tag{III.27}$$

where ρ_0, ρ_1, μ_0 and μ_1 are the densities and viscosities of fluid 0 and 1 respectively.
Note that the filtering performed by the LES method induces the appearance of new terms in the final set of equations (Labourasse et al., 2007). These terms have no known model representing them accurately. Their influences are considered negligible and are removed from the Navier-Stokes equations (Labourasse et al., 2007).

III.4.2 Numerical methods

The previous set of equations (III.13) is numerically solved by the code Thétis. Thétis is a CFD code developed at the Institut de Mécanique et d'Ingénierie I2M of the Université de Bordeaux. The code takes advantage of parallel computing to reduce the time to solve the equations and improve its memory capacity. It is used for industrial and academic applications such as geophysical flows, energetics, etc. The numerical tools used in the simulations will be presented in the following sections.

III.4.2.1 Temporal discretisation

The Navier-Stokes equations are time dependent. The physical time of the model is split into a discrete number of iterations $\{t_0, \ldots, t_n, \ldots\}$ and the time derivatives are calculated using a first or second order backward differentiation formula (BDF) (Ascher, 1998; Süli, 2003). The approximation of a function ϕ at the time t_n is written φ_n. After n iterations, the first order BDF method (BDF1) approximates the derivative at time t_{n+1} by:

$$\left(\frac{\partial \phi}{\partial t}\right)^{n+1} = \frac{\phi^{n+1} - \phi^{n}}{\Delta t_{n+1}} \tag{III.28}$$

where $\Delta t_{n+1} = t_{n+1} - t_n$ is the time step. Note that (III.28) is a classic implicit backward Euler scheme. The second order BDF method (BDF2) is also implemented in the code Thétis. Supposing a constant time step Δt and using the known values at the time t_{n-1} and t_n, the derivative of the function ϕ at the time t_{n+1} is approximated by:

$$\left(\frac{\partial \phi}{\partial t}\right)^{n+1} = \frac{3\phi^{n+1} - 4\phi^{n} + \phi^{n-1}}{\Delta t} \tag{III.29}$$

When the BDF2 method is used, the first iteration cannot be calculated directly because it requires two previous states to be known. Therefore the first iteration is realised with the BDF1 method.

III.4.2.2 Spacial discretisation

The two or three dimensional domain is discretised into a finite number of cells. A finite-volume method (Patankar, 1980) is used to discretise the Navier-Stokes equations (III.13) on staggered grids. The vertices of the cells are used to compute the pressure. The edges defined between two pressure nodes are used to compute the velocity in the edge direction. This creates control volume centred on the pressure node and delimited by the velocity nodes. Figure III.11 shows an example of the domain discretisation which corresponds to the method marker and cell (MAC).

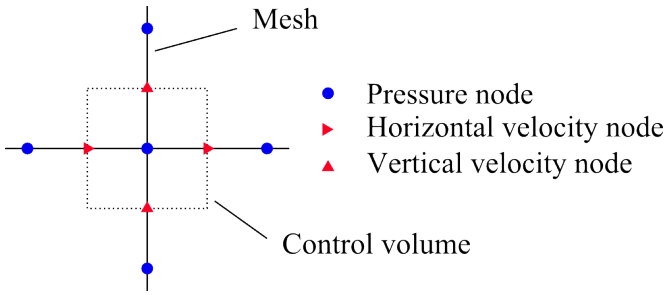

Figure III.11: Mesh and control volume for a staggered grid

The equations are integrated on each control volume and discretised in term of physical fluxes through the control volume faces. The Ostrogradsky theorem confirms the conservation of flux through the control volume and therefore on the entire domain. The variables still need to be known on the mesh edges. This is realised using specific interpolation schemes depending on the equation terms, convective or diffusive. The viscous term is approximated by a second order centred scheme and the inertial term can be solved by centred, upwind or hybrid scheme. The schemes used are detailed in Patankar (1980) and presented thereafter:

Central difference scheme

This scheme evaluates the variable on the face. It is obtained by a Taylor series truncated after the first derivative and corresponds to an arithmetic average between two neighbour points. This is a second order scheme but can be unstable on coarse grid for simulation with high Reynolds number.

Upwind scheme

It approximates the variable by the one locate upstream the flow. This is only a first order scheme and implies numerical diffusion. However, it remains adapted to flow where the convective term is preponderant.

Hybrid upwind-centred scheme

This scheme can be used to solve the space derivatives of the inertial term. The idea is to choose the numerical scheme the most adapted to the local characteristics of the flow when a spurious discontinuity is detected in the velocity signal. Sign variations of the velocity gradients are calculated over four neighbouring grid points. If parasitic variations are encountered, a switch from second order centred scheme to upwind scheme. It has been checked that second order centred scheme is employed in most of the numerical domain, whereas the upwind scheme is found to be used near the interface in restricted zones of strong shear and distortion.

III.4.2.3 Time splitting method

The Navier-Stokes equations require solving both the velocity and the pressure together with the incompressibility constraint. Those operations are performed by splitting the equations into two stages. The first step is to predict the velocity and the second step is to compute the pressure and solve the mass conservation equation to correct the velocity. This is a time splitting method (Goda, 1979). The following will present a simple form of the time splitting method applied to the Navier-Stokes equations (III.13) without extra term and using a BDF1 method (section III.4.2.1) for a constant time step Δt. The velocity and pressure approximations at the time $t_{n+1} = (n+1)\Delta t$ are obtained knowing $\mathbf{u}^n$ and p^n by firstly finding the prediction of the velocity $\mathbf{u}_*^{n+1}$:

$$\begin{aligned} \rho^n \left(\frac{\mathbf{u}_*^{n+1} - \mathbf{u}^n}{\Delta t} + \nabla \cdot \left(\mathbf{u}_*^{n+1} \otimes \mathbf{u}^n \right) - \mathbf{u}_*^{n+1} \nabla \cdot \mathbf{u}^n \right) \\ = \rho^n \mathbf{g} - \nabla p^n + \nabla \cdot \mu^n \left(\nabla \mathbf{u}_*^{n+1} + \nabla^T \mathbf{u}_*^{n+1} \right) \end{aligned} \tag{III.30}$$

Secondly, correcting the pressure with a pressure increment $\varphi^{n+1} = p^{n+1} - p^n$ such that

$$\begin{cases} \rho^n \dfrac{\mathbf{u}^{n+1} - \mathbf{u}_*^{n+1}}{\Delta t} + \nabla \varphi^{n+1} = 0 \\ \nabla \cdot \mathbf{u}^{n+1} = 0 \end{cases} \tag{III.31}$$

The pressure increment is obtained by taking the divergence of the previous equations (III.31). It yields the following Poisson equation

$$\nabla \mathbf{u}_*^{n+1} = \nabla \cdot \left(\frac{\Delta t}{\rho} \nabla \varphi^{n+1} \right) \tag{III.32}$$

Finally, φ^{n+1} can be calculated from (III.32). The pressure and the velocity at the iteration $n+1$ can be corrected with

$$\begin{cases} \mathbf{u}^{n+1} = \mathbf{u}_*^{n+1} - \dfrac{\Delta t}{\rho} \nabla \varphi^{n+1} \\ p^{n+1} = \varphi^{n+1} + p^n \end{cases} \tag{III.33}$$

The latter method can be performed for equations (III.13) and using a different time derivative scheme such as BDF2. The previous time splitting method can be improved for one-phased flow (Timmermans et al., 1996) with the rotational incremental scheme. It consists of correcting the pressure by $p^{n+1} = p^n + \varphi^{n+1} - \chi \mu \nabla \cdot \mathbf{u}_*^{n+1}$. The parameter χ is chosen to be strictly inferior to $2\mu/d$ with d the dimension. In Thétis, recent works were performed to improve the outgoing boundary conditions treatment for laminar and unsteady monophasic flow (Poux et al., 2012, 2011).

III.4.2.4 Interface discretisation for VOF methods

With the VOF method, the colour function C is advected with the flow velocity. The advection of C is realised by solving equation (III.26). Several models exist to solve equation (III.26), a review of the different method can be found in the article by Benson (2002). Yee (1987) proposed using a Lax-Wendroff scheme which is a Total Variation Diminishing scheme (TVD). Methods based on geometric reconstruction as the piecewise linear interface construction method (PLIC) also give accurate results (Youngs, 1982). The method proposed in this study are the following:

TVD scheme

The advection equation is solved by a numerical scheme. Equation (III.20) can be solved by a second order scheme reducing dispersion. A TVD scheme based on a Lax-Wendroff scheme was proposed by Yee (1987). The scheme reduces possible numerical oscillations and reduces the diffusion of the first order scheme. A three dimensional version of this VOF-TVD scheme was implemented in Thétis (Vincent, 1999; Vincent and Caltagirone, 2000). This method is

fast and reproduces accurately the interface but diffusion of the interface might appear when breaking and rupture happen at the free surface (Lubin et al., 2006).

PLIC scheme

The function C can also be known geometrically through its interface. Youngs (1982) proposed a two dimensional method VOF-PLIC. The interface orientation is determined by finding the intersection between a cell and the plan intersecting it using the plan normal vector. The function C is then reconstructed after finding for each cell and its neighbours the exact value of C within each cell by translation of the plan. This method was developed in Thétis in two dimensions by Abadie (2001) and in three dimensions by Breil (2001). In the code Thétis, the C function is smoothed before the calculation of the physical properties (density and viscosity), thanks to an inverse distance weighting average. The method is fast and induces no diffusion, however artificial surface tension and fragmentation can appear.

III.4.2.5 Linear system and parallel solving

The discretisation of the complete system of equations by an implicit method leads to the transformation of the equation into a sparse linear system. For a large number of points, the system is too big for everyday computers to handle. The numerical domain needs to be divided into sub-domains which are distributed to several processors. The sub-domains are divided with an equal size and the connection between processors is minimised to improve the communication speed. The code is parallelised by the Message Passing Interface (MPI) library (Pacheco, 1997). The matrices of the linear system are non symmetric and the linear system is solved by iterative methods implemented in the Hypre Library (Falgout et al., 2006). The prediction and correction steps are solved respectively by Bi-Conjugate Gradient Stabilized (BiCGStab) solver (Van Der Vorst, 1992) and Generalized Minimal Residual (GMRES) solvers (Saad and Schultz, 1986), associated with Jacobi and multi-grid preconditioner (Wesseling, 1992). The Hypre library is also developed using the MPI library.

III.4.2.6 Turbulent inflow conditions: the synthetic eddy method

The simulations aim to reproduce the experimental conditions of positive surges. The turbulence of the steady flow needs to be reproduced before quantifying the impact of the bore on the initially steady flow. This is done by creating a boundary condition injecting artificial turbulent structures.

For three dimensional simulations, realistic unsteady inflow conditions were specified at the inlet of the domain, i.e. the channel upstream using available experimental data. An effective method to generate synthetic eddies (SEM) on the inlet plane was implemented in the code

(Jarrin et al., 2006, 2009). The SEM generates explicitly large-scale coherent structures and convects them with the mean flow through the inlet plane. This method considers turbulence as a superposition of coherent structures. These structures or eddies are generated over the inlet plane of the calculation domain and defined by a shape function that encompasses the spatial and temporal characteristics of the structures. The method requires few parameters. Only the mean velocity, the Reynolds stresses and the typical size and number of eddies are necessary to recreate a coherent stochastic signal. Although the SEM involves the summation of a large number of eddies for each grid point on the inflow, the CPU time required to generate the inflow data for each iteration is negligible (Jarrin et al., 2006). The method performs well on any geometry and any kind of flow.

The SEM reconstructs the velocity fluctuations $\mathbf{u}'$ and adds the fluctuation to the mean velocity $\bar{\mathbf{u}}$ (Jarrin et al., 2006). The fluctuations are reconstructed by

$$\mathbf{u} = \bar{\mathbf{u}} + \mathbf{u}' = \bar{\mathbf{u}} + \frac{1}{\sqrt{N}} \sum_{k=1}^{N} \mathbf{A}(\mathbf{X}) \boldsymbol{\epsilon}_k \boldsymbol{f}_{\boldsymbol{\sigma}}(\mathbf{X} - \mathbf{X}_k) \tag{III.34}$$

with N the number of eddies, $\mathbf{A}$ the Cholesky decomposition (III.35) of the Reynolds stress $R_{i,j} = \overline{u_i' u_j'}$ in the i and j the directions, $\boldsymbol{\epsilon}$ is a random distribution of the eddies intensity with $\epsilon_{k,i} = \pm 1$. The position of eddies $\mathbf{X}_k$ is randomly generated. Finally, the function $\boldsymbol{f}_{\boldsymbol{\sigma}}$ determines the shape of eddies. It is taken as a compactly supported function, with $\boldsymbol{\sigma}$ being the support and therefore the eddy size. $\boldsymbol{f}_{\boldsymbol{\sigma}}$ is taken as a hat function, but other shape can be used (Jarrin, 2008).

$$\mathbf{A} = (a_{i,j})_{i,j} = \begin{bmatrix} \sqrt{R_{1,1}} & 0 & 0 \\ \dfrac{R_{2,1}}{a_{1,1}} & \sqrt{R_{2,2} - a_{2,1}^2} & 0 \\ \dfrac{R_{3,1}}{a_{1,1}} & \dfrac{R_{3,2} - a_{2,1} a_{3,1}}{a_{2,2}} & \sqrt{R_{3,3} - a_{3,1}^2 - a_{3,2}^2} \end{bmatrix} \tag{III.35}$$

The SEM generates the eddies in an extra sub-domain of the simulation. The velocity signal is extracted from this sub-domain and added to the main simulation. At each time step of the main simulation, the SEM transports eddies within its sub-domain with the modelled velocity. When eddies are convected outside of the sub-domain new eddies are added to maintain their number. The signal generated is thus a stationary ergodic random process (Jarrin et al., 2006). The SEM reproduces the same mean velocity and Reynolds stresses as those given in input. The skewness is zero and the flatness depends on the size of the sub-domain, the size of eddies and their numbers (Jarrin, 2008). Other methods were tested by generating turbulent inflow data consisting of the time-averaged experimental velocity profile with some superimposed random fluctuations. The generated data exhibited neither spatial, nor temporal correlations,

and dissipated quickly the pseudo turbulence. Several techniques generating inflow turbulence exist, a review can be found in Keating et al. (2004).
Improvements of the SEM were proposed by Pamiès et al. (2009) to adapt the creation of eddies to the local domain boundary but require a more detailed knowledge of the flow than the basic SEM. Poletto et al. (2012) developed a SEM generating a divergence free boundary inflow. Those two methods were not implemented in the code as the initial SEM implemented in Thètis needed more validation. The validation of the SEM is presented in section V.3.

III.5 Summary

The physical flow was studied experimentally with classical method using Pitot tube, non intrusive ADM sensors and ADV units. The instrumentations was well known which allowed comparisons with existing flow measurements. The unsteady flow properties were studied by means of ensemble average. An original method to measure turbulent scales in unsteady flow was presented using two ADV units to get information on the size of turbulence.
The numerical modelling of the physical flow was performed with a validated method. The Navier-Stokes equations were solved with common LES and VOF methods to study the turbulence of an air-water flow. My addition in the code of an existing method to model synthetic inflow turbulence is a key point to model a realistic flow with an initially steady turbulent flow. The numerical simulations used experimental data for initialisation such as the water depth, the flow velocity and the turbulent fluctuations. The experimental measurements were also used for validation.
Note that the numerical simulations reproduced experimental study, conducted in channel with a smooth PVC bed, not related to this thesis since a method to model gravel bed was not validated in time.

IV

Experimental study of positive surges in a fixed gravel bed channel

IV.1 Chapter overview

Tidal bores were studied with idealised models of tidal bores propagating upstream an initially steady flow generated after the impact of a stream against a fast closing gate. The study was conducted during my stay for eleven months in the University of Queensland. The facility and methods used were presented in section III.3. Bores were generated in a rectangular channel with a bed partially covered by fixed gravels. Measurements of the free surface evolution and velocity were performed on the channel centreline with relative high frequency probes. The unsteady turbulent properties were analysed by repeating each experiment several times to obtain an ensemble averaged data set. A unique study of the turbulent scales in steady and unsteady flow conditions was performed by a two-point measurement technique. The study was conducted at two different scales to test the Froude number dynamic similarity in terms of potential viscous scale effects.

IV.2 Basic steady flow properties

The steady flow conditions were investigated at several longitudinal and transverse locations summarised in Table IV.1. For two discharges, the flow field was thoroughly studied to gain some detailed information on the initial flow properties including the velocity and pressure distributions. Further instantaneous velocity measurements were conducted with another discharge to characterise the velocity field next to the open tainter gate. Herein, x is the longitudinal distance from the tainter gate positive upstream, y is the transverse distance from the channel centreline positive towards the right sidewall and z is the distance normal to the bed positive upwards. The reference flow conditions were the flow depth d_0 and velocity V_0 positive downstream calculated as $V_0 = Q/(d_0 W)$ at $x = 6.13$ m from the gate with Q the water discharge ($W = 0.5$ m was the channel width). The bed slope was set to $S_0 = 0.0077$ to reproduce undular and breaking bores. Without a slope, only undular bore could be performed. The fixed gravel bed was located from $x = 0.59$ m to 9.15 m (section III.3) similarly to setting in Docherty and Chanson (2012) and Khezri and Chanson (2012c).

For all investigated flow conditions, the flow was supercritical upstream of the fixed gravel bed. A small hydraulic jump with a weak breaking roller took place immediately upstream of the gravel bed transition (Figure IV.1). The position of the jump was the same for all investigated flow conditions. The flow was subcritical above the fixed gravel bed and the free surface not completely parallel to the channel bed. At the downstream end of the fixed gravel bed section, the flow accelerated and became supercritical over the smooth PVC bed between the end of the fixed gravel bed section and the free overfall.

Figure IV.2 presents the dimensionless free surface profiles along the entire channel. All the free surface elevation data are presented relative to the smooth PVC bed (d_{PVC}), with the critical flow depth $d_c = \sqrt[3]{Q^2/(gW^2)}$ and g the gravity acceleration. For each discharge, the free surface profile exhibited similar patterns.

Figure IV.3 shows some typical dimensionless pressure distributions along the channel, with d the local water depth at the measurement location x. The pressure distributions in the initially steady flow were estimated as hydrostatic at all measured locations along the channel.

IV.2.1 Velocity distribution

The time averaged velocity was recorded with a Pitot tube and an ADV unit. The Pitot tube data could be considered as a reference data set for the ADV data which were sampled at 200 Hz for 60 s (12 000 samples)[1]. Figure IV.4 presents some typical measurements and some

[1]Koch and Chanson (2005) performed measurements at 50Hz for 2 min (6 000 samples) to analyse the steady flow conditions, herein, larger sample sizes were used to access second statistical moments.

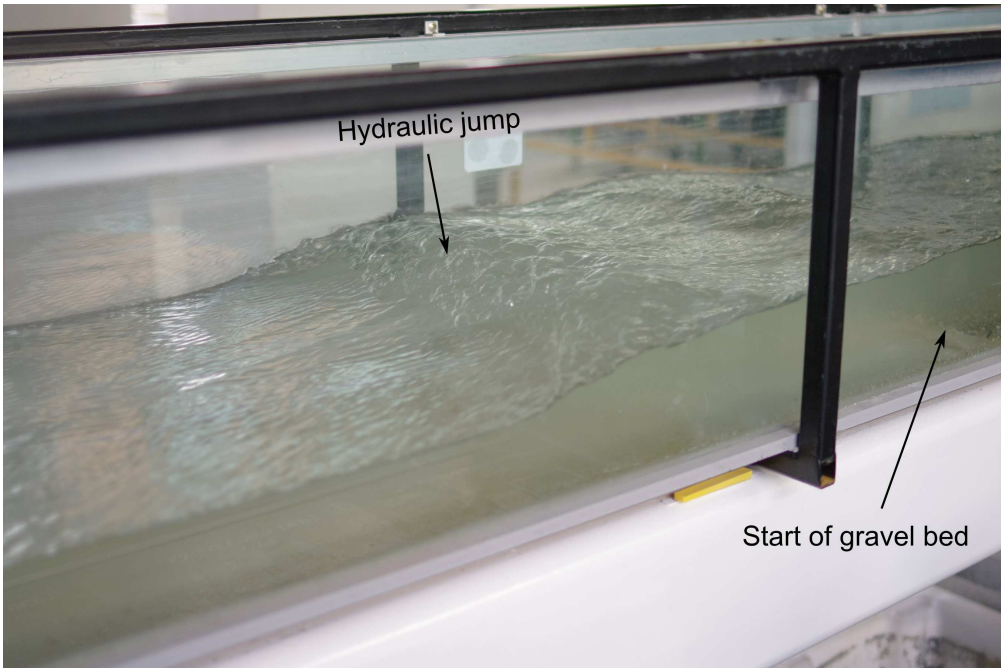

Figure IV.1: Photograph of the hydraulic jump upstream of the gravel bed for $Q = 0.036$ m^3.s^{-1}. Flow direction from left to right, with the photograph showing $10.1 > x > 8.6$ m

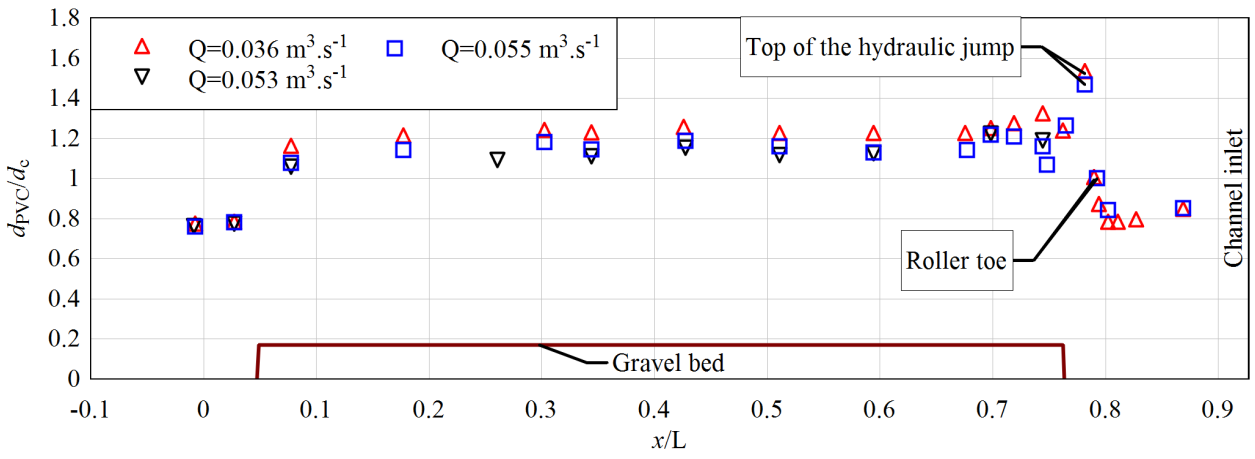

Figure IV.2: Dimensionless free surface profiles along the channel centreline in steady flows. The flow direction from right to left with the gate at $x = 0$ where $L = 12$ m was the channel length. Note that the gravel bed height is not at scale

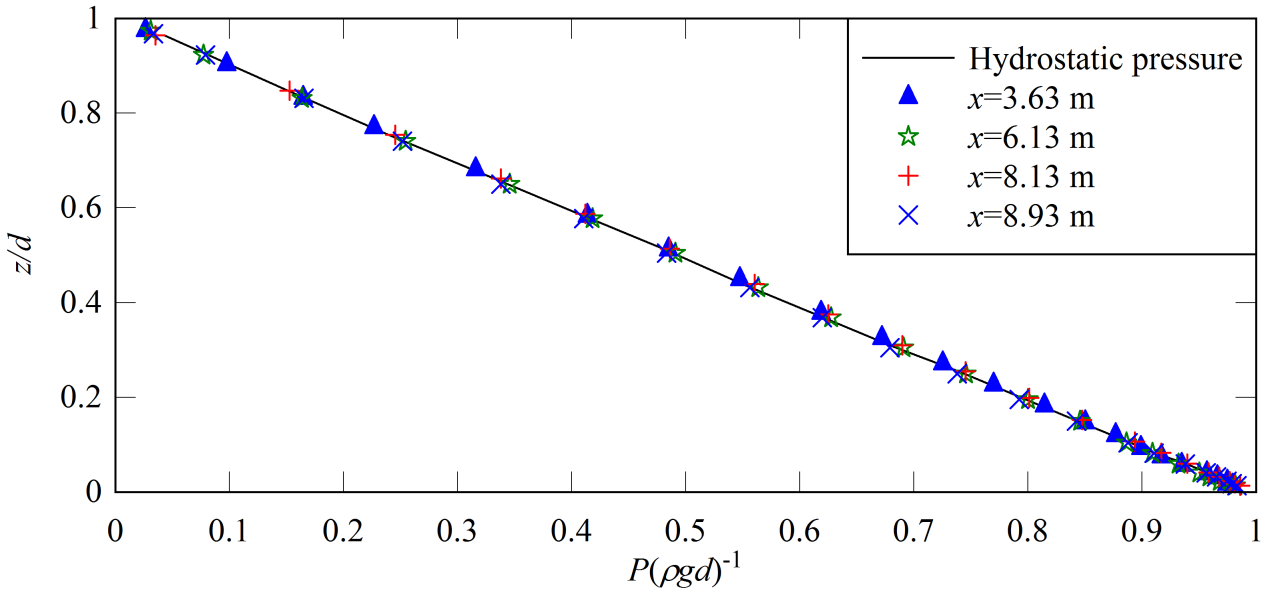

Figure IV.3: Dimensionless distributions of pressure on the channel centreline at 4 longitudinal positions. Flow conditions: $Q = 0.0546$ m^3.s^{-1}

Table IV.1: Experimental steady flow conditions and measurement locations

Q	d_0 at $x = 6.13$ m	V_0 at $x = 6.13$ m	Water depth measurements locations	Velocity probe longitudinal measurements locations
m^3.s^{-1}	m	m.s^{-1}	m	m
0.0364	0.085	0.85	–0.9 to 10.53	8.93^{*+}, 8.63^{*}, 8.38^{*}, 8.11^{*}, 7.13^{*+}, 6.13^{*+}, 5.11^{*}, 4.13^{*}, 3.63^{*+}
0.0534	0.107	0.99	–0.9 to 8.93	0.33^{+}, 0.93^{+}
0.0546	0.110	0.99	–0.9 to 10.53	8.93^{*+}, 8.63^{*}, 8.38^{*}, 8.13^{*}, 7.13^{*+}, 6.13^{*+}, 5.13^{*}, 4.13^{*}, 3.63^{*+}

Notes: * Pitot tube measurements, $^{+}$ ADV measurements. For $x = 3.63$ and 6.13 m, Pitot tube measurements made at $2y/W = -0.9, -0.8$ and -0.5. For $x = 7.13$ and 8.63 m, Pitot tube measurements made at $2y/W = \pm 0.5, \pm 0.8$ and ± 0.9. For $x = 6.13$ m, ADV measurements made at $2y/W =$ ś$0.32, \pm 0.5$ and ± 0.72. $W = 0.5$ m is the channel width.

comparison between Pitot tube and ADV data at $x = 6.13$ m for several transverse locations. The results showed a close agreement between Pitot tube and ADV velocity data. The velocity data indicated some sidewall effect in the near proximity of the glass sidewalls. For a smooth channel, Nezu and Nakagawa (1993) suggested a width to depth ratio W/d greater than 5 to 6 to achieve a quasi-two-dimensional flow. Herein the aspect ratio was $W/d_0 = 5.9$ and 4.5 at $x = 6.13$ m for $Q = 0.036$ and 0.055 m^3.s^{-1} respectively. The glass sidewalls were considerably smoother than the fixed gravel bed, thus justifying a quasi-two-dimensional flow approximation for measurement in the unsteady flow on the channel centreline.

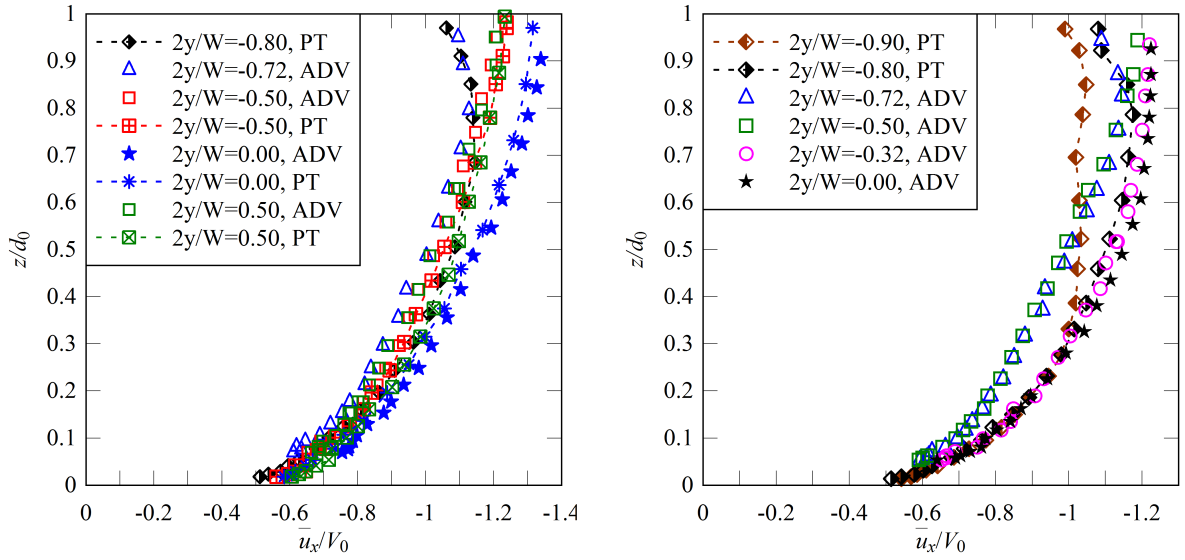

(a) Comparison between Pitot tube (PT) and ADV data, $Q = 0.036$ m^3.s^{-1}

(b) Profiles for the right half of the channel, $Q = 0.055$ m^3.s^{-1}

Figure IV.4: Dimensionless distributions of time-averaged longitudinal velocity at $x = 6.13$ m for several transverse position

The velocity distributions were integrated across the channel width to check for conservation of mass:

$$Q = \int_{z=0}^{d} \int_{y=-W/2}^{W/2} |\bar{u}_x(y,z)| dydz \tag{IV.1}$$

Assuming the velocity $\mathbf{u} = 0$ at the bed and sidewalls (no slip condition), the results showed a close agreement between the measured discharge and equation (IV.1) within 2%. For example, at $x = 6.13$ m, Equation (IV.1) yielded 0.0359 m^3.s^{-1} and 0.0530 m^3.s^{-1} compared to measured discharges of $Q = 0.0365$ m^3.s^{-1} and 0.0546 m^3.s^{-1} respectively. While the difference was within the measurement error of 2% (section III.3.2), Equation (IV.1) tended to underestimate the flow rate, possibly because of the linear interpolation of the velocity profile in the boundary vicinity.

Figure IV.5 shows the dimensionless velocity distributions on the channel centreline at various

longitudinal locations, where $u_c = \sqrt{g d_c}$ is the critical velocity. The velocity data indicated the presence of a developing boundary layer above the fixed gravel bed. For $Q = 0.036$ m^3.s^{-1} and 0.055 m^3.s^{-1}, the boundary layer became fully developed over the rough bed for respectively $7.13 > x$ m and $5.13 > x$ m: i.e., $(x_{\text{inlet}} - x)/d_c > 39$ and 46 respectively with $x_{\text{inlet}} = 11.13$ m the distance of the channel inlet from the gate.

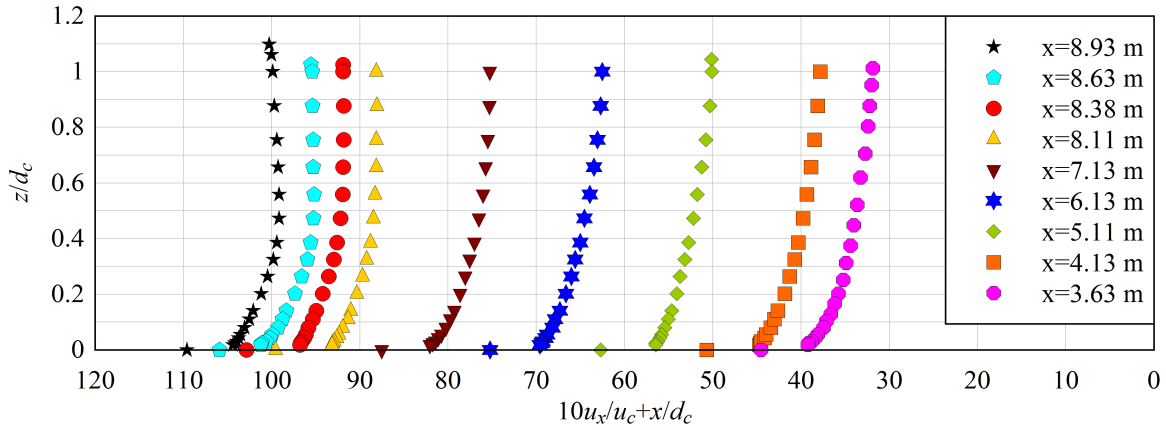

(a) $Q = 0.036$ m^3.s^{-1}

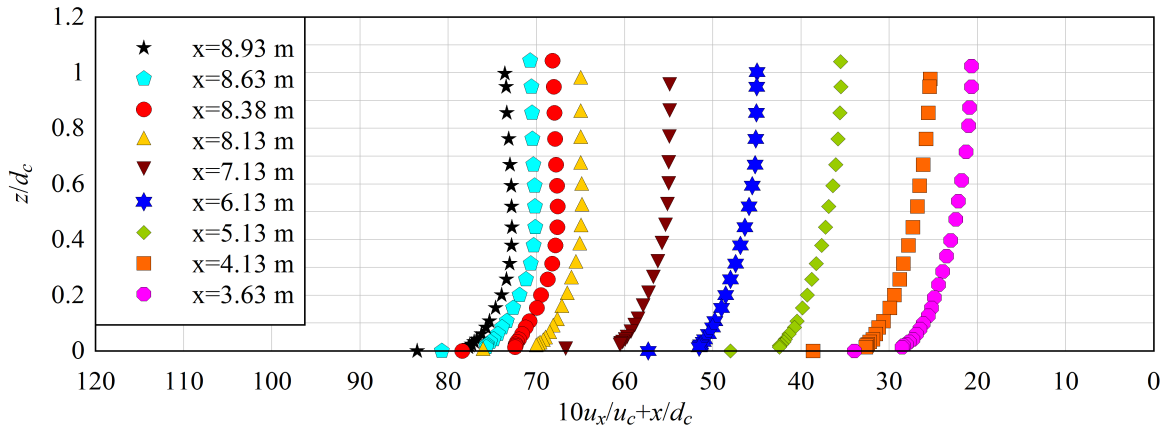

(b) $Q = 0.055$ m^3.s^{-1}

Figure IV.5: Dimensionless velocity distributions along the channel in the initially-steady flow. Centreline data, Pitot tube measurements and gate at $x = 0$

Within the developing boundary layer, the velocity distributions followed closely a power law (Chanson, 2004a; Schlichting, 1979):

$$\frac{|\bar{u}_x|}{\max_z |\bar{u}_x|} = \left(\frac{z}{\delta}\right)^{1/N} \tag{IV.2}$$

where $\max_z |\bar{u}_x|$ is the free-stream velocity calculated as the maximum of the absolute longitudinal velocity along the vertical axis and δ is the boundary layer thickness defined as the

elevation where $\bar{u}(\delta) = 99\%\max_z |\bar{u}_x|$. The finding is illustrated in Figure IV.6 showing some dimensionless velocity profile at $x = 6.13$ m. Herein, the boundary layer was fully developed at $x = 6.13$ m and $Q = 0.036$ m^3.s^{-1}, while the flow is partially developed for $Q = 0.055$ m^3.s^{-1} with $\delta/d_0 = 0.62$. For comparison, Docherty and Chanson (2010) used the experimental set-up and found $\delta/d_0 = 0.64$ at $x = 6.13$ m for $Q = 0.050$ m^3.s^{-1}.

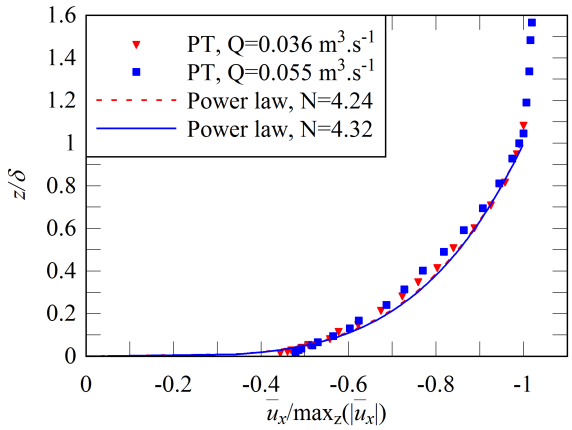

Figure IV.6: Dimensionless distributions of longitudinal velocity component in the developing boundary layer at $x = 6.13$ m on the channel centre line. Comparison between Pitot tube (PT) data and power law

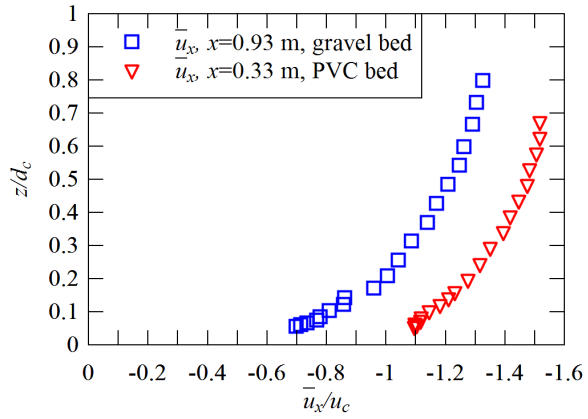

Figure IV.7: Dimensionless distributions of longitudinal velocity upstream and downstream of the downstream end of the fixed gravel bed. $Q = 0.053$ m^3.s^{-1}. Note that z is above the PVC bed at $x = 0.33$ m and above the gravel bed at $x = 0.93$ m

Figure IV.7 presents the velocity redistributions at the downstream end of the fixed gravel bed section: namely at $x = 0.33$ m from the gate above the smooth PVC bed and $x = 0.93$ m above the fixed gravel bed. At $x = 0.93$ m, the flow was fully-developed. As the flow passed from the rough fixed gravel bed to the smooth bed, the flow accelerated and became supercritical at $x = 0.33$ m. Above the smooth PVC bed, the velocity followed a power law with a velocity

exponent $N = 6.9$, a result similar to the velocity exponent $N = 7$ observed over a smooth bed (Chanson, 2004a; Koch and Chanson, 2005; Schlichting, 1979).

IV.2.2 Boundary shear stress estimate and equivalent sand bed roughness height

The boundary shear stress may be derived from the velocity measurements by a range of methods. Relevant reviews include Nezu (2005), Koch and Chanson (2009), Chanson (2009b) among others. Herein the focus is on the boundary shear stress estimates above the fixed gravel bed for the flow conditions listed in Table IV.1. The boundary shear stress τ_0 and the shear velocity $u_* = (\tau_0/\rho)^{1/2}$ were estimated using a range of methods, depending whether the boundary layer flow was partially or fully developed as detailed in Simon and Chanson (2013). Figure IV.8 illustrates the development of the boundary layer above the fixed gravel bed in the steady flow conditions.

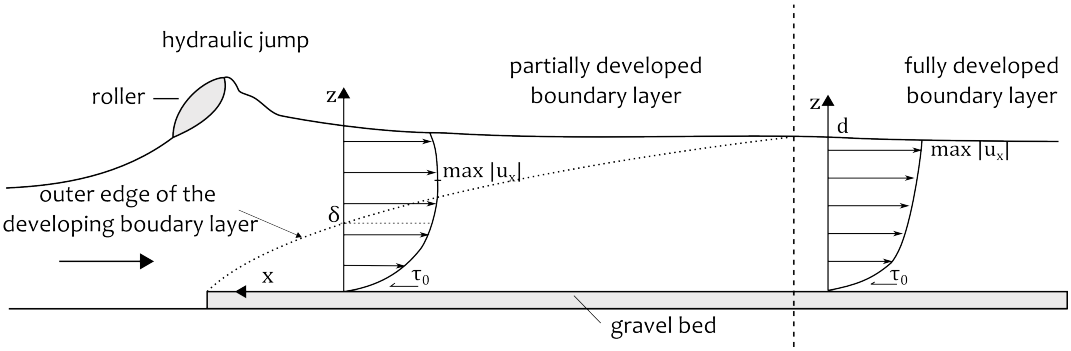

Figure IV.8: Sketch of boundary layer development above the fixed gravel bed in the steady flow conditions with the hydraulic jump upstream the gravel bed

After calculation, the equivalent sand roughness height was estimated as $k_s \approx 6$ mm which was comparable to the typical gravel size $d_s = 5.7$ mm and close to the findings of Docherty and Chanson (2010) ($k_s = 3.4$ mm) and is classified in the same roughness range. The shear velocity was estimated as $u_*/u_c = 0.076$ in the fully-developed flow region for both discharges herein.

IV.2.3 Turbulent fluctuations

In steady flows, turbulent measurements were performed using an ADV system. Figure IV.9 shows the vertical distribution of the dimensionless velocity standard deviations. The experimental data are compared with the correlation proposed by Nezu (2005) in fully-developed

flows over a smooth bed:

$$\frac{\text{RMS}\,(u_i)}{u_*} = D_i \exp\left(-C_i \frac{z}{d}\right) \tag{IV.3}$$

where RMS(u_i) is the fluctuation (root mean square) of the velocity component in the i-direction, and D_i and C_i are dimensionless constants[2]. At $x = 6.13$ m, the present data compared well with the analysis proposed by Nezu (2005) in terms of the longitudinal and transverse velocity component fluctuations (Figure IV.9a). Some larger values were measured in terms of the vertical velocity component fluctuations, and a previous study showed the adverse effect of the gravel bed on the ADV signal (Docherty and Chanson, 2010). On the channel centreline, the ratio RMS(u_y)/RMS(u_x) was on average 0.56 while the ratio RMS(u_z)/RMS(u_x) was on average 1.5. The findings were consistent with previous experiments performed in the same channel highlighting some turbulence anisotropy (Chanson, 2010b; Docherty and Chanson, 2012; Koch and Chanson, 2009). Figure IV.9b shows distributions of dimensionless tangential Reynolds stress on the channel centreline at $x = 6.15$ m. The tangential Reynolds stresses $\rho\overline{u'_x u'_y}$ were relatively small as previously found in Koch and Chanson (2009) over a smooth bed. But the tangential Reynolds stresses $\rho\overline{u'_x u'_z}$ and $\rho\overline{u'_y u'_z}$ were significantly larger, likely linked with the large fluctuations of the vertical velocity component.

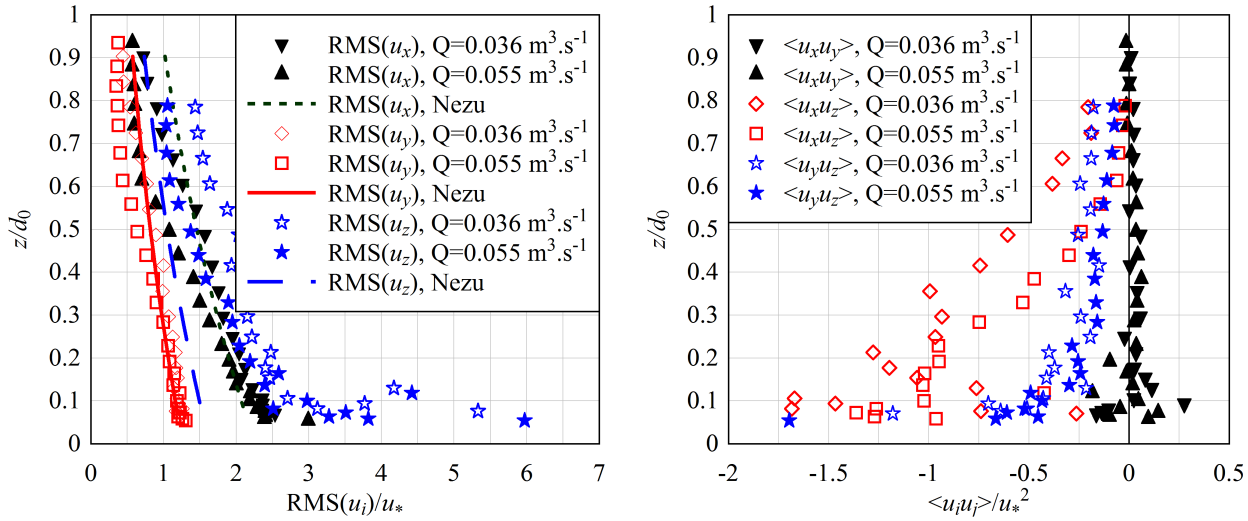

(a) Velocity fluctuations (b) Tangential stresses

Figure IV.9: Dimensionless distributions of velocity fluctuations and tangential turbulent stresses in steady flows at $x = 6.13$ m on the channel centreline

[2] D_i and C_i are dimensionless constants estimated as: $D_x = 2.26$, $D_y = 1.27$, $D_z = 1.63$, $C_i = 0.88$ based upon experiments performed above a smooth bed (Nezu, 2005).

IV.2.4 Turbulent length scales in the steady flow

The integral turbulent time and length scales were calculated based upon two-point measurements using two ADV units using an averaging time T of approximately $T = 60$ s, with their sampling volume separated in the transverse direction by a distance δ_y (section III.3.3.4). The averaging period T must be large such that the time-average data becomes independent of the time t in a steady flow and of the averaging period T. Figure IV.10 presents some typical cross-correlation functions for several transverse separation distances. Figure IV.11 shows the effects of the separation distance δ_y on the correlation time scales and maximum cross-correlation coefficients. Namely, a decreasing maximum correlation coefficient and integral time scale with increasing separation distance. The results indicated that the turbulence lost its coherence for $\delta_y > 0.02$ m (Figure IV.11). The maximum cross-correlation coefficient was observed at about $\tau = 0$ s indicating that a coherent turbulent structure, advected by the longitudinal velocity, passed the two control volumes at the same time (Figure IV.10). For comparison, in the study of Favre (1965), some two-point measurement correlations were performed in the streamwise direction of the flow, and the maximum cross-correlation coefficient was observed for a time lag $\tau > 0$.

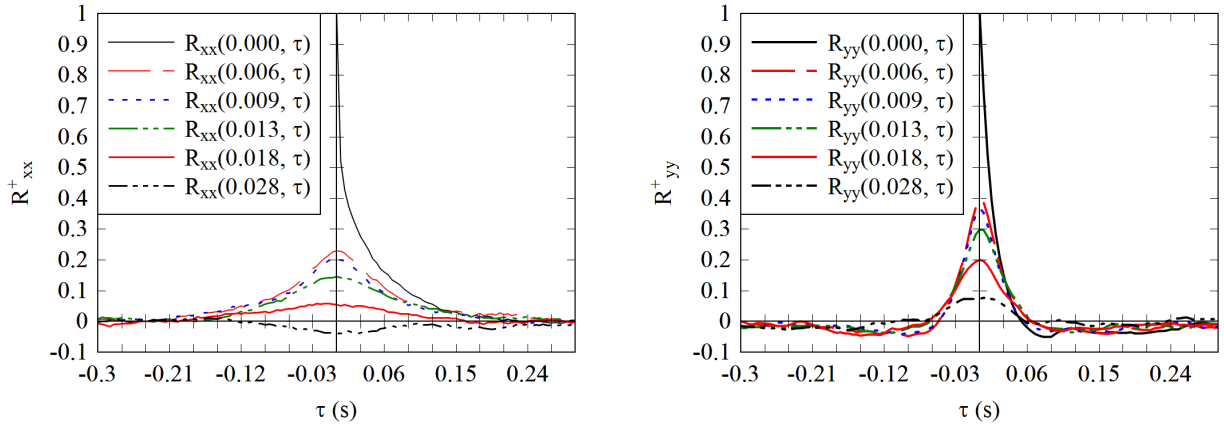

(a) Correlation functions for u_x (b) Correlation functions for u_y

Figure IV.10: Velocity cross-correlation functions for different transverse separation distances δ_y between probes at $x = 6.13$ m and $z = 0.03$ m

The turbulent integral time and length scale data are summarised in Table IV.2. Herein L_x and T_x are the turbulent integral length and time scales for the longitudinal velocity component based upon cross-correlations in the transversal direction. All the measurements were conducted within the boundary layer flow ($z/\delta < 1$). The turbulent length scales were larger for the transversal velocity than for the longitudinal velocity ($L_x/L_y \approx 1.7$) and the length scale data increased with increasing distance from the bed for $z/\delta < 0.71$. The turbulent length scales

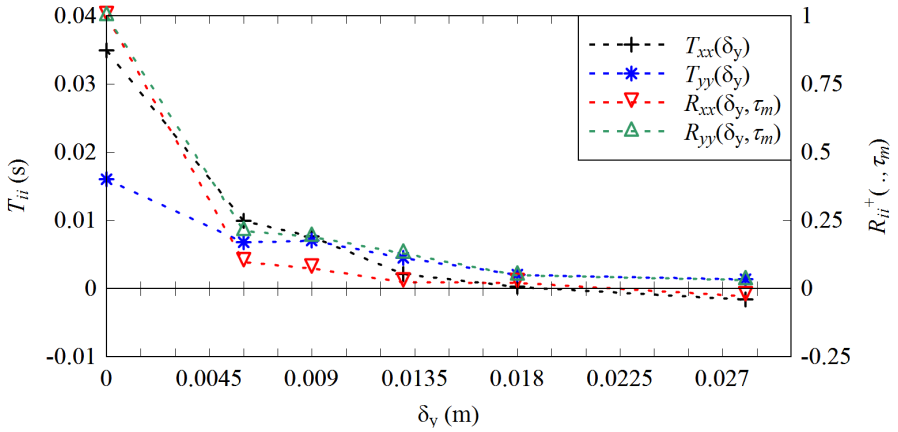

Figure IV.11: Cross-correlation time scales T_{xx} and T_{yy} and maximum cross-correlation coefficients as functions of the transverse separation distances δ_y between probes at $z = 6.13$ m and $z = 0.012$ m

were about the same order of magnitude as the equivalent sand bed roughness $k_s = 0.006$ m: i.e., $L_x/k_s \approx 0.83$ and $L_y/k_s \approx 1.4$ on average for all measurement points. The increase in turbulent length scale with increasing distance from the bed was consistent with the turbulent mixing length model proposed by Prandtl (1925). The turbulent integral time scale data tended to show a maximum value about $z/\delta < 0.43$. The data implied $T_y < T_x$ with $T_y/T_x \approx 0.6$ on average (Table IV.2).

Table IV.2: Turbulent integral time and length scale at $x = 6.13$ m. Flow conditions: $Q = 0.053$ m^3.s^{-1}, $d_0 = 0.011$ m, centreline data

z	z/d_0	L_x(*)	L_y(*)	T_x	T_y
m		m	m	s	s
0.012	0.11	0.0038	0.0058	0.040	0.018
0.03	0.27	0.0055	0.0095	0.056	0.020
0.05	0.45	0.0060	0.0100	0.031	0.017
0.07	0.63	0.0046	0.0085	0.011	0.013

Note (*): the accuracy of the values was about 1 mm because of the size of the ADV control volume and the accuracy of its spatial position.

The turbulent length scale of the velocity components characterised some flow coherence over the transversal direction. The results are presented in a dimensionless form in Figure IV.12. Interestingly, the length scale L_y was about proportional to the product of the time scale T_y by the advection velocity and the data were best correlated by:

$$\frac{L_y}{d_0} = 0.582 \frac{\bar{u}_x T_y}{d_0} \tag{IV.4}$$

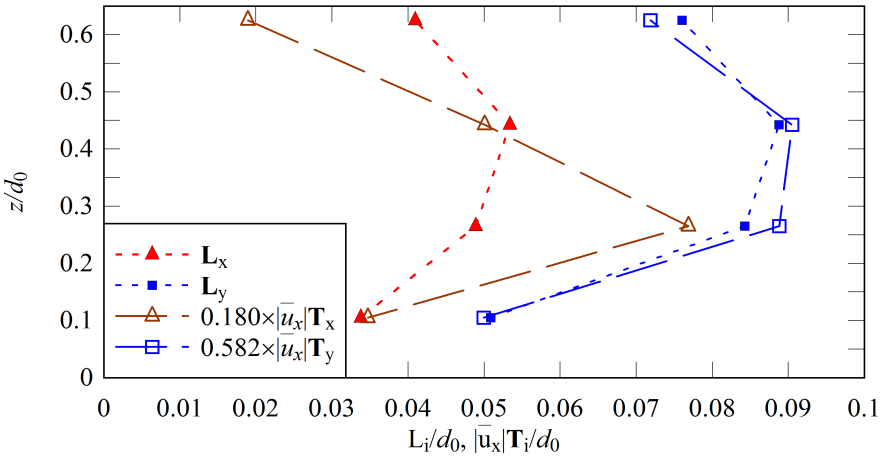

Figure IV.12: Dimensionless distributions of turbulent integral length and time scales. Flow conditions: $Q = 0.053$ m^3.s^{-1}, $x = 6.13$ m, $d_0 = 0.112$ m, centreline data

No such relationship was observed between L_x and T_x. This might be linked with some influence of the gravel bed on the inner flow region.
For completeness, the ADV sampling interval time was 0.005 s and the ADV sampling volume size was 1-2 mm. Those characteristics were smaller than the turbulent integral time and length scales, although their effects on the data accuracy were not negligible.

IV.3 Bore free surface characteristics and flow patterns

A detailed study of the bore free surface was performed for a range of flow conditions presented in Table IV.3 with the initial steady flow condition detailed in section IV.2. The fast closure of the tainter gate generated the unsteady flow (section III.3.2.4) and the evolution of the free surface was recorded using non-intrusive ADMs (section III.3.3.2) located along the channel centreline. For each set of flow conditions, the unsteady flow was reproduced 25 times and the free-surface data were ensemble averaged to calculate the wave properties. For each experiment, the initial water depth and flow velocity, d_0 and V_0 respectively, are given at $x = 6.13$ m upstream of gate. Appendix D presents movies of an undular bore (section D.2.1) and a breaking bore (section D.2.2) propagating in the channel. The complete data sets of the free surface measurements are reported in Appendix A.
Figure IV.13 presents typical shapes of positive surges. The following notations are used: h_g is the gate opening after bore generation, U_b is the bore celerity measured at $x = 6.13$ m, $Re_b = (V_0 + U_b)d_0/\nu$, d_b is the bore conjugated depth, $d_{\max}$ is the bore water depth beneath the first wave crest, a_w is the first undulation amplitude and L_w is the first undulation wave length.

Table IV.3: Experimental flow conditions for the positive surge free-surface measurement at $x = 6.13$ m, ensemble averaged data

Q	h_g	d_0	V_0	Fr	U_b	Re_b	d_b	$d_{\max}$	a_w	L_w	Bore type
$m^3.s^{-1}$	mm	m	$m.s^{-1}$		$m.s^{-1}$		m	m	m	m	
0.0365	0	0.0863	0.85	1.60	0.63	1.26E+5	0.166	0.192	0.027	0.590	Breaking + undulations
0.0365	0	0.0893	0.82	1.56	0.64	1.29E+5	0.167	0.191	0.030	0.602	Breaking + undulations
0.0365	3	0.0891	0.82	1.50	0.58	1.24E+5	0.165	0.203	0.043	0.573	Breaking + undulations
0.0365	9	0.0879	0.83	1.50	0.57	1.22E+5	0.160	0.202	0.048	0.554	Undular + cross
0.0365	21	0.0876	0.83	1.45	0.51	1.17E+5	0.145	0.173	0.036	0.567	Undular + cross
0.0365	27	0.0875	0.83	1.40	0.46	1.12E+5	0.139	0.160	0.029	0.597	Undular
0.0365	36	0.0880	0.83	1.32	0.40	1.07E+5	0.132	0.146	0.021	0.600	Undular
0.0365	43	0.0881	0.83	1.26	0.34	1.02E+5	0.125	0.135	0.014	0.606	Undular
0.0365	43	0.0866	0.84	1.29	0.35	1.02E+5	0.126	0.134	0.010	0.591	Undular
0.0365	51	0.0887	0.82	1.18	0.28	9.71E+4	0.119	0.123	0.008	0.598	Undular
0.0365	57	0.0877	0.83	1.14	0.23	9.23E+4	0.113	0.114	0.004	0.582	Undular
0.0547	0	0.1118	0.98	1.66	0.76	1.93E+5	0.216	0.234	0.023	0.758	Breaking + undulations
0.0547	9	0.1129	0.97	1.58	0.69	1.86E+5	0.208	0.234	0.031	0.749	Breaking + undulations
0.0547	21	0.1118	0.98	1.56	0.65	1.81E+5	0.203	0.236	0.040	0.758	Breaking + undulations
0.0547	31	0.1118	0.98	1.48	0.57	1.72E+5	0.189	0.236	0.048	0.698	Undular + cross
0.0547	44	0.1115	0.98	1.43	0.52	1.66E+5	0.176	0.208	0.036	0.722	Undular + cross
0.0548	55	0.1119	0.98	1.37	0.46	1.60E+5	0.169	0.192	0.028	0.731	Undular + cross
0.0547	62	0.1129	0.97	1.31	0.41	1.54E+5	0.163	0.178	0.019	0.709	Undular + small cross
0.0547	65	0.1116	0.98	1.31	0.39	1.52E+5	0.160	0.174	0.020	0.737	Undular + small cross
0.0548	79	0.1116	0.98	1.21	0.28	1.40E+5	0.148	0.153	0.009	0.744	Undular + small cross

Note: "cross" is for cross waves observed over the secondary undulations

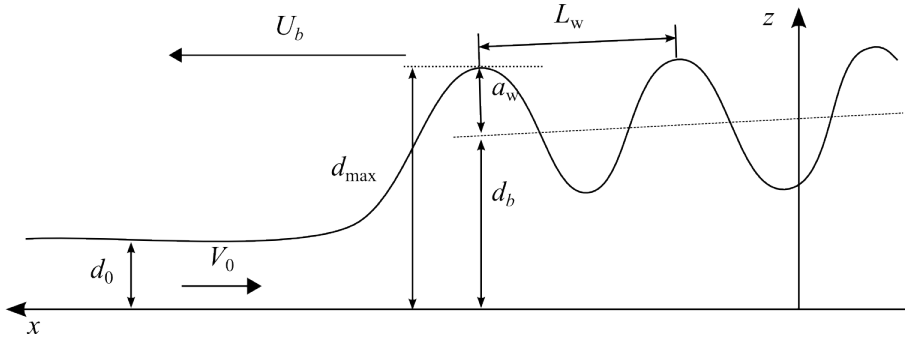

(a) Undular bore, $1 < Fr < 1.4$ to 1.5

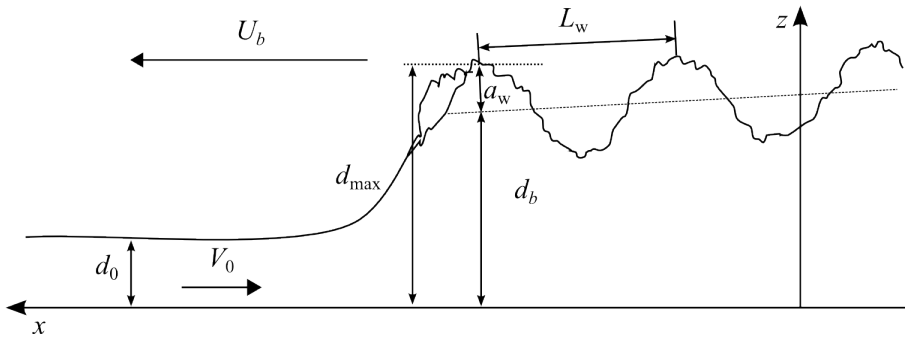

(b) Undular bore with breaking, 1.4 to $1.5 < Fr < 1.7$ to 1.8

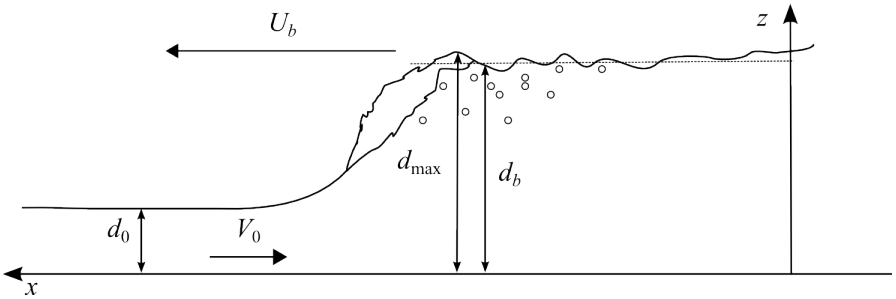

(c) Breaking bore, $Fr > 1.8$

Figure IV.13: Definition sketches of bores observed in the present study

IV.3.1 Description of the flow free surface

The experimental observations showed several flow patterns and will be described here based upon the bore Froude number defined as $Fr = (U_b + V_0)/\sqrt{(gd_0)}$ (II.3). In this study, the bore was observed at $x = 6.13$ m from the gate, it was either undular or undular with a breaking front. A bore can also be completely breaking with no undulation after the roller but such a bore could not be generated with the present setup.

For a Froude number inferior to 1, no bore was visible. For Froude numbers between 1 and 1.5, bores were undular (Figures IV.13a and IV.14a). The bore front, leading wave, was characterised by a smooth rise of mean water level followed by a train of secondary undulations.

For small Froude numbers less than 1.2 to 1.3, the free surface of the bore was smooth and nearly two-dimensional. The undulation amplitude and wave steepness increased with increasing Froude numbers. For larger Froude numbers ($1.2 - 1.3 < Fr < 1.4 - 1.5$), the undulations became three-dimensional and some cross-wave patterns were seen on the leading wave and on the secondary waves (Figures IV.14a and IV.15). The cross-waves initiated from both sidewalls close to the leading wave toe and intersected on the channel centreline. After intersection, the cross-waves continued to propagate over the secondary undulations yielding a lozenge pattern (Figure IV.15). For Froude numbers about 1.4, the cross wave started to intersect on the first wave crest leading to the development of a small breaking roller from the crest centre (Figure IV.13b and Figure IV.14a). For larger Froude numbers $Fr > 1.5$ as the Froude number increased, the roller expended across all the channel width with a quasi two-dimensional appearance and the cross-waves disappeared (Figure IV.14b). The bore roller was followed by small secondary undulations. The height of these secondary waves decreased with the increasing Froude number (Figure IV.13c). Once the breaking roller formed, some air entrainment took place in the bore front and downstream the surge inducing a chaotic flow motion (Figure IV.14b). Similar flow patterns were observed in earlier studies using similar configurations with variation of the Froude number corresponding in the transition of undular bores to breaking bores (Docherty and Chanson, 2012; Khezri and Chanson, 2012a; Koch and Chanson, 2009) or for propagation of dam break waves (Hornung et al., 1995). In rivers and estuaries, undular and breaking bores are observed for similar Froude numbers than the bore studied in laboratory (Chanson, 2011a, and Table II.1).

Note that a bore shape evolved as it propagated away from the gate and with change in bed roughness. The measurements were stopped when the bore reached the upstream end of the channel.

IV.3.2 Ensemble averaged free surface properties

In some unsteady experiments performed under controlled flow conditions, such as the present positive surge study, the experiments may be repeated and the results may be ensemble-averaged to characterise the flow properties when a time average is not meaningful (Cousteix, 1989). Herein, each experiment was repeated 25 times and the free-surface characteristics of the bore were deduced from the ensemble-average using a median average (section III.3.3.2). Further details on the ensemble-average method and the synchronisation of bores are presented in Simon and Chanson (2013). The present section is focused on the unsteady free surface fluctuations around the ensemble averaged measurements at $x = 6.13$ m upstream of the tainter gate.

Figures IV.16 and IV.17 present some typical ensemble-averaged median water depth at $x =$

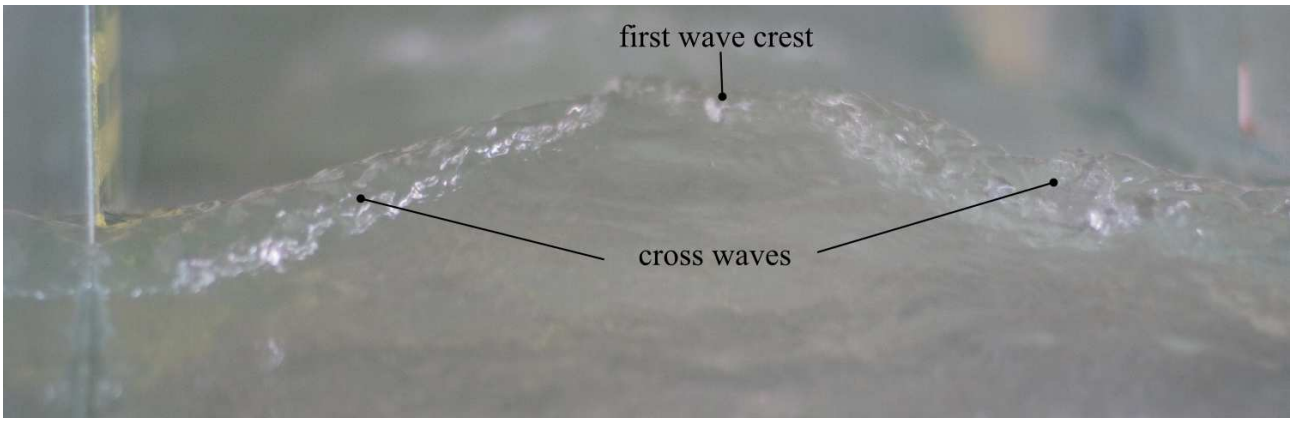

(a) Focus on an undular bore front with cross wave propagating upstream, looking downstream at $x \approx 6$ m, $Q = 0.036$ m^3.s^{-1}, $d_0 = 0.088$ m, $Fr = 1.45$ (Photo: Chanson Hubert)

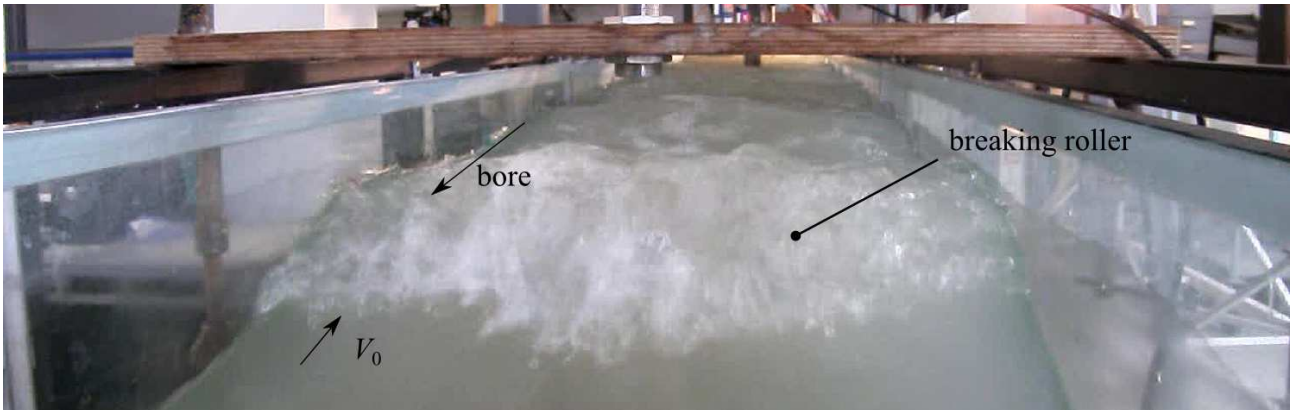

(b) Breaking bore propagating upstream with secondary undulations, looking downstream at $x \approx 6$ m, $Q = 0.055$ m^3.s^{-1}, $d_0 = 0.112$ m, $Fr = 1.55$. Note the air entrainment created by the bore roller (Photo: Bruno Simon)

Figure IV.14: Photographs of bores propagating upstream

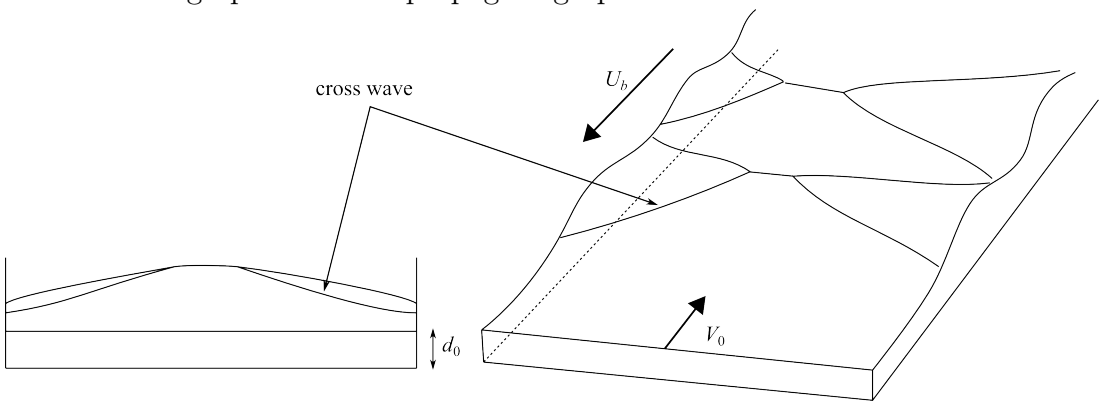

Figure IV.15: Sketch of an undular bore with cross waves. Left: front view looking downstream, right: bird's eye view looking downstream

6.13 m for 25 runs. Each graph includes the 25 runs, the median water depth, the difference between the third and first quartiles $d_{75} - d_{25}$, the difference between the 90% and 10% percentiles $d_{90} - d_{10}$, and the difference between the maximum and minimum water depths $d_{\max} - d_{\min}$. The percentile differences characterised the free-surface fluctuations around the median value.

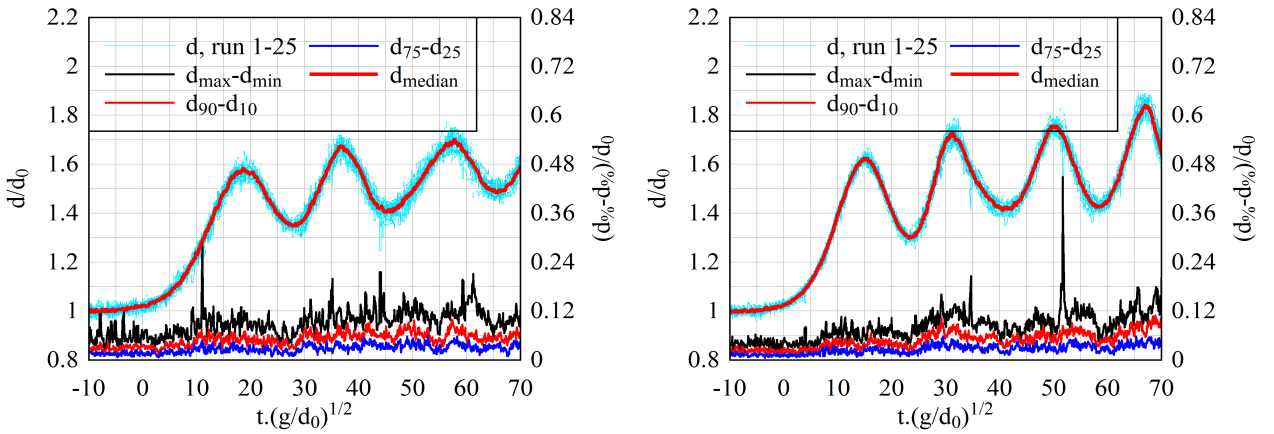

(a) $Q = 0.036$ m^3.s^{-1}, $d_0 = 0.086$ m, $Fr = 1.29$, $h_g = 43$ mm (b) $Q = 0.055$ m^3.s^{-1}, $d_0 = 0.111$ m, $Fr = 1.31$, $h_g = 62$ mm

Figure IV.16: Time variation of the water depth at $x = 6.13$ m during the upstream propagation of an undular bore ($Fr \approx 1.3$). The data include the 25 runs, the median water depth, the difference between the third and first quartiles $d_{75} - d_{25}$, the difference between the first and ninth deciles $d_{90} - d_{10}$ and the difference between maximum and minimum water depths $d_{\max} - d_{\min}$, for two discharges

Figure IV.16 presents some results for an undular bore with $Fr = 1.3$ and two discharges, $Q = 0.036$ and 0.055 m^3.s^{-1}. The data highlighted the smooth free-surface profile of the undular bore with relatively small water depth fluctuations during the passage of the bore and the secondary undulations. For the other undular bores, the range of fluctuations was similar as long as the cross-waves did not induce perturbations on the water free surface. It was observed that the cross wave effects induce slightly larger fluctuations of the free surface for $1.3 < Fr < 1.5$.

Figure IV.17 shows some data for a breaking bore with $Fr = 1.6$ and two discharges, $Q = 0.036$ and 0.055 m^3.s^{-1}. For these flow conditions, the bore had a marked roller followed by secondary undulations. The percentile differences slowly increased as the free surface rose prior the roller, then a sudden jump of fluctuations happened beneath the discontinuity of the free surface, that is the roller. The maximum free-surface fluctuations were observed during the bore roller. The fluctuations decreased in the secondary undulations but were significantly larger than for the undular bores. This is coherent with the chaotic bubbly free surface observed.

All the data showed some larger free-surface fluctuations beneath the bore and beneath the

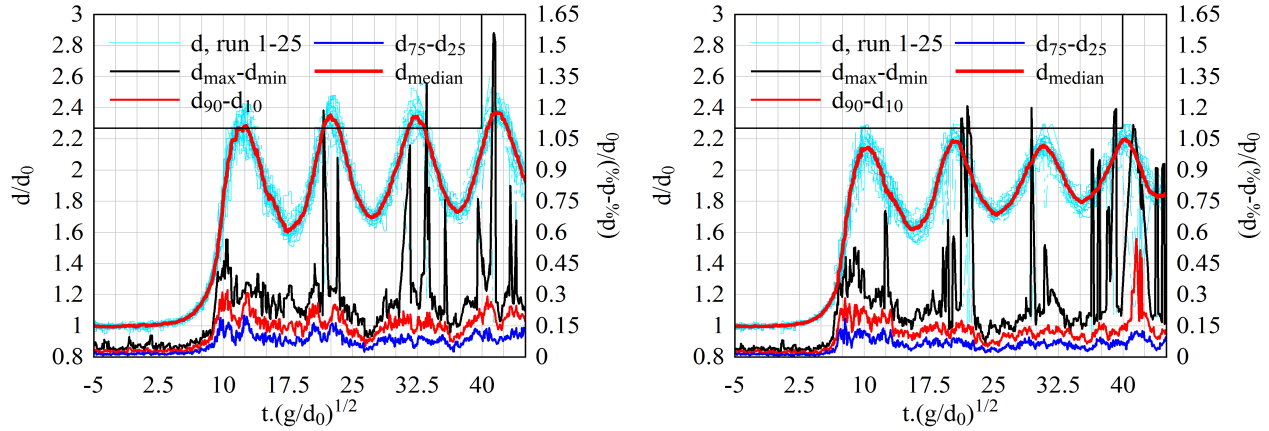

(a) $Q = 0.036$ m^3.s^{-1}, $d_0 = 0.084$ m, $Fr = 1.64$, $h_g = 0$ mm (b) $Q = 0.055$ m^3.s^{-1}, $d_0 = 0.111$ m, $Fr = 1.62$, $h_g = 9$ mm

Figure IV.17: Time variation of the water depth at $x = 6.13$ m during the upstream propagation of an undular bore ($Fr \approx 1.6$). The data include the 25 runs, the median water depth, the difference between the third and first quartiles $d_{75} - d_{25}$, the difference between the first and ninth deciles $d_{90} - d_{10}$ and the difference between maximum and minimum water depths $d_{\max} - d_{\min}$, for two discharges

undulations compared to the initial flow properties. Beneath the undulations, the free-surface fluctuations tended to be larger under the wave crests and smaller below the wave troughs (Figure IV.16 and Figure IV.17). Breaking bores induced stronger fluctuations than undular bores. It is believed to be linked with bubble entrainments and fluctuations induced by the breaking roller. The present results were similar to the findings of Docherty and Chanson (2012) on breaking bores.

IV.3.3 Longitudinal evolution of free surface properties

IV.3.3.1 Free surface properties along the channel

The visual observations showed some evolution of the bore shape and properties between its generation, immediately upstream of the gate at $x = 0$, to the upstream end of the channel. Visually, the bore formation took place at $x \approx 1$ to 1.5 m upstream the gate where strong splashing and turbulences took place, after the waters started to accumulate against the closed gate (Figure III.5). After formation, the surge accelerated briefly as it detached away from the gate and reached its final form: undular or breaking with secondary undulations. For an undular bore, the secondary undulations developed once the bore had travelled for approximately 1 to 2 m upstream the gate. For a bore with a breaking roller, the secondary undulations appeared once the bore front travelled over a longer distance, typically 1.5 to 2 m. The properties of

the undulations were characterised by the amplitude a_w of the first wave length, the first wave length L_w and its steepness a_w/L_w (Figure IV.18).
Figure IV.18 presents the dimensionless longitudinal evolution of the bore celerity, Froude number and secondary wave steepness with increasing distance from the gate, where u_c is the critical flow velocity and L is the channel length (herein $L = 12$ m). In Figure IV.18a, the ADV sampling location ($x = 6.13$ m) is shown with a thick vertical dashed line. The bore celerity data showed that the surge accelerated during the first two meters corresponding to the bore generation zone (Figure IV.18a). Afterwards, the bore propagation decelerated gradually. The longitudinal evolution of the bore Froude number is presented in Figure IV.18b. Basically, the Froude number decreased gradually as the surge propagated upstream. The wave steepness data showed some scattered data (Figure IV.18c). For breaking bores, the secondary wave steepness tended to increase with increasing distance from the gate. The trend may be linked with the gradual decrease in Froude number associated with some strengthening of the secondary waves. The Froude number decreased to reach $Fr = 1.5$ where the secondary undulations were the steeper. For undular bores, the wave steepness data tended to decrease with increasing distance of propagation. This might be linked with the Froude number decrease. It was observed that the wave steepness decreased with the Froude number getting smaller than $Fr = 1.5$.

IV.3.3.2 Free surface properties based upon Froude number comparison

In a positive surge, the flow properties upstream and downstream the bore front must satisfy the continuity and momentum principles (Chanson, 2012; Henderson, 1966; Liggett, 1994). Assuming a hydrostatic pressure distribution in the bore front, a rectangular horizontal channel and negligible friction losses, the equations of conservation of mass and momentum gives a relationship between the conjugate depth ratio and the Froude number:

$$\frac{d_b}{d_0} = \frac{1}{2}\left(\sqrt{1 + 8Fr^2} - 1\right) \tag{IV.5}$$

where d_0 and d_b are respectively the water depth immediately before and behind the bore. Equation (IV.5) is compared with present observations (Red stars symbols) as well as previous observations on smooth and rough beds in Figure IV.19. A reasonably good agreement was found between the experimental observations and theoretical equation, although the latter was developed ignoring bed friction. A similar finding was reported by Chanson (2010b), Docherty and Chanson (2012) and Khezri and Chanson (2012b).
Considering an undular bore, the undulations have a quasi-periodic shape (Chanson, 2010a). Figure IV.20 shows the dimensionless wave amplitude and wave steepness for the present data set. The data are compared to previous results, a cnoidal wave solution (Andersen, 1978) and

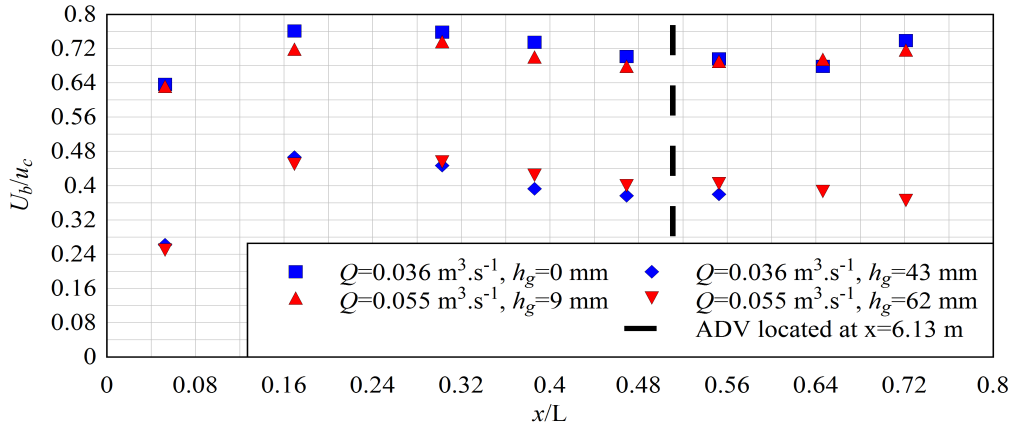

(a) Ensemble-averaged bore celerity

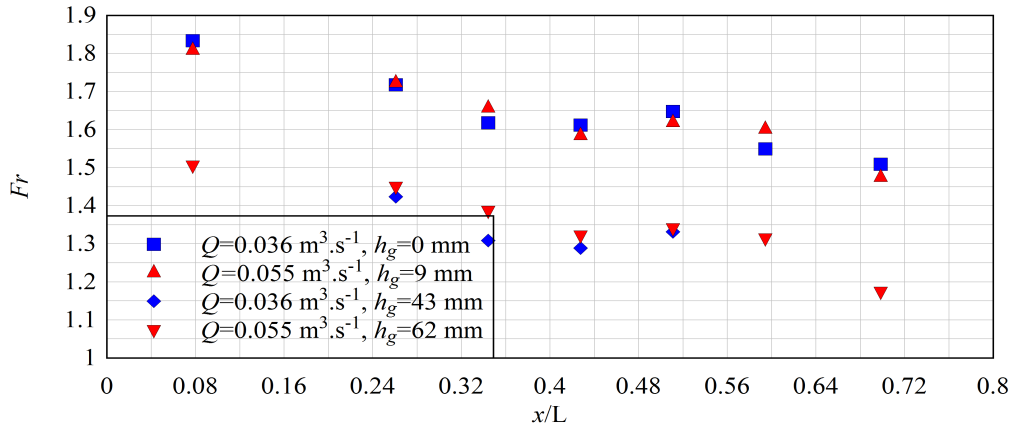

(b) Ensemble-averaged bore Froude number

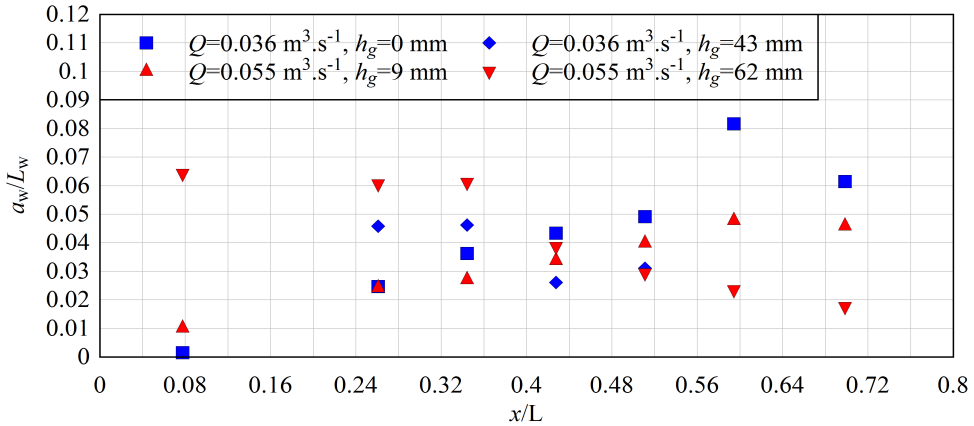

(c) Ensemble-averaged bore steepness a_w/L_w

Figure IV.18: Evolution of the bore ensemble-averaged properties with the distance from the gate

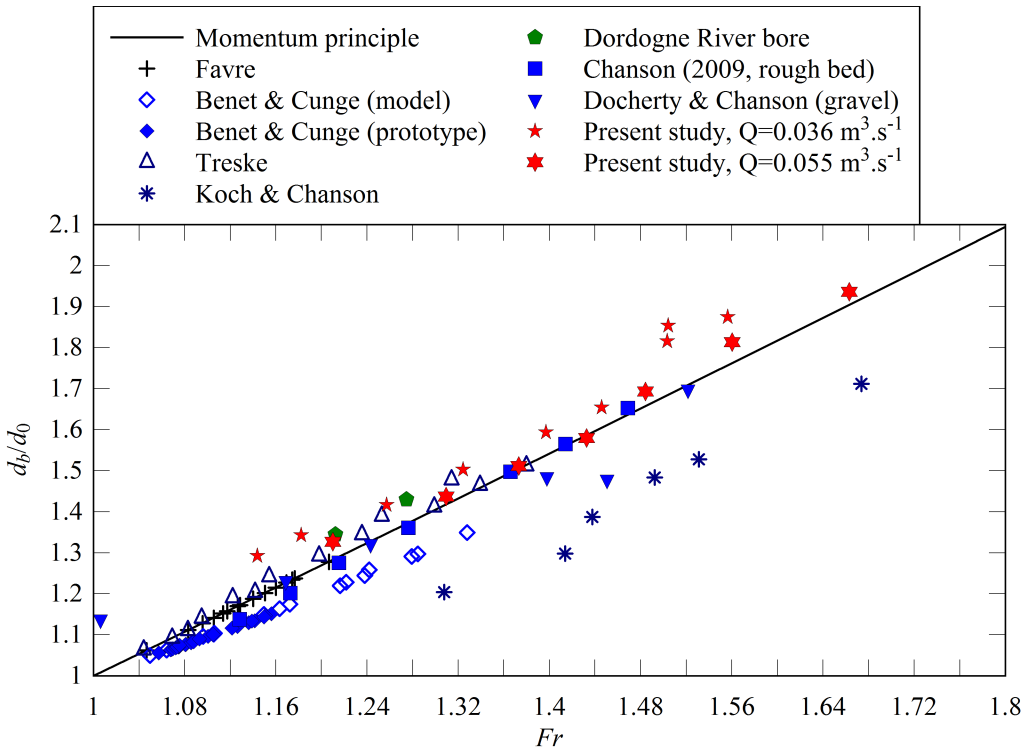

Figure IV.19: Dimensionless conjugate depth as a function of the Froude number. Comparison with the Bélanger equation (Eq. (IV.5)) and earlier experimental data on smooth bed (Benet and Cunge, 1971; Favre, 1935; Koch and Chanson, 2008; Treske, 1994), rough bed (Chanson, 2010b; Docherty and Chanson, 2012) and in the field (Benet and Cunge, 1971; Navarre, 1995). The present data are ensemble-averaged

the analytical solution of Lemoine (1948) based upon a linear wave theory approximation:

$$\frac{a_w}{d_b} \approx \frac{1}{\sqrt{3}} \left(\frac{d_b}{d_0} - 1 \right) \tag{IV.6}$$

$$\frac{L_w}{d_b} \approx 2\pi \sqrt{\frac{2}{3}} \left(\frac{d_b}{d_0} - 1 \right)^{-1/2} \tag{IV.7}$$

The characteristics of the breaking with secondary undulations bore secondary waves are also shown in Figure IV.20. The data showed the wave amplitude and steepness increased with increasing Froude number up to $Fr \approx 1.4$ to 1.5. For larger Froude numbers, the amplitude and steepness decreased with increasing Froude number. The maximum in wave amplitude and steepness was observed to appear with the onset of some light breaking at the first wave crest. Previous study reported a similar observation (Chanson, 2010b; Koch and Chanson, 2008). The overall data trend was close to previous results (Chanson, 2010b; Docherty and Chanson, 2012; Koch and Chanson, 2008). Herein, the bore shape and undulation properties were basically identical for both discharges.

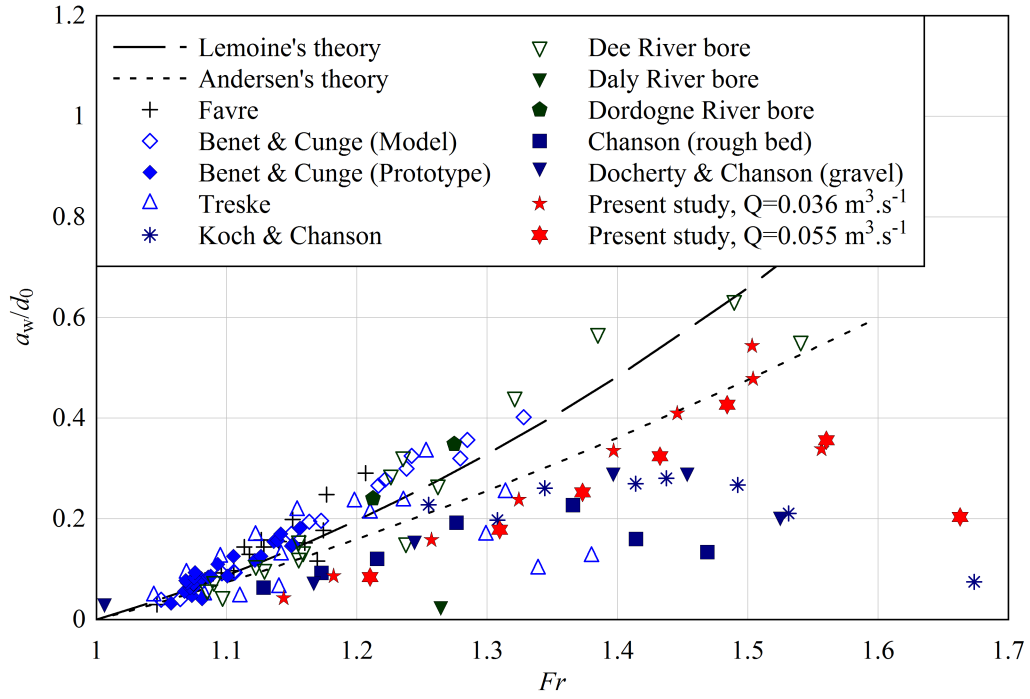

(a) Ensemble-averaged bore Froude number

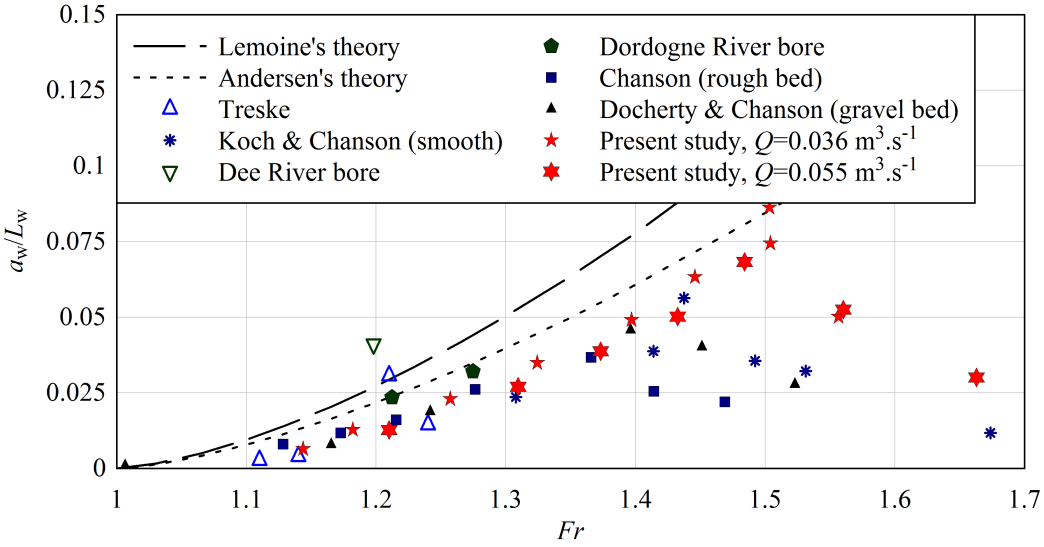

(b) Ensemble-averaged bore steepness a_w/L_w

Figure IV.20: Secondary wave amplitude and steepness as functions of the Froude number. Comparison with the linear wave theory (Lemoine, 1948), cnoidal wave theory (Andersen, 1978), laboratory data (Chanson, 2010b; Docherty and Chanson, 2012; Koch and Chanson, 2009; Treske, 1994), and prototype data (Lewis, 1972; Navarre, 1995; Wolanski et al., 2004). The present data are ensemble-averaged

A comparison between present and earlier data on smooth bed suggested that the wave amplitude and steepness were slightly smaller on rough bed for a given Froude number. The observation was supported by the data of Chanson (2010b) and Docherty and Chanson (2012) on rough beds, but not by the data set of Khezri and Chanson (2012c) also on rough bed (Figure IV.20). Note that the maximum in wave amplitude and wave steepness, corresponding to the propagation of a bore with a breaking roller, was reached for different Froude numbers depending upon the study. For example, Treske (1994) observed the propagation of a bore with a roller for Froude number superior to 1.25, whereas in some studies on dam break a bore propagated with a breaking roller for $Fr > 1.23$ (Favre, 1935; Soares Frazao and Zech, 2002). The present study the propagation of a bore with a roller for $Fr > 1.5$. The differences of Froude number for the propagation of bores with a breaking roller might be linked with differences in initial flow conditions.

Figure IV.21 shows the Ursell number U_r as function of the Froude number. The Ursell number is a dimensionless parameter used in wave mechanics to quantify the degree of nonlinearity of a wave (Holthuijsen, 2007). In classical wave study, the cnoidal wave theory is commonly used when $Ur < 10$, whereas the Stokes theory is used for $Ur > 26$. Herein the Ursell number was typically less than 10 (Figure IV.21). It increased with increasing Froude number until Fr = 1.4 to 1.5. The data did not follow Lemoine's linear wave theory. They were similar to previous results (Docherty and Chanson, 2012; Koch and Chanson, 2009).

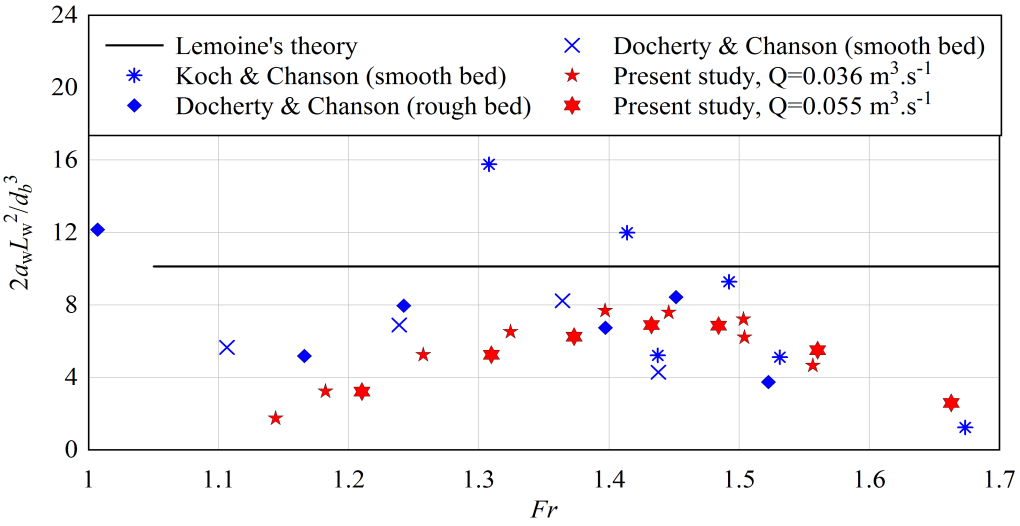

Figure IV.21: Ursell number as a function of the Froude number. Comparison between the present study (ensemble averaged), earlier laboratory studies (Docherty and Chanson, 2012; Koch and Chanson, 2009) and the linear wave theory (Lemoine, 1948)

Figure IV.22 presents the dimensionless relationship between maximum amplitude and water depth using the presentation style from Le Méhauté (1976), where T_w is the wave period. Note

that the Le Méhauté's diagram was developed originally for ocean waves (Le Méhauté, 1976), which have a different mechanisms to the tidal bore undulations. For undular bores, the present data fitted within the cnoidal theory. Chanson (2010a) argued that the linear theory gave the best fit of tidal bore undular shape, while Keulegan and Patterson (1940) showed that the undular surge data of Favre (1935) had properties close to those of cnoidal waves.

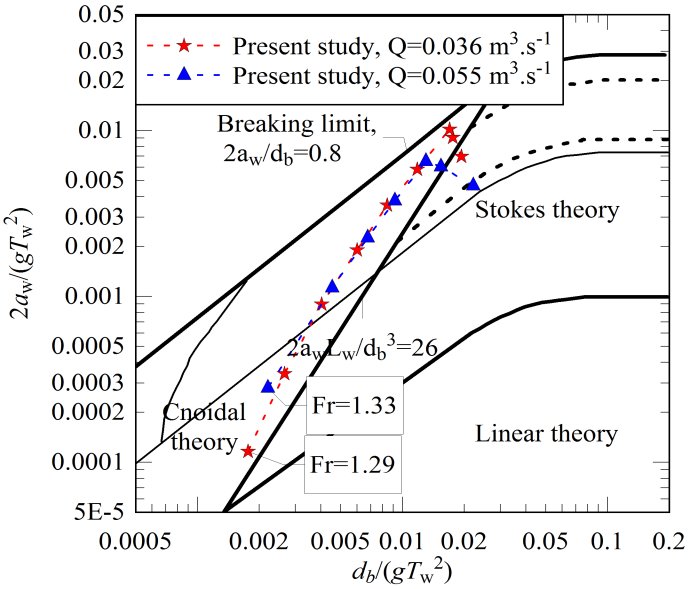

Figure IV.22: Dimensionless maximum amplitude as function of the dimensionless water depth (Present data ensemble averaged). Comparison with Le Méhauté's (1976) classification for regular waves

IV.4 Unsteady turbulent velocity characteristics

Velocity and free-surface measurements were performed simultaneously during the propagation of positive surges using one or two acoustic Doppler velocimeters (ADVs) (section III.3.3.3). The data were recorded over the gravel bed at $x = 6.13$ m with the ADV sampling volume on the channel centreline. The experiments were performed for two Froude numbers and two discharges as reported in Table IV.4. Undular bores and breaking bores with secondary undulations were generated. Note that the breaking bore with secondary undulations will be referred as breaking bore in the text for simplification.

For each set of flow condition, the experiment was repeated N times and the ensemble average median was calculated by $\mathbf{u}_{EA} = \text{median}_{i=1,...,N}(\mathbf{u}_{run\ i})$. An ensemble average technique was performed as in previous studies of positive surges (Chanson and Docherty, 2012; Reichstetter, 2011). For each experiment, the reference water depth and velocity, d_0 and V_0 respectively, were selected at $x = 6.13$ m from the gate.

Table IV.4: Summary of experimental flow conditions for unsteady velocity measurements at $x = 6.13$ m

Q $m^3.s^{-1}$	d_0 m	V_0 $m.s^{-1}$	h_g mm	Fr	U_b $m.s^{-1}$	Re_b	Bore type	Elevation of recording z/d_0
0.036	0.084	0.87	0	1.60	0.63	1.25E+5	Breaking + undulations	0.07, 0.08, 0.10, 0.15, 0.21, 0.29, 0.40, 0.53, 0.71, 0.90, 1.14
			43	1.33	0.35	1.02E+5	Undular	
0.055	0.11	0.99	9	1.58	0.70	1.85E+5	Breaking + undulations	0.05, 0.07, 0.09, 0.10, 0.15, 0.21, 0.28, 0.40, 0.53, 0.70, 0.88, 1.12
			62	1.34	0.40	1.52E+5	Undular	
0.053	0.11	0.96	0	1.59	0.69	1.80E+5	Breaking + undulations	0.11, 0.27, 0.45, 0.64
			62	1.30	0.40	1.49E+5	Undular	

IV.4.1 Velocity properties beneath bores

Both undular and breaking bores presented a number of similar unsteady flow patterns. Figures IV.23 and IV.24 present some time-variations of the ensemble averaged free-surface and velocity measurements with instantaneous velocity measurements. Figures IV.25 and IV.26 present some interpolated contour mappings of the three components of ensemble averaged velocity together with the ensemble averaged free surface elevation. In each contour, the black dotted line corresponded to the vertical elevation of the ADV sampling volume. In Figures IV.26a and IV.26b, the black broken line denotes $\bar{u}_x = 0$.

The data analysis showed that the passage of the bore was characterised by a sudden longitudinal flow deceleration associated with a rapid increase in water depth. After the passage of the bore front, the longitudinal velocity tended to oscillate in response to the free surface secondary undulations as observed by Koch and Chanson (2008). The increase in water depth yielded a slower flow motion satisfying the conservation of mass (Koch and Chanson, 2009). The longitudinal velocity deceleration was larger near the bed than in the upper part of the water column (Figures IV.23a, IV.23b, IV.24a, IV.24b, IV.25a and IV.26a). Similar deceleration magnitudes were observed by Chanson and Docherty (2012) in a breaking bore with secondary undulations over the same rough bed for $Fr = 1.5$. For example, in the present study and for both discharges, at $z/d_0 = 0.15$ for the breaking bore ($Fr = 1.6$), the longitudinal ensemble averaged velocity magnitude between the steady flow and the first crest was $(u_{x,crest} - u_{x,steady}) = -1.2V_0$ and associated to a deceleration of -0.88 $m.s^{-2}$ whereas in Chanson and Docherty (2012), for $Fr = 1.5$ at $z/d_0 = 0.135$, the longitudinal velocity magnitude beneath the first crest and the

steady flow was $(u_{x,crest} - u_{x,steady}) = -1.1V_0$ associated to a deceleration of -0.79 m.s^{-2}.
The transverse velocity $\bar{u}_y$ was subjected to marked fluctuations during and after the bore passage. Although the ensemble averaged transverse velocity was nearly zero, the instantaneous transverse velocity presented fluctuations with relatively longer periods than in steady flow (Figures IV.23c, IV.23d, IV.24c and IV.24d). These fluctuations did not appear to be linked with the period of secondary oscillations but they may reflect the advection of large scale vortical structures behind the bore (Chanson, 2011c). These macro-scale structures may have a great significance for sediment scour and transport.
Finally, the vertical velocity data $\bar{u}_z$ presented a similar oscillating pattern evolution as the free surface undulations but out of phase by about a quarter of the wave period of oscillations (Figures IV.23e, IV.23f, IV.24e, IV.24f, IV.25c and IV.26c). The observation was consistent with that of Chanson (2010a). The vertical velocity $\bar{u}_z$ was typically positive when the free surface increased and negative when the free surface decreased, following the evolution of the water depth derivative. At the free surface and a given position (x, y), the vertical velocity component is the derivative of the water depth with respect of time:

$$u_z\,(z = d) = \frac{\partial d}{\partial t} \tag{IV.8}$$

Figure IV.27 presents a comparison between the ensemble-averaged vertical velocity component $\bar{u}_z$ and the time derivative of ensemble averaged water depth $\partial\bar{d}/\partial t$ at two vertical elevations. The data showed that the largest amplitude of vertical velocity oscillations was reached on the upper water column. The smallest amplitude of vertical velocity oscillations was seen next to the bed as predicted by the ideal flow theory. Note that the bed is a streamline (Liggett, 1994) and the data should tend to $\bar{u}_z(z = 0) = 0$ for a flat smooth bed.
Some typical instantaneous velocities measurement in a breaking and an undular bore are presented in Figure IV.23 and Figure IV.24 respectively, and the data are compared with the ensemble averaged velocity results. The instantaneous transverse velocity presented longer period fluctuations in the unsteady flow than in the steady flow. These low frequency fluctuations took place around an averaged transverse velocity of zero and they were the larger during the breaking bore than during the undular bore. The instantaneous vertical velocity showed high frequency fluctuations with large magnitude beneath the bore.
The undular and breaking bore data presented however some marked differences. The flow deceleration was stronger in the breaking bore than in the undular bore for identical initial flow conditions. In breaking bores, the flow reversal was clearly observed in terms of the ensemble averaged longitudinal velocity component for $z/d_0 < 0.4$ beneath the bore front and the secondary undulations (Figure IV.26a). Some positive longitudinal velocity samples were observed at higher depths in terms of the instantaneous velocity data. On the other

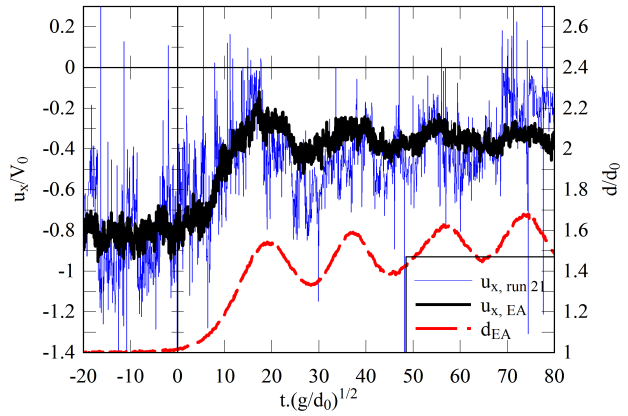

(a) Longitudinal velocity at $z/d_0 = 0.15$

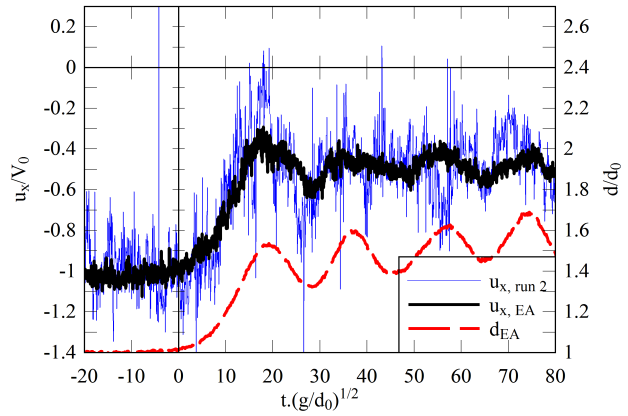

(b) Longitudinal velocity at $z/d_0 = 0.29$

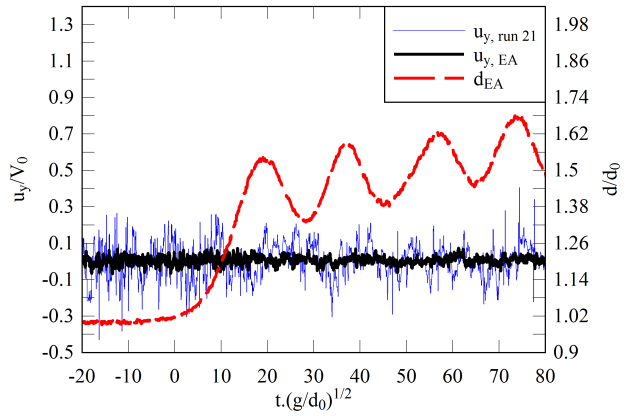

(c) Transversal velocity at $z/d_0 = 0.15$

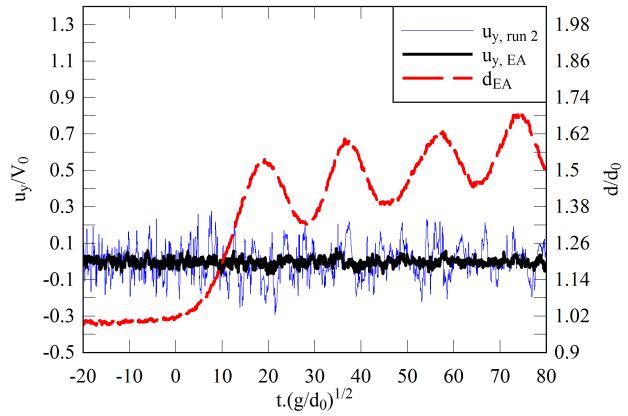

(d) Transversal velocity at $z/d_0 = 0.29$

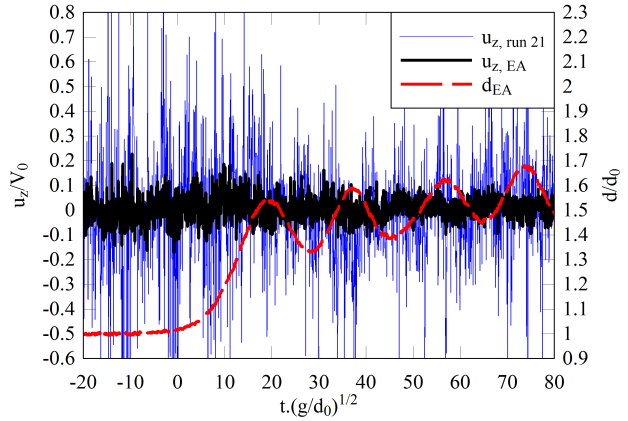

(e) Vertical velocity at $z/d_0 = 0.15$

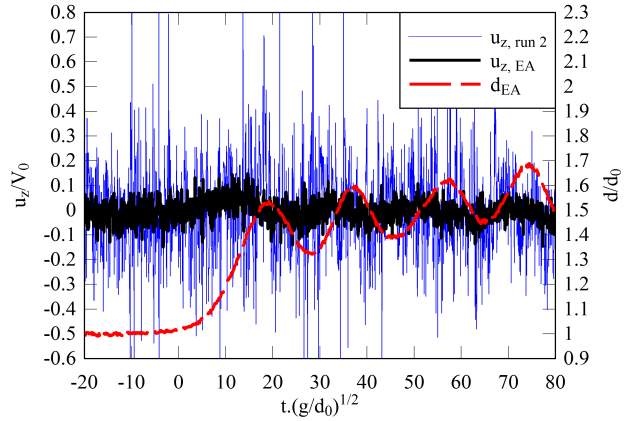

(f) Vertical velocity at $z/d_0 = 0.29$

Figure IV.23: Time-variations of instantaneous velocity components, ensemble averaged velocity component and water depth in an undular bore. Flow conditions: $Q = 0.036$ m^{3}s^{-1}, $d_0 = 0.084$ m, $V_0 = 0.87$ m.s^{-1}, $Fr = 1.33$, $x = 6.13$ m

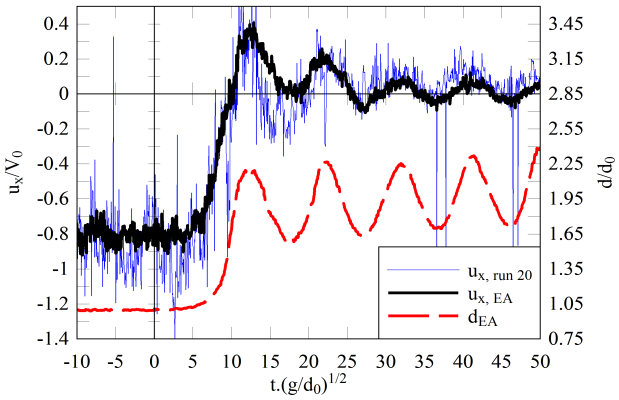

(a) Longitudinal velocity at $z/d_0 = 0.15$

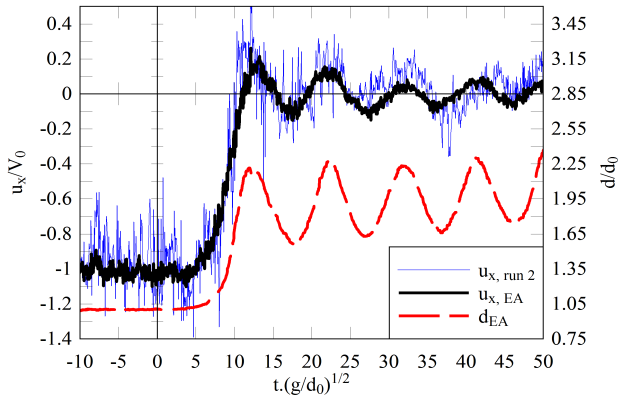

(b) Longitudinal velocity at $z/d_0 = 0.24$

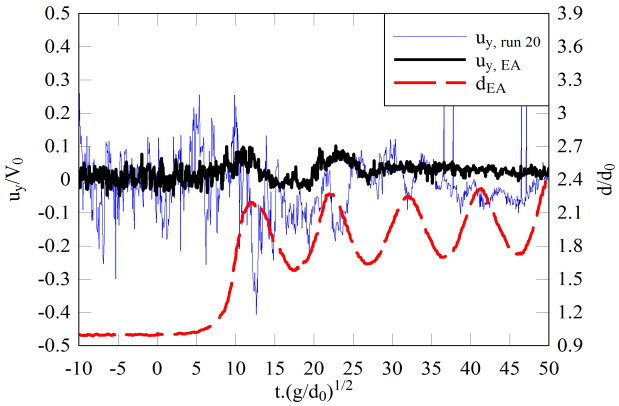

(c) Transversal velocity at $z/d_0 = 0.15$

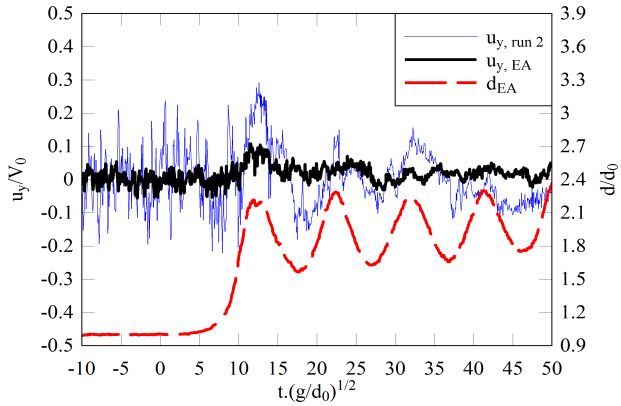

(d) Transversal velocity at $z/d_0 = 0.24$

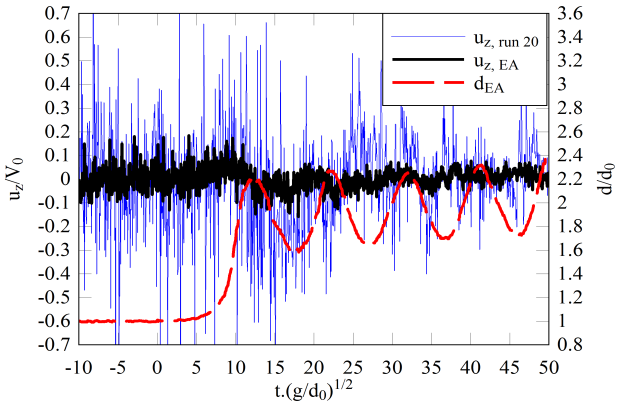

(e) Vertical velocity at $z/d_0 = 0.15$

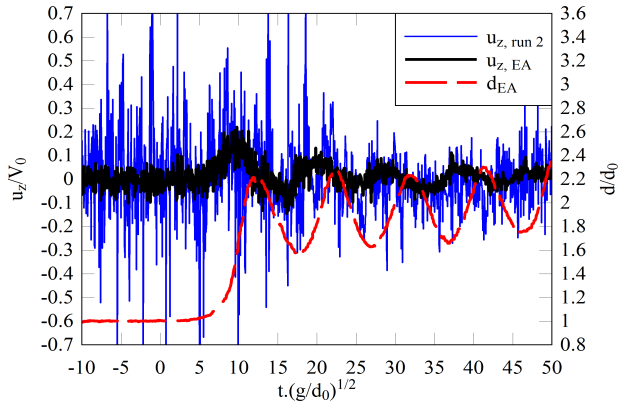

(f) Vertical velocity at $z/d_0 = 0.24$

Figure IV.24: Time-variations of instantaneous velocity components, ensemble averaged velocity component and water depth in a breaking bore. Flow conditions: $Q = 0.036$ m^3.s^{-1}, $d_0 = 0.084$ m, $V_0 = 0.87$ m.s^{-1}, $Fr = 1.60$, $x = 6.13$ m

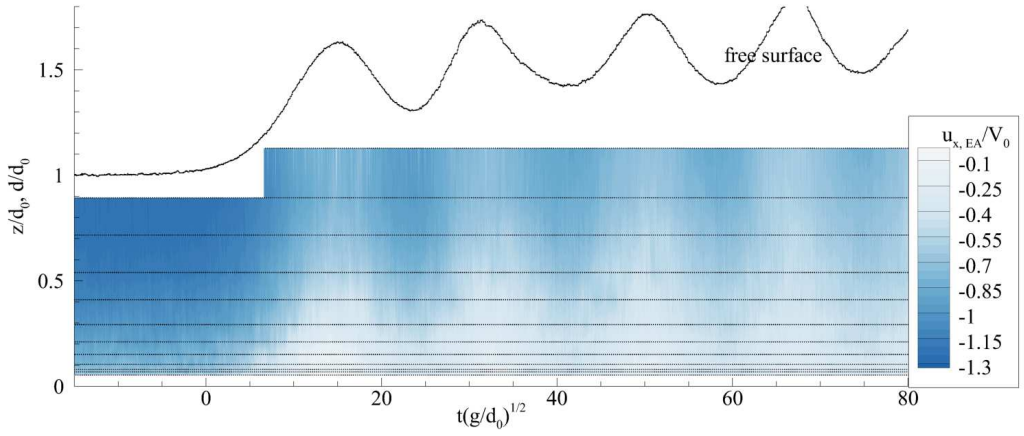

(a) Longitudinal velocity

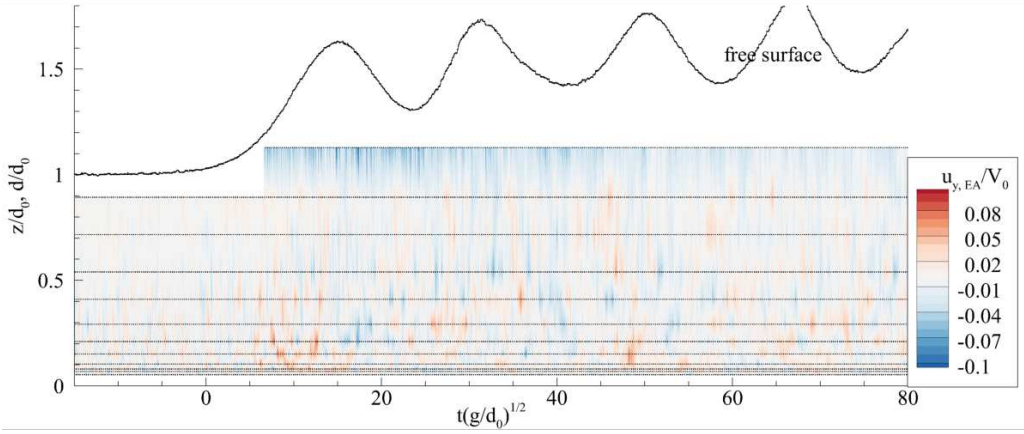

(b) Transversal velocity

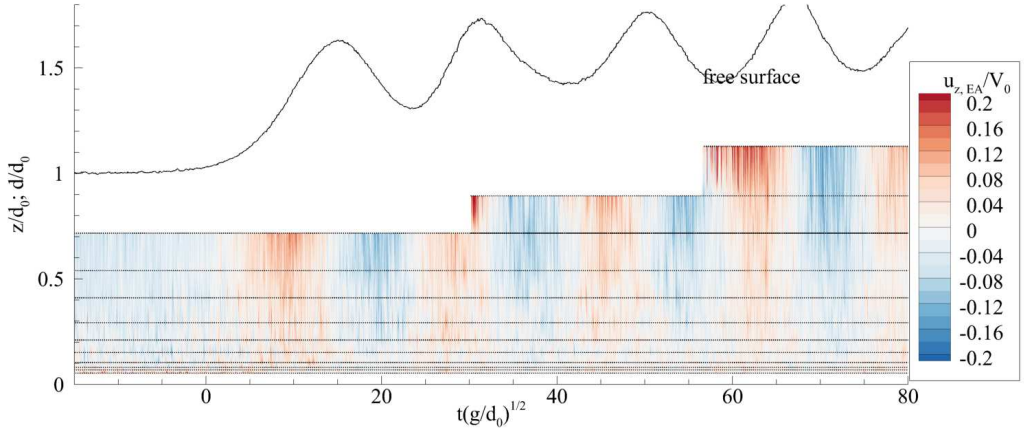

(c) Vertical velocity

Figure IV.25: Dimensionless ensemble averaged velocity contour and ensemble averaged water depth in undular bores. Flow conditions: $Q = 0.055$ m^3.s^{-1}, $Fr = 1.34$, $x = 6.13$ m, $h_g = 62$ mm

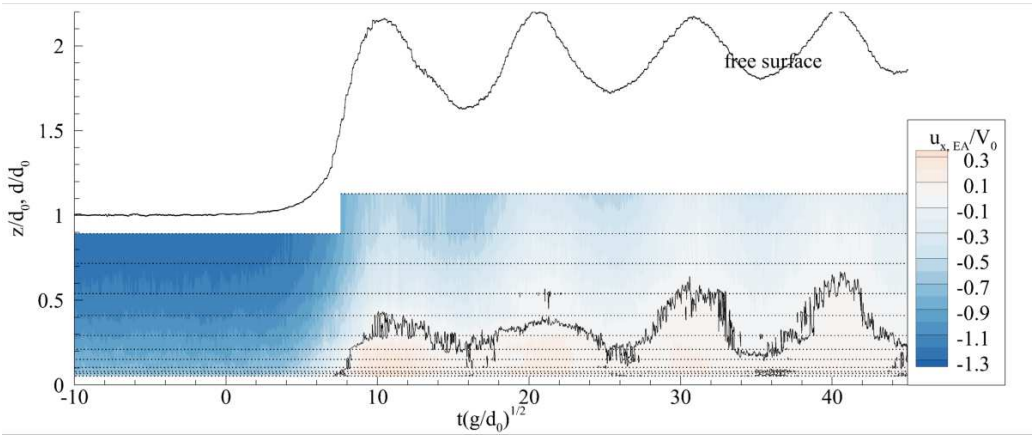

(a) Longitudinal velocity

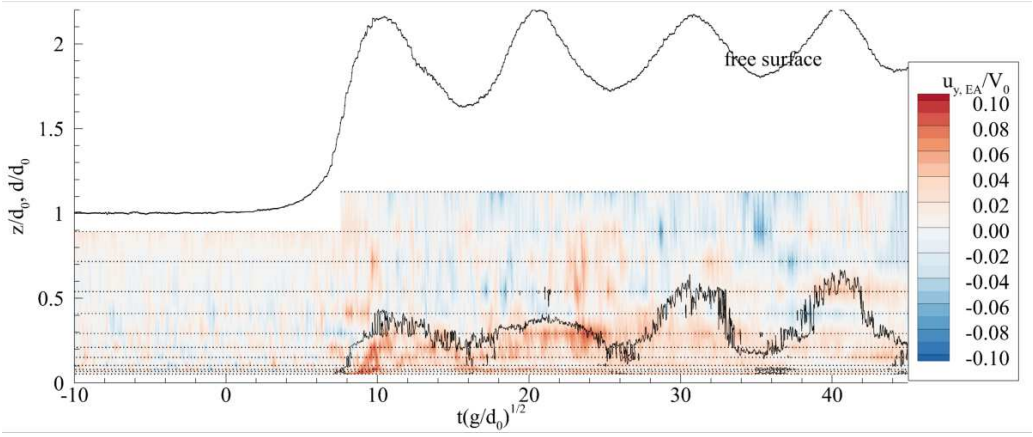

(b) Transversal velocity

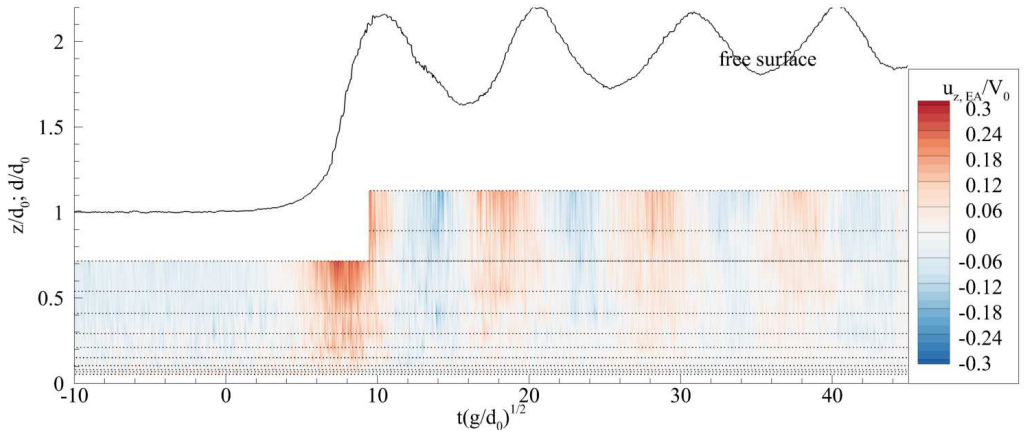

(c) Vertical velocity

Figure IV.26: Dimensionless ensemble averaged velocity contour, ensemble averaged water depth and isoline $u_x = 0$ in breaking bores. Flow conditions: $Q = 0.055$ m^3.s^{-1}, $Fr = 1.58$, $x = 6.13$ m, $h_g = 9$ mm

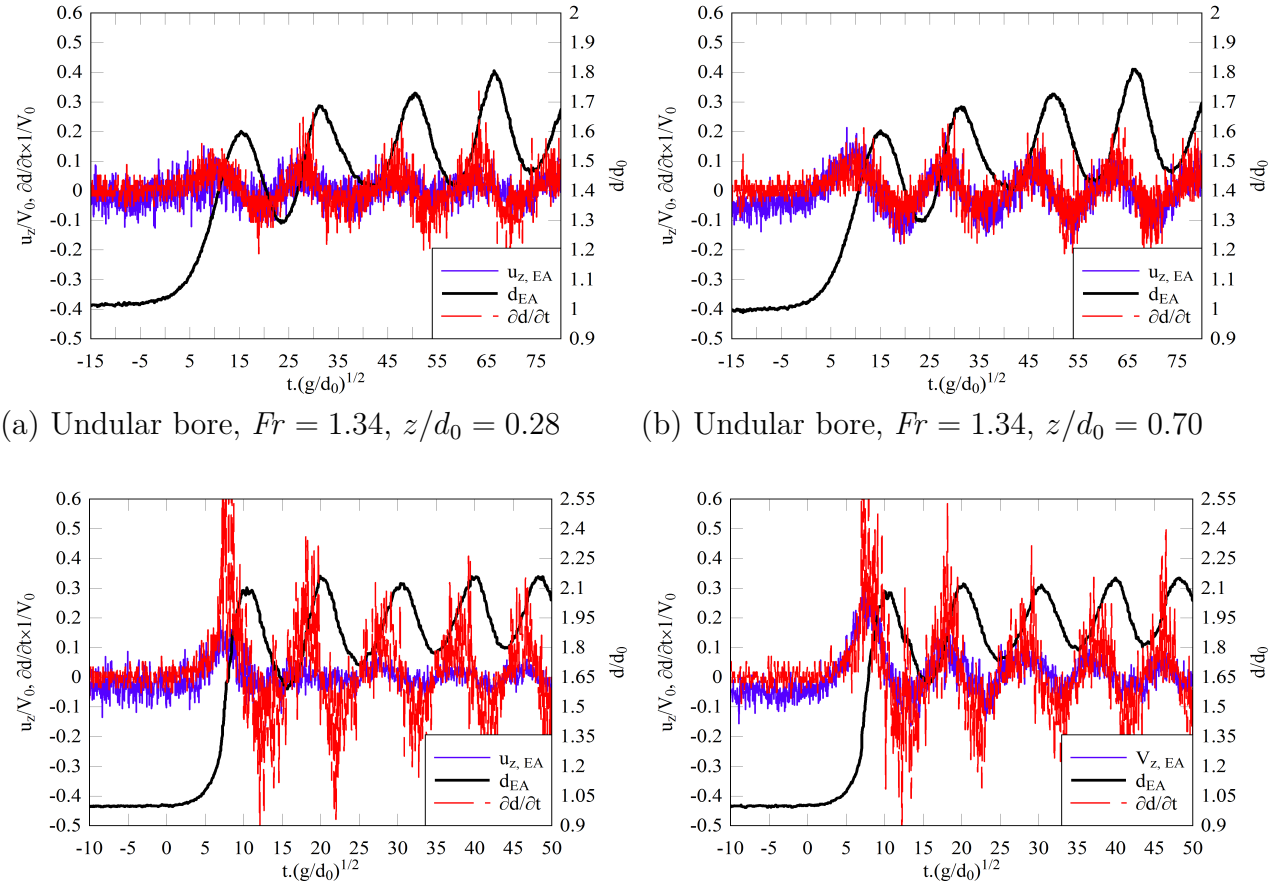

(a) Undular bore, $Fr = 1.34$, $z/d_0 = 0.28$

(b) Undular bore, $Fr = 1.34$, $z/d_0 = 0.70$

(c) Breaking bore, $Fr = 1.58$, $z/d_0 = 0.28$

(d) Breaking bore, $Fr = 1.58$, $z/d_0 = 0.70$

Figure IV.27: Comparison between the ensemble averaged vertical velocity data and the derivative of the ensemble averaged water depth $\partial d/\partial t$. Flow conditions: $Q = 0.055$ m^3.s^{-1}, $x = 6.13$ m, $d_0 = 0.11$ m, $V_0 = 0.99$ m.s^{-1}. Top: undular bore, bottom: breaking bore

hand, no ensemble-averaged transient recirculation was observed beneath the undular bore, although some instantaneous positive longitudinal velocity components were recorded under the crest of the bore front next to the bed (Figure IV.23a). Note that longitudinal velocity reversals in undular bores were observed for numerical simulations (section VI) and mentioned in experimental study (Ryabenko, 1998). In breaking bores, some transient velocity reversals were also observed close to the gate, for example at $x = 0.93$ m (Figure IV.28). Figure IV.28 present ensemble averaged longitudinal velocity data with the water depth close to the gate for undular and breaking bores. Previous experimental studies on smooth and rough beds showed the presence of transient velocity recirculation beneath the front of breaking bores (Chanson, 2010a; Chanson and Docherty, 2012; Khezri and Chanson, 2012c; Koch and Chanson, 2009). This was also reported in numerical studies (Furuyama and Chanson, 2010; Lubin et al., 2010a). It is proposed that the transient flow recirculation developed beneath the bore front close to the

gate and was advected upstream with the bore has observed in numerical simulations (Lubin et al., 2010a) and section VI.

For the transverse velocity component $\bar{u}_y$, some large deviations from zero were observed next to the bed beneath the breaking bore front: for example, in Figures IV.24c and IV.24d. It is unclear whether this pattern is typical of the breaking bore or the result of intrusive wake effects induced by the ADV head. In the undular bore, such large fluctuations in transverse velocity were not observed. This might indicate an effect of the ADV unit on the flow during the transient velocity reversal process.

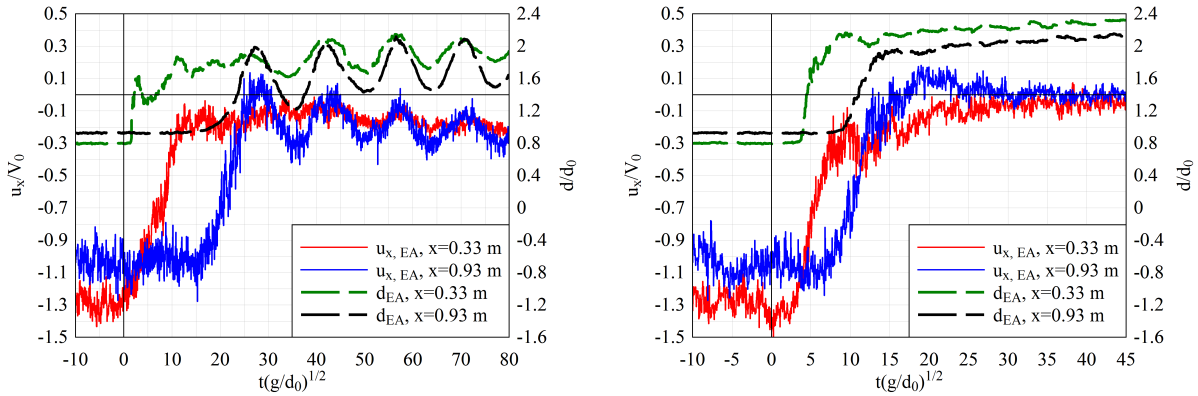

(a) Undular bore, $Fr = 1.30$, at $z = 63$ mm and $h_g = 0.62$ mm

(b) Breaking bore, $Fr = 1.59$ at $z = 63$ mm and $h_g = 0$

Figure IV.28: Time-variations of ensemble averaged longitudinal velocity and water depth close to the gate after generation of bores. Flow conditions: $Q = 0.053$ m^3.s^{-1}, $d_0 = 0.11$ m, $V_0 = 0.96$ m.s^{-1}

Concerning the vertical velocity component, the data showed larger oscillations in the breaking bore than in the undular bore. This was likely linked with the steeper free-surface slope during the bore front and following secondary oscillations behind the breaking bore.

For a similar Froude number, the time-variations of all velocity components were similar for both discharges, suggesting no particular scale effect in terms of the velocity field within the investigated flow conditions (Table IV.4). Overall, the detailed velocity measurements yielded findings which were similar to a number of earlier observations (Docherty and Chanson, 2012; Khezri and Chanson, 2012c; Koch and Chanson, 2009).

IV.4.2 Ensemble averaged velocity fluctuations

An ensemble median was systematically calculated with all 25 runs synchronised on the passage of the bore. For all velocity components, the differences between first and third quartiles ($\mathbf{u}_{75} - \mathbf{u}_{25}$), 90% and 10% percentiles ($\mathbf{u}_{90} - \mathbf{u}_{10}$), and maximum and minimum values ($\mathbf{u}_{max} - \mathbf{u}_{min}$)

were calculated providing information on the turbulent velocity fluctuations. Some typical results are shown in Figures IV.29, IV.30 and IV.31. Figure IV.29 present some typical velocity percentile differences in a undular and breaking bore at $x = 6.13$ m and $z/d_0 = 0.40$. Contour mappings of first and third quartile difference are presented in Figures IV.30 and IV.31 for a undular and breaking bore respectively.

The data showed that the passage of the bore was always associated with large velocity fluctuations. The experimental results showed that the largest velocity fluctuations were observed beneath the bore front for $4 < t\sqrt{g/d_0} < 12$ in the breaking bore and $2 < t\sqrt{g/d_0} < 20$ for the undular bore, with $t = 0$ at the leading edge of the bore. For all velocity components, the velocity fluctuations were large next to the bed. During the bore passage, the largest velocity fluctuations were found first very close to the bed. With increasing time, the location of maximum velocity fluctuations tended to shift upwards towards the mid-water column (Figures IV.30 and IV.31). For example, for $Fr = 1.6$ and $Q = 0.055$ m^3.s^{-1}, the maximum longitudinal velocity fluctuation $(u_{x,75} - u_{x,25})$ was seen at about $z/d_0 = 0.1$ for $t\sqrt{g/d_0} = 6$, and at $z/d_0 = 0.53$ for $t\sqrt{g/d_0} = 11$. The largest velocity fluctuations occurred at about the same time as the largest free surface fluctuations (section IV.3.2).

For the longitudinal velocity component, the data showed the largest fluctuations beneath the bore during the rapid flow deceleration. The transverse and vertical velocity fluctuation data showed the largest magnitudes during the bore passage. The level of fluctuations decreased slightly with increasing time after the bore passage, the largest values being typically seen in the mid-water column.

The breaking bore flow exhibited larger fluctuations than the undular bore flow. The maximum fluctuations in longitudinal velocity beneath the breaking bore were about 20% larger than those in the undular bore. The transverse and vertical velocity fluctuations in the breaking bore were respectively about 40% and 30% larger than those in the undular bore.

Altogether the results were observed for both discharges. Little difference was seen between the two series of experiments suggesting no scale effects within the range of experimental flow conditions (Table IV.4). The present observations on ensemble-averaged velocity fluctuations were similar to that of Chanson and Docherty (2012), with the same intensities of velocity fluctuations in an experiment with similar Froude number ($Fr = 1.49$) on the same gravel bed.

IV.4.3 Turbulent stress beneath bores

The Reynolds stress tensor is a transport effect resulting from turbulent motion induced by velocity fluctuations with its subsequent increase of momentum exchange and mixing (Piquet, 1999). This turbulent transport is a property of the turbulent flow. In a turbulent flow, the instantaneous velocity is typically the sum of an average velocity plus a fluctuating component:

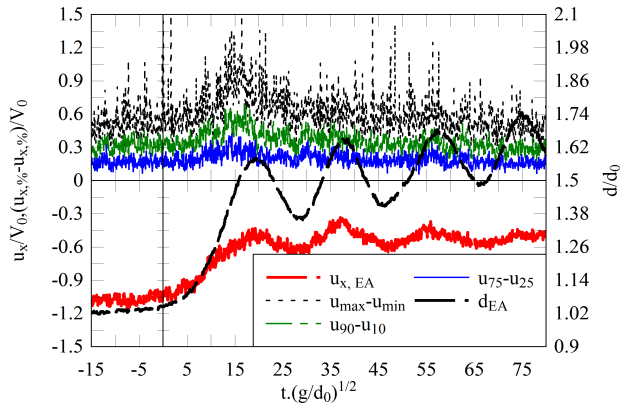

(a) Undular bore, longitudinal component

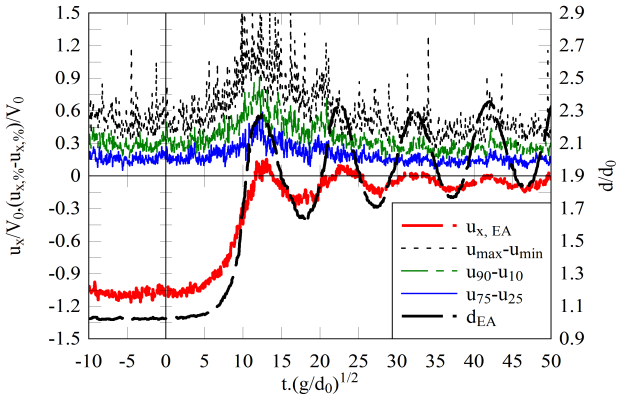

(b) Breaking bore, longitudinal component

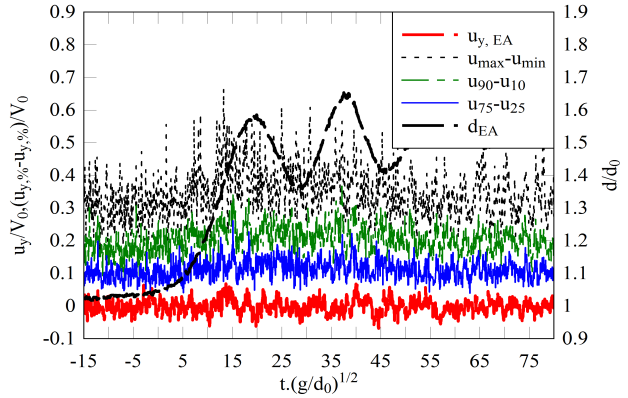

(c) Undular bore, transversal component

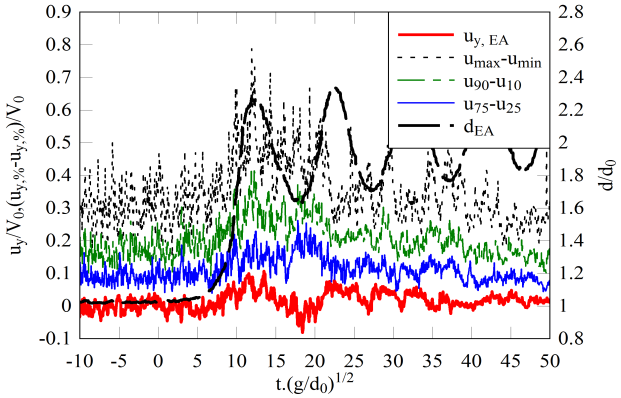

(d) Breaking bore, transversal component

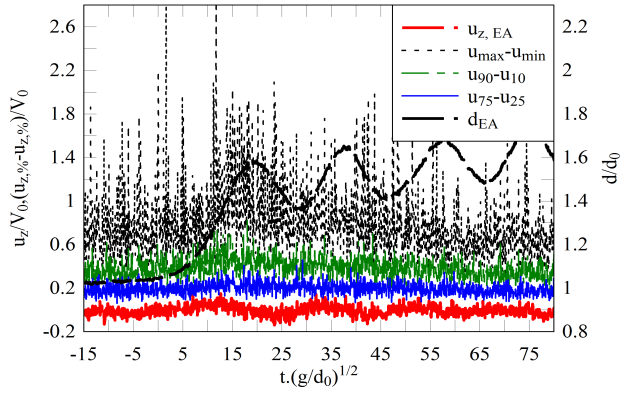

(e) Undular bore, vertical component

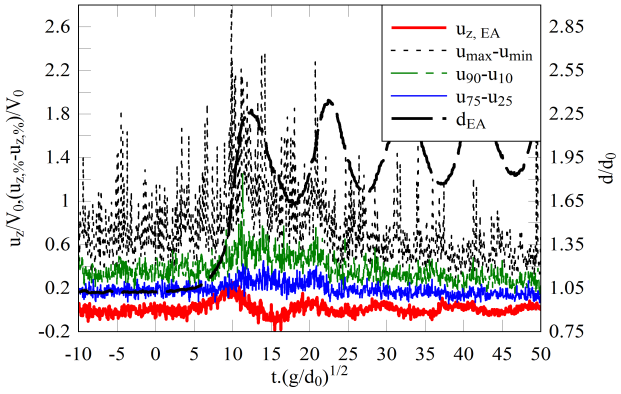

(f) Breaking bore, vertical component

Figure IV.29: Ensemble-average water depth, median velocity data and velocity fluctuations in undular ($Fr = 1.33$) and breaking bore ($Fr = 1.60$): differences between first and third quartiles ($u_{i,75} - u_{i,25}$), first and ninth deciles ($u_{i,90} - u_{i,10}$), and maximum and minimum values ($u_{i,max} - u_{i,min}$). Flow conditions: $Q = 0.036$ m^3.s^{-1}, $x = 6.13$ m, $d_0 = 0.084$ m, $z/d_0 = 0.40$ m

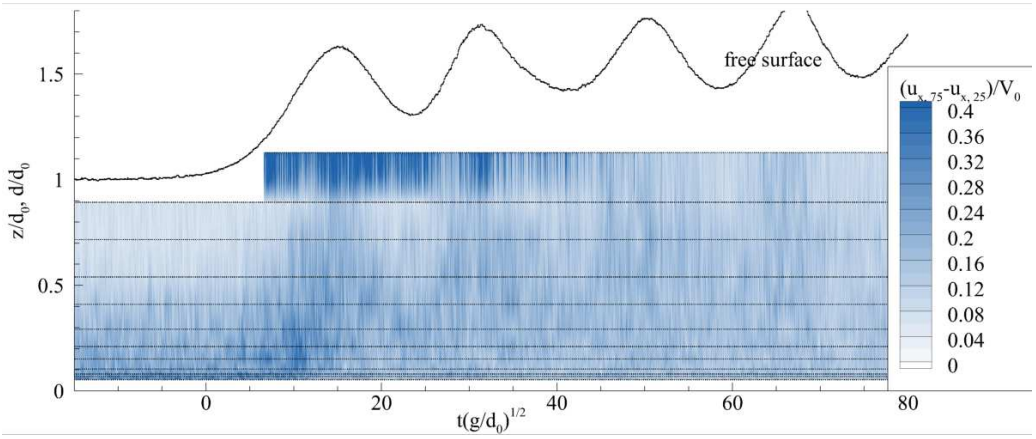

(a) Longitudinal velocity

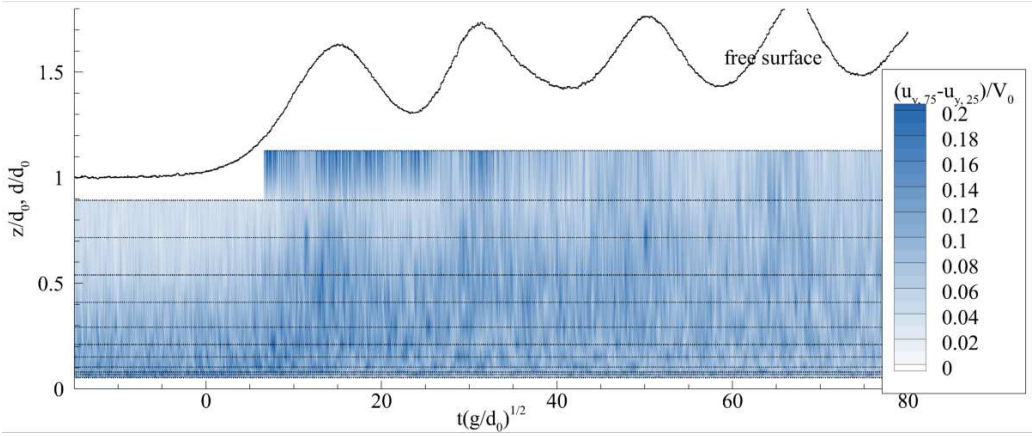

(b) Transversal velocity

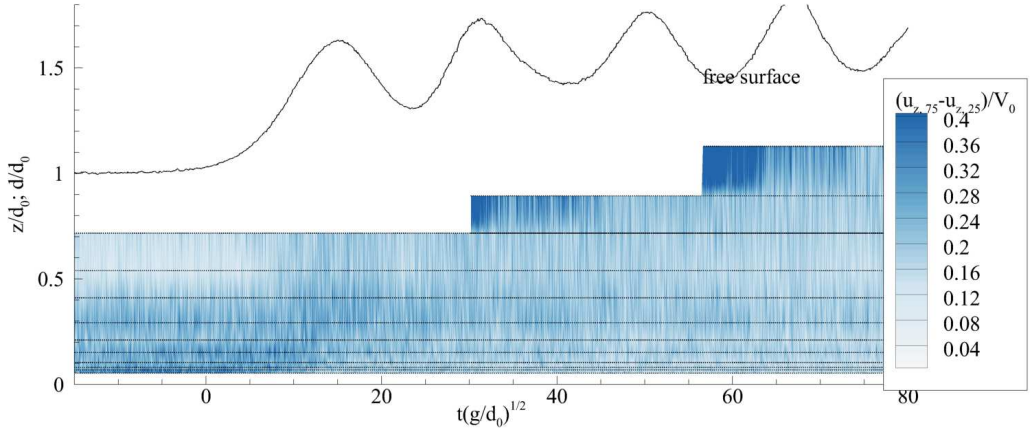

(c) Vertical velocity

Figure IV.30: Dimensionless difference between the first and third quartiles ($u_{i,75} - u_{i,25}$) and ensemble averaged water depth in undular bores. Flow conditions: $Q = 0.055$ m^3.s^{-1}, $x = 6.13$ m, $d_0 = 0.11$ m, $Fr = 1.34$

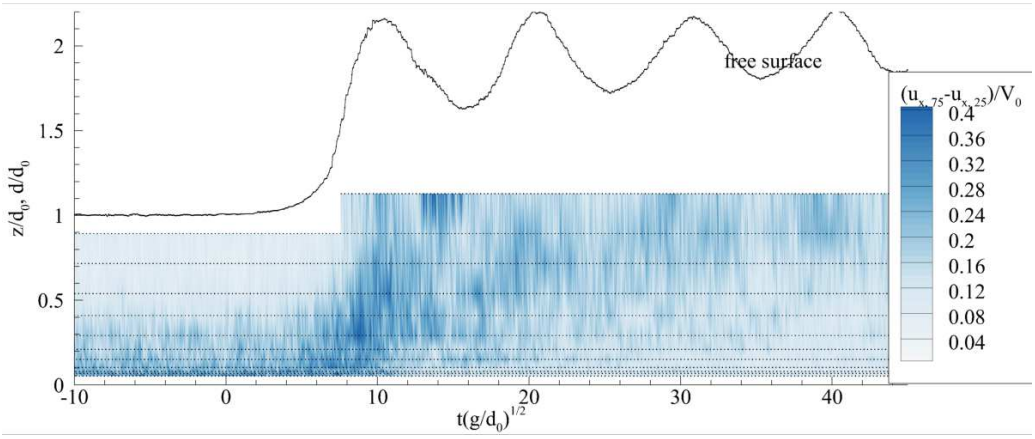

(a) Longitudinal velocity

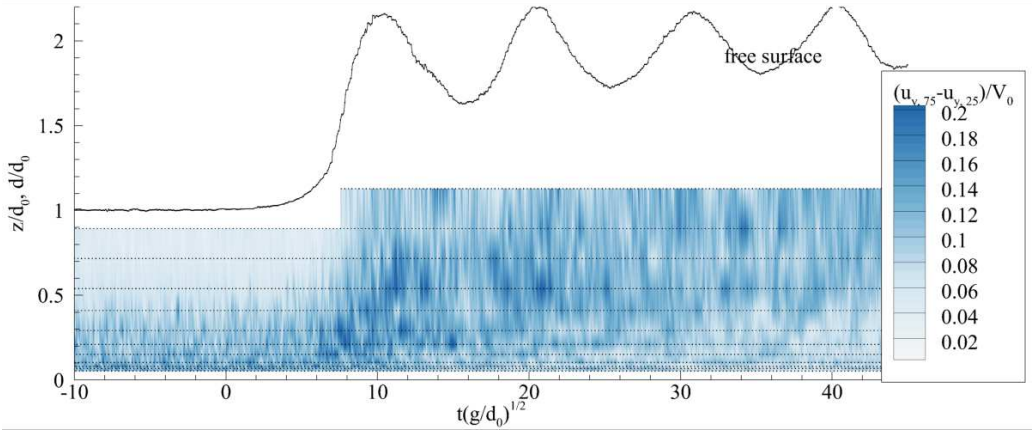

(b) Transversal velocity

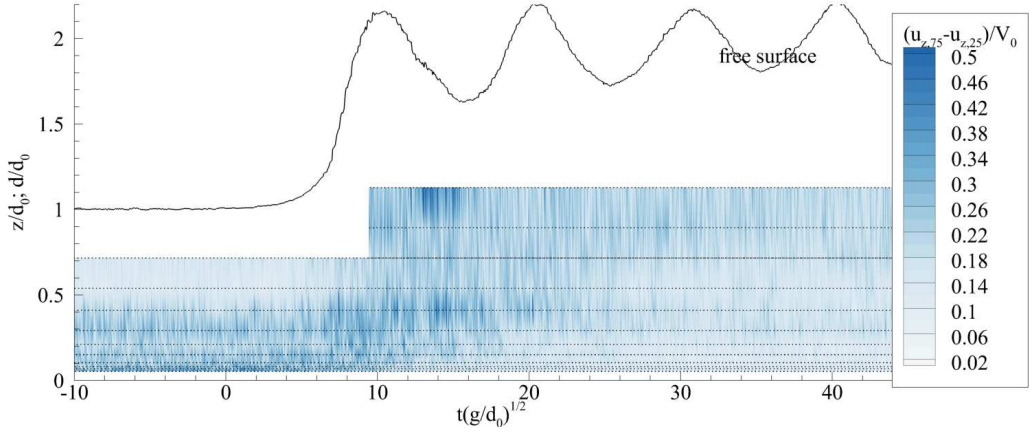

(c) Vertical velocity

Figure IV.31: Dimensionless difference between the first and third quartiles ($u_{i,75} - u_{i,25}$) and ensemble averaged water depth in breaking bores. Flow conditions: $Q = 0.055$ m^3.s^{-1}, $x = 6.13$ m, $d_0 = 0.11$ m, $Fr = 1.58$

$\mathbf{u} = \bar{\mathbf{u}} + \mathbf{u}'$. In a steady flow, the average is the time average. In an unsteady flow with distinct large terms and short term fluctuation frequencies, the averaged velocity may be calculated as a low-pass filtered component, or a variable-interval time average (VITA) (Chanson and Docherty, 2012; Koch and Chanson, 2009; Piquet, 1999). For laboratory experiments under controlled flow conditions like herein, the experiments are repeated several times and the average is the ensemble average (Bradshaw, 1971; Chanson and Docherty, 2012). In the present study, each experiment was repeated 25 times to perform an ensemble average median of the velocity components and to calculate the fluctuation of a run $\mathbf{u}'_k = \mathbf{u}_k - \bar{\mathbf{u}}_{EA}$. The averaged turbulent stress tensor components were calculated as: $\rho\overline{(u'_i u'_j)}_{EA} = \rho\langle u_i u_j \rangle$.

The turbulent stress tensor includes the normal and tangential stresses tensor, although there is no fundamental difference between the two types of Reynolds stress component (Bradshaw, 1971).

Figures IV.32, IV.33 and IV.34 illustrate some typical Reynolds stress data. Figure IV.32 presents dimensionless ensemble median turbulent stresses at $z/d_0 = 0.40$, while Figures IV.33 and IV.34 show some contour maps of the dimensionless normal stresses in undular and breaking bores.

The results showed a number of typical features in positive surges. For both discharges and both undular and breaking bores, the turbulent normal and tangential stresses were larger beneath the bore front than in the steady flow: that is, in terms of both the amplitude of and fluctuations in shear stresses. The largest values of turbulent stress were found close to the bed during the bore front passage. With increasing time, large shear stresses were observed in the mid-water column. Generally, the shear stresses throughout the water column were larger behind the bore than in the initially-steady flow. The turbulent stress levels seemed to be linked with the rapid flow deceleration and the oscillations of the free surface. Large values were observed during the bore passage and flow deceleration, as well as beneath the wave crests, particularly for the longitudinal and transverse normal stresses.

Compared to the undular bore, the breaking bore showed larger longitudinal and vertical normal stresses. On the other hand, the large turbulent stresses lasted longer at all measured depths in the undular bore than in the breaking bore as observed by Koch and Chanson (2008). These results were consistent with the velocity fluctuation data (section IV.4.2), as well as with previous studies (Chanson, 2010a; Chanson and Docherty, 2012; Khezri and Chanson, 2012c; Koch and Chanson, 2009). The data showed that, beneath the bore front, the turbulent stresses had larger values close to the bed. During and after the passage of the bore front, the largest normal stresses were observed at an elevation which increased with increasing time. In previous studies (Chanson, 2010a; Koch and Chanson, 2009), it was proposed that the large values of turbulent stressed observed in a breaking bore for $z/d_0 > 0.5$ were caused by the

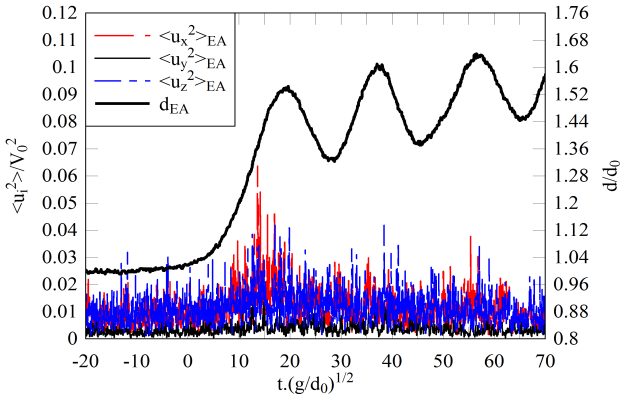

(a) Undular bore, normal stresses, $Fr = 1.34$

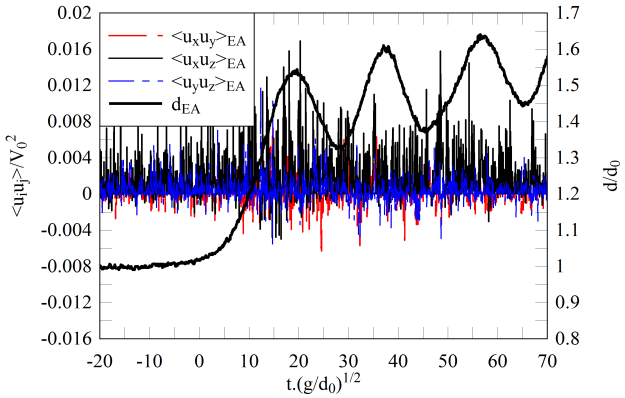

(b) Undular bore, tangential stresses, $Fr = 1.34$

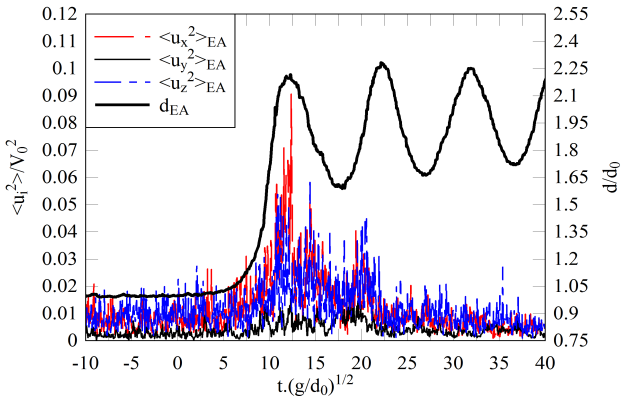

(c) Breaking bore, normal stresses, $Fr = 1.60$

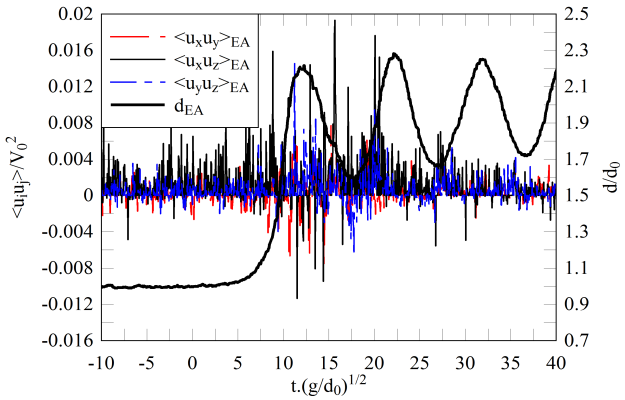

(d) Breaking bore, tangential stresses, $Fr = 1.60$

Figure IV.32: Dimensionless ensemble-averaged turbulent Reynolds stresses beneath bores at $z/d_0 = 0.40$ and ensemble averaged water depth. Flow conditions: $Q = 0.036$ m^3.s^{-1}, $x = 6.13$ m, $d_0 = 0.085$ m

turbulent mixing layer developing in the roller. In this study, the turbulent stress distribution patterns did not differ close to the initial free surface between undular and breaking bores, and no effect of a turbulent mixing layer could be inferred. Note that the ADV did not give reliable measurements when its beams were above the steady flow water depth ($z/d_0 > 1$) and the ADV metrology did not allow some detailed, accurate measurements of the turbulent flow field in the bore roller for the ADV located above the initial water level.

The present observations might be difficult to compare with field data since, after the passage of a tidal bore, a strong flow reversal was generally observed during and after the passage of the bore followed by a fast-flowing flood flow (Chanson et al., 2011; Kjerfve and Ferreira, 1993; Mouazé et al., 2010; Reungoat et al., 2012; Simpson et al., 2004). However, both field data and the present laboratory findings demonstrated large fluctuations and amplitude of the turbulent stress tensor components beneath the bore front.

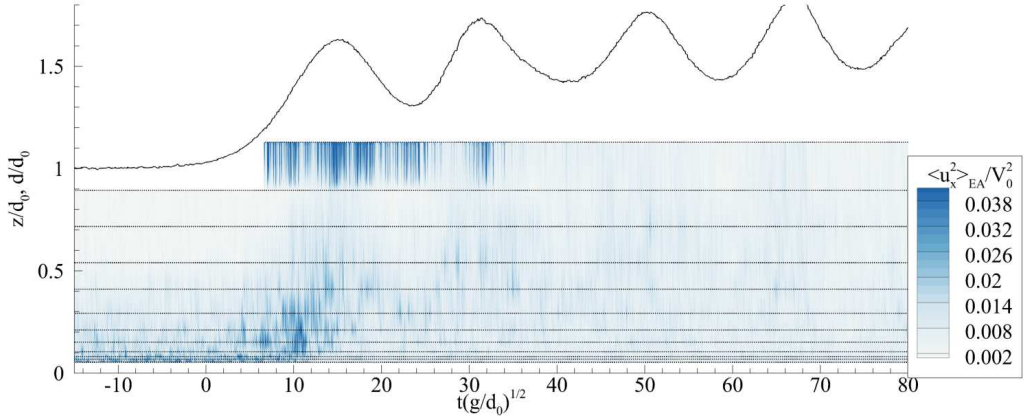

(a) Longitudinal velocity stress

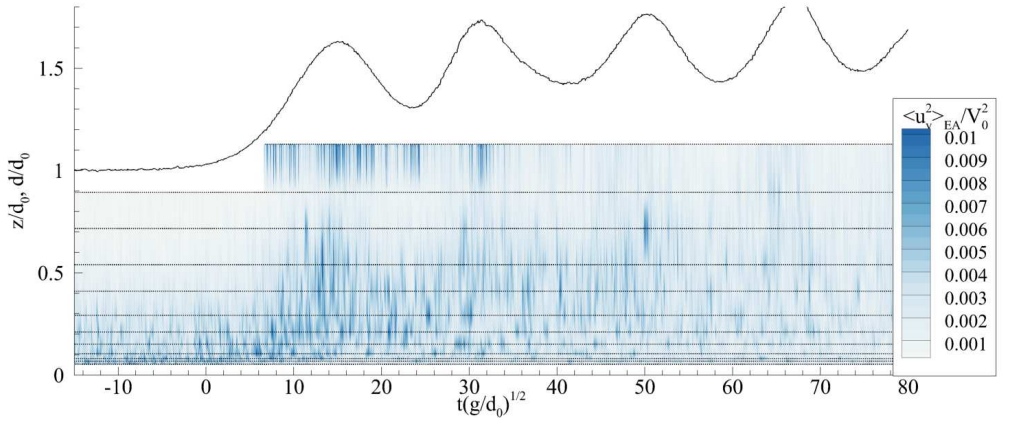

(b) Transversal velocity stress

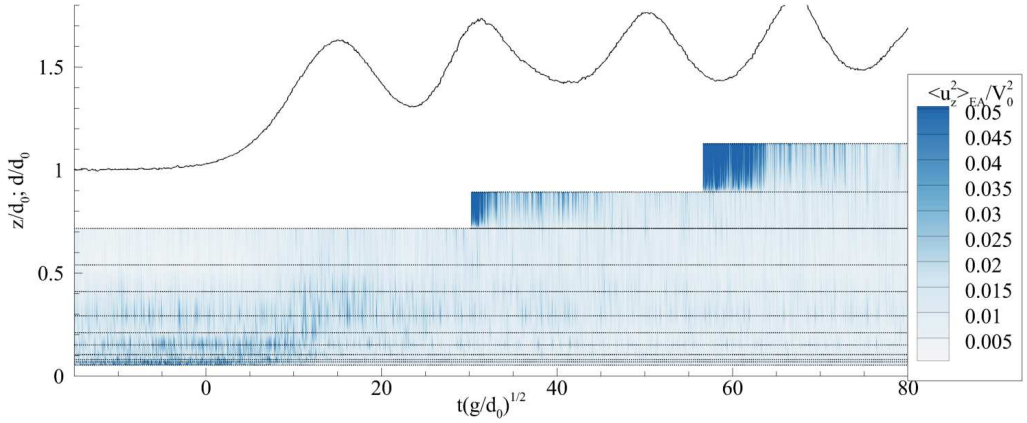

(c) Vertical velocity stress

Figure IV.33: Contour of ensemble-averaged turbulent normal stresses in an undular bore with ensemble averaged water depth. Flow conditions: $Q = 0.055$ m^3.s^{-1}, $x = 6.13$ m, $d_0 = 0.110$ m, $Fr = 1.34$

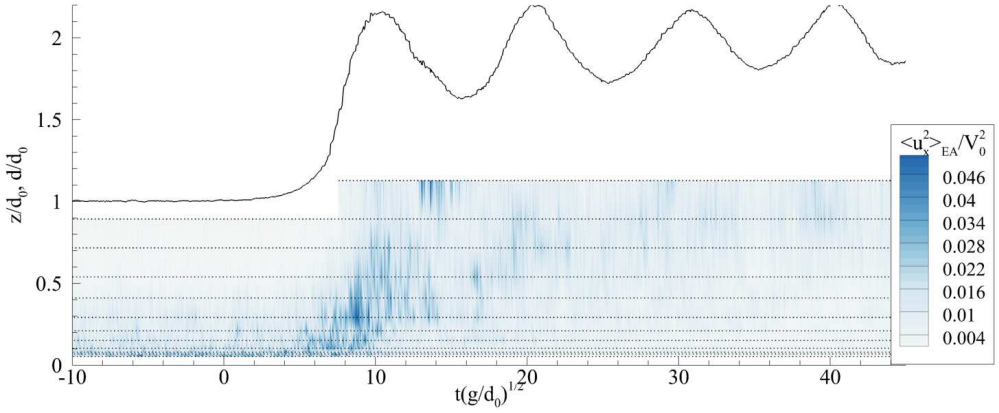

(a) Longitudinal velocity stress

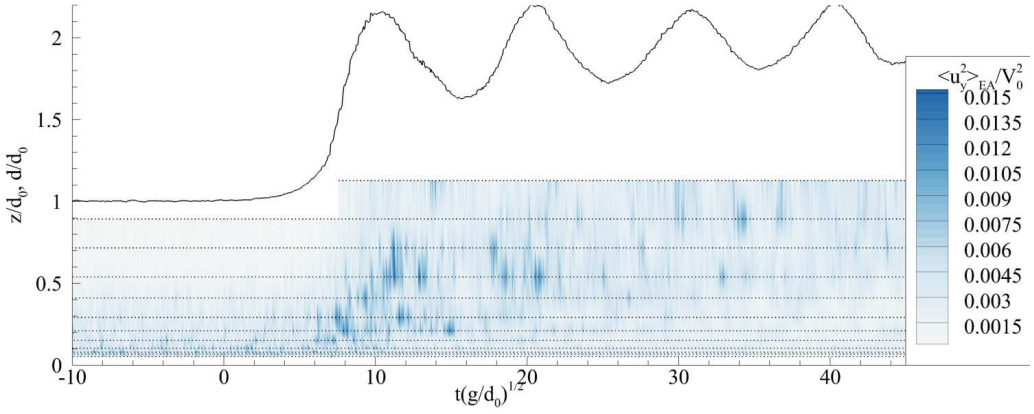

(b) Transversal velocity stress

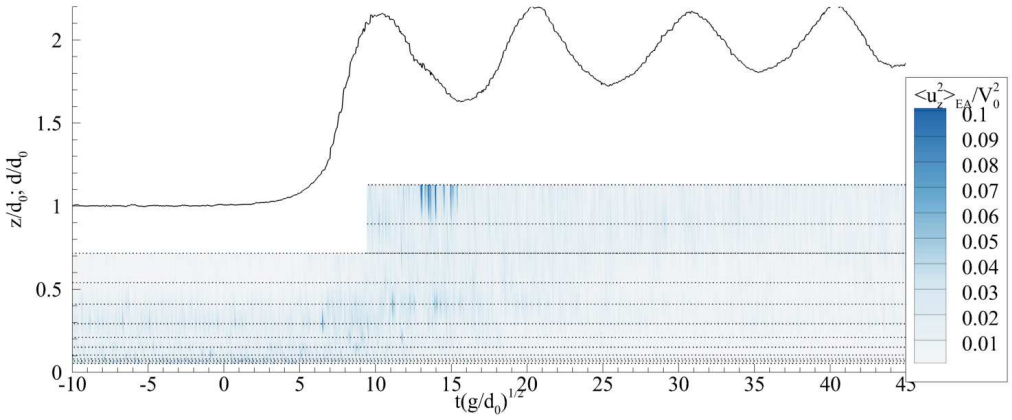

(c) Vertical velocity stress

Figure IV.34: Contour of ensemble-averaged turbulent normal stresses in a breaking bore with ensemble averaged water depth. Flow conditions: $Q = 0.055$ m^3.s^{-1}, $x = 6.13$ m, $d_0 = 0.110$ m, $Fr = 1.58$

IV.4.4 Turbulent integral time and length scales in unsteady flows

For undular and breaking bores, series of measurements were performed at several depths with two ADVs facing each other in the transverse direction to obtain quantitative information on the turbulent integral time and length scales beneath the bore front. The measurements took place at $x = 6.13$ m from the channel intake at several depths and for several transversal distances between the probes. Table IV.5 summarises the experimental configuration. In a first approach, the cross-correlation functions presented in section III.3.3.4 were calculated over the instantaneous velocity $\mathbf{u}$ and averaged with 5 runs. However, the longitudinal velocity component data presented a strong deceleration and it is believed that the correlations were biased by this flow pattern because the correlation calculations were no longer related to the small scale of the flow turbulence.

Table IV.5: Flow conditions and measurements configurations for turbulent integral time and length scale measurements at $x = 6.13$ m and $Q = 0.053$ m^3.s^{-1}

d_0	V_0	Fr	Bore Type	T	z/d_0	δ_y
m	m.s^{-1}			s		m
0.112	0.957	1.30	undular	2.4	0.012, 0.03,	0.0, 0.006, 0.009,
		1.59	breaking	1.6	0.05, 0.07	0.013, 0.018, 0.028

In a second approach, the biases were removed by calculating the cross-correlation function based upon the velocity fluctuation $\mathbf{u}' = \mathbf{u} - \bar{\mathbf{u}}_{EA}$, where $\bar{\mathbf{u}}_{EA}$ is the ensemble-averaged velocity and will be denoted $\bar{\mathbf{u}}$ in the following. The correlations were computed for each velocity fluctuation and the correlations were ensemble averaged over 5 runs. The cross-correlation function was calculated during the passage of the front from the moment the free surface started rising and over a time T, from the moment when the water started to rise to the first wave trough for both breaking and undular bores. This time interval T was selected to study the turbulent properties beneath the bore front. Note that the time period T was longer for the undular bore because the bore front was slower and the leading wave length longer than for the breaking bore.

Figure IV.35 presents typical correlation function in bores measured at $x = 6.13$ m and for several spacing $\delta_y = 0$. In the undular bore (Figure IV.35a and IV.35b), the correlation function for the longitudinal and the transversal unbiased velocity presented a Gaussian function shape relatively close to the shape obtained in steady flow, but for $\delta_y = 0$. In the breaking bore (Figures IV.35c and IV.35d), the correlation functions did not present an obvious bell shape typical of Gaussian distributions. For the fluctuation of the longitudinal velocity, the maximum cross-correlation coefficient values were scattered. The correlations of transversal velocities were centred about $\tau = 0$ and the shape of the correlation curves was more like a Gaussian.

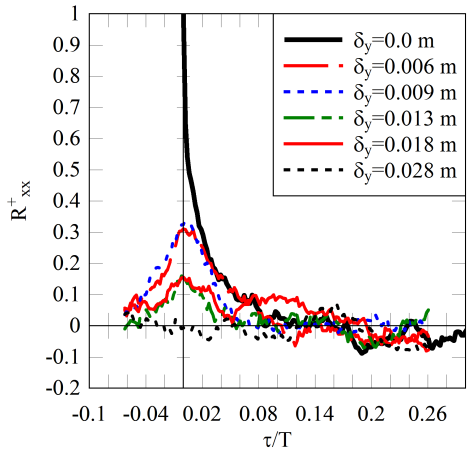

(a) Undular bore, $Fr = 1.30$, $z = 0.050$ m, R^+_{xx}

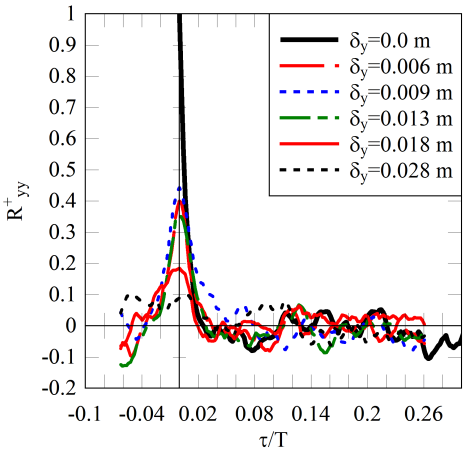

(b) Undular bore, $Fr = 1.30$, $z = 0.050$ m, R^+_{yy}

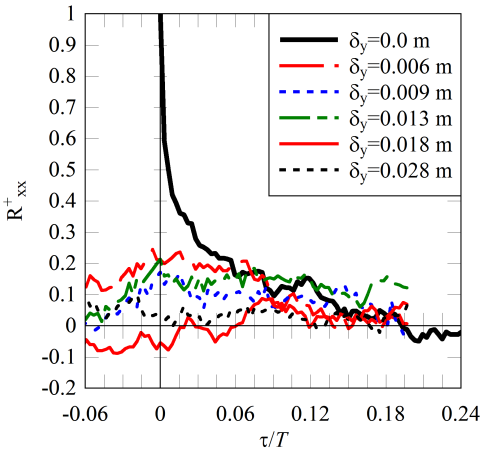

(c) Breaking bore, $Fr = 1.30$, $z = 0.030$ m, R^+_{xx}

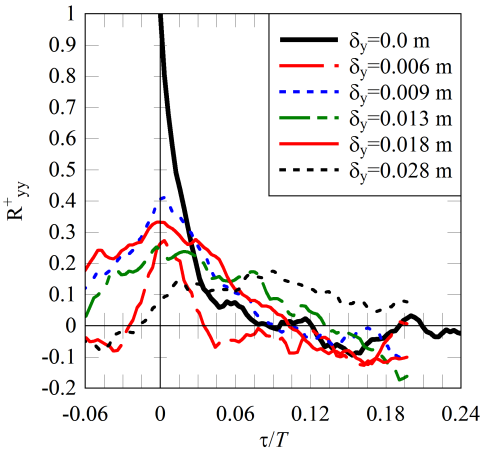

(d) Breaking bore, $Fr = 1.30$, $z = 0.030$ m, R^+_{yy}

Figure IV.35: Ensemble averaged correlation functions in terms of u_x (right) and u_y (left) in undular (top) and breaking (bottom) bores beneath the bore front. Flow conditions: $Q = 0.053$ $m^3.s^{-1}$, $x = 6.13$ m, $d_0 = 0.112$ m

IV.4.4.1 Turbulent integral scales for the instantaneous velocities beneath the bores

The turbulent time and length scales were calculated from the correlations of the instantaneous velocities. Table IV.6 presents the results in terms of the turbulent integral time and length scales for both breaking and undular bores. The integral time and length scales showed large values, particularly for the longitudinal velocity component. It is believed that the correlations were not meaningful of the turbulent macro-scales. For example, a time scale T_x of 1.4 s would correspond to a Taylor length scale of the order of 1 m which was physically meaningless, since

the largest turbulent structures were bounded by the flow depth (~ 0.1 m) and channel width (0.50 m). Moreover a time scale $T_x = 1.4$ s is similar to the time T used to compute the correlation to give a meaningful result. In a breaking bore, the transversal velocity presented a specific pattern with a negative value beneath the bore which biased the correlation as well. Only the transversal velocity in an undular bore (Table IV.6) had a reasonable correlation values beneath the bore. It will be shown latter that the values compared well with the unbiased velocity correlations since there was no marked bias on the transverse velocity of the undular bore.

Table IV.6: Turbulent integral time and length scales, calculations based upon the instantaneous velocity signal

Bore type	z	z/d_0	$L_x(*)$	$L_y(*)$	T_x	T_y
	m		m	m	s	s
Breaking with	0.012	0.11	0.019	0.008	0.670	0.060
secondary undulations,	0.03	0.27	0.025	0.011	0.922	0.081
$Fr = 1.6$	0.05	0.45	0.025	0.012	1.275	0.083
	0.07	0.63	0.024	0.011	1.424	0.065
	0.012	0.11	0.013	0.006	0.393	0.041
Undular,	0.03	0.27	0.019	0.010	0.930	0.035
Fr=1.3	0.05	0.45	0.021	0.011	1.166	0.029
	0.07	0.63	0.022	0.012	1.640	0.026

IV.4.4.2 Turbulent integral scales for the unbiased velocities or fluctuations beneath the bore

The turbulent length and time scales were calculated for the breaking and undular bores based upon the cross-correlation functions calculated in terms of the velocity fluctuations. The results are presented in Table IV.7.

In the undular bore, breaking bore and steady flow, the turbulent integral length scales L_x and L_y had a similar order of magnitude at all elevations. The turbulent length scales ranged from 4 mm to 12 mm. At the depth $z/d_0 = 0.63$, the length scales L_x and L_y were larger in the unsteady flow than in the steady flow (section IV.2.4). Close to the bed, the turbulent length scales were about the same order of the estimated equivalent sand bed roughness $k_s = 6$ mm. The average ratios of the turbulent integral length scales $\overline{L_x/L_y}$ were 0.67 and 0.72 in breaking and undular bores respectively. Overall, the values were similar, this might indicate that the bore type (breaking or undular) had little effect on the coherent length of the turbulence beneath the bore front.

The turbulent time scale data showed some marked difference between the breaking bore, undular bore and steady flow. For the longitudinal velocity time scale T_x, the values were

similar close to the bed ($z/d_0 < 0.27$) in both steady and unsteady flows. In the upper part of the flow, the unsteady flow conditions presented larger time scales T_x than in the steady flow. This might be an effect of the rough gravel bed creating similar turbulent length scales T_x. The turbulent time scale T_y was larger in the unsteady flow than in the steady flow with T_y larger in the breaking bore than in the undular bore. The larger turbulent integral time scales T_y in the unsteady flow, particularly in the breaking bore, might be linked with the flow deceleration. As the flow decelerated, the coherence of the velocity over the two spaced points remained for a longer time. The average ratios of the turbulent integral time scales $\overline{T_x/T_y}$ was 1.13 and 1.86 in breaking and undular bores respectively. The difference is believed to be linked with the stronger flow deceleration of the breaking than the undular bore. For breaking and undular bores, the change in magnitude of the longitudinal velocity at a given depth was calculated as the difference between the longitudinal steady velocity time average ($\bar{u}_x$) and the velocity values between the first wave crest and trough ($u_{x,bore}$). It yielded that $\bar{u}_x - u_{x,bore}$ was approx -0.92 m.s^{-1} and -0.52 m.s^{-1} in breaking and undular bores respectively. The ratio of velocity amplitude changes between breaking and undular bores yielded 1.77, similar to the ratio of the turbulent integral time scales of the undular and the breaking bores, yielding 1.64, also similar to the ratio of the breaking and the undular bore celerity, yielding 1.73.

Table IV.7: Turbulent integral time and length scales, calculations based upon the unbiased velocity signal

Bore type	z	z/d_0	L_x(*)	L_y(*)	T_x	T_y
	m		m	m	s	s
Breaking with secondary undulations, $Fr = 1.6$	0.012	0.11	0.0043	0.0069	0.038	0.039
	0.03	0.27	0.0068	0.0102	0.058	0.049
	0.05	0.45	0.0062	0.0097	0.050	0.051
	0.07	0.63	0.0066	0.0089	0.051	0.037
Undular, Fr=1.3	0.012	0.11	0.0052	0.0064	0.042	0.033
	0.03	0.27	0.0063	0.0095	0.053	0.032
	0.05	0.45	0.0075	0.0101	0.062	0.027
	0.07	0.63	0.0079	0.0117	0.055	0.025

Note (*): the accuracy of the values was not inferior to 1 mm because of the size of the ADV control volume and the accuracy of its spatial position.

The ADV sampling interval time was 0.005 s and the ADV sampling volume height was a few millimetres. These characteristics were smaller than the turbulent integral time and length scale data, although impacted onto the accuracy of the results.

Note that the turbulent length scale L_y and time scale T_y calculations yielded similar results for the unbiased transversal velocity and instantaneous transverse velocity. This would indicate that the removal of the averaged velocity component kept the size and time scale of the coherent

turbulent structures.

IV.4.4.3 Concluding remarks

In the steady and unsteady flows, the turbulent length scales L_x and L_y were comparable, indicating that the bore front had limited effects on the size of coherent structures in the transversal direction. However, the turbulent integral time scale T_x and T_y (for $z/d_0 > 0.45$) were significantly different in the unsteady bore flow. This might result from the flow decelerating and the turbulent structures advected in the wake of the bore front. It is acknowledged that the two-point correlation study was limited to the analysis of the turbulent time and length scale only in the transversal spacing at few vertical elevations with a small number of run repeats and with two intrusive probes.

IV.5 Summary

A broad range of unsteady flow conditions was thoroughly investigated. Both undular and breaking bores were studied based upon a Froude number similarity using ensemble-average data. Classical observations in bores were confirmed such as the sudden free surface rising in synchronisation with a sudden flow deceleration. In breaking bore, a longitudinal velocity reversal was observed near the bed for the ensemble averaged data but not for the undular bores where only instantaneous transient velocity reversals were observed. The free surface evolution was associated with larger fluctuations during the bore passage particularly marked for breaking bores. The unsteady flow velocity was also marked by larger fluctuations within bore propagations. Turbulent stresses were observed to increase in the bore wake close to the bed and move upward in the water column, in contradiction to prior study in breaking bores implying a turbulence generated by the breaking roller and moving downward the water column. Some measurements were performed using a two-point correlation technique to calculate the turbulent integral time and length scales in the transverse direction. The data analyses showed similar magnitude of turbulent integral scales in the steady and unsteady flow with slightly larger value of the turbulent integral time scale in the unsteady flow.
Overall, the experimental study showed a strong and intense mixing. Strong velocity fluctuations would have a non negligible effect on the sediment motion in tidal bores propagating in rivers with a moveable boundary.

V

Numerical model test cases and validations

V.1 Chapter overview

Before simulating three dimensional positive surges in channels, a number of simple configurations were tested to validate the numerical tool. The first case will be the generation of a positive surge after a dam break over a motionless layer of water. Then, the methods used to model a turbulent inflow (Jarrin et al., 2006) will be tested and the turbulent flow generated will be compared with experiments. Simulations of two dimensional idealised tidal bores will be thoroughly compared to experimental results, in which bores were created by the impact of a stream against a fully or partially closed gate. Finally, the three dimensional cases will be compared to experiments.

V.2 Two dimensional dam break wave propagation over a wet bed

V.2.1 Presentation

The rupture of a dam with an initial water depth d_1 into a layer of water with a depth $d_0 < d_1$ produces a surge propagating in the water layer. The surge propagates as a bore with a

visual aspect similar to tidal bores. The bore can be undular and/or breaking. As the bore propagates in one direction, the dam water decreases and forms what is called a rarefaction wave. As long as the rarefaction wave does not reach the end of the dam, the water level of the surge stays constant (Figure V.1). Those theoretical aspects were detailed in section II.3.2. An approximation of the complete flow evolution can even be obtained with suitable hypotheses (Stoker, 1957). The bore height and celerity as well as the flow beneath the bore can be estimated using the equation (II.4). Figure V.1 presents the water evolution of the simulated dam break with velocity streamlines and a colour mapping of the longitudinal velocity.

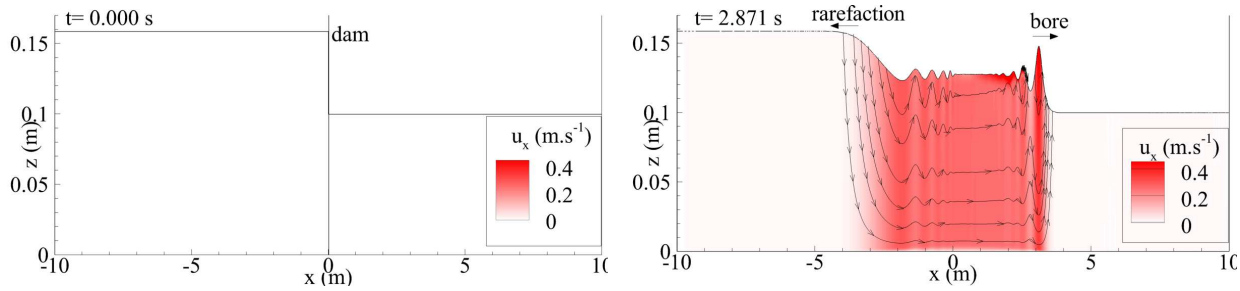

Figure V.1: Longitudinal velocity colour mapping with velocity streamlines at $t = 0$ and 2.871 s. The domain is cropped above the water

Studies of dam break wave effects on the flow were performed for breaking surges (Hornung et al., 1995; Yeh and Mok, 1990). But detailed studies on undular dam break wave are more limited. Nonetheless, dam break waves are interesting simulations to perform in preparation of positive surge studies due to the shared features in term of quasi steady flow analogy of the two phenomenon. The numerical domain and initial conditions are relatively simple and several conditions can be generated with the change of only two parameters that are the water depth in the dam and the tail water height. Note that detailed experiments of undular bores propagating over a layer of water were not found in the literature. The numerical simulation will only be compared to analytical solution. Works from from Marche et al. (1995) and Hornung et al. (1995) gave complementary information on the flow evolution.

V.2.2 Numerical configuration

The dam break was modelled with two rectangles of quiescent water with a hydrostatic pressure distribution separated by an infinitely thin wall. The dam reservoir had a water depth $d_1 = 0.158$ m superior to the small reservoir water depth $d_0 = 0.1$ m (Figure V.1). The domain was 20 m long and 0.5 m high. At the instant $t = 0$, the dam wall located at $x = 0$ instantaneously disappeared. x was positive towards the low water depth reservoir and z was the distance from the bed. The domain boundaries were set with no slip boundary conditions. The domain was discretised in the vertical direction by 500 meshes. The mesh sizes were increasing exponentially

with the smallest mesh above the bed ($\Delta_{z,\min} = 5 \times 10^{-5}$ m). In the longitudinal direction, 4 100 meshes had a constant size between $x = 0$ to 10 m and 500 meshes increased size exponentially from $x = 0$ to -10 m with $\Delta_{x,\min} = 2.4 \times 10^{-3}$ m. The simulation was run with a Courant–Friedrichs–Lewy (CFL) condition inferior to 2/3 to insure the scheme stability. The water and air densities and viscosities were $\rho_w = 1000$ kg.m^{-3}, $\rho_a = 1.1768$ kg.m^{-3}, $\mu_w = 10^{-3}$ kg.m^{-1}.s^{-1} and $\mu_a = 1.85 \times 10^{-5}$ kg.m^{-1}.s^{-1}. The gravity acceleration was set with the gravity acceleration of Brisbane, Australia, $g_z = 9.80$ m.s^{-2}. The simulation was run as a large eddy simulation (LES) using the mixed scale (MS) model. The interface was modelled with a VOF-PLIC scheme and identified by $C = 0.5$ with C the phase function. 36 processors were used in parallel during approximately 20 hours.

V.2.3 Free surface evolution

The dam break wave shape was similar to positive surges generated in section II.3.2. The bore created a sudden water level elevation followed by secondary undulations (Figure V.1). The free surface was compared with the analytical formula given by equation (II.4). Figure V.2 presents the free surface evolution during the passage of the bore. The bore free surface converged towards the conjugate depth d_b given by equation (II.4) (Figure V.2). A Froude number of $Fr = 1.202$ was calculated at $x = 3.2$ m close to the estimated value $Fr_{theo} = 1.215$ ($Fr = U_b/\sqrt{gd_0}$). The difference in conjugate depth was only 0.2%. The delay between bore fronts from the analytical theory and the simulation was due to the analytical estimation assuming a bore with a constant celerity. However, the bore from the simulation reached an almost constant celerity for $x > 2.5$ m. Note that the shape of the undulations was similar to measurements performed by Marche et al. (1995).

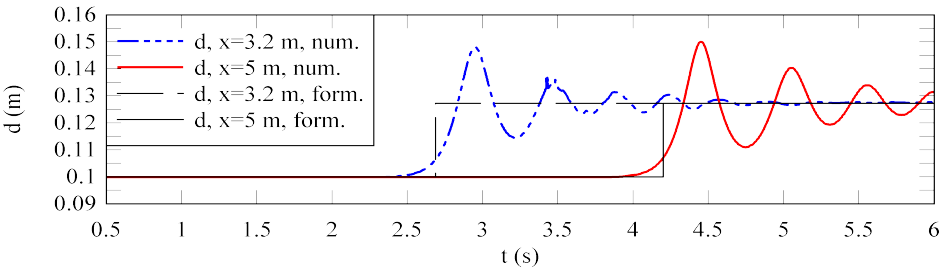

Figure V.2: Free surface time evolution at two different locations from the dam. Comparison with equation (II.4)

V.2.4 Flow velocity evolution

The bore created a sudden flow change. Beneath the bore front, the water started moving in the direction of the bore propagation. The largest velocity values were recorded beneath wave crests.

The flow accelerated and decelerated when the water increased and decreased respectively (Figure V.1). The velocity evolution beneath the bore is compared to the analytical formula (II.4) $V_{b,theo} = 0.255$ m.s^{-1}. Figure V.3a presents the longitudinal velocity time evolution during the bore passage. Figure V.3b presents a vertical profile of the longitudinal velocity beneath the first crest of the bore. Beneath $z = 5$ mm, a boundary layer started to develop after the bore passage due to the no slip boundary condition (Figure V.1 and V.3). Above $z = 5$ mm, the velocity was converging toward $V_{b,theo}$ (Figure V.3a). Unfortunately, no detailed time evolution of the longitudinal velocity beneath an undular dam break wave could be found in the literature. Nonetheless, the simulation was in agreement with the analytical theory. The study of Hornung et al. (1995) gave similar velocity profiles beneath the wave crest of a breaking dam break wave.

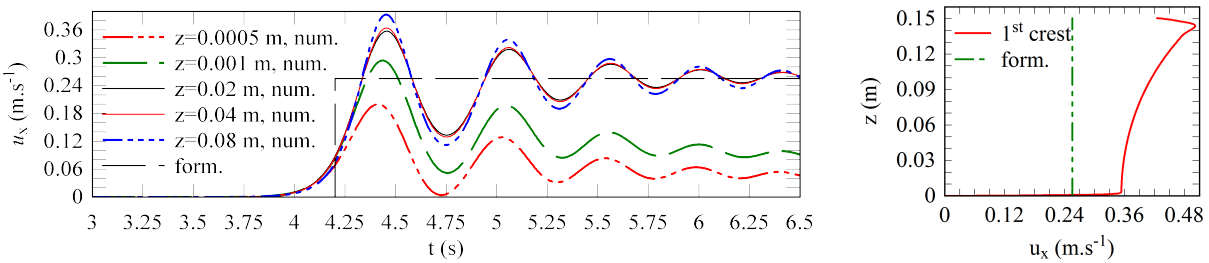

(a) Time evolution at several depths and $x = 5$ m. Comparison with the estimated flow velocity equation (II.4)

(b) Vertical profile beneath the first crest. $x = 4.125$ m

Figure V.3: Longitudinal velocity below an undular dam break wave

V.2.5 Pressure evolution

The pressure evolved in synchronisation with the free surface evolution. Figure V.4 compares the numerical simulation pressure and the hydrostatic pressure calculated from the numerical free surface evolution at $x = 5$ m. Compared to hydrostatic pressure, the numerical pressure field was larger beneath the crest and lower beneath the troughs (Figure V.4). This pressure evolution was also found in the study of dam break wave by Marche et al. (1995), this is predicted by the Boussinesq equations and similar findings were reported for undular hydraulic jumps (Montes and Chanson, 1998).

V.2.6 Concluding remark

After a dam failure, the generated surge looks similar to a tidal bore. For this case, the dam break wave propagates over motionless water whereas tidal bores mostly propagate against steady river flows. This case is interesting for numerical studies since all the boundary conditions

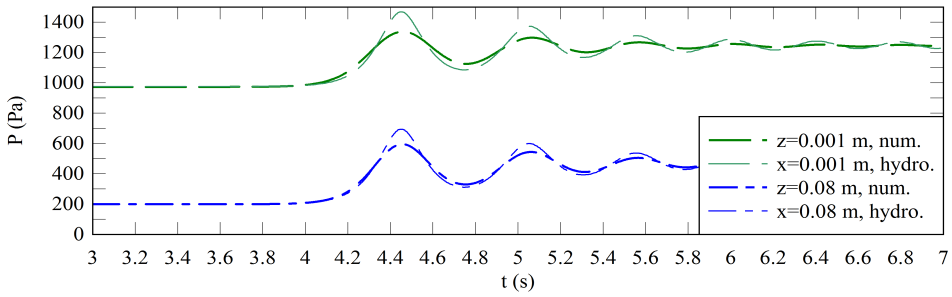

Figure V.4: Pressure time evolution at two elevations during the dam break wave propagation measured at $x = 5$ m. Comparison with an hydrostatic pressure distribution

are no-slip conditions. No matter can come in or out of the domain which makes the control of the simulation easier. Moreover, only two parameters control the bore characteristics: the water depth in the dam and in the initial downstream water. The comparison was limited by the absence of detailed experimental measurements for undular dam break. Nonetheless, the numerical simulation showed a good agreement with theoretical estimations.

V.3 Modelling of turbulent inflow conditions in a water channel

The synthetic eddy method (SEM), developed by Jarrin et al. (2006) and described in section III.4.2.6, allows to recreate turbulent inflow conditions using only the mean flow velocity, Reynolds stress profiles, an estimated eddy size and an estimated number of eddies. Such information can be obtained from simulations using, for example, a RANS (Reynolds-averaged Navier–Stokes) model, or from experimental data. If the eddy length scales and the number of eddies are unknown, they can be determined depending on the simulation configurations (Jarrin et al., 2009). Thereafter, the simulations reproduced an experiment performed in the rectangular water pipe of the I2M laboratory of Bordeaux based on measurements performed for the ANR project MASCARET (Caplain and Reungoat, 2013). The ability of the SEM to produce a turbulence that will propagate coherently will be verified together with the implementation of the method in the code Thétis. In the next chapter, the SEM will be used to create a turbulent steady flow before and during the propagation of bores.

V.3.1 Experimental configuration

Experiments (Caplain and Reungoat, 2013) were conducted in a 2 m long horizontal channel with a $D = 0.1$ m square diameter with PMMA walls on every faces. Figure V.5 presents the experimental channel with the location of measurements and the grid used to generate the

turbulence. The water discharge was given by an automatic pump adjusted by one electronic discharge metres located downstream the channel with a 2% error margin. A grid with $M = 6.6$ mm square meshes (Figure V.5), including a 1.2 mm flat rod between holes, was set at the upstream part of the channel to generate a controlled isotropic and homogeneous turbulence (Caplain and Reungoat, 2013). The flow measurements were performed by a laser Doppler velocimetry (LDV) unit and particles image velocimetry (PIV) unit.

Here, and only for this case, x is the longitudinal direction positive downstream with $x = 0$ at the grid, y is the horizontal distance from the right sidewall and z is the vertical distance from the channel bed. According to Caplain and Reungoat (2013), only the instantaneous longitudinal and vertical velocities (u_x and u_z) were measured on the channel centreline and on the horizontal and vertical centrelines of transversal sections with the LDV unit and, with the PIV unit, the vertical and longitudinal velocities were measured on two slices in the x, z-plan on the centreline (Figure V.5). The measurements were performed for a discharge of 100 L.min^{-1} (1.667×10^{-3} m^3.s^{-1}).

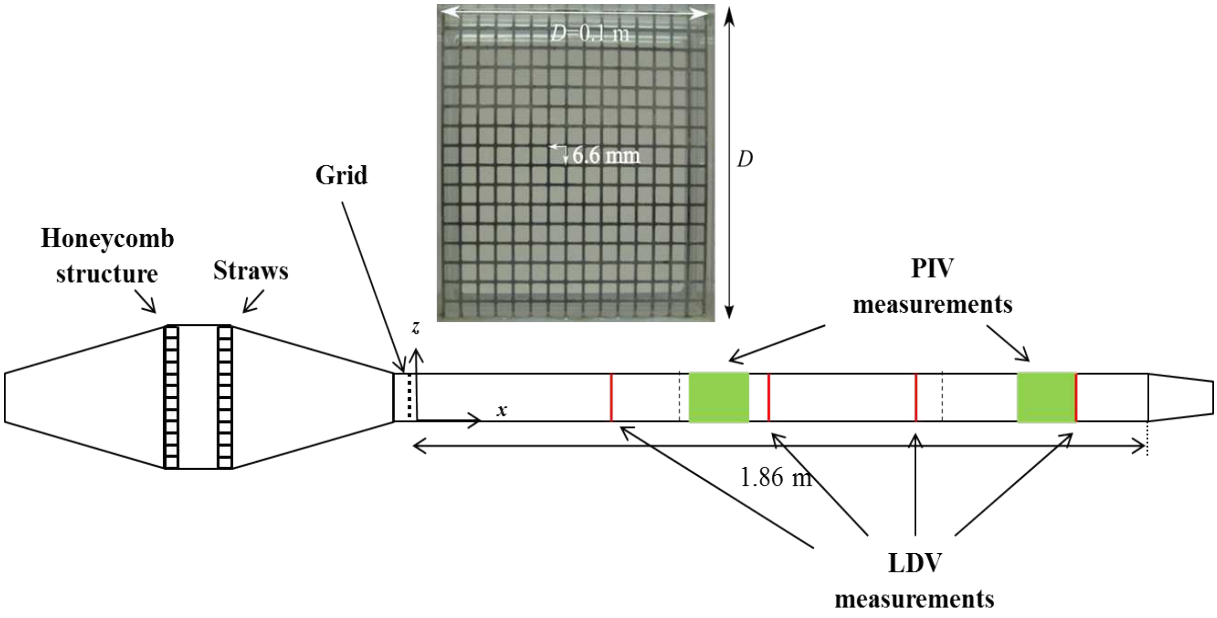

Figure V.5: Experimental channel with the grid view from upstream and the measurement locations. Water flows from left to right

V.3.2 Numerical modelling

The numerical domain was a 3 m long, 0.1 high and 0.1 wide parallelepiped. The simulation was performed with monophasic flow. The water characteristics were a density $\rho = 1000$ kg.m^{-3} and a viscosity $\mu = 10^{-3}$ kg.s^{-1}.m^{-1}. The flow was initialised with a velocity $V_0 = 0.167$ m.s^{-1}. A no-slip boundary condition was applied on the lateral walls. The channel outlet was set

with a Neumann condition. Upstream the outlet boundary, in order to prevent numerical perturbations, a 1 m layer absorbing linearly the tangential velocities was added at the channel downstream end (Hafsia et al., 2009) (section III.4.1.3). The simulation was tested for two mesh sizes $875{\times}10^3$ ($350{\times}50{\times}50$) meshes and $7{\times}10^6$ ($700{\times}100{\times}100$) meshes (Table V.1). The characteristics of simulations are presented in Table V.1. The mesh was constant along the longitudinal axis and exponentially increasing from the lateral wall towards the channel centre in the transversal and vertical directions (Table V.1). A MS model was used for the LES (section III.4.1.5). The simulations were run with a dynamic time step insuring that a CFL condition inferior to 0.5. Configurations run 2 and run 4 were simulated on 108 processors for approximately 200 000 iterations corresponding to 80 s of flow propagation in the channel.

Table V.1: Simulation meshes and SEM configurations

Run	Number of meshes	Δ_x m	$\Delta_{y,\min}$, $\Delta_{z,\min}$ m	$\Delta_{y,\max}$, $\Delta_{z,\max}$ m	Type of RMS profile on the inflow
1	875×10^3	2/300	5×10^{-4}	5×10^{-3}	Profile from experiment
2	7×10^6	2/600	1×10^{-4}	3.6×10^{-3}	at $x = 0.485$ m
3	875×10^3	2/300	5×10^{-4}	5×10^{-3}	Constant value
4	7×10^6	2/600	1×10^{-4}	3.6×10^{-3}	0.06 m.s^{-1}

Note: Δ_i is a mesh size in the i-direction

The channel inflow condition was set with the SEM (Jarrin, 2008). The parameters were set with $N = 1000$ eddies with a length scale $\boldsymbol{\sigma} = 6$ mm, a value similar to the grid mesh size 6.6 mm with 5.4 mm hole. The velocity profile was given by experimental measurements from vertical and horizontal centred profiles (Caplain and Reungoat, 2013). The mean velocity profile was interpolated from measurement at $x = 0.485$ m from the grid and applied on the full inflow boundary diminished by 6% to obtain a discharge close to 100 L.s^{-1}. This was done to reduce the overestimation of the discharge when interpolating the velocity profiles due to the absence of measurement in the channel edges. Two different profiles of turbulent stress, calculated as the root mean square velocity (RMS), were used for the simulations. One using the measurements performed at the closest distance from the grid $x = 0.485$ m, and another condition assuming RMS$(u_i) = 0.06$ m.s^{-1} on the whole transversal section (Table V.1). Figure V.6 presents the longitudinal velocity signal created by the SEM and injected in the numerical domain. The SEM produced coherent turbulent structures randomly located and independent after all eddies in the SEM box were renewed (Jarrin, 2008) (Figure V.6). Figure V.7 presents flow streamrubans in the domain coloured with the vertical velocity magnitude. The streamrubans show the turbulence in the flow. They straighten within the absorption layer starting at $x = 2$ m (slice in Figure V.7). This illustrates the progressive diminution of the transversal and vertical velocities.

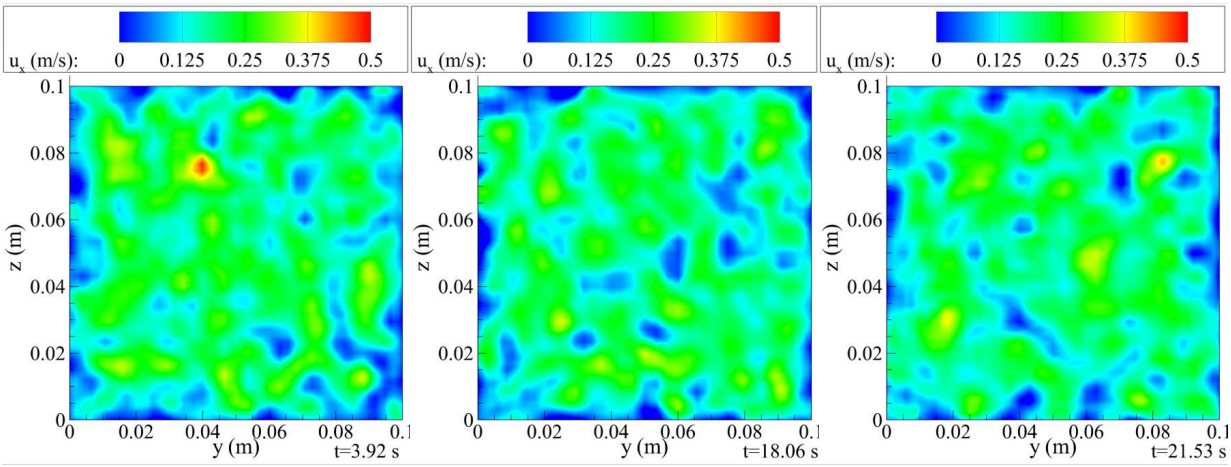

Figure V.6: Longitudinal velocity signal created by the SEM at three different times for the run 4

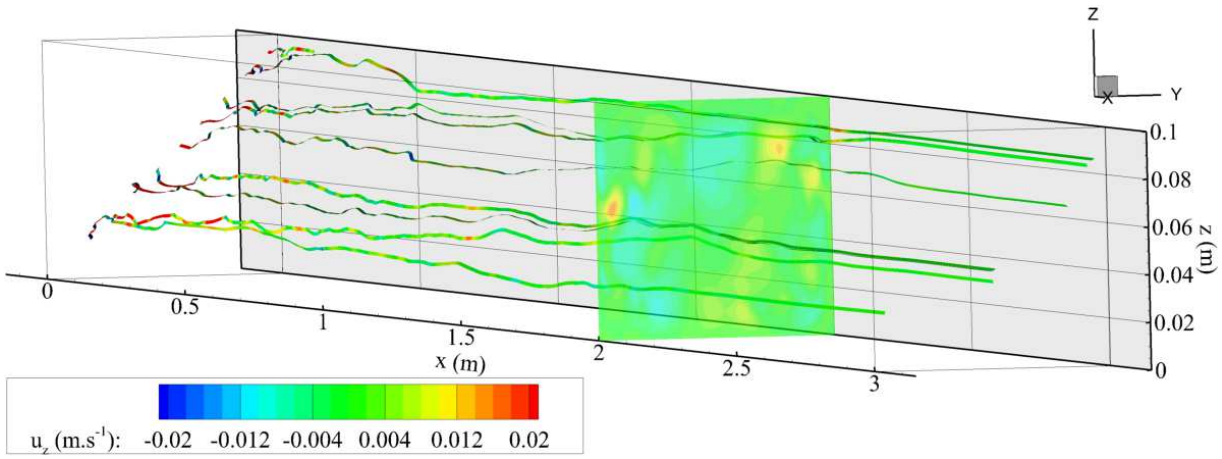

Figure V.7: Numerical domain with streamrubans. The slice at $x = 2$ m indicates the position of the damping layer downstream the channel. Run 4 at $t = 21.53$ s

V.3.3 Results

The results are compared for the four numerical configurations (Table V.2). The average discharge of the numerical simulations was first compared to the experimental discharge by integrating the time averaged velocity simulated by the SEM. Table V.2 shows the flow velocity $V_0 = Q/D^2$. The maximum difference of the flow velocity is similar to the 2% error accuracy of the experiment. In the following, the distances were made dimensionless by using the grid mesh size M as it is one of the parameters characterising the flow (Chassaing, 2000).

Table V.2: Flow velocity for each numerical configuration and the physical experiment (Caplain and Reungoat, 2013)

Case	Run 1	Run 2	Run 3	Run 4	Experiment
V_0 m.s^{-1}	0.167	0.171	0.171	0.170	0.167

V.3.3.1 Numerical sensitivity

The results of the time averaged mean and RMS velocities of the simulations were compared with one another. Figure V.8 and V.9 present the mean and RMS velocity profiles of the four numerical configurations (Table V.1). The longitudinal velocity $\bar{u}_x$ of the four configurations increased with the distance from the grid. For run 1, 2 and 3, the evolution was similar along the longitudinal axis, however for run 4, with the thinnest mesh and largest velocity fluctuations on the inflow, the velocity profile reached a smaller magnitude at the channel end (Figure V.8a). Close to the walls and for the vertical profiles, the longitudinal velocities measured were underestimated for run 1, 2 and 3 and overestimated at the centre in comparison to the velocity profiles of run 4 for $x/M > 100$ ($x = 0.70$ m) (Figure V.9a). The vertical and transversal velocities $\bar{u}_y$ and $\bar{u}_z$ were nearly zero on the entire domain (Figure V.8b and V.9b).

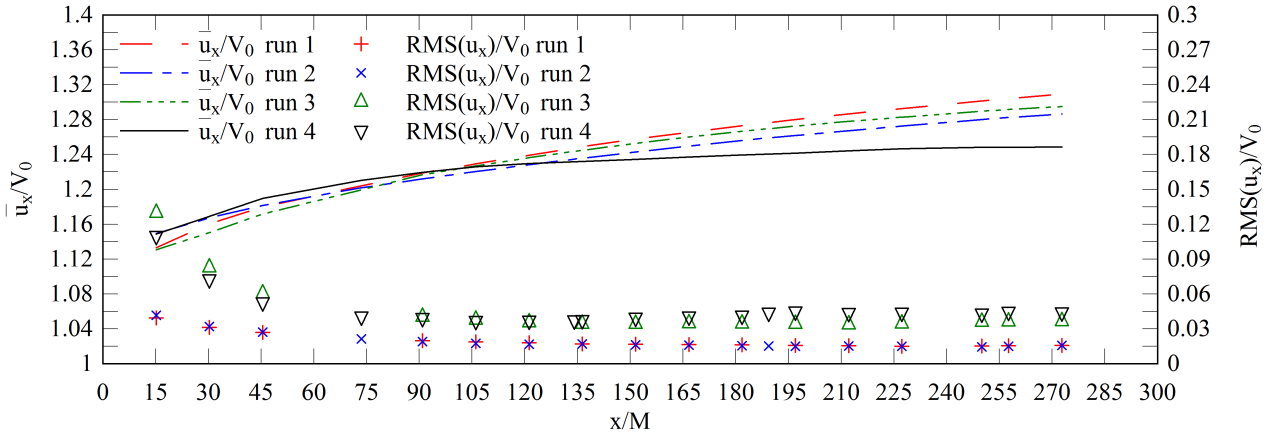

(a) Longitudinal velocity and RMS profiles

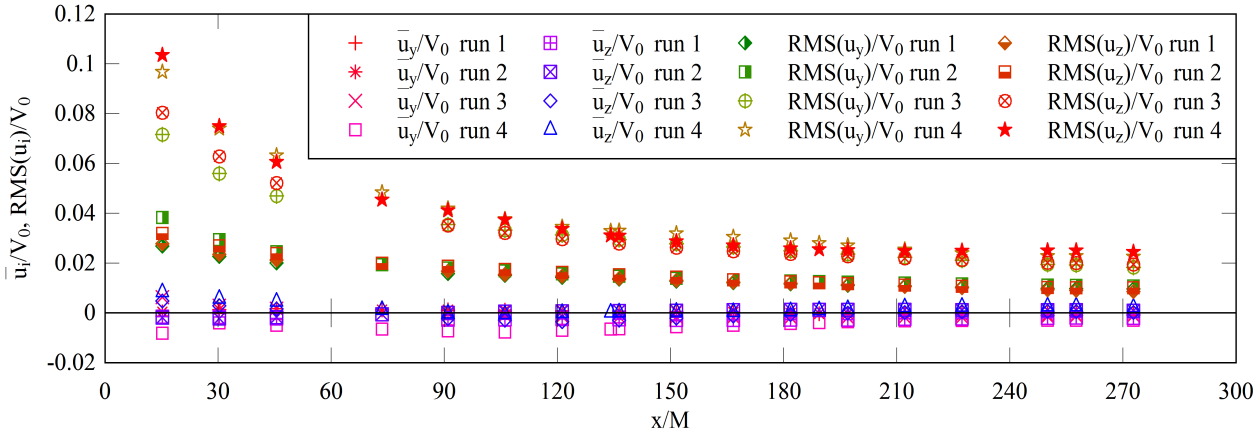

(b) Tangential velocity and RMS profiles

Figure V.8: Dimensionless numerical velocity profiles comparison along the x-axis on the channel centreline at $y = z = 0.05$ m

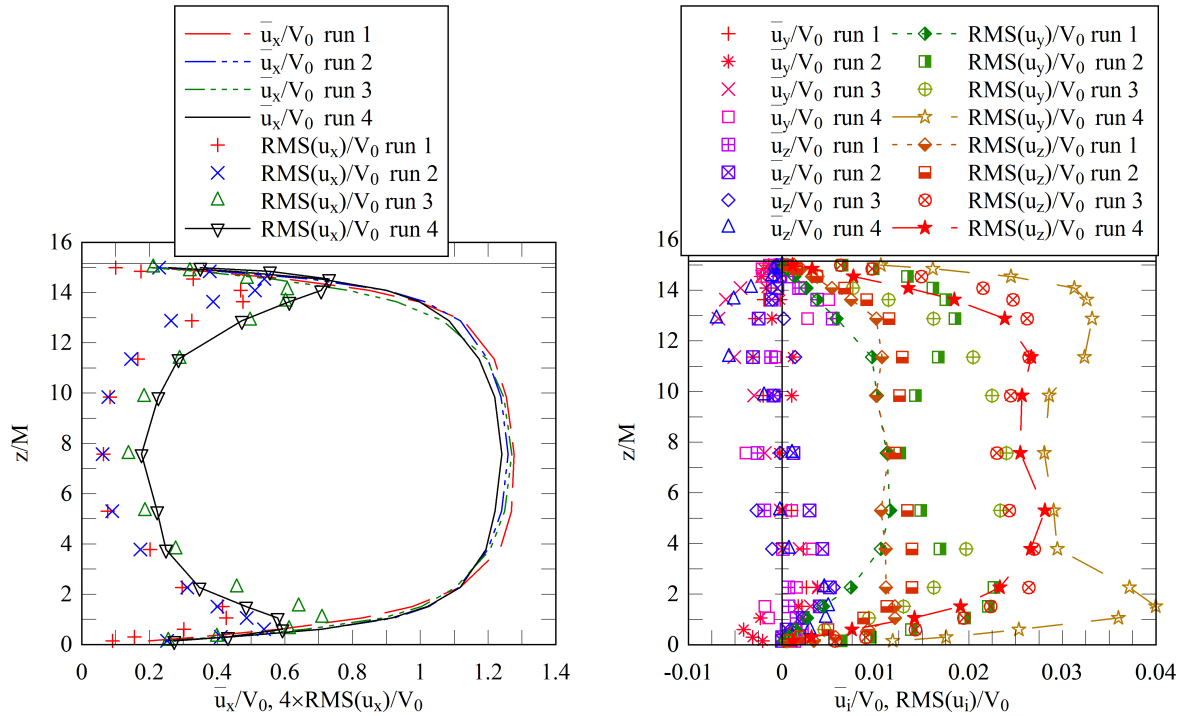

(a) Longitudinal velocity and RMS profiles (b) Tangential velocity and RMS profiles

Figure V.9: Dimensionless numerical velocity profiles comparison along the z-axis on the channel centreline at $x = 1.25$ m ($x/M = 190$)

Concerning the velocity fluctuations, the longitudinal and vertical profiles of the velocity followed similar trends (Figure V.8b and V.9b). Along the x-axis, the fluctuation levels decreased sharply from the inlet of the domain to $x/M = 90$. Their values stabilised on the rest of the domain except for RMS(u_x) which slightly increased after $x/M = 135$. Past $x/M = 90$, the velocity RMS were two times larger for the simulations with a fluctuation set with RMS(u_i) = 0.06 m.s^{-1} (run 3 and 4) than for the two other runs (1 and 2), set with the velocity RMS profiles from the experiment at $x/M = 73.5$. Along the vertical profile, a maximum of the vertical velocity fluctuations was observed at $z/M = 1.52$ from the walls. Close to the walls, the fluctuations were underestimated by the simulation with a coarse mesh (run 1 and 3) (Figure V.9b).
According to Jarrin (2008) when testing the sensitivity of the SEM to its initial parameters, the turbulence recovers a coherent value after a distance of 15 times half the channel height. Here, a stabilisation of fluctuations around $x/M = 90$ was observed which correspond to 12 times half the channel height which is coherent with Jarrin (2008) estimations.

V.3.3.2 Comparison with experiments

The experiments (Caplain and Reungoat, 2013) generated a turbulence using a grid with 6.6 mm square holes including a 1.2 mm flat rod. The closest measurements from the grid were

performed at $x = 0.485$ m. The velocity fluctuations were found to decrease progressively toward the end of the channel (Figure V.10a). Therefore, the fluctuations generated by the grid were estimated by extrapolation of the general trend of measured RMS toward a value $\text{RMS}(u_i) \approx 0.06$ m.s^{-1}. Both simulations run 3 and run 4 (Table V.1) were initialised with this constant RMS profile. Since run 4 used a thinner grid than run 3, only this simulation will be compared to experimental results.

Figure V.10 presents comparisons of the time averaged velocity and velocity RMS between experimental measurements and the numerical simulation at various locations in the channel. The numerical longitudinal velocity was in agreement with the experimental measurements always bound by the LDV and PIV measurements (Figure V.10). The mean longitudinal velocity was within 3% of difference with the LDV and PIV measurements. The longitudinal velocity fluctuations were underestimated close to the centre of a channel transversal section with up to 27% of difference with the PIV measurement for x/M between 230 and 250 (Figure V.10). The vertical velocity fluctuations were underestimated by the numerical simulation with up to 37% of difference with the PIV and LDV measurement for x/M between 230 and 250 (Figure V.10). The differences in the reproduction of fluctuations might come from some unknown values to set the best parameters of the SEM (velocity fluctuations and eddy sizes at the channel inlet) or from the large tangential meshes on the channel centreline (Δ_y and Δ_z) inducing a filtering of the turbulence linked to the LES method. For the first cause, several simulations performed with different size of eddies and fluctuation intensities could be conducted with the SEM. For the second cause, refining the mesh even more on the channel centreline would be a straightforward solution. Note that the level of fluctuations and the mesh size were tested (section V.3.3.1) and basic variations showed significant improvements of the simulations.

Figure V.11 present comparisons of the velocity skewness between the simulation results and the LDV measurements. The skewness gives a measure of the shape of the velocity distribution toward the mean value. The numerical simulation and the experiments showed scattered skewness values (Figure V.11). A general trend was found to be similar to both the simulation and the experimental measurements particularly along tangential axes (Figure V.11b).

V.3.4 Concluding remarks

Several numerical configurations were tested to estimate the potential of the SEM to produce a coherent turbulence in the simple case of a grid generated turbulence in a water channel. The mean and RMS velocity followed similar trends with the experiments but the level of fluctuations was underestimated. The lack of measurements directly downstream the channel grid only allowed the use of estimated parameters for the SEM. Parametrisation of the velocity profile, fluctuation profile and size of eddies could improve the simulations. Note that the

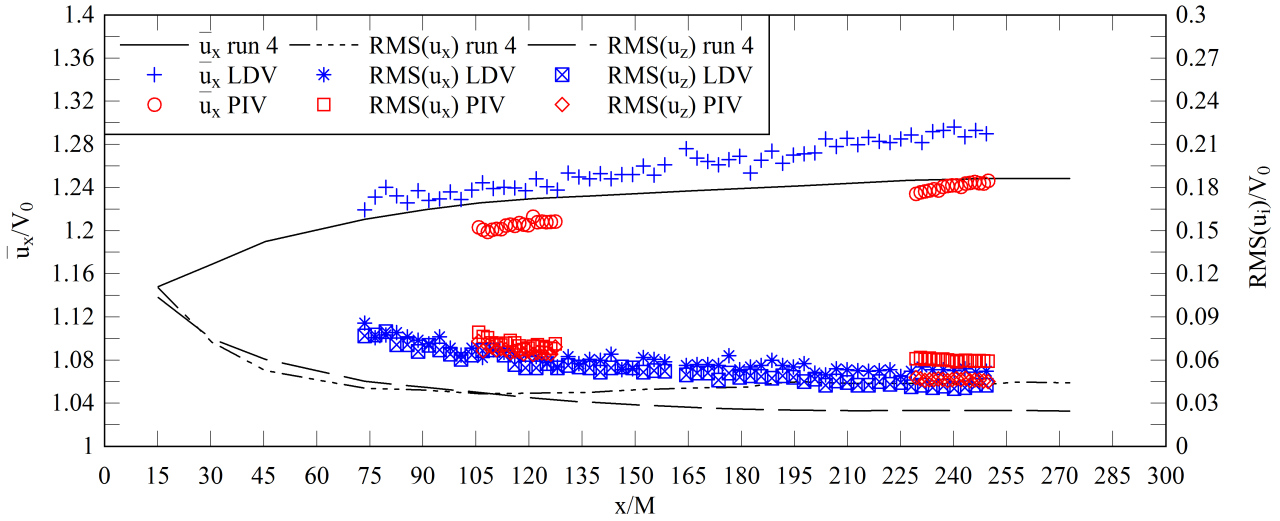

(a) Longitudinal profile on the channel centreline

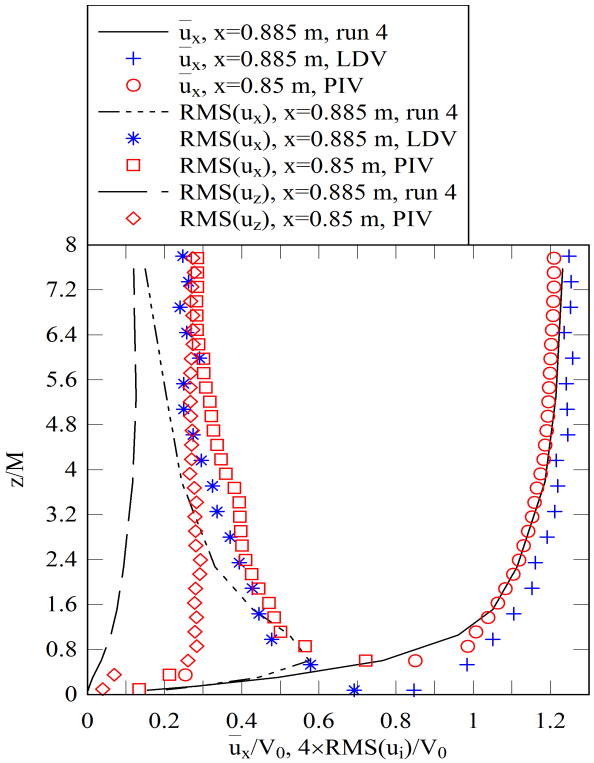

(b) Half of the vertical profile at $x \approx 0.9$ m and $y = 0.05$ m

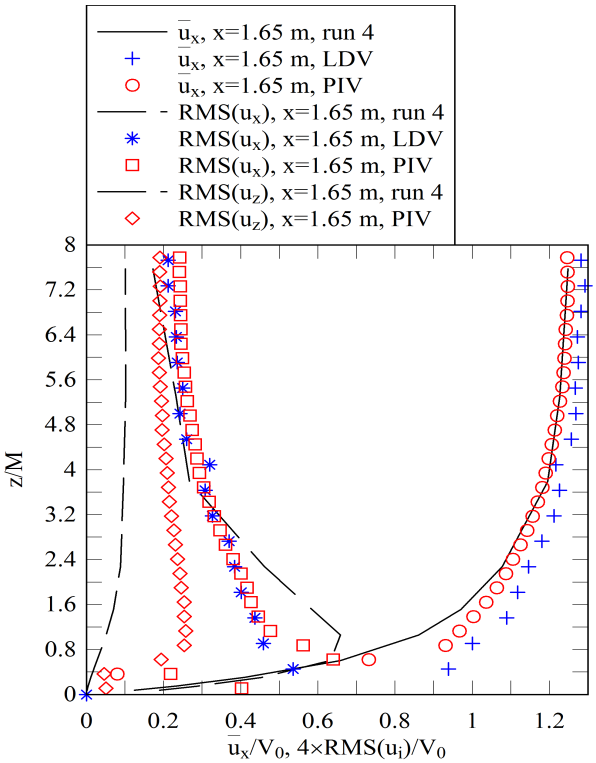

(c) Half of the vertical profile at $x = 1.65$ m and $y = 0.05$ m

Figure V.10: Dimensionless profile of the mean velocity and RMS velocity. Comparison between numerical results from run 4 and experimental measurements (Caplain and Reungoat, 2013)

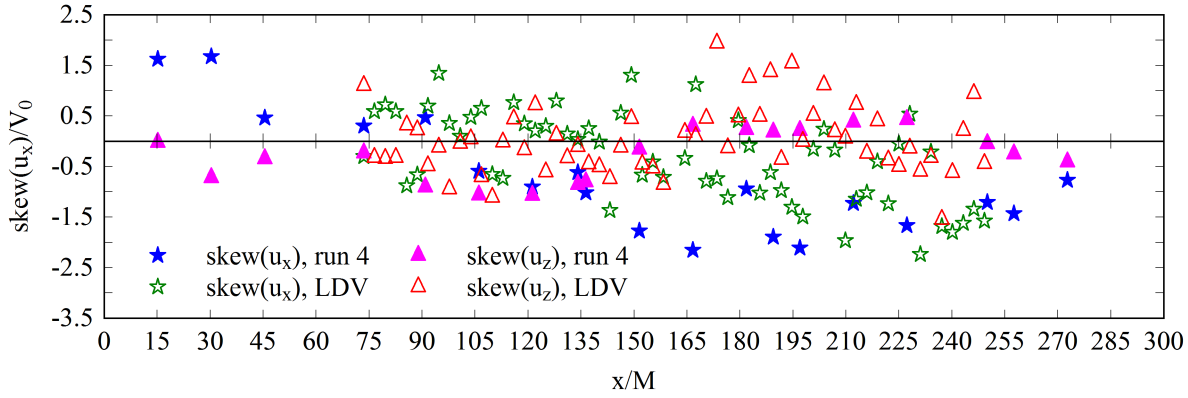

(a) Longitudinal and vertical velocity skewness along the x-axis

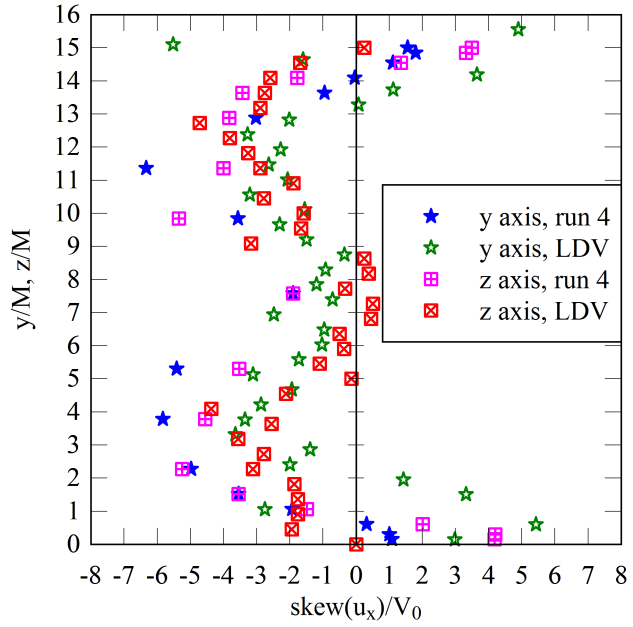

(b) Half of the vertical profile at $x \approx 0.9$ m and $y = 0.05$ m

Figure V.11: Dimensionless velocity skewness profile. Comparison between run 4 results and LDV measurements (Caplain and Reungoat, 2013)

size of the tangential meshes (Δ_y and Δ_z) on the channel centreline were half the size of the experimental grid mesh, potentially inducing some filtering of the turbulence. Overall, the numerical results were in agreement with the experimental data.
The SEM will be used to create a turbulent steady flow prior the generation of the bore since the ability of the method to recreate a coherent turbulence was verified.

V.4 Two dimensional propagation of undular positive surges

V.4.1 Presentation

Undular positive surges were reproduced by two dimensional numerical simulations based upon simplified conditions of experiments. In the experiments (Chanson, 2010a,b), the bore propagated over an initially steady turbulent flow. In the numerical model, the bore propagated over a flow without initial turbulence and three dimensional effects were omitted. A validation of the simulated bore is performed for the free surface and the velocity evolution.

V.4.2 Experimental flow conditions

Several conditions of positive surge were numerically simulated based on experiments. Table V.3 reports the different flow conditions used. The experiments took place in the University of Queensland and were conducted by Chanson (2008, 2009a, 2010a,b). The channel characteristics and instrumentations used were similar to the one presented in section III.3, except that the channel was completely horizontal and the channel bed was smooth (PVC bed). The instruments (ADMs and ADV) were located at other locations but a similar instrumentation as presented in section III.3 was used. For some experiments (Chanson, 2010a) a radial gate was located downstream the tainter gate to control the steady flow conditions. The unsteady flow was controlled by the manual closure of a tainter gate similar to the one illustrated in Figure III.5.

V.4.3 Two dimensional numerical configurations

The channel was modelled as a 10 m long rectangle with a 0.5 m height. Herein, x is the longitudinal distance from the gate positive upstream and z is the distance from the bed positive upward. The steady flow was initiated by a water rectangle with an height d_0 and a velocity $-V_0$ at all depths (Table V.3). Above the water, the air was set with a zero velocity. The pressure was initialised as hydrostatic. The gate was modelled by a vertical wall set on the

Table V.3: Experimental flow conditions reproduced by the numerical simulation and type of unsteady flows generated by the experiments and the simulations

Experimental data set	d_0	V_0	h_g	Fr	U_b	Bore type	Gate type	Position of reference
	m	m.s^{-1}	m		m.s^{-1}		m	
Chanson (2010a), 090429_938-939	0.199	0.189	0	1.08	1.32	Undular	Radial gate, tainter gate	7.15
Chanson (2010a), 090427_921-927	0.165	0.230	0	1.13	1.21			
Chanson (2010b), 080422	0.1385	0.830	0.1	1.17	0.553	Undular	Only tainter gate	6.15

Note: V_0 is the flow velocity positive downstream, d_0 is the initial water depth, U_b is the bore celerity, h_g is the gate opening of the downstream boundary and Fr is the bore Froude number

domain boundary instantaneously appearing at the beginning of the simulation at $x = 0$. In order to reproduce the partial opening beneath the experimental gate, a Neumann condition was set from $z = 0$ to h_g at the downstream vertical boundary to let the stream flow freely out of the domain. The boundary conditions of the numerical domain was a no slip condition on the bed, a Neumann condition on the top of the domain coupled with an absorption layer from 0.35 to 0.5 m in order to damp the influence of the Neumann condition. The Neumann condition let the flow come freely in and out of the domain. This can result in spurious conditions where the flow goes in or out of the domain with an overestimated velocity over a small number of meshes. It was observed for some simulations that an absorption layer reduced non physical effects of the Neumann condition. The layer was set using a lower permeability than the air. The water inflow was injected in the domain at a velocity $-V_0$ on the channel inlet from $z = 0$ to d_0 ($x = 10$ m). Figure V.12 shows the numerical domain with V_0, d_0 and h_g as initial flow condition. The domain was discretised by $5\,000 \times 500$ meshes with a constant spacing on the longitudinal direction and an exponentially increasing spacing on the vertical direction starting with $\Delta_{z,\min} = 0.1$ mm. The water and air characteristics were $\rho_w = 1000$ kg.m^{-3}, $\rho_a = 1.1768$ kg.m^{-3}, $\mu_w = 10^{-3}$ kg.m^{-1}.s^{-1} and $\mu_a = 1.85 \times 10^{-5}$ kg.m^{-1}.s^{-1} for the water and air densities and viscosities respectively. The gravity acceleration was set with the gravity acceleration of Brisbane, Australia, $g_z = 9.80$ m.s^{-2}. The time steps were calculated to respect a CFL condition inferior to 0.1.

The simulations were run as LES using the MS model. The interface was modelled with a VOF-PLIC scheme using 36 processors. For cases with a fully closed gate, approximately 20 000 iterations were necessary and for the configuration with a partially closed gate 250 000 iterations were performed for the bore front to travel across the entire channel.

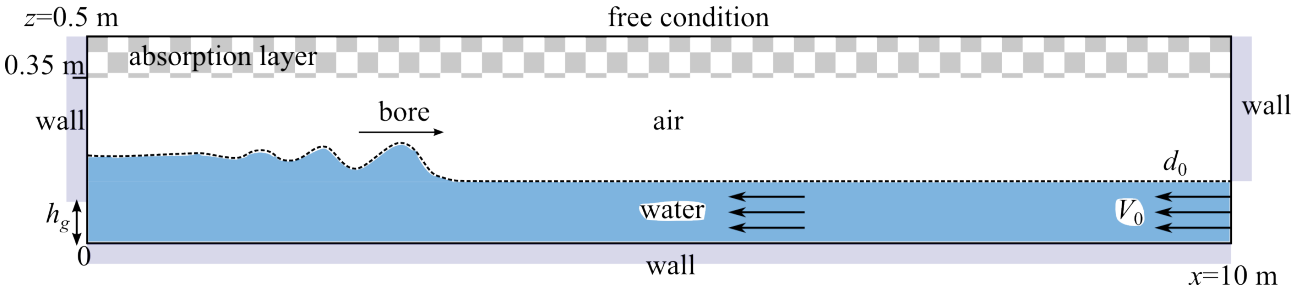

Figure V.12: Numerical domain configuration with an undular bore propagating against the steady flow

Note that the simulations were only two dimensional and did not reproduce the turbulent boundary layer present next to the channel bed and lateral wall of the experiments.

V.4.4 Bores generated with a fully closed gate

V.4.4.1 Free surface comparisons

At the beginning of the simulations, the water directly accumulated against the fully closed downstream wall at $x = 0$. The water started to rise against the wall and the bore propagated away from the wall taking the shape of an undular bore. Figure V.13 presents the dimensionless time evolution of the free surface for bores generated with two different steady flow conditions with comparisons between the numerical simulations, the experiments (Chanson, 2010a) and equation (II.6).

The free surface time evolutions of the numerical simulations followed a shape similar to the free surface measurements (Figure V.13). The free surface time evolutions showed good agreements between the numerical simulations and both experiments and equation (II.6). Table V.4 presents some basics bore characteristics and free surface patterns of the first undulation. The free surface surface characteristics are illustrated in Figure IV.13. An error inferior to 1.5% was observed for the conjugated depth d_b (Table V.4). For the numerical simulation, the bore celerities U_b were similar to the celerity measured during experiments at $x = 7.15$ m (Chanson, 2010a) and to the bore celerity given by equation (II.5) (Table V.4). The bore celerity was computed with the passage time of the first wave crests between three longitudinal positions. The bore free surface stayed synchronised during the propagation and the maximum and minimum of the free surface evolution ($d_{\max}$ and $d_{\min}$) were found at similar instant (Figure V.13). Overall, all characteristics of the first undulation were in agreement with the experimental data and differences of less than 2% of error were observed except for the wave amplitude (Table V.4). Note that, in Figure V.13, the experimental data were synchronised with the numerical simulation maximum at $x = 7.15$ m only, as there was no recording of the exact instant the manual gate closure.

Table V.4: Bore free surface patterns and characteristics for an undular bore generated with a completely closed gate at $x = 7.15$ m

Data	Fr	U_b m.s^{-1}	d_0 m	d_{max}/d_0	d_{min}/d_0	d_b/d_0	a_w/d_0	$T_w U_b/d_0$
Chanson (2010a) 080422	1.08	1.32	0.199	1.206	1.096	1.146	0.055	7.761
Equations (II.5) and (II.6)	1.10	1.35	0.199	/	/	1.141	/	/
Num. sim., rad2D08	1.10	1.34	0.199	1.221	1.091	1.151	0.065	7.676
Chanson (2010a) 080422	1.13	1.21	0.165	1.303	1.097	1.200	0.103	8.067
Equations (II.5) and (II.6)	1.14	1.22	0.165	/	/	1.188	/	/
Num. sim., rad2D13	1.14	1.23	0.165	1.327	1.097	1.206	0.115	7.901

Note: a_w and T_w are the wave amplitude and the wave period respectively, Num. sim.: Numerical simulation

V.4.4.2 Velocity comparisons

As the undular bores propagated, the longitudinal flow velocity suddenly decelerated as the water rose for measurements at a fixed x. Beneath the crest, the flow changed direction at all measured depths for the experiments and in the entire water column for the simulations. After the first crest and beneath the wave troughs, the flow velocity changed direction and flowed downstream in almost the whole water column. Beneath the secondary oscillations, the longitudinal velocity was oscillating in synchronisation with the free surface in a similar way than the first wave crest and trough. Figures V.14 and V.15 compare the dimensionless flow velocity evolution at $x = 7.15$ m between the experiments (Chanson, 2010a) and the numerical simulations for the two flow configurations used with a completely closed gate. The experimental velocity measurements are presented with a moving average over 49 points (0.245 s) to display the data trend. Additional data comparisons are presented in Appendix C.

The longitudinal velocity of the numerical data followed a trend similar to the experimental data. A good agreement was found between the simulated longitudinal velocities and the experimental data close to the bed (Figure V.15a). Elsewhere, differences were noticeable particularly for the maximum flow inversion and after the first wave trough (Figures V.14a, V.14c and V.15c). The discrepancies might possibly be linked with the absence of turbulence in the idealised initial numerical flow conditions of the simulation. They might also be linked with effects of the wake of the ADV on the reversing flow as many high frequency fluctuations

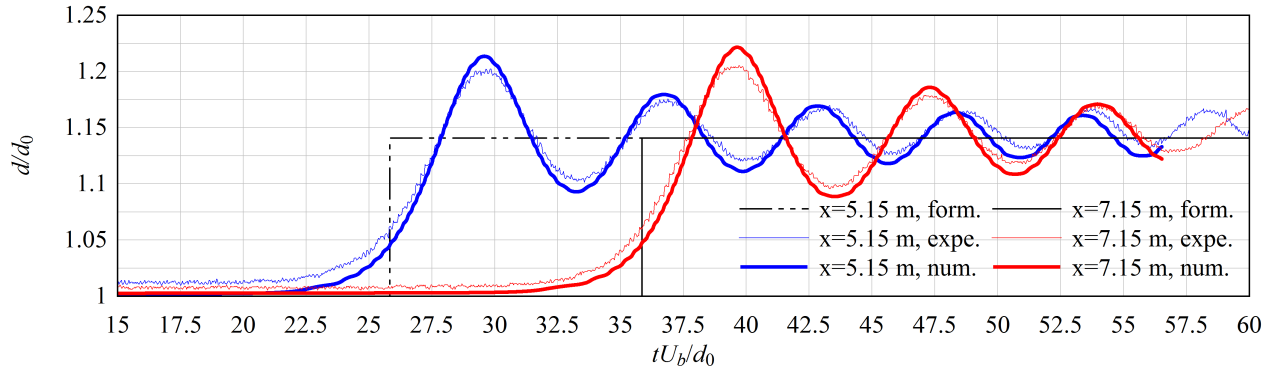

(a) Simulation rad2D08, bore Froude number $Fr = 1.10$

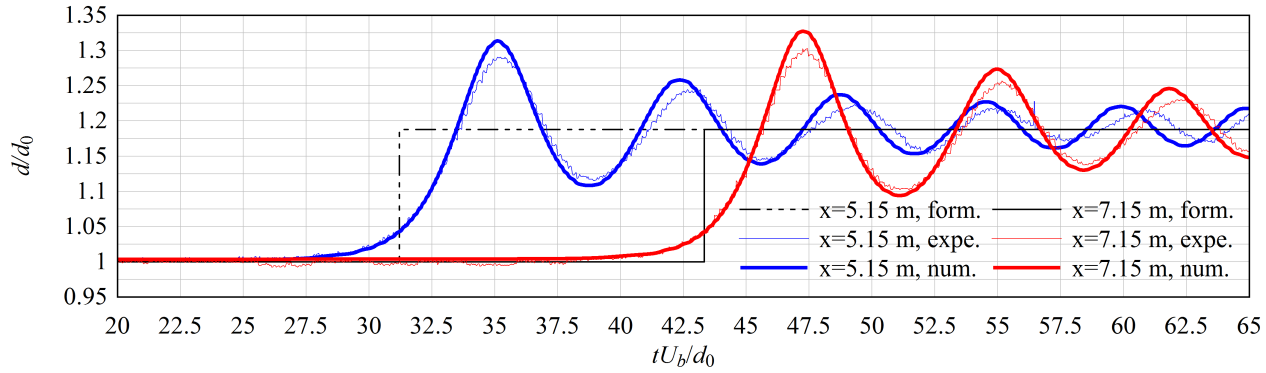

(b) Simulation rad2D13, bore Froude number $Fr = 1.14$

Figure V.13: Dimensionless free surface time evolutions for undular bores with a completely closed gate. Comparisons between numerical simulations (num.), experimental data (Chanson, 2010a) (expe.) and equation (II.6) (form.)

were observed on the experimental measurements and effects also mentioned in experiments presented in section IV.4.1. The global longitudinal velocity evolution beneath the crests and the troughs shared a similar tendency. The longitudinal velocity tended to flow upstream and downstream beneath the crests and troughs respectively with an overall convergence toward $u_x = 0$ as estimated analytically (section II.3.3).

The vertical velocity data oscillated also in synchronisation with the free surface. The simulated vertical velocity was positive when the water level increased and negative when the water level decreased as predicted by ideal fluid flow considerations. Close to the bed, the vertical velocity evolution showed small amplitude variation. Note that the channel bed is a streamline where the velocity is zero. The vertical velocity data close the free surface had larger amplitude oscillations (Figures V.14b, V.14d, V.15b and V.15d). Close to the bed, the numerical vertical velocity was small in agreement with experiments (Figures V.14b and V.15b). Close to the initial free surface d_0, some agreements were found between the simulations and the experiments

(Chanson, 2010a) with similar maximum and minimum values during the undulations.

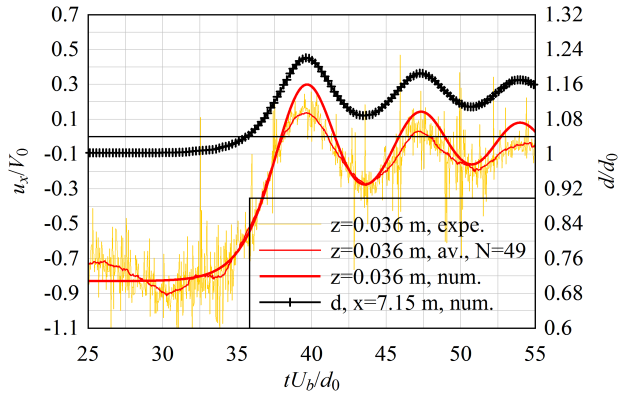

(a) Longitudinal velocity at $z/d_0 = 0.181$

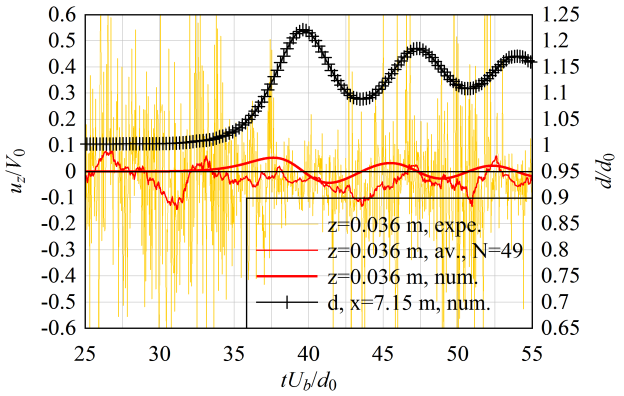

(b) Vertical velocity at $z/d_0 = 0.181$

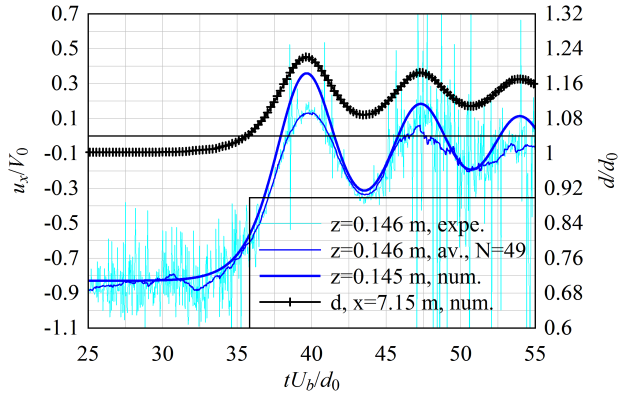

(c) Longitudinal velocity at $z/d_0 = 0.734$

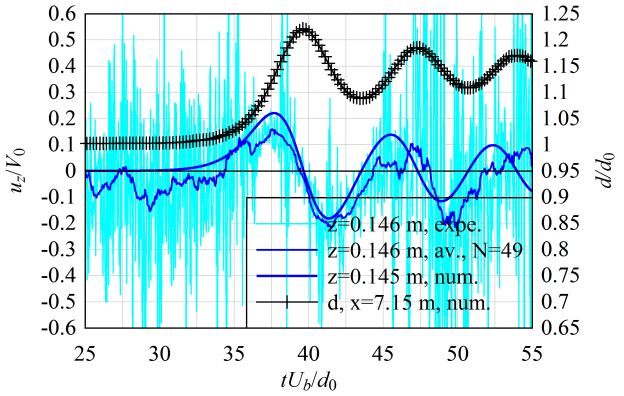

(d) Vertical velocity at $z/d_0 = 0.734$

Figure V.14: Dimensionless time evolutions of the velocity at two different elevations with the free surface evolution at $x = 7.15$ m for the simulation rad2D08. Comparison between numerical simulation and experiments (Chanson, 2010a)

V.4.5 Bore generated with a partially open gate

V.4.5.1 Free surface comparisons

This case was performed to validate the methods when the bore was generated with a partially open downstream boundary. Herein, the gate is partially open with $h_g = 0.1$ m, therefore the equation (II.6) can no longer apply and the numerical data were only compared to experimental data which perform the experiment with the same gate opening (Chanson, 2010b). When the simulation started, the water accumulated against the door with a gentle splash. The water propagated away from the door, with a small roller during the first metre and transformed into an undular bore. For both the experiment and the numerical simulation, the bore was undular

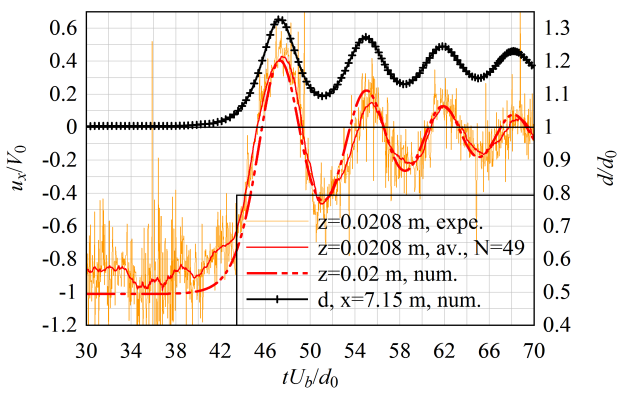

(a) Longitudinal velocity at $z/d_0 = 0.126$

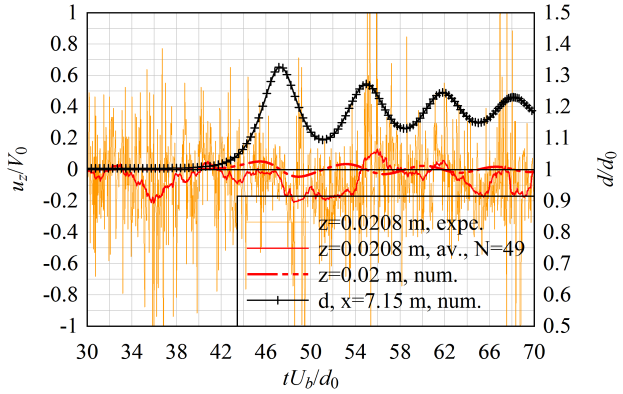

(b) Vertical velocity at $z/d_0 = 0.126$

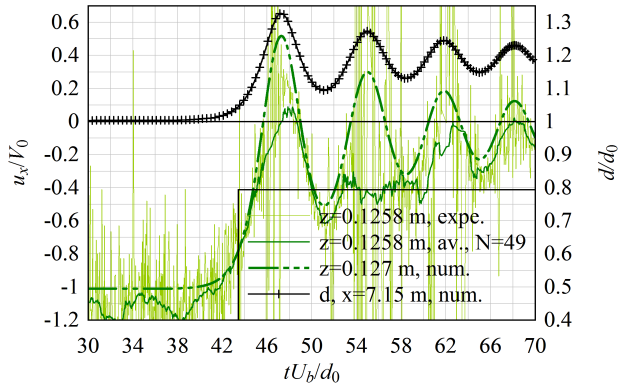

(c) Longitudinal velocity at $z/d_0 = 0.762$

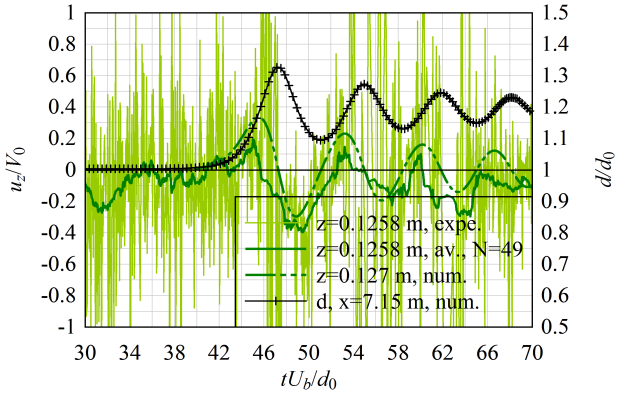

(d) Vertical velocity at $z/d_0 = 0.762$

Figure V.15: Dimensionless time evolutions of the velocity at two different elevations with the free surface evolution at $x = 7.15$ m for the simulation rad2D13. Comparison between numerical simulation and experiments (Chanson, 2010a)

at the reference location $x = 6.15$ m. Figure V.16 presents comparisons of the dimensionless free surface time evolution between the numerical simulation and the experiments (Chanson, 2010b). Note that, for the experiment, the water depth was not parallel to the channel bed since no radial gate was used downstream the channel moreover the ADV could have a significant effect on the water depth as mentioned in section IV.4.1 and detailed by Simon and Chanson (2013, p. 100). This might induce variations of bore celerity as the bore propagated away from the gate. For the numerical simulation, the water depth was parallel to the bed at all longitudinal positions. Despite this difference, the global trend of the simulated bore free surface was similar to the experimental free surface data. A de-synchronisation of the crest passage was observed as the bore propagates with a different celerity U_b (Figure V.16). The simulated bore propagated faster than the bore from experiment (Table V.5). Table V.5 presents some basic bore characteristics and free surface patterns of the first undulation. Differences ranging from

4% for the wave trough (d_{min}/d_0) to 26% for the wave length (a_w/d_0) were observed between models. Those discrepancies can be partially explained by significant differences in initial flow conditions as well as the use of a two dimensional numerical simulation.

Table V.5: Bore free surface patterns and characteristics for an undular bore generated with a partially closed gate at $x = 6.15$ m

Data	Fr	U_b m.s^{-1}	d_0 m	d_{max}/d_0	d_{min}/d_0	d_b/d_0	a_w/d_0	T_wU_b/d_0
Chanson (2010b) 080422	1.17	0.553	0.1385	1.408	1.090	1.242	0.159	8.025
Num. sim., ond2D17	1.25	0.625	0.1385	1.502	1.134	1.314	0.181	7.681

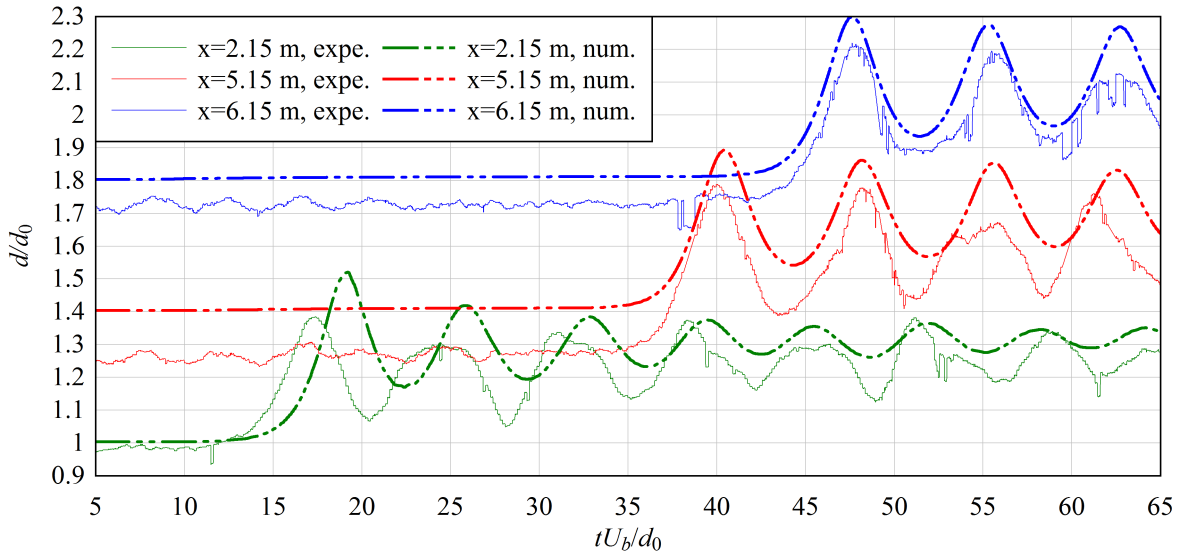

Figure V.16: Dimensionless free surface time evolutions for an undular bore. Comparison between numerical simulation and experiments (Chanson, 2010b). The curves for measurements at different longitudinal position are off-set vertically to one another by 0.4

V.4.5.2 Velocity comparisons

For this case (Chanson, 2010b), the initial steady flow velocity was $V_0 = 0.83$ m.s^{-1}, significantly larger than for the cases in the previous section (V.4.4). The free surface evolution showed more differences than the case with a completely closed gate (section V.4.4.1).

Figure V.17 compares dimensionless flow velocity evolution at $x = 6.15$ m between the experiments (Chanson, 2010b) and the numerical simulation. Additional data comparisons are presented in Appendix C. At a fixed longitudinal position, the longitudinal velocity suddenly decreased as the water level rose. The flow velocity globally decreased and accelerated as the

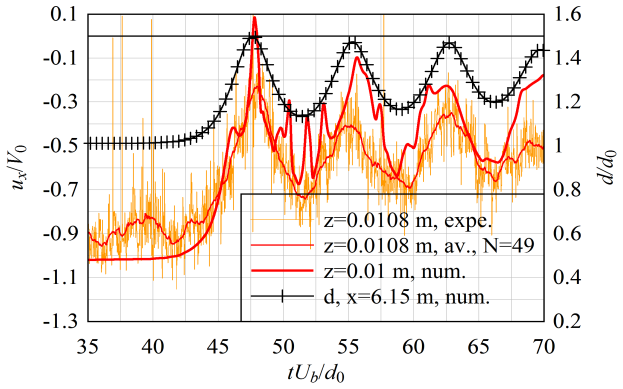

(a) Longitudinal velocity at $z/d_0 = 0.078$

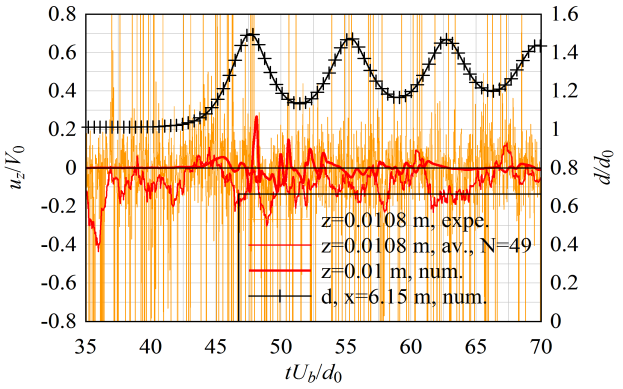

(b) Vertical velocity at $z/d_0 = 0.078$

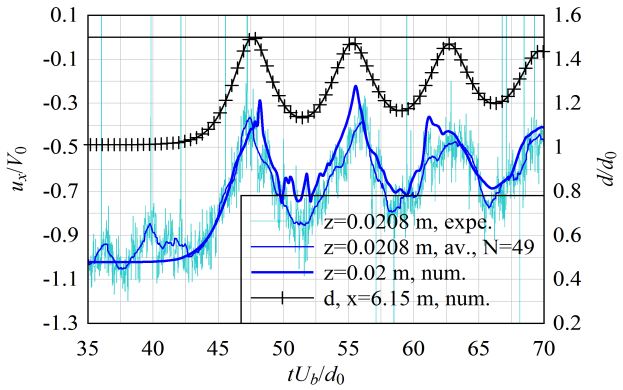

(c) Longitudinal velocity at $z/d_0 = 0.150$

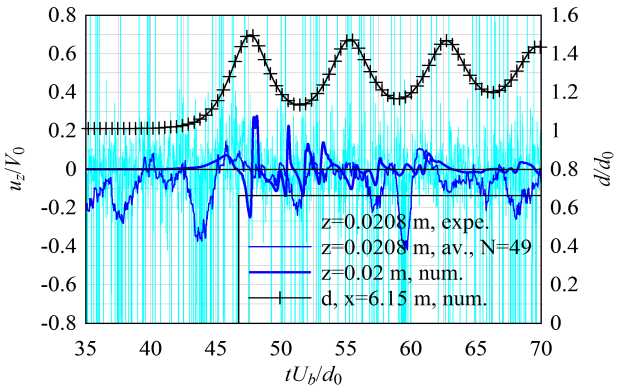

(d) Vertical velocity at $z/d_0 = 0.150$

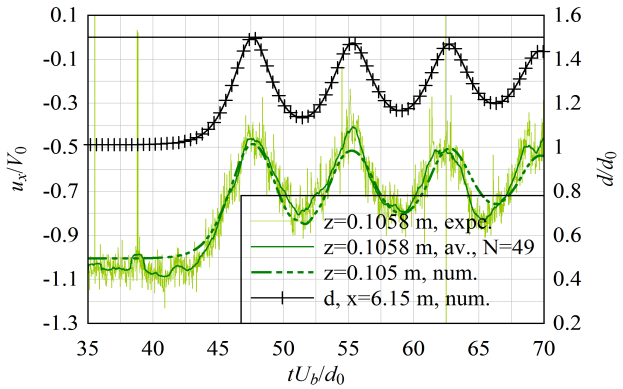

(e) Longitudinal velocity at $z/d_0 = 0.764$

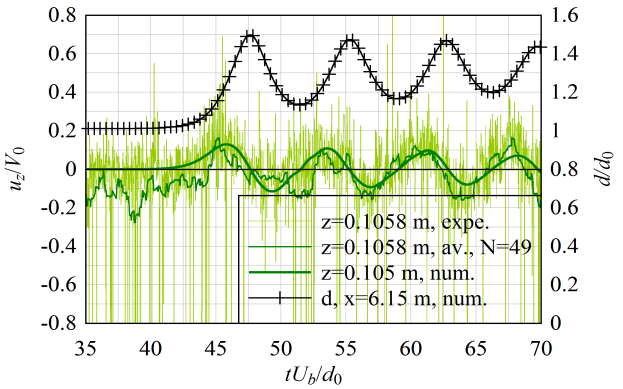

(f) Vertical velocity at $z/d_0 = 0.764$

Figure V.17: Dimensionless time evolutions of the velocity at two different elevations with the free surface evolution at $x = 6.15$ m for a numerical bore with a Froude number $Fr = 1.25$. Comparison between numerical simulation and experiment (Chanson, 2010b)

water level increased and decreased respectively. The trend was similar for numerical simulation and experiments with a good agreement in terms of velocity signals (Figure V.17). The longitudinal velocity evolutions were similar, with similar maximum and minimum values beneath the wave crests and troughs respectively. Before and after the maximal longitudinal velocity value beneath crest, the time evolution of the velocity was linear giving a triangle waveform shape to the velocity plot for both the numerical and experimental data (Figures V.17a and V.17c). Close to the free surface, the time evolution of the longitudinal velocity was more smooth and undulant (Figure V.17e). However, close to the bed, fluctuations of the velocity appeared for the numerical simulation. The appearance of fluctuations will be discussed in section VI.2. Note that close to the bed ($z < 0.015$ m), the longitudinal velocity changed direction, creating a transient recirculation (Figure V.17a). It was not observed for the experimental study but the ADV unit could not measure beneath $z = 5.8$ mm and the measurements were performed above $z = 10.8$ mm (Chanson, 2010b).
The vertical velocity tended to be positive when the water level rose and negative when the water level decreased. This trend was similar between the numerical simulation and the experiment (Figure V.17f). Close to the bed (Figures V.17b and V.17d), this tendency was less visible and fluctuations of the vertical velocity was observed for the numerical simulation as fluctuations also appear on the longitudinal velocity signal.
Overall, the two dimensional numerical simulation was in agreement with the experiments (Chanson, 2010b) despite some difference in initial steady conditions and free surface results.

V.4.6 Concluding remark

Overall, the comparisons between simulations and experiments showed some agreement considering the two dimensional nature of simulations. For the simulation modelling the experiment with a controlled flow and a gate fully closed (Chanson, 2010a), the free surface and flow velocity were modelled correctly with a similar flow evolution. For the simulation modelling an experiment with a gate partially close (Chanson, 2010b), some differences were observed for the free surface whereas the flow velocity was in agreement with the experimental data. Some of the discrepancies between simulations and experiments were probably due to the simulation being two dimensional and the initial flow prior bore generation being not turbulent. Other parameters, such as the time of gate closing and the gate angle, imperfections of the channel such as water leaks and joints were not modelled and could lead to further discrepancies. The experimental probe was also believed to have an impact on the flow. Three dimensional simulations, with and without turbulent steady flow, need to be performed in order to see the interactions of bores on more realistic initial conditions.

V.5 Three dimensional modelisation of undular positive surges

V.5.1 Presentation and numerical configurations

Three dimensional simulations were performed and compared to experiments (Chanson, 2010a,b). Comparisons were also performed for two dimensional simulations (section V.4). This gave an opportunity to compare some performances between two dimensional and three dimensional models. The description and basic results of the simulations are presented in section VI.3. The domain was modelled as a 10 m long, 0.5 m high and wide rectangular and horizontal channel discretised by $2000 \times 250 \times 100$ meshes (50×10^6 meshes). The mesh sizes were constant along the longitudinal axis ($\Delta_x = 5$ mm), exponentially increasing from the bed to the top in the vertical direction with $\Delta_{z,\min} = 0.25$ mm and increasing towards the channel centre on the transversal axis starting with $\Delta_y = 0.5$ mm on the sidewalls. Herein, y is the transverse distance from the right sidewall looking upstream. The simulations were all initiated with a parallelepiped of water filling the bottom of the channel with a heigth d_0, a water velocity $-V_0$ and a hydrostatic pressure distribution. Table V.6 presents the different configurations simulated. A no-slip condition was set on the lateral walls and the bed. The generation of undular bores was controlled by setting a Neumann condition from $z = 0$ to h_g at $x = 0$ and a no slip condition above h_g. A Neumann condition was set on the top of the domain, between $z = 0.35$ to 0.5 m (Figure V.12), with an absorption layer similarly to the two dimensional simulation in section V.4.3. The absorption layer was modelled by changing the domain permeability. For the inflow condition at $x = 10$ m, either a boundary condition injecting water at a velocity $-V_0$ or a turbulent inflow condition was set using the SEM (section III.4.2.6). The SEM was initialised with the mean and fluctuation velocity values at $x = 6.15$ m and 7.15 m given by experiments (Chanson, 2010a,b). The number of eddies was set with $N = 1000$ and with their size with $\boldsymbol{\sigma} = 0.02$ m.

The simulations with the SEM started to run without closing the downstream gate in order to let the turbulence propagates in the domain. The simulations without the SEM were run with the gate closed from the start of the simulation. The simulations were run with 640 processors. The steady flow simulations with the SEM were run for 10 500 and 45 000 iterations prior to the gate closure corresponding to approximately 3 and 12 days of computations for the cases ond3DSEM and rad3DSEM respectively. The unsteady flows in the cases rad3D(SEM) were simulated for approximately 15 000 iterations and the cases ond3D(SEM) for 75 000 iterations. The time steps were dynamically calculated to insure a CFL condition inferior to 0.2. The simulations were stopped before the bore reached the upstream boundary.

The turbulence was modelled using a LES method with a MS model and the interface was tracked using a VOF-PLIC scheme similarly to the two dimensional simulations.

Table V.6: Initial configuration of the simulations, bores basic characteristics of the simulation and corresponding experiments

Simulation	d_0 m	V_0 m.s^{-1}	h_g m	Inflow condition	Bore type	Experiments
rad3D rad3DSEM	0.165	0.23	0	V_0 SEM	Undular	(Chanson, 2010a) 090427
ond3D ond3DSEM	0.1385	0.83	0.1	V_0 SEM	Undular	(Chanson, 2010b) 080422

V.5.2 Steady flow modelled using turbulent inflow with the SEM

For simulations rad3DSEM and ond3DSEM, the models were run without closing the gate at the downstream end of the domain until the turbulence generated by the SEM reached the end of the domain. A limitation was observed on the simulation of the steady flow conditions. When the turbulence reached the end of the domain, the numerical simulation became unstable with non physical tearing up of the free surface near the downstream boundary as well as solver errors. To avoid the simulations becoming unstable, the gate was closed (partially or completely depending on the case) to generate the positive surge. The steady flow properties could be analysed for only a short physical time, 7.5 s for the case ond3DSEM and 10 s for case rad3DSEM which is short to characterise the time averaged velocity and its fluctuations. The SEM was configured with extrapolated experimental data from the channel centreline (Chanson, 2010a,b). The profiles measured on the channel centreline were applied on the whole channel width without considering lateral walls effects. As a result, a small difference of inflow discharge was observed. For the simulation rad3DSEM, the flow was injected in the domain with a time averaged discharge of 0.0197 m^3.s^{-1} compared to a discharge 0.0190 m^3.s^{-1} for the experiment (Chanson, 2010a). For the simulation ond3DSEM, the water discharge was 0.0575 m^3.s^{-1} compared to a discharge 0.0578 m^3.s^{-1} for the experiment (Chanson, 2010b).
Figure V.18 presents a comparison of the mean velocity and its fluctuation for the numerical simulation and the experimental measurements (Chanson, 2010a,b).
For the simulation rad3DSEM (Figure V.18a), the longitudinal velocity followed closely the experimental data with an average error of 2.7%. However, the turbulent normal stresses were largely underestimated (Figure V.18a). Note that the value of the RMS for the experiment (Chanson, 2010a) were unusual and did not follow the decrease of the fluctuations with the distance from the bed as mentioned by Nezu and Nakagawa (1993) (also equation IV.3) or as

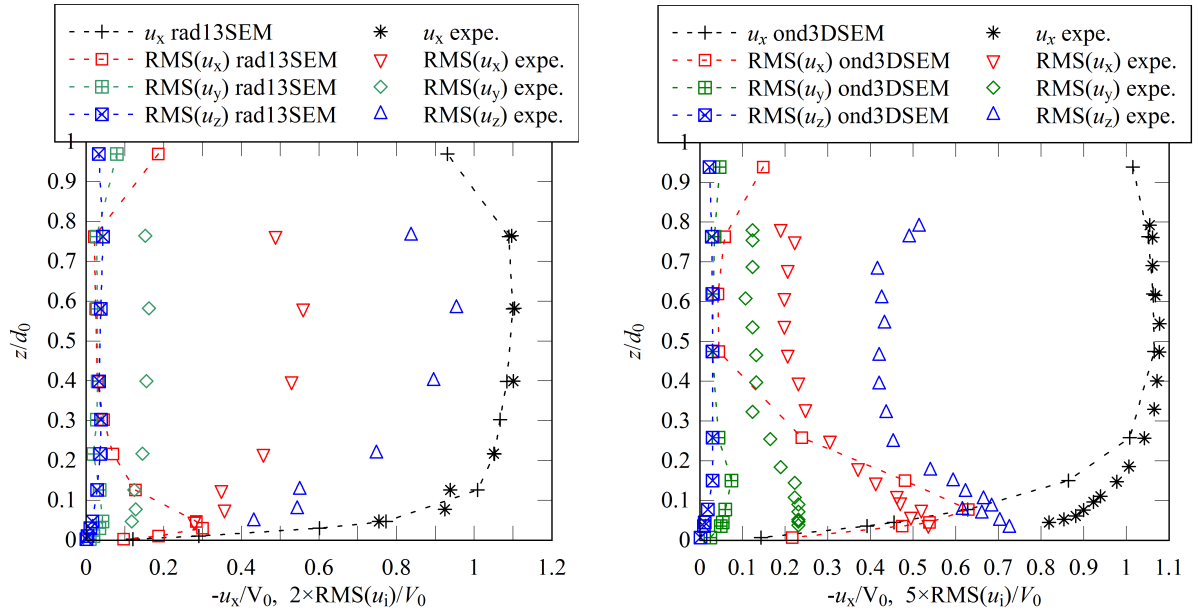

(a) $x = 7.15$ m, with experimental data (Chanson, 2010a)

(b) $x = 6.15$ m, experimental data (Chanson, 2010b)

Figure V.18: Steady flow condition, mean and RMS of the velocity generated using the SEM. Comparison with experiments

measured during the experiment of Chanson (2010b) and during the present study over a rough bed (section IV.2.3).

For the case ond3DSEM, the vertical velocity profile tended to underestimate the flow velocity close the bed, with an agreement on the maximal longitudinal fluctuation close to the bed (Figure V.18b). For $z/d_0 > 0.3$, the longitudinal velocity was in agreement with the experiment but the turbulent stress were underestimated. Globally, the transversal and vertical velocity fluctuations were underestimated by the numerical model compared to the experimental data (Figure V.18b).

The comparison can only be qualitative as the time for averaging the numerical data was short. Moreover, the size of the transversal meshes in the middle of the channel was large ($\Delta_{y,\max} = 18.1$ mm) and contributed in the filtering of the turbulent properties of the flow. Another limitation was the parameterisation of the SEM with inflow conditions measured at $x = 6.15$ m and $x = 7.15$ m from the gate and only on the channel centreline (Chanson, 2010a,b). Information on velocity fluctuations upstream of those locations would have helped a better parameterisation of the SEM.

Nonetheless, the steady flow was turbulent which gave the possibility to observe effects of bores on both turbulent and non-turbulent steady flow.

V.5.3 Bores generated by a fully closed gate

V.5.3.1 Free surface comparison

The free surface evolution and the bore characteristics were calculated and compared to experimental data measured on the channel centreline at several distances from the gate (Chanson, 2010a) and two dimensional simulation data (rad2D13). Figure V.19 present the dimensionless time evolution of bores free surface.

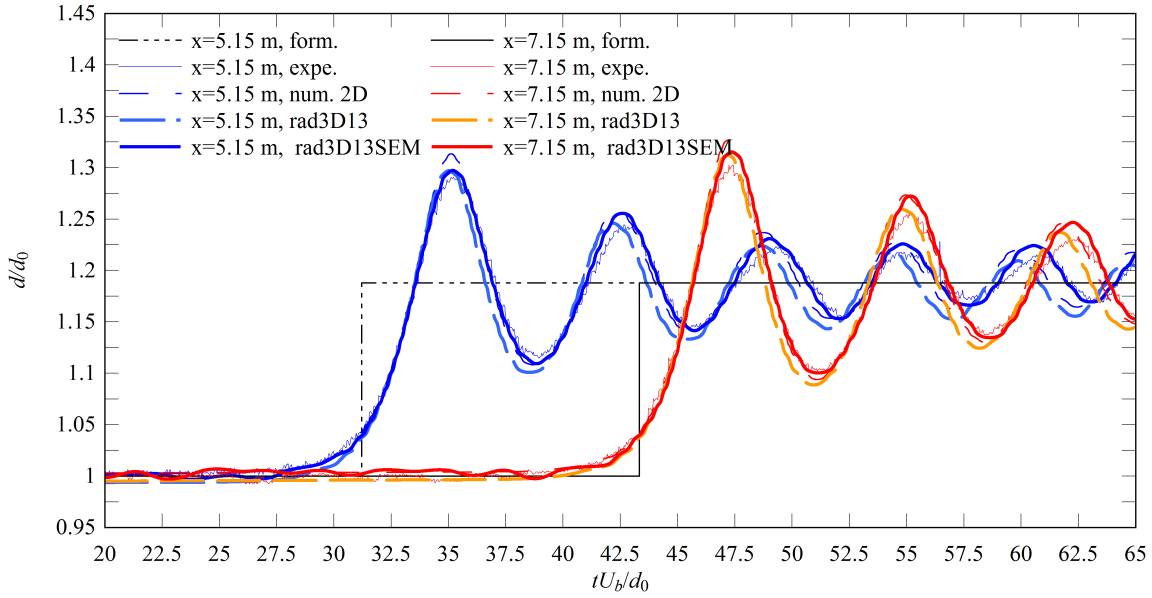

Figure V.19: Dimensionless free surface time evolutions for undular bores with a completely closed gate. Comparison between numerical simulations, experimental data (Chanson, 2010a) (expe.) and equations (II.5) and (II.6) (form.)

The bore passage was characterised by the sudden elevation of the water free surface. For simulations rad3D and rad3DSEM, the bore undulations aspects was mainly two dimensional with small cross waves on the sidewalls (detail in section VI.3). Note that section VI.3.2.1 presents a complete descriptions of the bore free surface evolution. The free surface time evolutions showed good agreements between the numerical simulations, experiments and equations (II.5) and (II.6) giving estimations for the bore celerity U_b and the bore conjugated depth d_b. Table V.7 presents some basics bore characteristics and free surface patterns of the first undulation. The free surface characteristics were illustrated in Figure IV.13. For both three dimensional simulations, the bore conjugated depth (d_b), the first undulation maximum (d_{max}) and the first undulation minimum (d_{min}) were within 2% of error with the experimental data (Chanson, 2010a). The wave length ($T_w U_b/d_0$) and wave amplitude (a_w) were simulated within 9% of error. The bore celerity (U_b) was also within 1% of error which showed the good synchronisation of the bore propagation (Figure V.19). A small difference in the bore Froude number

was found and might be attributed to the slightly different inflow discharge generated by the SEM (section V.5.2). Overall, the bore propagation and characteristics were in agreement with the experimental data (Chanson, 2010a) and also with the two dimensional simulation. Moreover, the aspect of the bore undulations was mainly two dimensional as described in section VI.3.2.1 and as mentioned by Chanson (2010a).
Note that, in Figure V.19, the experimental data were synchronised with the numerical simulation maximum at $x = 7.15$ m only, as there was no recording of the exact instant of the manual gate closure.

Table V.7: Bore free surface patterns and characteristics for undular bores generated with a completely closed gate at $x = 7.15$ m

Data	Fr	U_b m.s^{-1}	d_0 m	d_{max}/d_0	d_{min}/d_0	d_b/d_0	a_w/d_0	$T_w U_b/d_0$
Chanson, 2010a, 090427	1.13	1.21	0.165	1.303	1.097	1.200	0.103	8.067
Equations (II.5) and (II.6)	1.14	1.22	0.165	/	/	1.188	/	/
rad2D13	1.14	1.23	0.165	1.327	1.097	1.206	0.115	7.901
rad3D	1.14	1.22	0.165	1.312	1.091	1.176	0.112	7.634
rad3DSEM	1.15	1.22	0.165	1.315	1.103	1.194	0.107	7.321

V.5.3.2 Velocity comparisons

The data are compared to experimental measurements (Chanson, 2010a) realised on the channel centreline at $x = 7.15$ m from the gate at several elevations using an ADV with single run measurements. The numerical simulations recorded the flow evolution at the same locations than the ADV. Figures V.20 and V.21 present comparisons of the numerical and experimental data at two depths. The experimental velocity measurements are presented with a moving average over 49 points (0.245 s) to display the data trend. Additional data comparisons are presented in Appendix C.
Concerning the longitudinal velocity, it showed a similar evolution between the three dimensional simulations, the experiment and the two dimensional simulation. Beneath the first crest, the velocity reached a maximal value underestimated by approximately $0.16 \times V_0$ with the experimental data (Figure V.20a). The bore propagating against a steady turbulent flow (rad3DSEM) underestimated the most the velocity. Beneath the first crest, the velocity data were in agreement with the experimental data close to the bed. Close to the initial free surface the velocity data showed a difference of approximately $0.1 \times V_0$ with the experiments (Figure V.21a). A similar evolution was observed beneath the following crests and troughs with

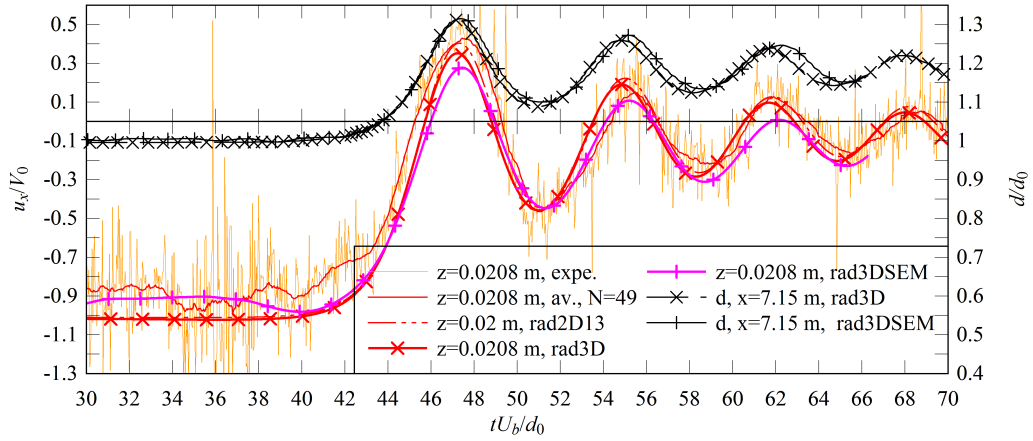

(a) Longitudinal component

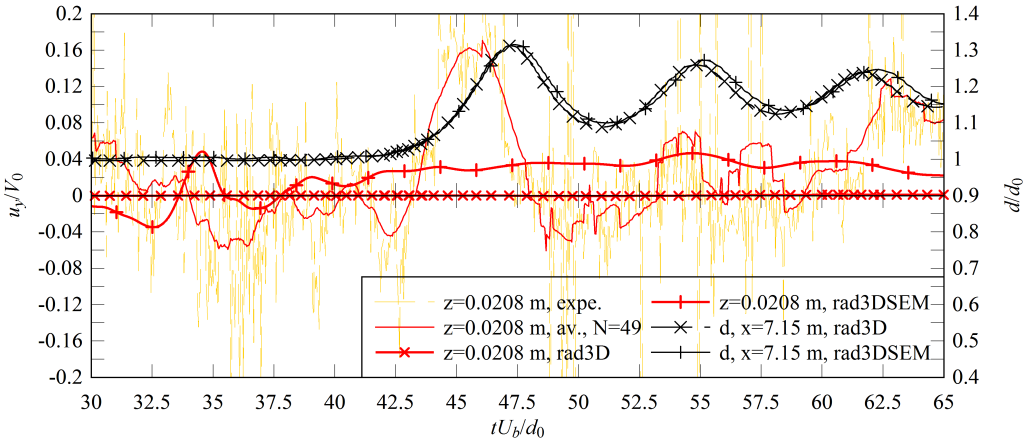

(b) Transversal component

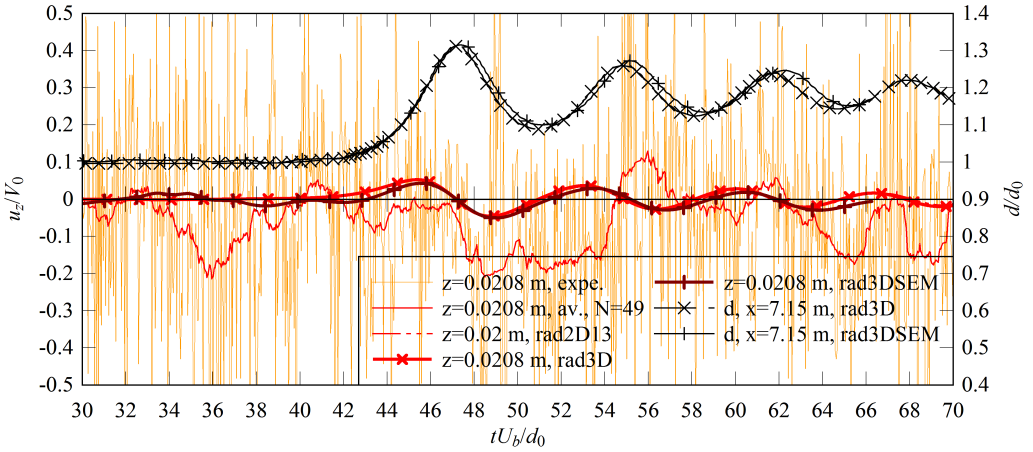

(c) Vertical component

Figure V.20: Dimensionless time evolutions of the velocity at $z/d_0 = 0.12$ with the free surface evolution at $x = 7.15$ m for rad3D and rad3DSEM. Comparison between numerical simulation and experiments (Chanson, 2010a)

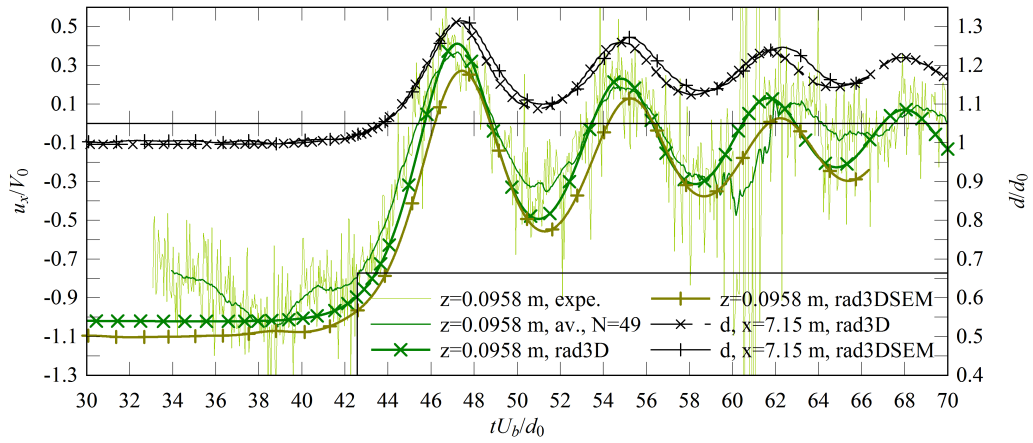

(a) Longitudinal component

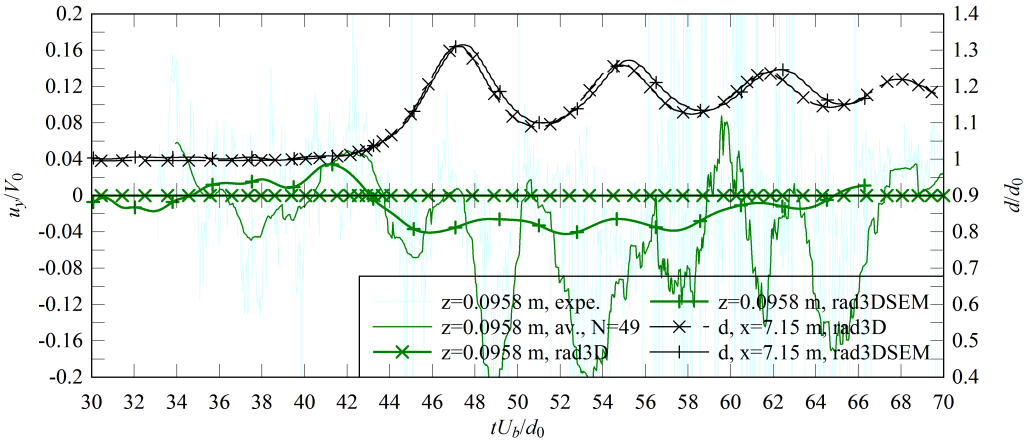

(b) Transversal component

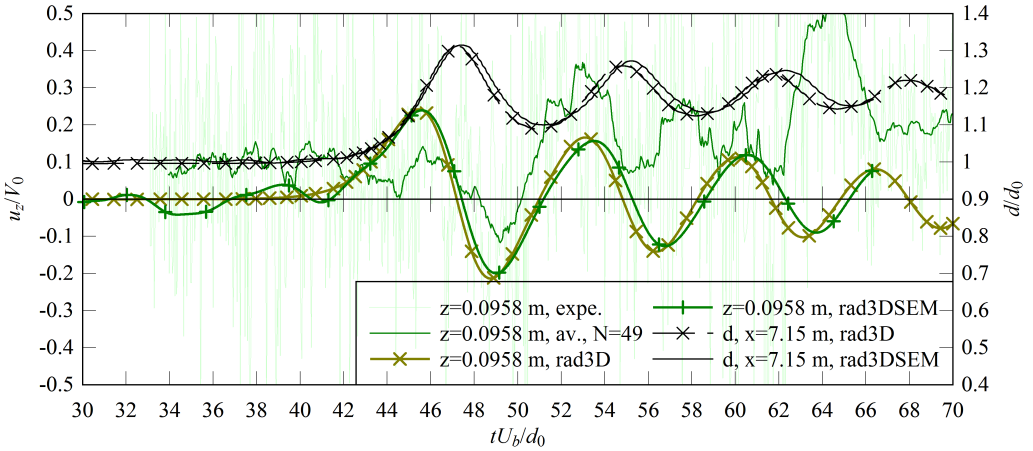

(c) Vertical component

Figure V.21: Dimensionless time evolutions of the velocity at $z/d_0 = 0.58$ with the free surface evolution at $x = 7.15$ m for rad3D and rad3DSEM. Comparison between numerical simulation and experiments (Chanson, 2010a)

a slight de-synchronisation of the crests and troughs with the experiment, as observed with the free surface. For the simulation rad3DSEM, the velocity signal recorded every time step on the channel centreline (Figure V.21) did not show fluctuations of the velocity whereas the observation of complete flow evolution (section VI.3.2.1) showed a complex three dimensional flow.

The transversal velocities were compared to the experimental data (Chanson, 2010a). For the simulation rad3D, the maximal variations were of order $10^{-4} \times V_0$ close to the bed (Figures V.20b and V.21b). No particular fluctuations of the transversal velocity were expected for the simulation rad3D since there was no initial turbulence in the flow and the data were on the channel centreline. On the other hand, the experimental data showed large fluctuations of the velocity up to $0.2 \times V_0$, whereas the transversal fluctuations for the simulation rad3DSEM were approximately $0.05 \times V_0$ (Figures V.20b and V.21b).

The longitudinal and vertical velocities from the numerical simulations showed an evolution in synchronisation with undulation of the free surface. u_z was positive and negative when the water level increased and decreased respectively. Close to the bed the vertical velocity oscillation amplitudes were small in agreement with the experiment (Figure V.20c). Near the initial free surface, some agreements were found for the vertical velocity with the experimental measurements with similar maximum and minimum values and oscillations in synchronisation (Figure V.21c). Concerning the longitudinal velocity for rad3D and rad3DSEM, the u_x evolutions were relatively similar and no significant fluctuation of u_x was observed. Several hypotheses can explain the absence of velocity fluctuations beneath the bore. The mesh discretisation associated with the LES might have contributed to filter the fluctuations. The SEM might require different parameters to recreate the turbulence. But, this would require more detailed experimental measurements and a simulation of the steady flow during a longer physical time. Finally, it could be a physical effect since the flow velocity alternated between negative and positive values and tended towards zero, thus decreasing the fluctuations. Note that this happened mainly on the channel centreline. Within 20 cm from the sidewalls, the flow seemed less homogeneous as described in section VI.3.2.1.

V.5.4 Bore generated by a partially open gate

V.5.4.1 Free surface comparisons

The free surface evolution was recorded on the channel centreline at several distances from the gate. The bore characteristics were calculated and compared to experimental data (Chanson, 2010b) and two dimensional simulation data (ond2D17). Figure V.22 presents comparisons of the dimensionless free surface time evolution between the numerical simulations and the

experiments (Chanson, 2010b). Table V.8 presents some basic bore characteristics and free surface patterns of the first undulation.

Table V.8: Bore free surface patterns and characteristics for undular bore generated with a partially closed gate at $x = 6.15$ m

Data	Fr	U_b m.s^{-1}	d_0 m	d_{max}/d_0	d_{min}/d_0	d_b/d_0	a_w/d_0	$T_w U_b/d_0$
(Chanson, 2010b) 080422	1.17	0.553	0.1385	1.408	1.090	1.242	0.159	8.025
ond2D17	1.25	0.625	0.1385	1.502	1.134	1.314	0.181	7.681
ond3D	1.25	0.626	0.1385	1.391	1.145	1.336	0.126	6.965
ond3DSEM	1.27	0.640	0.1385	1.414	1.177	1.300	0.117	8.230

As mentioned for the validation of the two dimensional simulation (section V.4.4), during the experiment, the water depth was not parallel to the channel bed since no radial gate was used downstream the channel to control the flow. Moreover, the ADV could have a significant effect on the water depth as mentioned in section IV.4.1 and detailed by Simon and Chanson (2013, p. 100). This might induce differences of bore celerity as the bore propagated away from the gate. Herein, the bore celerity and therefore, the bore Froude number was different between the three dimensional simulation and the experiment (Chanson, 2010b) with an error within 15% (Table V.8). Nevertheless, the three dimensional simulations were undular with cross waves on the secondary undulations similarly to the experiment (Chanson, 2010b). The cross waves intersected in the middle of the channel creating deformation of the secondary undulations (Figure V.22). Some deformations had even similar patterns between experiment (Chanson, 2010b) and numerical simulations (Figure V.22) for the simulation ond3DSEM with intersections of the cross waves at similar locations on the wave train. The two dimensional simulation ond2D17 showed relatively regular undulations and did not reproduce the effects of the cross waves. Note that the three dimensional simulation showed difference whether the steady flow was turbulent or not, as mentioned in section VI.3.2.2. Differences ranging from 0.5% for the wave crest (d_{max}/d_0) to 12% for the wave length (a_w/d_0) were observed between models. Those discrepancies could be partially explained by significant differences in initial flow conditions (water depth and flow velocity). Overall, the simulation ond3DSEM tended to give slightly better comparison with the experiment than simulation ond3D.

V.5.4.2 Velocity comparisons

The velocity data were recorded at $x = 6.15$ m from the gate on the channel centreline. Figures V.23, V.24 and V.25 present comparisons of the numerical and experimental data at

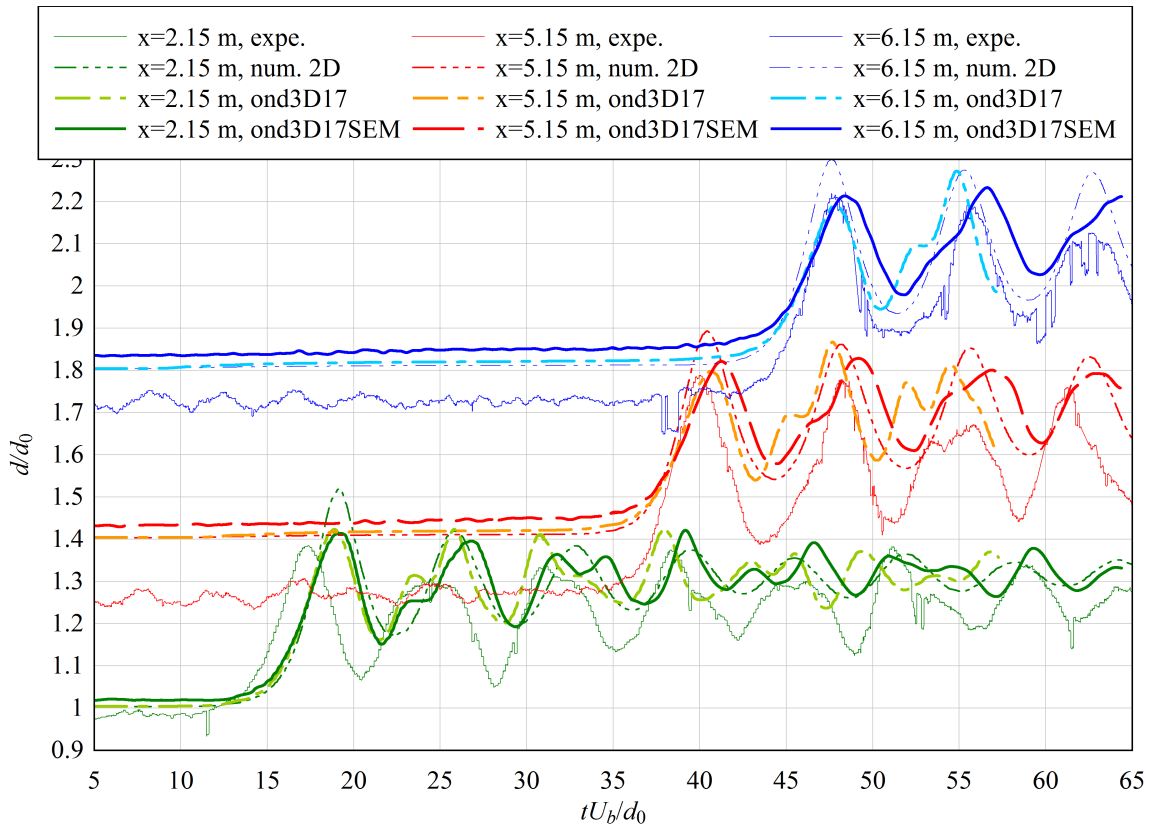

Figure V.22: Dimensionless free surface time evolutions for undular bores with a partially closed gate. Comparison between numerical simulations and experimental data (Chanson, 2010b) (expe.). Measurements at different positions are offset vertically by 0.4

three depths. The experimental velocity measurements are presented with a moving average over 49 points (0.245 s) to display the data trend of single run measurements. Additional data comparisons are presented in Appendix C.

The longitudinal velocity data from the experiments ond3D and ond3DSEM showed some similarities with the experiment with variations in synchronisation with the free surface. Close to the bed and beneath the first crest, the longitudinal velocity from the simulations showed some differences with the experiment. The simulation ond3DSEM had velocity values beneath the first crest different by approximately $0.7 \times V_0$ with the experiment (Figures V.23a and V.24a). Note that close to the bed and in the steady flow, the velocity was also underestimated by the simulation ond3DSEM (Figure V.18b). Beneath the crest and close to the bed, the data from the simulation ond3D were more in agreement with the experiment than the simulation ond3DSEM. Close to the bed, a velocity reversal was observed for the numerical simulation data that was not observed in the experimental data (Figures V.23a). For the measurement performed higher in the water column (Figure V.25a), the velocity time evolution were more in agreement with the experiment (Chanson, 2010b). The numerical data showed large discrepancies close to the bed for $z/d_0 < 0.2$ but a better agreement was found for $z/d_0 > 0.2$.

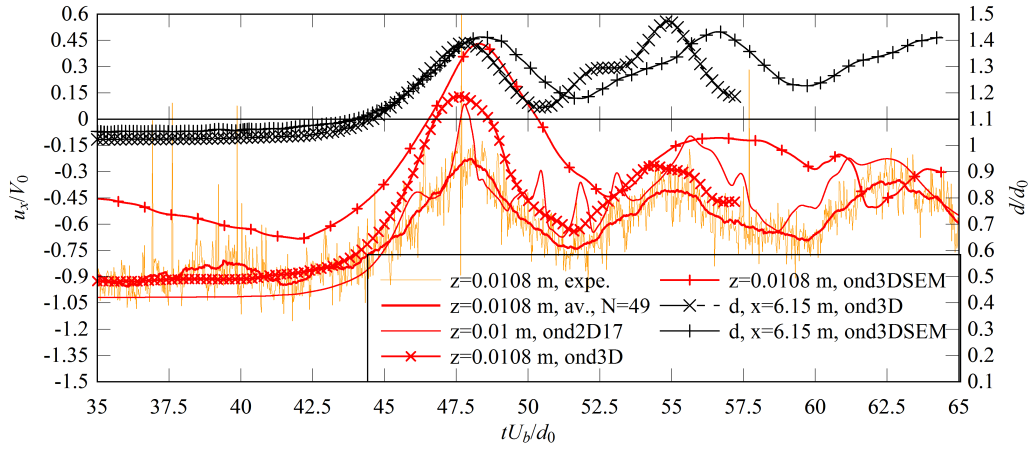

(a) Longitudinal component

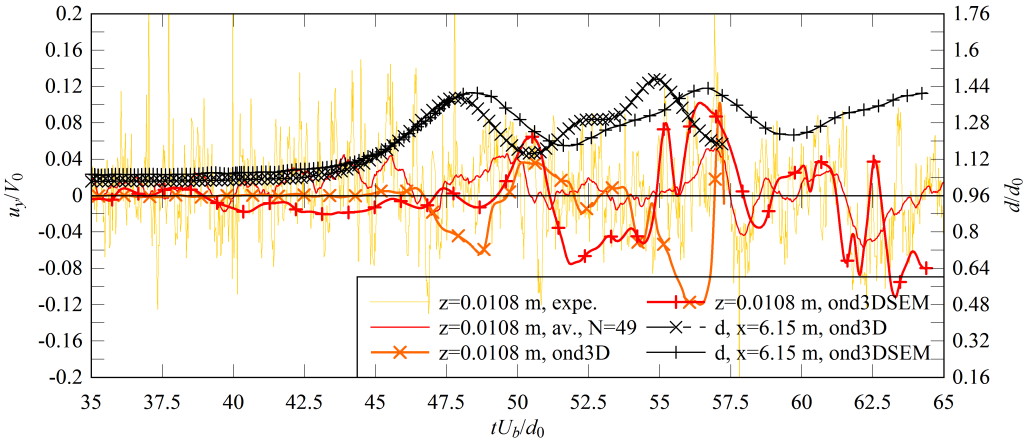

(b) Transversal component

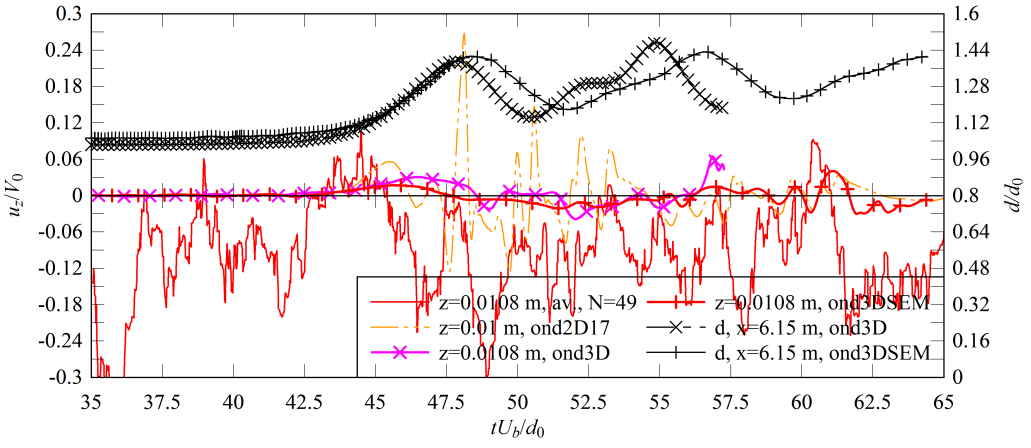

(c) Vertical component

Figure V.23: Dimensionless time evolutions of the velocity at $z/d_0 = 0.078$ with the free surface evolution at $x = 6.15$ m for simulations ond3D and ond3DSEM. Comparison between numerical simulations and experiment (Chanson, 2010b)

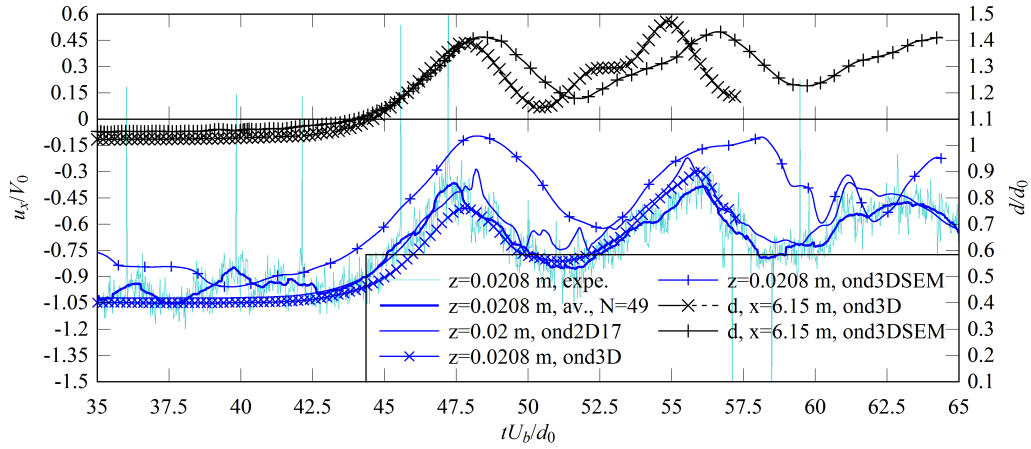

(a) Longitudinal component

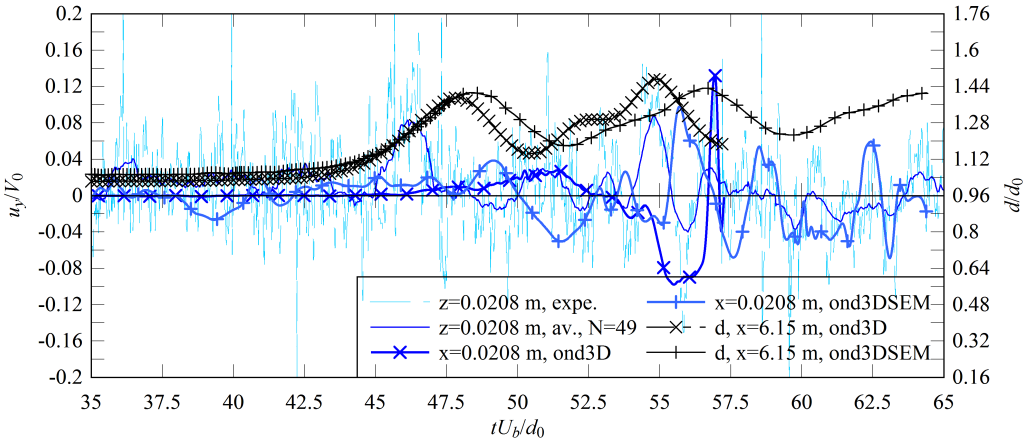

(b) Transversal component

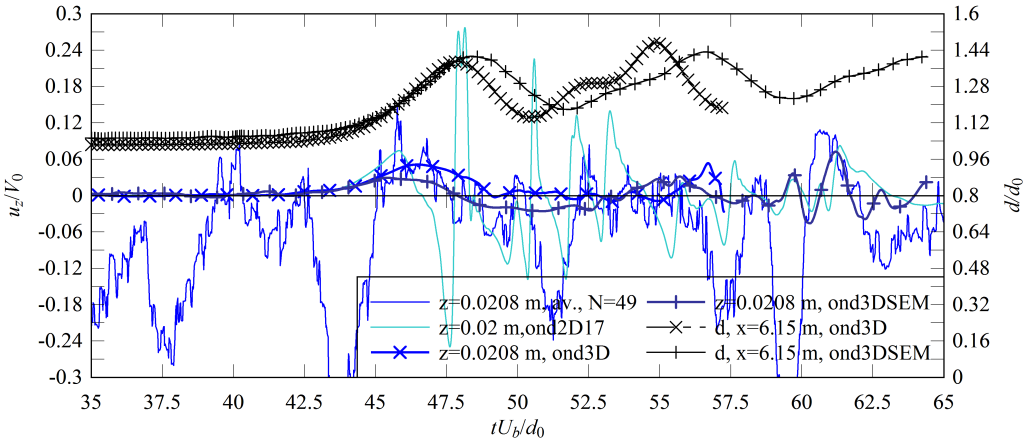

(c) Vertical component

Figure V.24: Dimensionless time evolutions of the velocity at $z/d_0 = 0.15$ with the free surface evolution at $x = 6.15$ m for simulations ond3D and ond3DSEM. Comparison between numerical simulations and experiment (Chanson, 2010b)

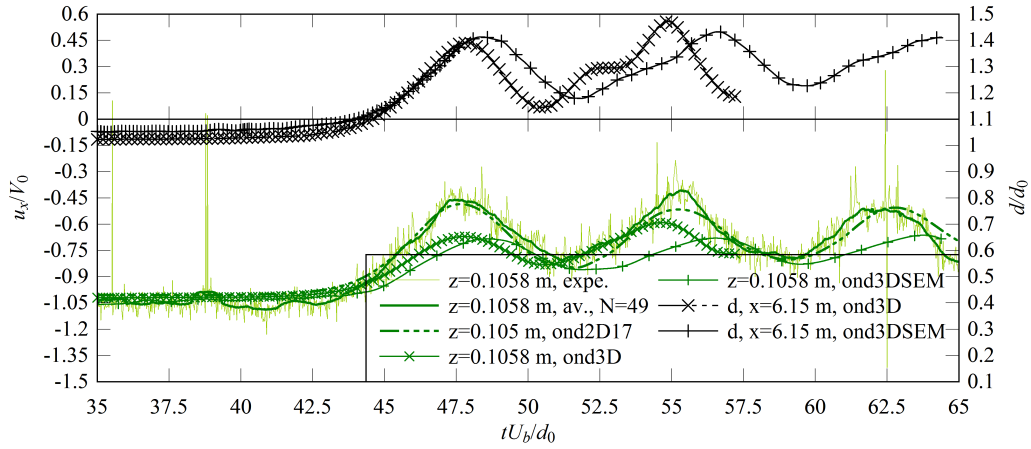

(a) Longitudinal component

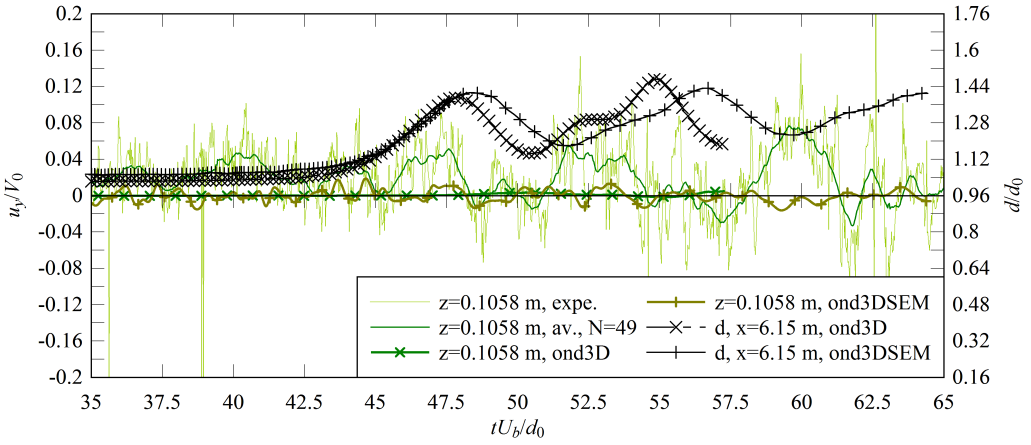

(b) Transversal component

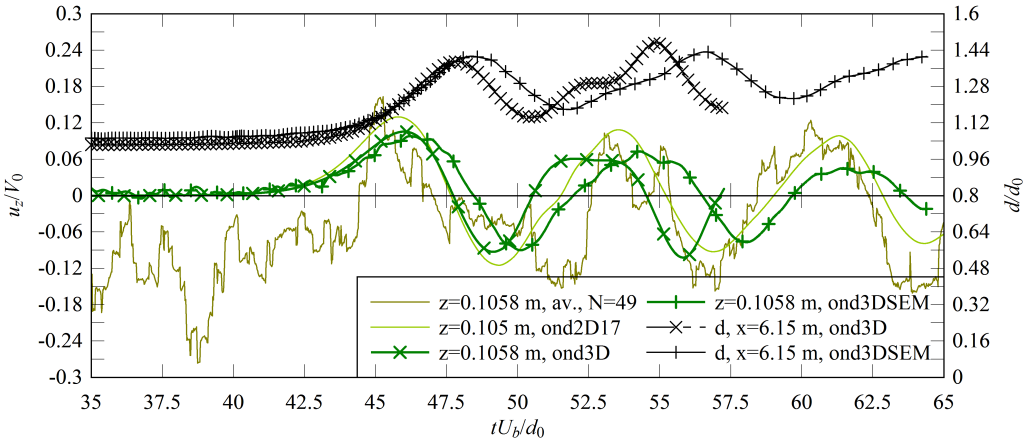

(c) Vertical component

Figure V.25: Dimensionless time evolutions of the velocity at $z/d_0 = 0.77$ with the free surface evolution at $x = 6.15$ m for simulations ond3D and ond3DSEM. Comparison between numerical simulations and experiment (Chanson, 2010b)

A de-synchronisation of the velocity undulations remained and was linked to the difference of bore celerity U_b. Note that the two dimensional simulation ond2D17 showed large fluctuation of the velocity that were not observed by the three dimensional simulations. The fluctuation for ond2D17 could be an effect of the simulation being only two dimensional.
Concerning the transversal velocity, it should fluctuate around zero since the measurements are performed on the channel centreline. This was observed for the simulations and the experiment (Figures V.23b and V.24b). Moreover, similar intensities of fluctuations were observed close to the bed. Whereas, higher in the water column the intensity of the velocity variations tended to be underestimated for simulation ond3DSEM. Simulation ond3D showed small velocity variations of order $10^{-3} \times V_0$ (Figure V.25b). Velocity fluctuations were generated close to the bed in the wake of the longitudinal flow reversal observed beneath the crest as described in section VI.3.2.2. Therefore, the simulations ond3D run without an initially turbulent flow also presented fluctuations downstream the wake of the recirculation and mainly located close to the bed.
The vertical velocity from the simulations was globally positive and negative when the water increase and decreased respectively (Figures V.23c, V.24c and V.25c). Close to the bed, small fluctuations appeared on the velocity signal, but of lesser intensity than the experiment or the two dimensional simulation. Near the free surface, some agreements were found between experimental and numerical data. The amplitude of the oscillations synchronised with the free surface had similar magnitudes between experiment and simulations (Figure V.25c).
Overall, some agreement was found between the numerical simulations and the experiment. Close to the bed, some discrepancies of the longitudinal velocity were observed with the experiment. Those discrepancies are believed to be linked with the underestimated velocity in the steady flow close to the bed. The horizontal and vertical velocities, showed some agreement with the experiment. Surprisingly, the longitudinal velocity data of the two dimensional simulation was in better agreement with the experiments, but it failed at reproducing the cross wave observed in the experiments. Moreover, large velocity fluctuations were observed that are believed to be linked with the simulation being only two dimensional (section VI.3). The three dimensional simulations, on the other hand, reproduced the cross waves, and three dimensional effects within the flow could appear, together with effects of the lateral walls.

V.5.5 About the validation process

Some limitations for the validation with the experimental data (Chanson, 2010a,b) should be pointed out. The experimental data were recorded with a single run and variations can be found between single run data filtering and ensemble averaged measurements (Chanson and Docherty, 2012). The ADV unit is an intrusive probe. The placement of the probe in the flow had an

effects on the free surface and was believed to have an impact on the velocity by creating a drag (section IV.4). The drag of the ADV could have an effect on the propagating bore. Moreover, the turbulence generated by the ADV wake could also be pushed upstream when the bore created a flow reversal therefore affecting the velocity measurements (section IV.4). Close to physical boundary, ADV measurements can lack accuracy (Docherty and Chanson, 2010; Koch and Chanson, 2005; Precht et al., 2006). Another limitation for the validation of the numerical data was the location of the experimental measurements which were performed on the channel centreline at one distance from the gate. This gave scarce datasets to validate LESs. An "ideal" data set for LES validations should contain measurements at various locations, with first and second order moments and should include turbulent scales (Kempf, 2008; Sagaut, 2006). Here, comparing second order moments was not relevant due to the unsteady nature of the flow, the Eulerian type of measurements and the LES filtering. The datasets from the study by Koch and Chanson (2008) providing measurement at different transversal locations were considered for the validation. However, the undular bore was not reproducible neither experimentally or numerically since the gate opening after closure was higher ($h_g = 0.08$ m) than the initial steady flow ($d_0 = 0.079$ m) as reported in Koch and Chanson (2008). Turbulent scales were measured in the present experimental study (section IV) but for channel with a gravel bed and the CFD code could not model the gravel bed therefore the data set from the experimental study (Chapter IV) could not be used.

V.5.6 Concluding remarks

Overall, the comparisons between simulations and experiments showed some agreements considering some initial steady flow differences in term of velocity profiles and fluctuations. The simulation modelling a controlled flow and a bore generated with a completely closed gate (Chanson, 2010a) was in good agreement with the experiment. The simulation reproducing an uncontrolled flow with a bore generated by the partial closure of the gate (Chanson, 2010b) showed more discrepancies than the controlled case. In the non controlled case, the steady flow velocity close to the bed was underestimated by the simulation and the initial steady flow free surface in the numerical domain was different than the experiment. Nonetheless, some agreement was found for longitudinal and vertical velocity data above $z/d_0 > 0.2$. Close to the bed, transversal velocity variations were similar in amplitudes with the experiments for all simulations. A more accurate validation would require more detailed experimental data.

V.6 Summary

Several configurations were tested and compared to existing studies and analytical developments. The dam break configuration would require having access to detailed experimental measure to be accurately validated, although it was in agreements with theory. The propagation of bore generated by the reflection of a stream against a wall was compared to experiments. For the two dimensional simulation some limitations were observed linked with the nature of the simulations. The use of three dimensional simulations was then necessary to study the turbulence in bores. Three dimensional simulations were performed with and without initial steady turbulent flow, using the SEM method to generate coherent turbulent flows. Some agreements were found with the experiments despite some limitation coming from both the simulations configurations and the experimental data sets available.

Unfortunately, a validation using the experimental data presented in Chapter IV could not be realised in time. Before using the data with a gravel bed, it was necessary to process one step at a time and perform a validation of the code in the simplest case: using data for a smooth PVC bed. Moreover, the data presented in sections V.4 and V.5 represents the first simulation with the Navier-stokes equations for undular bores.

VI

Numerical results: effects of undular bore propagation

VI.1 Chapter overview

Numerical simulations reproduced idealised models of tidal bores generated after the impact of the stream against a downstream gate and propagating upstream an initially steady flow. The configurations used for the simulations were based on experimental studies performed in a rectangular channel (Chanson, 2010a,b), similar to the one used in this experimental study (chapter IV) with the difference that a smooth PVC bed was used. Bores hydrodynamics were studied using two and three dimensional simulations. The three dimensional simulations were performed with and without turbulent initial steady flows using a synthetic eddy method (SEM). The simulations were realised using a large eddy simulation (LES) to model the turbulence and volume of fluid (VOF) method to track the air-water interface.
The two dimensional simulations were compared with the three dimensional ones to highlight some limitations of the two dimensional simulations. In three dimensions, two different configurations were used both with and without initial flow turbulence to show the impact of initial flow turbulences on bore propagation.

VI.2 Two dimensional simulations of undular bores

VI.2.1 Numerical configurations

The two dimensional numerical simulations presented and validated in section V.4 are analysed in the following sections. The main aspects of the simulations are recalled in Table VI.1 with U_b and Fr the bore celerity and bore Froude number respectively. Herein, x is the longitudinal distance from the gate positive upstream and z is the vertical distance from the bed positive upwards. The numerical simulations modelled a two-phase flow with air and water. The initial conditions of the domain were set with a zero velocity in the air and a velocity $-V_0$ in the water layer. V_0 was defined positive by $V_0 = Q/(d_0 W)$, Q being the discharge, W the channel width ($W = 0.5$ m) and d_0 the water depth based on experimental measurements (Chanson, 2010a,b). At the inflow condition from $z = 0$ to d_0, the water was continuously injected in the domain with a velocity V_0 (Figure V.12). The generation of undular bores was controlled by setting a Neumann condition from $z = 0$ to h_g at $x = 0$ and a no slip condition for $z > h_g$. The complete numerical configuration was given in section V.4.3. Note that only the water was studied. In the domain, the water was recognised by the phase function being superior to 0.5 and the free surface by the isoline $C = 0.5$.

Table VI.1: Domain configurations and basic bore characteristics of the simulations

simulation	d_0 m	V_0 m.s^{-1}	h_g m	Fr	U_b m.s^{-1}	Bore type	Based on experiment
rad2D13	0.165	0.230	0	1.14	1.22	Undular	(Chanson, 2010a)
ond2D17	0.1385	0.830	0.1	1.25	0.625	Undular	(Chanson, 2010b)

VI.2.2 Descriptions of the flow, basic results

VI.2.2.1 Bore with a completely closed gate

Figure VI.1 shows colour mappings of the water velocity magnitude ($\|u\| = \sqrt{u_x^2 + u_z^2}$) in the domain with some streamlines (lines with arrows) and the isoline corresponding to $u_x = 0$ (black line) for the simulation rad2D13 (Table VI.1). Note that the simulation was stopped before the bore reached the upstream end of the domain at $x = 10$ m. Figure VI.2 presents a colour mapping of the longitudinal velocity u_x, with focus on the recirculation appearing near the channel bed beneath the wave trough. The black lines are isolines of $u_x = 0$ and the lines with arrows are velocity streamlines. The Appendix D shows a video of the bore propagation (section D.3.1).

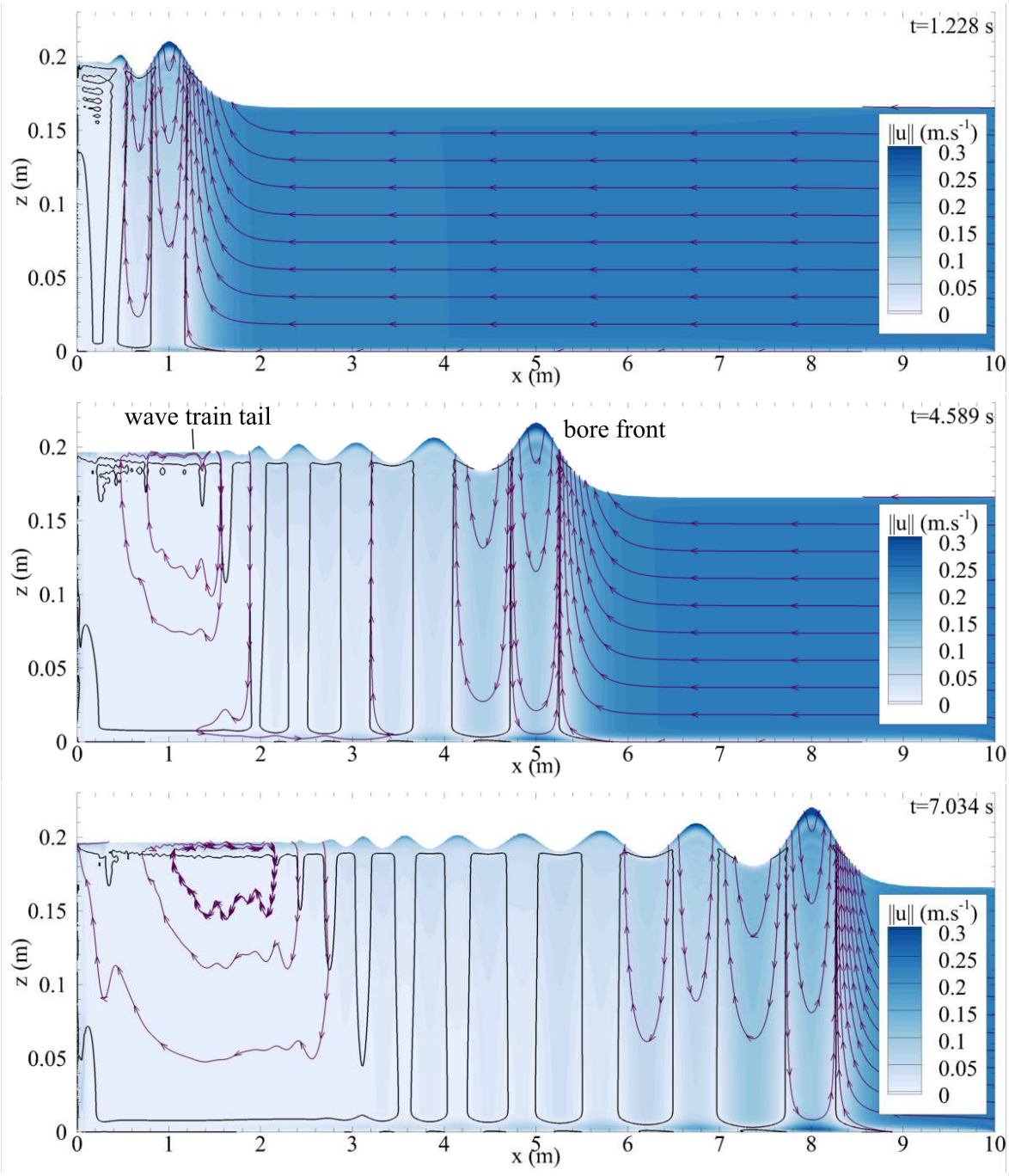

Figure VI.1: Velocity magnitude evolution during the bore propagation at 3 different times with velocity streamlines (lines with arrows) and isoline $u_x = 0$ (black lines). Scale axes are independents. Simulation rad2D13

At the beginning of the simulation, the flow directly impacted the completely closed wall ($h_g = 0$) with no identified splash. The bore quickly took the form of an undular bore within the first metre of propagation (Figure VI.1). As the bore propagated upstream, new undulations appeared from the tail of the secondary undulations. Between the tail of the wave train and the gate ($x = 0$), the water level remained mostly unchanged for the entire bore propagation, i.e. with variations of the interface within the size of the mesh crossed by the interface ($\Delta_z = 1.1$ mm). The wave length and the wave amplitudes from a secondary undulation to the next one progressively decreased (Figure VI.1).

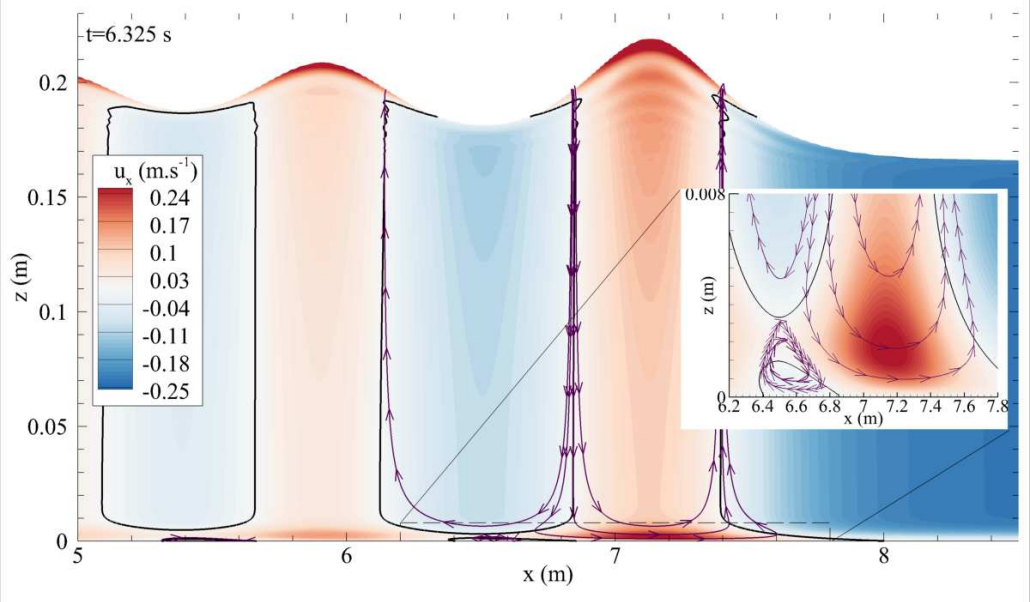

Figure VI.2: Detail on the longitudinal velocity field for the simulation rad2D13 with zoom below the first undulation crest and trough close to the bed. With velocity streamlines (green lines with arrows) and isoline for $u_x = 0$ (black line)

The flow velocity changed beneath the bore. As the water level increased, the longitudinal velocity decelerated. Beneath the first crest, the longitudinal velocity changed direction flowing upstream on all the water column (contour line of Figure VI.1). Beneath the first wave trough, the flow changed direction once more flowing downstream on almost the entire water column. On a small zone detached from the bed, for a height between approximately 1 to 3 mm, the longitudinal velocity was flowing upstream, but for $z < 1$ mm, the longitudinal velocity flowed downstream creating a small transient recirculation beneath the wave trough (Figure VI.2). Such a recirculation beneath the wave trough was not measured nor observed for experimental undular bores, probably due to its proximity to the channel bed. Beneath the following secondary undulations, the longitudinal velocity followed a trend similar to the one observed beneath the first wave crest and trough with a longitudinal velocity flowing alternatively upstream and downstream (Figure VI.1). Nonetheless, after the second or third wave trough,

the longitudinal velocity was oriented upstream a few millimetres beneath the free surface of the wave troughs (isoline $u_x = 0$ in Figures VI.1). The vertical velocity followed the evolution of the free surface. u_z was globally positive and negative when the water level increased and decreased respectively (Figure VI.1) as predicted by the ideal fluid flow theory and tended to follow the derivative of the free surface evolution.

Concerning the stream reversal underneath the crest, from the top of the bore crest to the channel bed, three zones were remarkable for the longitudinal velocity. Figure VI.3 presents longitudinal velocity profiles along the vertical axis in the steady flow beneath the bore passage, beneath the first wave crest and beneath the first wave trough at $x = 6.15$ m. First, less than 10 mm from the crest, a zone with a strong flow reversal was observed, the longitudinal velocity u_x became positive with a maximal longitudinal velocity reversal of approximately $1.7 \times V_0$ located at the free surface (Figure VI.1 and VI.3). Approximately 50 mm beneath the first zone, a second zone was notable, the flow velocity globally decreased as z decreased with an oscillating pattern with the oscillation amplitudes decreasing (Figures VI.1 and VI.3). The third and last zone was located just 10 mm above the channel bed. It was characterised by a sharp and strong velocity reversal with an intensity 0.9 to $1.1 \times V_0$ at $z \approx 2$ mm. In this third zone, the maximal velocity was not in the direct vertical alignment of the bore front maximal elevation. The maximal value of u_x was located 10-20 mm upstream the crest, contrarily to the rest of the water column where maximum values of u_x were observed on the vertical alignment of the wave crest (Figures VI.2). Below the other secondary oscillations, a similar pattern took place with velocity intensities progressively decreasing (Figures VI.1 and VI.2).

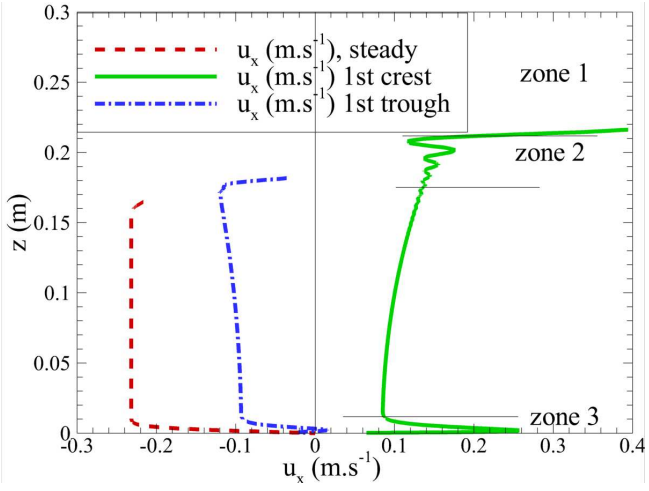

Figure VI.3: Vertical profile of the longitudinal velocity in the steady flow before the bore, beneath the maximal elevation of the first wave crest and beneath the minimal elevation of the first wave trough. Measurements at $x = 6.15$ m and $d_{\max} = 0.219$ m. Simulation rad2D13

Overall, the flow evolution was globally similar to experimental observations (Chanson, 2010a) and provided new information on the flow velocity near the bed or in the secondary undulations

above the initial water depth d_0.

VI.2.2.2 Bore with a partially closed gate

For this bore configuration, the initial steady flow velocity $V_0 = 0.83$ m.s^{-1} was larger than for the case rad2D13 with $V_0 = 0.23$ m.s^{-1}. The bore was generated with a partially opened gate ($h_g = 0.1$ m).

Figure VI.4 presents colour mappings of the water velocity magnitude ($\|u\| = \sqrt{u_x^2 + u_z^2}$) beneath the undular bore with some streamlines (lines with arrows) and the isoline corresponding to $u_x = 0$ (black lines) for the simulation ond2D17 (Table VI.1). The Appendix D shows a video of the bore propagation (section D.3.2).

As the water impacted the door, a splash occurred with air trapped in the water and air bubbles dragged below the gate by the flow. The water accumulating against the door was chaotic and bubbly during the first metre of propagation (Figure VI.4). Then the free surface became smooth and propagated as an undular bore. As the bore propagated, more secondary undulations appeared. The tail of secondary undulations never detached from the gate during the propagation of the bore in the 10 m long domain, contrarily to the simulation rad2D13. Within 20 cm from the gate, the flow remained tumultuous with occasional breaking and air entrainment. The mean average water depth near the gate slightly increased by 2-3 cm as the bore propagated between 2 to 8 m from the gate. From a secondary undulations to another, both the wave amplitude and the wave length decreased (Figure VI.4). The bore front lost its shape when the bore reached approximately $x \approx 9$ m due to undulations of the free surface downstream the inflow boundary ($x = 10$ m).

Figure VI.5 presents a detailed mapping of the longitudinal velocity evolution with a zoom focused on the recirculation. Concerning the flow velocity during the bore passage, the longitudinal velocity u_x decelerated and re-accelerated beneath the crest and trough respectively (Figure VI.4). However, the water continuously flowed downstream, except very close to the bed, beneath the largest secondary undulation crests at a depth $z < 2$ cm (Figure VI.4 and VI.5). Beneath the first wave crest, the maximum velocity reversal in the recirculation was up to $0.84 \times V_0$ ($u_x = 0.7$ m.s^{-1}). Figure VI.6 presents a vertical profile of the velocity beneath the first wave crest at $x = 5.5$ m. The longitudinal velocity beneath a crest presented a similar vertical distribution of velocity with 3 distinguished zones (Figure VI.6), similarly to case rad2D13, but without the complete velocity reversal for ond2D17. The first zone was located 1 cm beneath the free surface, a strong flow velocity decrease was observed with the velocity u_x reaching -0.1 m.s^{-1} at the free surface (Figure VI.6). The second zone was 4 to 5 cm long below the first zone. An oscillating pattern of the velocity u_x was observed. The third zone was approximately 2 cm above the channel bed where the velocity distribution abruptly

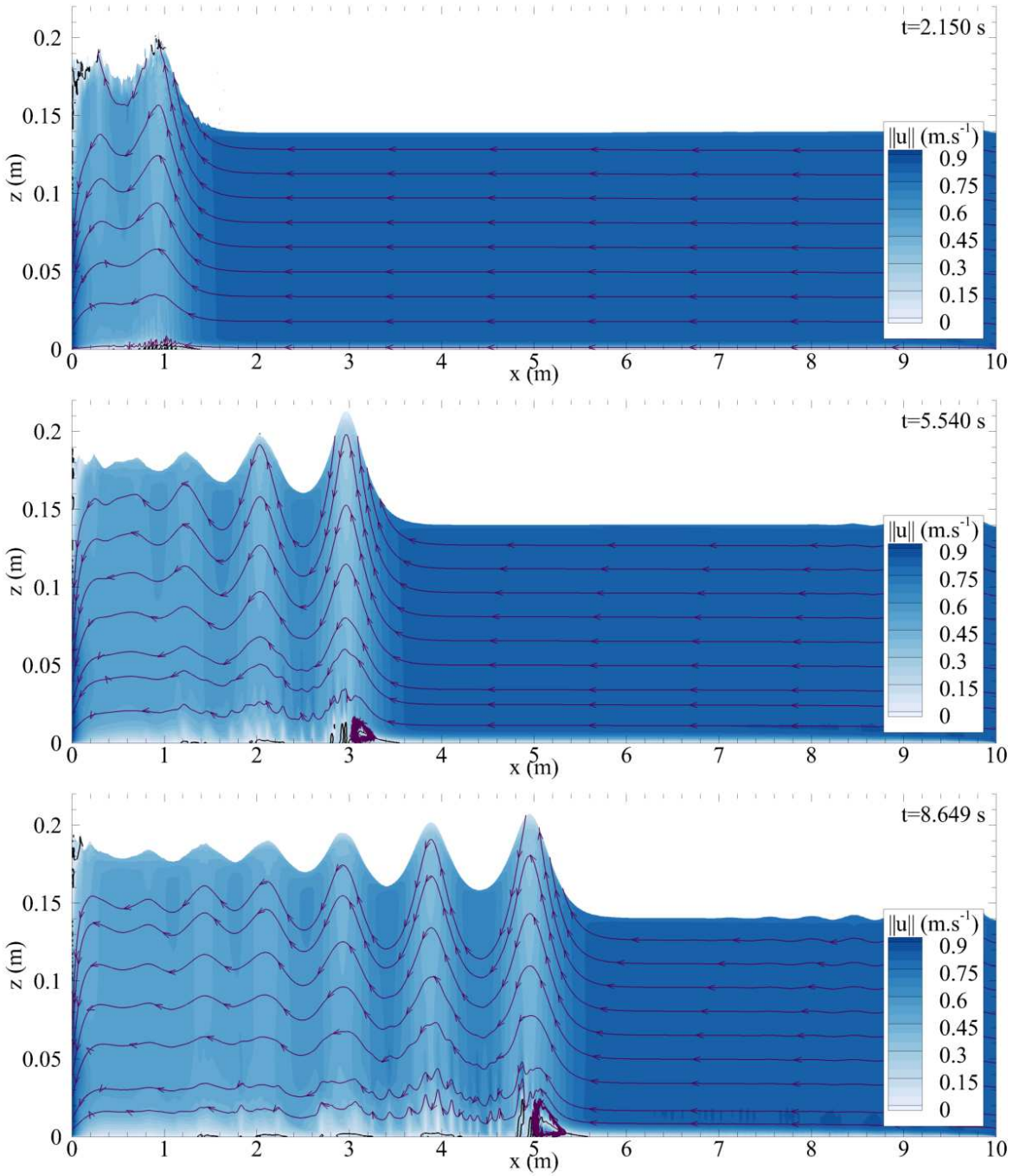

Figure VI.4: Velocity magnitude evolution during the bore propagation at 4 different times with velocity streamlines (lines with arrows) and isoline of $u_x = 0$ (line). Axis scales are independents, simulation ond2D17, $V_0 = 0.83$ m.s^{-1} and $d_0 = 0.1385$ m

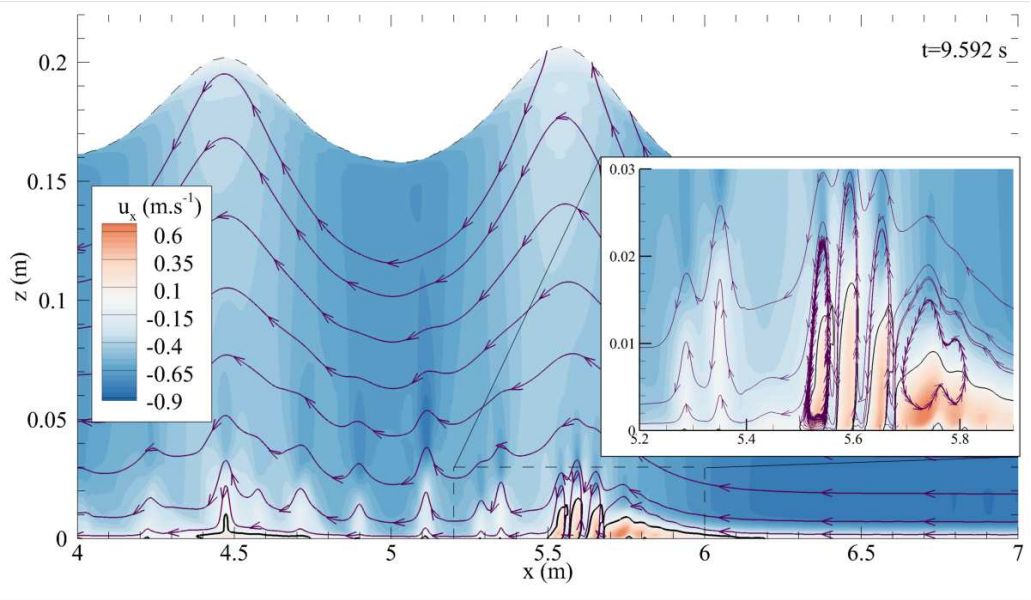

Figure VI.5: Detail on the longitudinal velocity field beneath the bore front of simulation ond2D17 with zoom beneath the first crest and trough close to the bed. With velocity streamlines (green line with arrow) and isoline for $u_x = 0$ (black line)

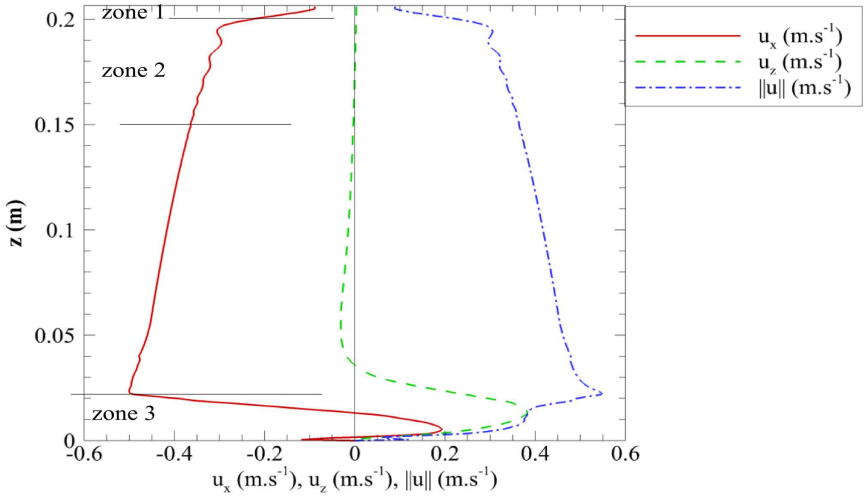

Figure VI.6: Vertical profile of the velocity beneath the first wave crest at $x = 5.5$ m, $d_{\max} = 0.206$ m, case ond2D17

changed with a velocity reversal occurring. Similar recirculations were observed experimentally (Ryabenko, 1998), but not specifically for the experimental study that was used for the simulation configuration (Chanson, 2010b). Downstream of the velocity reversal region, fluctuations of the velocity were generated and two dimensional coherent structures detached from the recirculation zones. Finally, concerning the vertical velocity, u_z was globally positive and negative when the water level increased and decreased respectively (Figure VI.4). Close to the bed, the fluctuations induced sporadic events with vertical velocity values down to -0.4 or up

to 0.6 m.s^{-1} (-0.5 to $0.7 \times V_0$).
Overall, the pattern observed beneath the first crest and trough tended to reproduce itself during the passage of the following secondary oscillations. The velocity fluctuations are discussed in the next section.

VI.2.3 Discussion

The two different configurations (Table VI.1) presented some similarities. Away from the channel bed ($z > 2d_0/3$), the longitudinal velocity increased and decreased when the free surface increased and decreased respectively. Vertical distributions of the longitudinal velocity u_x beneath crests showed three typical zones (Figures VI.3 and VI.6). Close to the free surface, the longitudinal flow velocity went under large variations, with the velocity following the bore direction similarly to orbital patterns in classical wave theory (Stoker, 1957). The second zone showed an oscillating pattern. Such oscillations were not explained nor observed experimentally. Note that this zone was not observed for simulation of undular dam break waves (Figure V.3b). No experimental work on positive surges generated by the reflection of the flow against a downstream boundary was able to measure the flow velocity above the initial steady water depth. PIV measurements might help explaining those longitudinal velocity oscillations. Close to the bed, a third zone with a strong velocity change following the bore direction appeared which induced some strong shear. This was also different to the dam break wave (Figure V.3b) where the vertical distribution of the longitudinal velocity simply tended toward zero close to the bed whereas, for undular bores propagating over a steady flow, the vertical distribution showed a local maximum (Figures VI.3 and VI.6).
The two cases presented also some differences. For the case simulated with a completely closed gate (rad2D13), the bore induced a complete flow reversal in the whole water column beneath wave crests (Figures VI.1 to VI.3). The corresponding experiment (Chanson, 2010a) showed similar flow evolution for depths where measurements were performed. However, this was not detailed as the experimental study focused on the effects an obstacle have on the bore propagation. For the simulation with a gate partially opened (ond2D17), the longitudinal velocity reversal only occurred close to the bed for $z < 2$ cm. Such flow reversals were observed for experimental studies (Ryabenko, 1998) but without further details available. This was previously observed for similar bore generated by similar procedure during experiments and simulations, but only for breaking bores (Chanson and Docherty, 2012; Koch and Chanson, 2009; Lubin et al., 2010a). For breaking bores, the flow reversal propagated together with the bore front (Lubin et al., 2010a), the present simulations showed that it is the same for the undular bore modelled (Figure VI.4).
Beneath wave troughs, for the case rad2D13, the flow mostly reversed in the opposite direction

of the bore, except on small areas detached from the bed (Figure VI.2). This induced flow recirculations that were observed with streamlines (Figures VI.2 and VI.3). However, the velocity magnitude of the recirculations were small (Figure VI.1). In comparison, the longitudinal velocity in simulation ond2D17 was mainly oriented downstream and a velocity reversal was observed only close to the bed and beneath the crest.

Another difference between simulations rad2D13 and ond2D17 was that, for the case with a complete gate closure (rad2D13) the tail of the wave train detached from the gate as the bore propagated and fluctuating patterns of the velocity were observed between the gate and the tail of the wave train with a small velocity magnitude (Figure VI.1). The depth averaged velocity in this area was of order 10^{-5} m.s^{-1} (Figure VI.1). For the case ond2D17, the secondary undulations never detached from the gate. Downstream of the velocity reversal zone located close to the bed, velocity fluctuations appeared and propagated upwards into the water column (Figures VI.4 and VI.5) that did not occurred for the simulation rad2D13.

Figure VI.7 presents a colour mapping of the vorticity ($\omega = \omega_y = \partial u_z/\partial x - \partial u_x/\partial z$) based upon the two dimensional velocity field with velocity streamlines for the simulation ond2D17. Figure VI.8 presents the same vorticity together with isoline of the pressure. In the wake of the recirculation close to the bed, vortical structures were observed by looking at the velocity field (Figure VI.2). They were characterised by large vorticity values moving upwards in the water column (Figure VI.7). The large vorticity values were associated with local low pressure values (Figure VI.8). Note that the core of rotating structures can often be identified by low pressure zone (Post et al., 2003), and such structures were also identified in breaking bores (Lubin et al., 2010a). The vorticity field showed ellipsoid structures being ejected mainly from the flow reversal zone beneath the first crest. Most ellipsoids were connected to the bed by a filament-like structure identified by the vortcity pointing downwards in the upstream direction (Figure VI.7 and VI.8). The vorticity values progressively decreased after ejection. The structures were ejected with different sizes and intensities but at relatively regular intervals. Between $x = 2$ to 8 m, the Strouhal number, calculated based upon a quasi-steady flow analogy ($St = f_{vort} d_0/(U_b + V_0)$), was estimated as $St = 0.99$. Lubin et al. (2010a) also performed calculation of the Strouhal number but with a different approach by computing $St_2 = f_{vort} d_b/V_b$ where V_b is the average flow velocity after the bore. They found $St_2 = 1.42$ for a breaking bore and in the case ond2D17, with the same method the Strouhal number in simulation ond2D17 was $St_2 = 3.70$. A video of the bore propagation showing the colour mapping of the vorticity is also included as extra material (section D.3.2).

Velocity fluctuations appeared downstream the velocity reversal region in simulation ond2D17 but not in simulation rad2D13. This is believed to be linked with the partial velocity inversion beneath crests observed for simulation ond2D17. Considering the velocity reversal region as

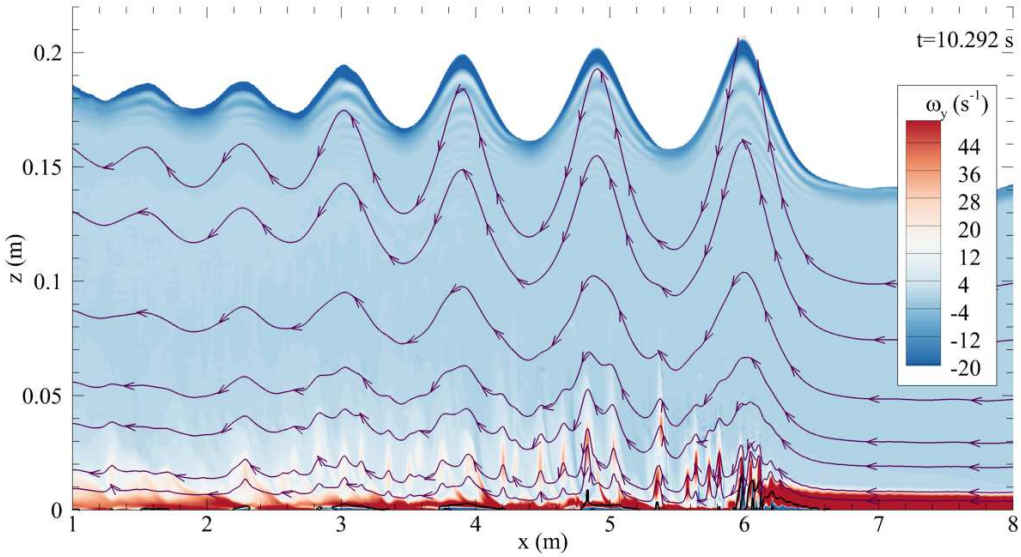

Figure VI.7: Vorticity field beneath the bore with velocity streamlines (green line with arrow) and isoline for $u_x = 0$ (black line), case ond17

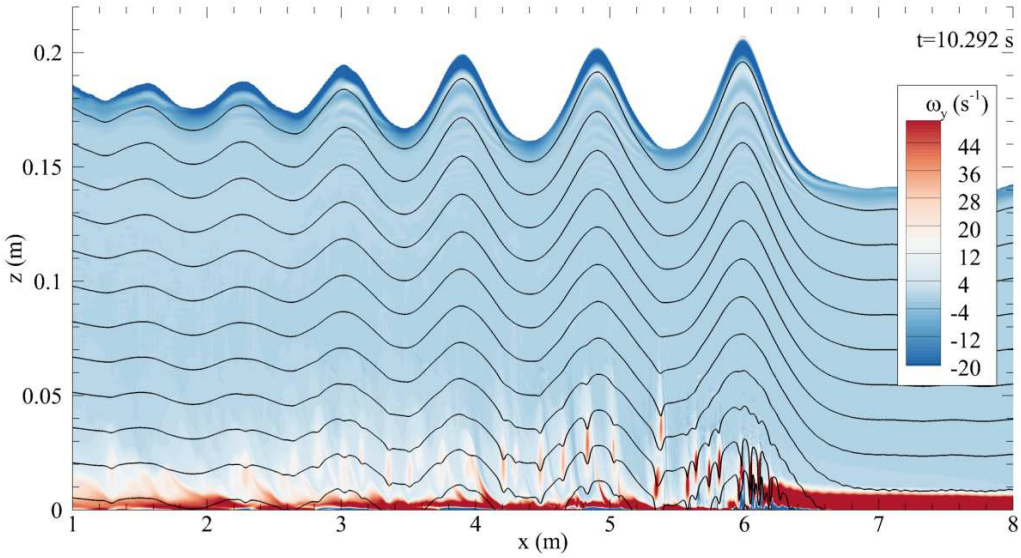

Figure VI.8: Vorticity field beneath the bore with pressure isolines every 150 Pa (black line), case ond17

a submerged object, an analogy can eventually be made with the drag observed downstream an obstacle in a fluid at large Reynolds number. In simulation ond2D17, the velocity reversal close to the bed showed a small velocity magnitude ($\|\mathbf{u}\|$) where the longitudinal velocity (u_x) was zero (Figure VI.4 and VI.5). This would be similar to an obstacle with a no slip boundary condition located within the flow creating an effect of friction. Beneath the first crest, the flow Reynolds number was 73 250 and below the first trough 92 690 (measured with the bore front at $x = 6.15$ m). A first comparison can be made with flow detachments observed downstream a cylinder. In the wake of cylinders, eddies are shed continuously for large Reynolds number

($Re \approx 40$) from each side of the body (Williamson, 1996). Herein, the Strouhal number calculated considering the average height of the recirculation (2 cm) was 0.14. For a flow around a cylinder, the Strouhal number usually varies between 0.14 to 0.24 increasing with the Reynolds number and is calculated using the diameter of the cylinder (Williamson, 1996). Here, the Strouhal number of 0.14 might indicates that the generation of vortical structures after the flow recirculation was a similar phenomenon to vortices appearing in the wake of immersed bodies. A second comparison, more consistent in term of shape, can be made with the flow detachment observed downstream a bump attached to a flat plate (Ehrenstein and Gallaire, 2008; Marquillie and Ehrenstein, 2003). Since the recirculation region was fluid rather than a solid object, some part of the recirculation region was also ejected. In the case of a solid bump (Ehrenstein and Gallaire, 2008), the flow reattached to the bed downstream the bump. Here, due to the physical boundary associated with the oscillating pattern of the free surface, the structure moved upwards into the water column. This phenomenon could not appear for simulation rad2D17, because the flow mostly reversed between crests and troughs despite the strong inversion near the bed beneath the crests.

Some limitations remain to be considered as the flow was two-dimensional. First the development of the channel bed boundary layer was omitted due to the absence of initial turbulence in the flow. Interactions with the lateral walls might also have an impact the flow. Three dimensional simulations with and without initial turbulence in the steady flow would allow to see eventual effect of the bore on the initial flow.

Overall, the two-dimensional simulations showed that positive surges were really sensitive to the generation conditions. Bores generated with a gate completely closed or partially closed will produce different unsteady flows. Note that for tidal bores in estuaries and river, all reported studies observed a complete flow reversal beneath and after the bore passage. The absence of complete flow reversal in the present idealised bores might limit the comparison with the geophysical phenomenon, as mentioned in section IV.4.

Nevertheless, both cases of bores ond2D17 and rad2D13 shared one important feature: the strong flow reversal just above the bed. Similar observations were made on velocity data from field studies on tidal bore (personal communication with Lucille Furgerot and Dominique Mouazé, working on field studies for the ANR project MASCARET). Note that beneath a positive surge generated by a dam break (section V.2), the flow beneath the wave crest did not produce the intense longitudinal velocity just above the bed (Figure V.3b). The strong shear observed just above the bed might be a particularity of positive surge propagating over an opposite flow.

VI.3 Three dimensional simulations of undular bores

VI.3.1 Numerical configurations

The configurations for the three dimensional simulations were presented in section V.5.1. Some basic aspects are recalled here and summarised in Table VI.2. The numerical domain was 10 m long, 0.5 m large and 0.5 m high. The numerical simulations modelled a two-phase flow with air and water. The initial conditions of the domain were set with a zero velocity in the air ($z > d_0$) and a velocity $-V_0$ in the water layer. Water was injected in the domain by two conditions, one injecting water at a constant velocity V_0 from 0 to d_0, the other creating a turbulent inflow condition using the SEM. The generation of undular bores was controlled by setting a Neumann condition from $z = 0$ to h_g at $x = 0$, and a no slip condition on the rest of the wall. The coordinate y is the transverse distance from the right sidewall looking upstream. The simulations using the SEM (rad3DSEM and ond3DSEM) started to run without closing the downstream gate in order to let the turbulence propagates in the domain, whereas the simulations without the SEM were run with the gate closed from the start of the simulations. The time $t = 0$ corresponds to the time of gate closure during the simulations.

Table VI.2: Domain configurations and basic bore characteristics of the three dimensional simulations

simulation	d_0 m	V_0 m.s^{-1}	h_g m	Fr	U_b m.s^{-1}	Bore type	Based on experiment
rad3D	0.165	0.230	0	1.14	1.22	Undular	(Chanson, 2010a)
rad3DSEM		0.243*		1.15	1.22		
ond3D	0.1385	0.830	0.1	1.25	0.626	Undular	(Chanson, 2010b)
ond3DSEM		0.837*		1.27	0.640		

Note: * based on the estimated discharge generated by the SEM (section V.5.2).

VI.3.2 Propagation of undular bores upstream turbulent and non turbulent steady flows

VI.3.2.1 Simulations of bores genereated by a completely closed gate

Free surface description

Figure VI.9 and Figure VI.11 illustrate the propagation of undular bores for the cases rad3D and rad3DSEM respectively. The free surface was identified by $C = 0.5$ where C is the phase function (section III.4.2.4). Figure VI.10 and Figure VI.12 show details of the undular bore free surface propagation for the cases rad3D and rad3DSEM respectively. Note that the visualisation

files were saved during the simulation at different physical times t because the simulation time steps Δt were calculated dynamically for each iteration. Appendix D presents video of the simulation rad3DSEM (section D.3.3).

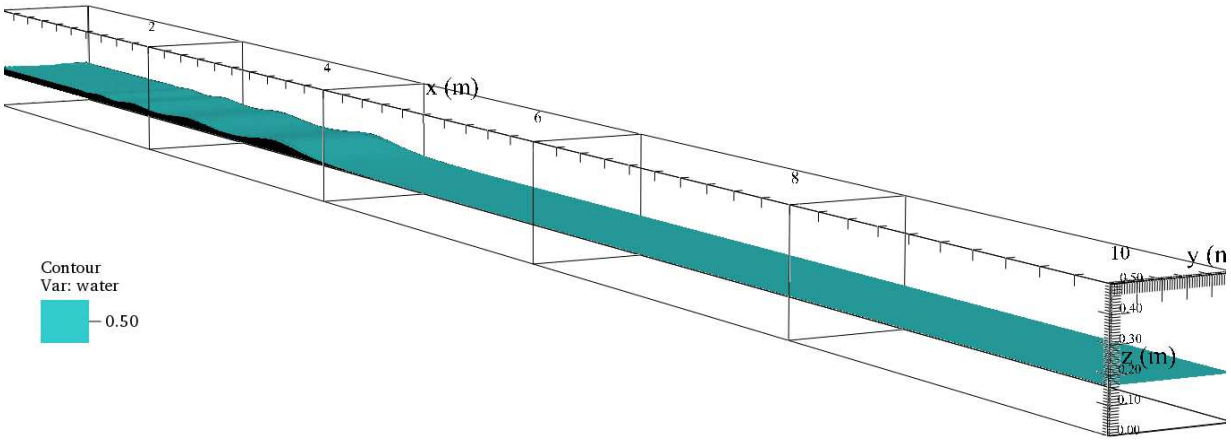

(a) $t = 3.33$ s

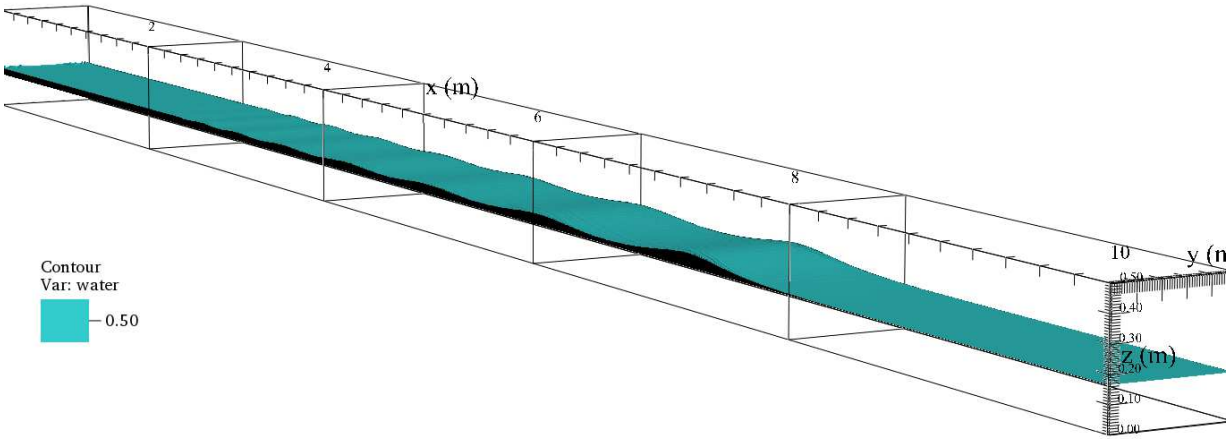

(b) $t = 6.45$ s

Figure VI.9: Undular bore propagation for the simulation rad3D at two different times. The bore propagates from left to right

After the complete closure of the downstream boundary (gate), the flow impacted the completely closed gate with no identified splash. The simulation rad3D started with the gate fully closed whereas for simulation rad3DSEM, the gate was closed after the inflow turbulence created by the SEM reached the downstream end of the domain. For each case, the bore quickly took the form of an undular bore within the first metre of propagation (Figures VI.9 and VI.11). The undulation shape was mainly two dimensional with small cross waves initiated against the sidewalls at the middle of the first wave elevation. The cross waves were slightly more pronounced for the simulation without turbulent steady flow conditions (rad3D) than for the simulation rad3DSEM (Figures VI.10 and VI.12). Small cross waves also appeared on

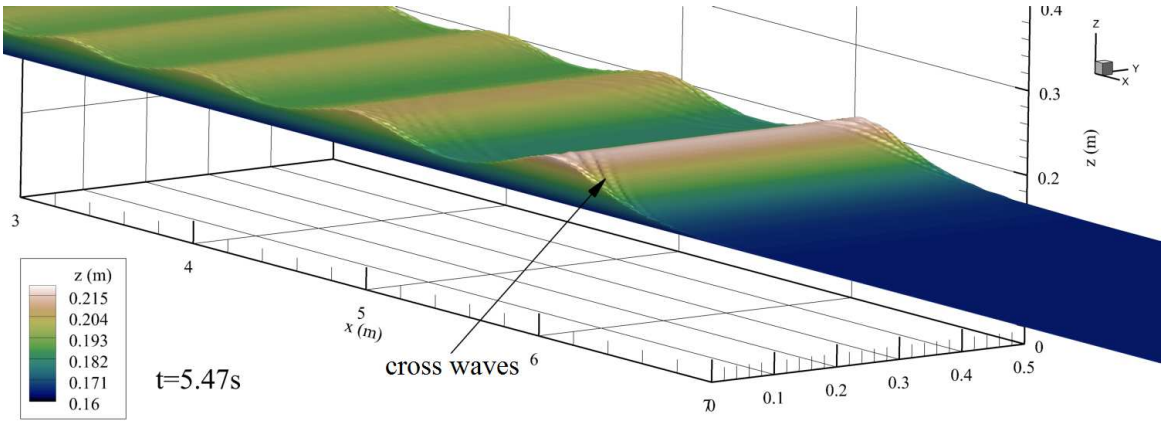

Figure VI.10: Details of the undular bore propagation at $t = 5.47$ s for the simulation rad3D

the secondary undulations close to the sidewalls when the water level increased in the case of simulation rad3D (Figures VI.10). As the bore propagated, the end of the wave train (tail) detached from the gate. New undulations appeared from the tail. Between the tail of the secondary undulations and the gate ($x = 0$), the water level remained globally unchanged during the bore propagation with small variations within the size of the mesh ($\Delta_z = 2.4$ mm). The wave length and amplitude of the secondary undulations from the front to the tail progressively decreased (Figure VI.9 and VI.11). Overall, the bore propagation showed a two dimensional aspect similar to the experiment (Chanson, 2010a) and similar to the two dimensional simulation rad2D13 with the addition of small cross waves on the sidewalls also seen during experiments (Chanson, 2010a).

Unsteady flow velocity description

The flow velocity presented some similarities between simulations rad3D and rad3DSEM. Figures VI.13 and VI.14 present slices of the velocity field in the channel during the propagation of bores. For both simulations, a sudden flow deceleration was observed beneath bores (Figures VI.13a and VI.14a). Beneath the first crest, the flow changed direction in the whole channel width and water column and was orientated in the bore propagation direction in the complete water column and the complete channel width. Below the first bore trough, the flow changed direction one more time in most of the water column, except on a thin zone of a few millimetres from the bed similarly to the two dimensional simulations. Figure VI.15 presents the longitudinal velocity profile beneath the first bore crest for simulation rad3D and rad3DSEM. The global flow evolution was similar to the two dimensional simulations and the vertical profile on the channel centreline presented also three different zones. A strong flow reversal was observed next to the top of the water column beneath the crest (zone 1). Beneath this region and for 50 to 60 mm (zone 2), the vertical profile of the velocity showed an oscillating pattern. Finally, close to the bed (zone 3), a strong flow reversal was also observed (Figure VI.15). A large velocity

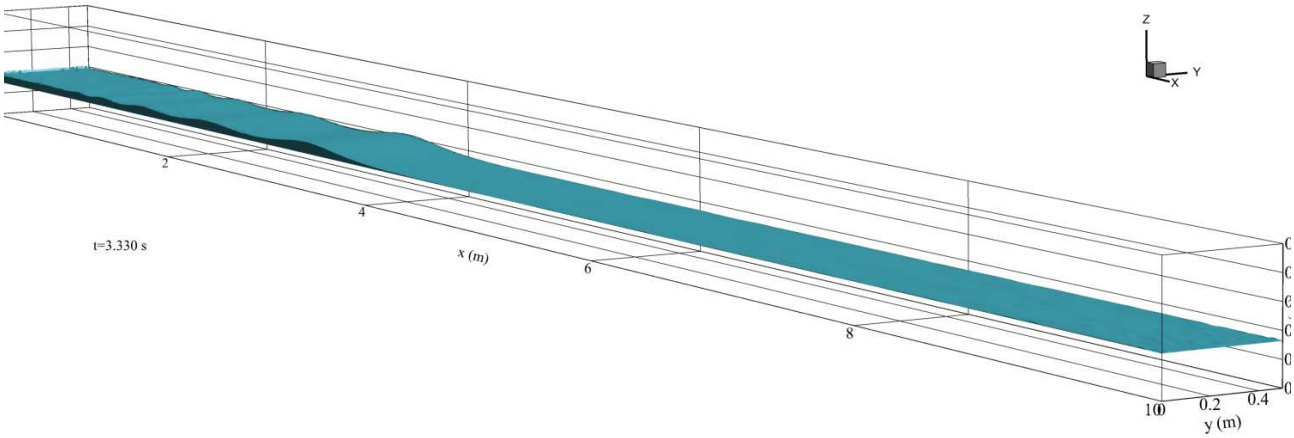

(a) $t = 3.33$ s

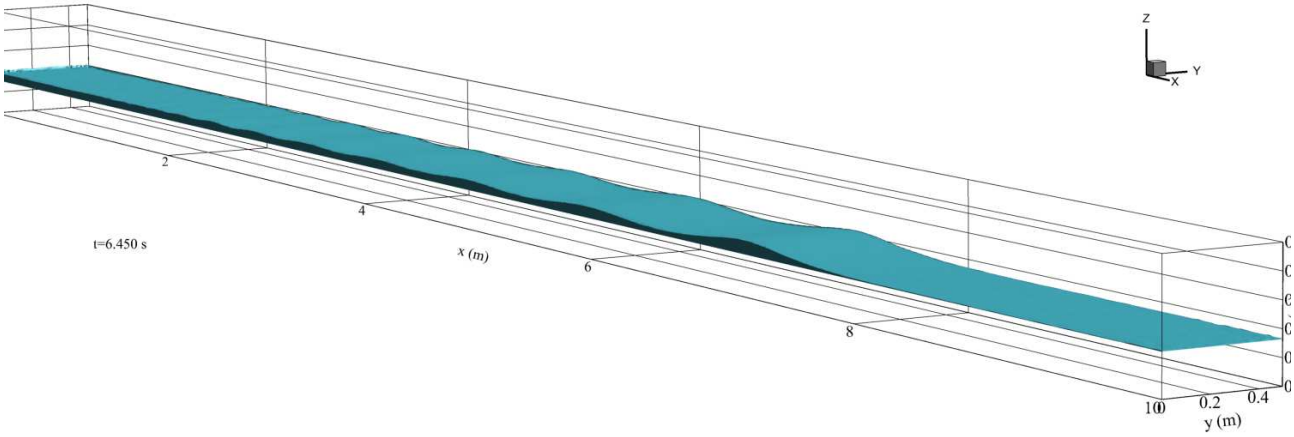

(b) $t = 6.45$ s

Figure VI.11: Undular bore propagation for the simulation rad3DSEM at two different times. The bore propagates from left to right

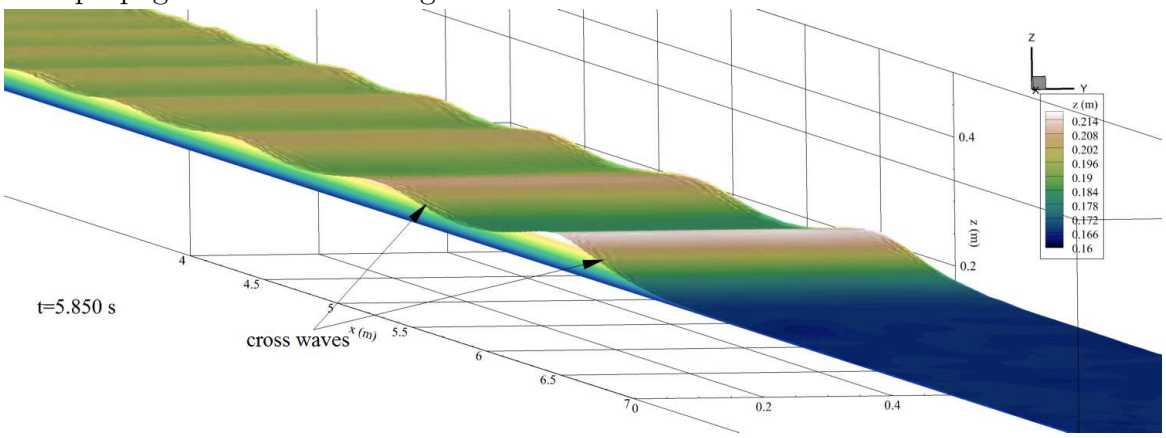

Figure VI.12: Details of the undular bore propagation at $t = 5.85$ s for the simulation rad3DSEM

reversal was also observed close to the lateral walls in the entire water column (Figure VI.15). The longitudinal velocity also showed some differences between the two simulations. For the simulation rad3D, the longitudinal velocity followed a homogeneous pattern of flow reversal beneath crest and trough. However, for the simulations rad3DSEM, the steady flow turbulence had a significant effect on the flow reversal. Their shapes were not homogeneous and less two dimensional than for the simulation rad3D (Figure VI.15). Beneath the bore crest and for simulation rad3D, the height of zone 3 was approximately 3 cm whereas it was varying between 2 to 5 cm for the simulation rad3DSEM. Beneath the wave trough, the size of the recirculation was also influenced by the initial turbulent flow. The zones where the flow kept flowing upstream near the bed, was located between $z = 2$ to 4 mm for simulation rad3D and between approximately $z = 0.5$ to 15 mm for simulation rad3DSEM with variations along the channel width. Moreover, between the gate and the tail of the secondary undulations, a zone of flow reversal was observed at a distance of $\approx 3/10W$ from both laterals walls for simulation rad3DSEM (with $W = 0.5$ m the channel width), whereas the flow was mainly negative, with small velocity intensities, for the case rad3D (Figure VI.13a and VI.14a).

The transversal velocity evolution beneath the bore differed for the two simulations (Figures VI.13b and VI.14b). The simulations rad3D showed little fluctuations of the transversal velocities during the bore passage. Whereas the simulations rad3DSEM, seemed to change the intensity of the turbulence present in the initial turbulent flow (Figure VI.14b). In the wave train and as the bore propagated, the velocity intensity of some turbulent structures generated in the steady flow seemed to increase and decrease in synchronisation with the free surface motion. Note that between the gate and the end of the wave train, the maximum values of u_y seemed to increase at mid water column close to the sidewalls. But the simulation had to be stopped when the bore reached the upstream end of the domain, limiting the physical time to study the phenomenon. Some similarities between the two simulations were observed against the sidewalls and close to the free surface. A 6 mm zone just below the bore crest showed transversal velocity oriented toward the channel centreline followed, beneath it, by a 1 cm zone with transversal velocities oriented in the opposite direction toward the walls (Figures VI.13b and VI.14b).

For both simulations, the vertical velocity globally followed the evolution of the free surface and was positive and negative when the water level increased or decreased respectively (Figures VI.13c and VI.14c). A difference was observed in term of fluctuations. Close to the wall for the simulation rad3DSEM, the vertical velocity was more fluctuant than in the steady flow whereas the simulation rad3D did not show any fluctuations of the vertical velocity.

Comparing the bore shape between simulations rad3D and rad3DSEM, the free surface evolution was similar (Figures VI.9, VI.11 and section V.5) with the same bore celerity and same

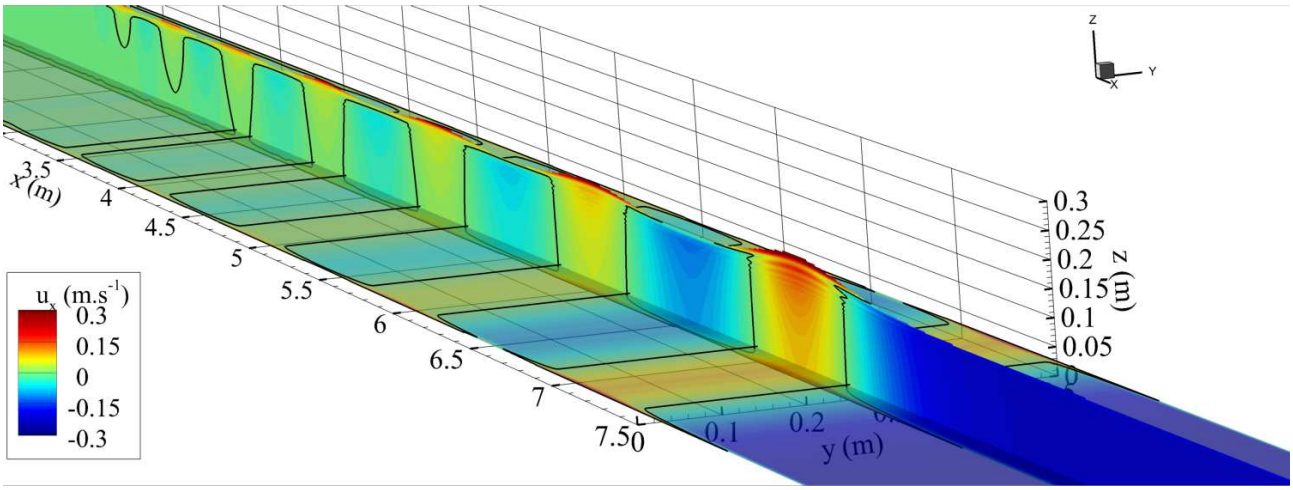

(a) u_x, vertical slice on the channel centreline and horizontal slice at $z = 0.025$ m plotted with transparency. Black line: isoline of $u_x = 0$

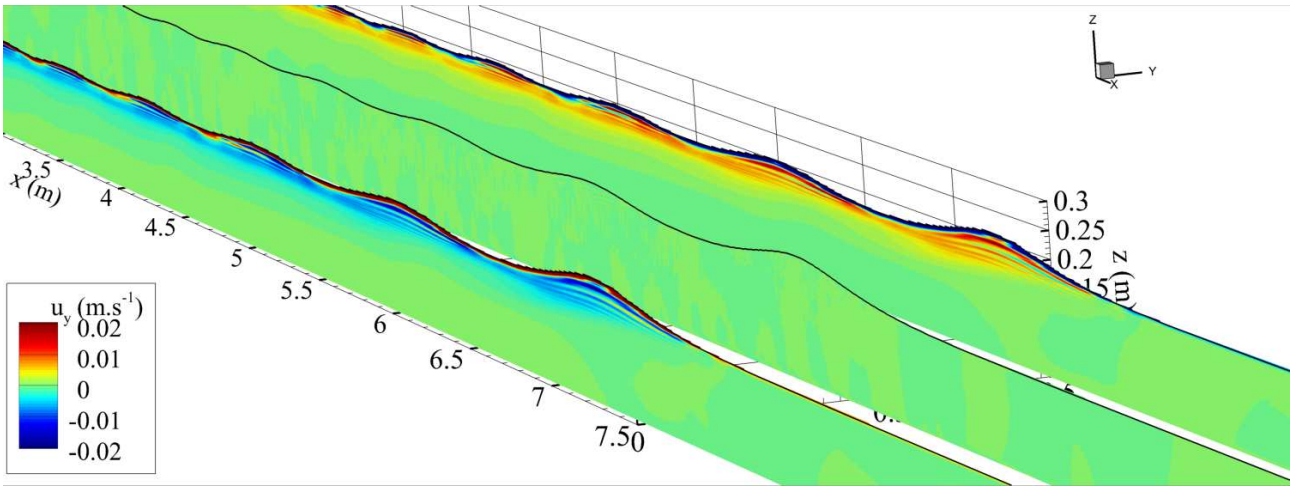

(b) u_y, vertical slices at $y = 0.01$, 0.25 and 0.49 m. Black line: Free surface

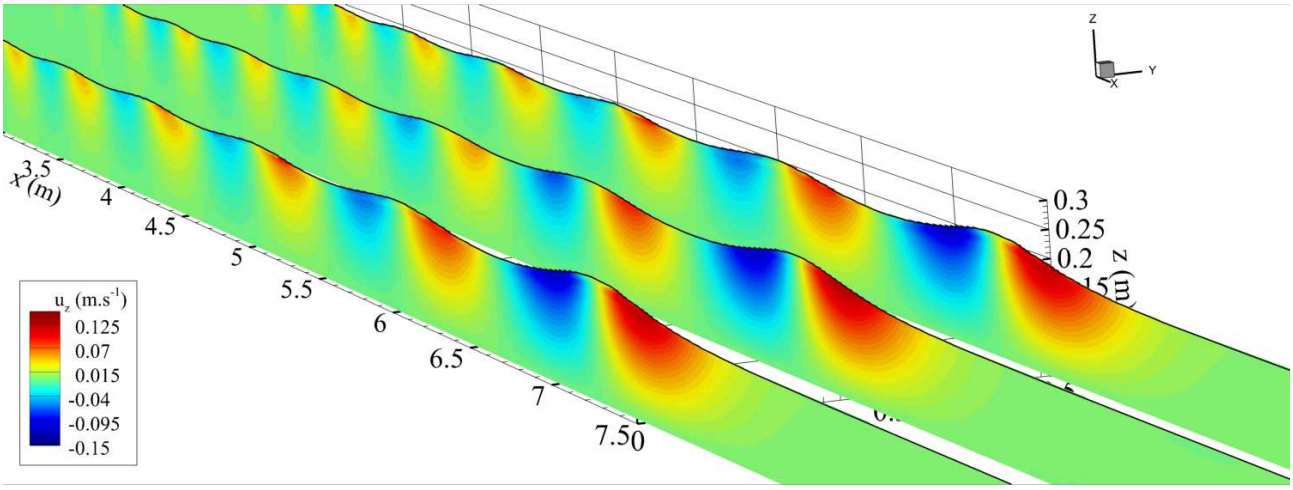

(c) u_z, vertical slices at $y = 0.01$, 0.25 and 0.49 m. Black line: Free surface

Figure VI.13: Velocity fields in the undular bore of simulation rad3D. Bore propagation from left to right, bore at $x = 7.2$ m and $t = 6.45$ s

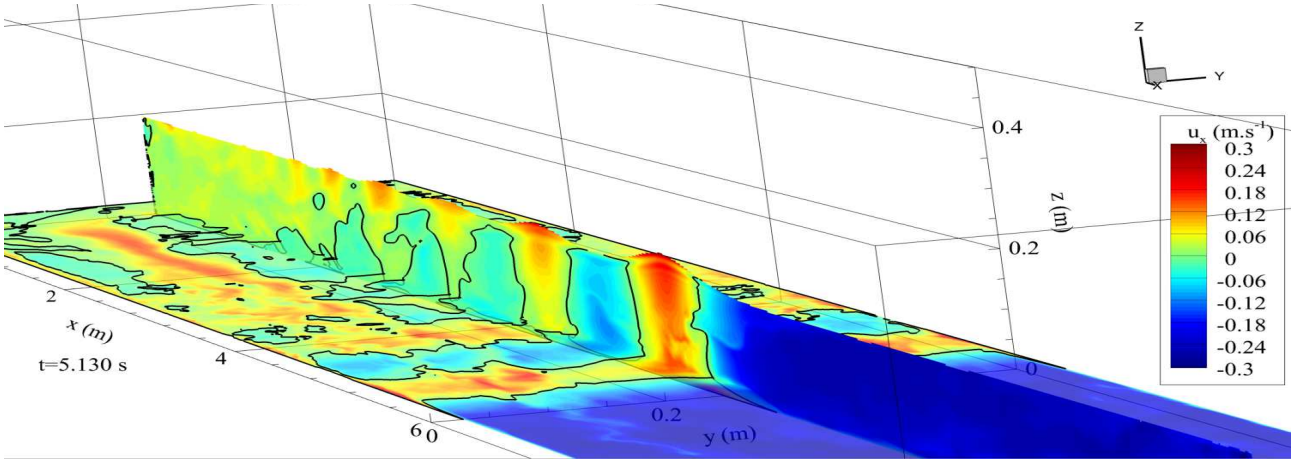

(a) u_x, vertical slice on the channel centreline and horizontal slice at $z = 0.025$ m plotted with transparency. Black line: isoline of $u_x = 0$

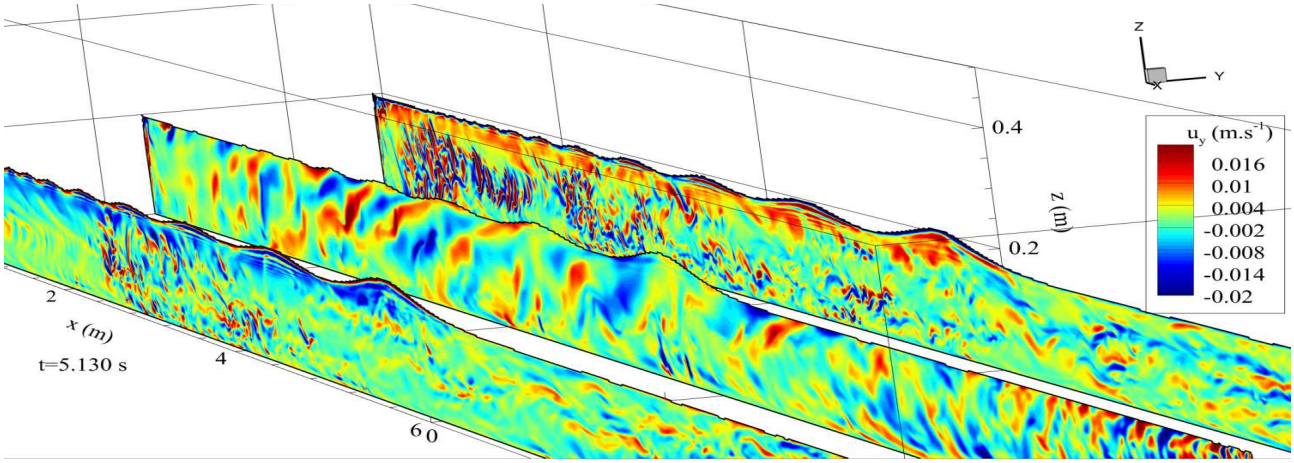

(b) u_y, vertical slices at $y = 0.01$, 0.25 and 0.49 m. Black line: slice contour

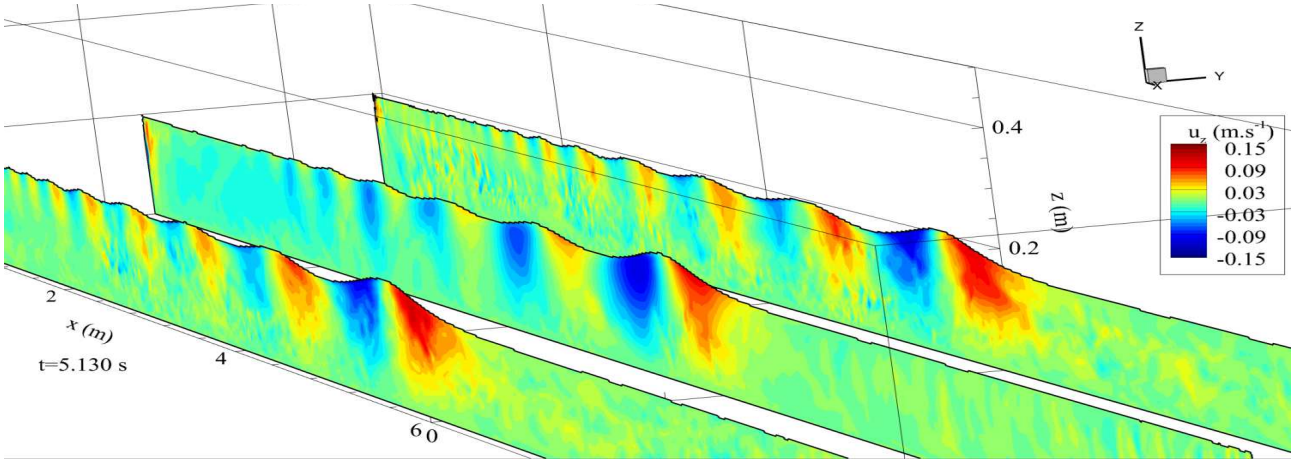

(c) u_z, vertical slices at $y = 0.01$, 0.25 and 0.49 m. Black line: slice contour

Figure VI.14: Velocity fields in the undular bore of simulation rad3DSEM. Bore propagation from left to right, bore at $x = 5$ m and $t = 5.13$ s

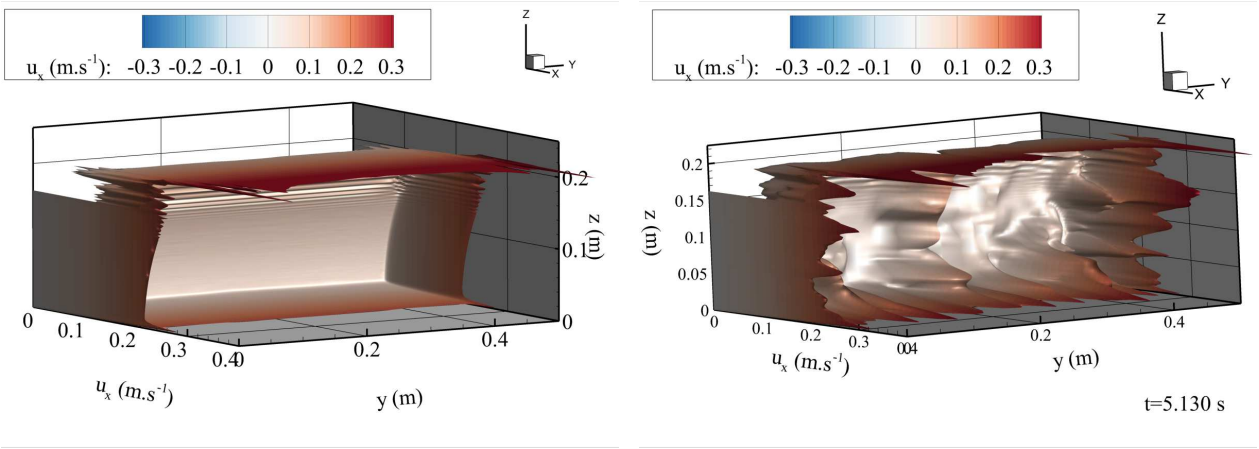

(a) Simulation rad3D, $x = 5.3$ m, $t = 4.83$ s (b) Simulation rad3DSEM, $x = 5.595$ m

Figure VI.15: Profile of the longitudinal velocity beneath the maximal elevation of the bore front

undulation patterns. Concerning the velocity fields, more differences were observed between the simulations with and without inflow turbulence. The simulation rad3D had a look nearly two dimensional over the channel width, whereas the simulation rad3DSEM was completely three dimensional with an amplification of the fluctuation due to the free surface undulations of the bore. In both cases, a strong flow reversal was observed near the sidewalls.

VI.3.2.2 Simulations of bores genereated by a partially closed gate

Free surface description

Figure VI.16 and Figure VI.17 illustrate the propagation of undular bores for the cases ond3D and ond3DSEM respectively. Figure VI.18 shows details of the undular bore front free surface for the case ond3DSEM. Appendix D presents video of the simulation ond3DSEM (sections D.3.4 and D.3.5).

As the water impacted the door, a splash occurred with air trapped in the water and air bubbles dragged below the gate by the flow. The water accumulating against the door was chaotic and bubbly during the first metre of propagation. Then, the free surface became smooth and propagated as an undular bore (Figures VI.16 and VI.17). As the bore propagated, more secondary undulations appeared. The secondary undulation tail never detached from the gate during the propagation in the 10 m long domain, contrarily to configurations rad3D and rad3DSEM. Within 20 cm from the gate, the flow stayed tumultuous with occasional breaking and air entrainment next to the lateral walls. During the presented experimental measurements (Chapter IV), air entrainment was also observed to take place next to the sidewalls. The mean average water depth near the gate slightly increased by 2-3 cm as the bore propagated between

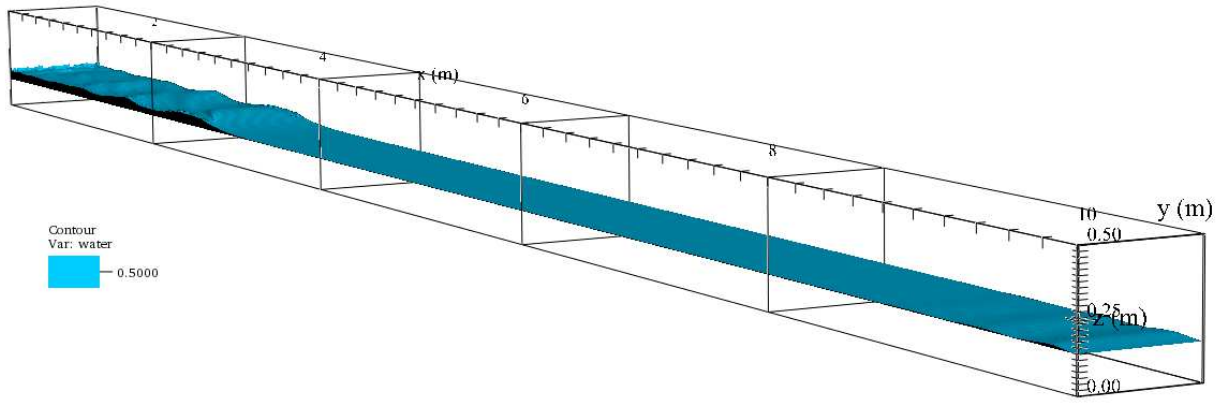

(a) $t = 4.61$ s

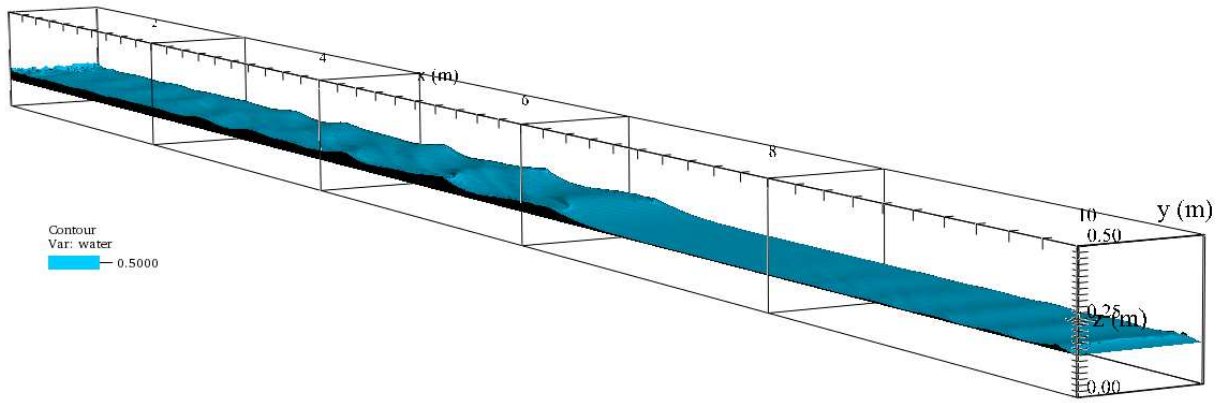

(b) $t = 10.46$ s

Figure VI.16: Undular bore propagation for the simulation ond3D at two different times. The free surface is estimated at $C = 0.5$. The bore propagates from left to right

2 to 8 m from the gate.

The undulations were three dimensional and presented cross waves patterns as seen during experiments (Chanson, 2010b). Cross waves were also observed during the present experimental study (Figure IV.15). The cross-waves were initiated from both sidewalls and intersected on the second wave of the secondary undulations (Figure VI.16, VI.17 and VI.18). The bore front lost its shape when the bore reached approximately $x \approx 9$ m due to undulations of the free surface downstream the inflow boundary ($x = 10$ m). Note that, for the simulation ond3DSEM, the cross waves progressively diminished as the bore propagated which might be linked with the steady flow velocity and the bore celerity being slightly different than for simulation ond3D (Figures VI.16b and VI.17b).

Unsteady flow velocity description

Figures VI.19 and VI.20 present the three components of the velocity field in the channel

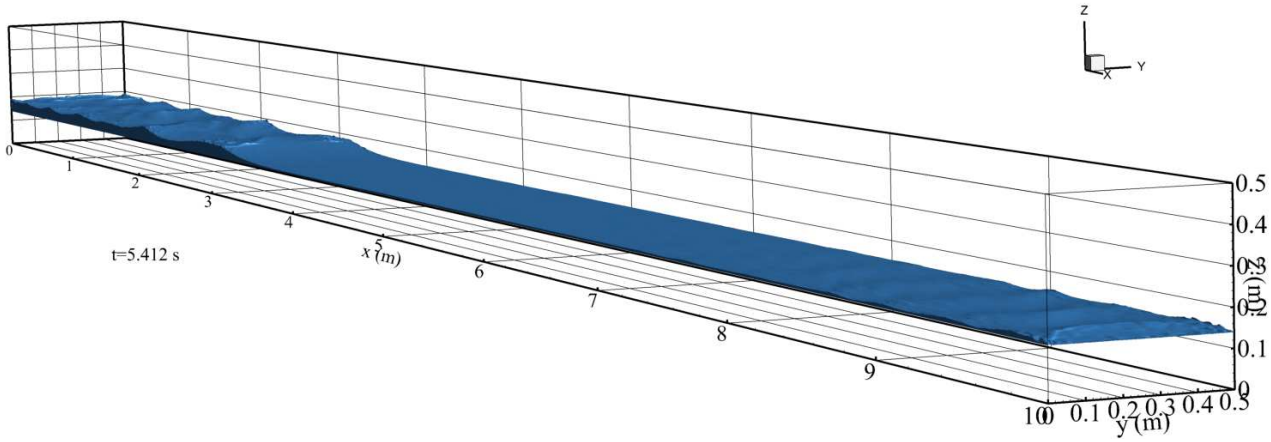

(a) $t = 5.41$ s

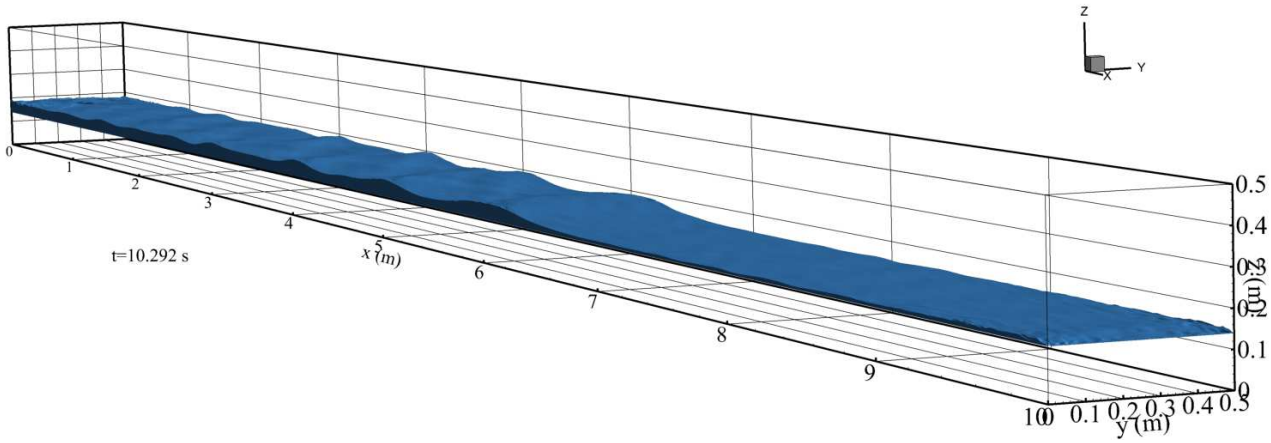

(b) $t = 10.29$ s

Figure VI.17: Undular bore propagation for the simulation ond3DSEM at two different times. The free surface is estimated at $C = 0.5$. The bore propagates from left to right

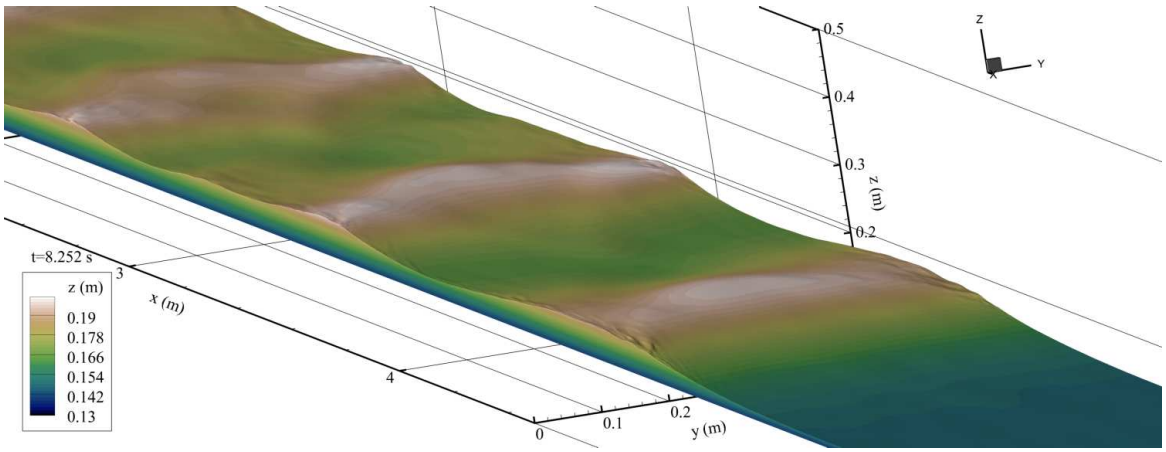

Figure VI.18: Details on the secondary undulations of the undular bore propagation at $t = 8.252$ s for the simulation ond3DSEM. The bore first crest is on the right. The free surface is coloured with the water depth

with the isoline of $u_x = 0$. Figure VI.21 presents the isocontour of $u_x = 0$, during the bore propagation with the isocontour of the bore free surface plotted with transparency.
Concerning the longitudinal velocity, for both simulation ond3D and ond3DSEM, a sudden velocity deceleration was observed beneath the bore front on the whole channel width. Beneath wave crests and troughs the longitudinal velocity u_x decelerated and re-accelerated respectively. Beneath the three first crest and close to the bed, a velocity reversal was observed for both simulations (Figures VI.19a and VI.20a). For the two simulations, the height of the recirculation differed. A height of approximately 2 cm above the bed was observed for the simulation ond3D and a maximal height of 3 cm for the simulation ond3DSEM. Note that, for the simulation ond3DSEM, some zones of recirculation detached from the bed and reached a height of 7 cm ($d_0 = 13.85$ cm). Another difference was observed in the shape of the recirculation zone. For the simulation ond3D, the upstream part of the recirculation was two dimensional and homogeneous over the channel width and the lateral wall, whereas the recirculation for the simulations ond3DSEM showed discontinuities toward the channel width and the lateral walls with large variations of its shape as illustrated in Figure VI.21. The velocity reversal next to the bed and sidewalls created fluctuations of the velocity which propagated toward the upper part of the water column and toward the channel centreline for the fluctuations initiated on the sidewalls (Figures VI.19 and VI.20).
The transversal velocity for both simulations fluctuated largely after the bore passage particularly close to the bed and lateral walls, downstream of the longitudinal velocity reversal. Looking at the transversal velocity variations downstream the flow reversal, the successive positive and negative values of u_y indicated the generation of coherent structures smaller near the sidewalls than near the bed (Figure VI.19b and VI.20b).
Concerning the vertical velocity, the velocity was globally positive and negative when the water level increased and decreased respectively. It had an oscillating pattern following the derivative of the free surface which had larger amplitudes close to the free surface than near the bed. For both simulations, fluctuations were larger downstream of the velocity reversal region beneath the first crest, close to the bed and the lateral walls. For the simulation ond3DSEM, the fluctuations propagated higher in the water column than for the simulation ond3D (Figure VI.19c and VI.20c).
The steady flow turbulence in ond3DSEM was seen to have an effect on the flow velocity particularly beneath the bore front. In the case ond3D, the zone of flow reversal was mainly two dimensional over the channel width. Whereas the zone of flow reversal was strongly deformed by the initial turbulence for ond3DSEM (Figure VI.21). Beneath the secondary undulations, due to the generation of turbulence downstream the flow reversal the effect of the initial turbulence was diminished, but could still be observed as the turbulence reached higher depth beneath

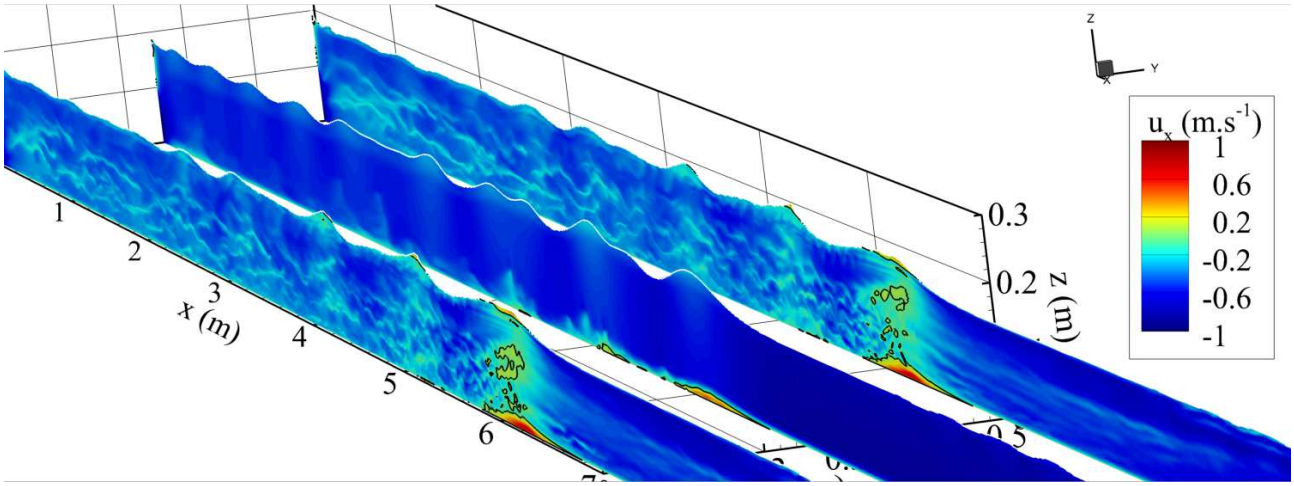

(a) Longitudinal component

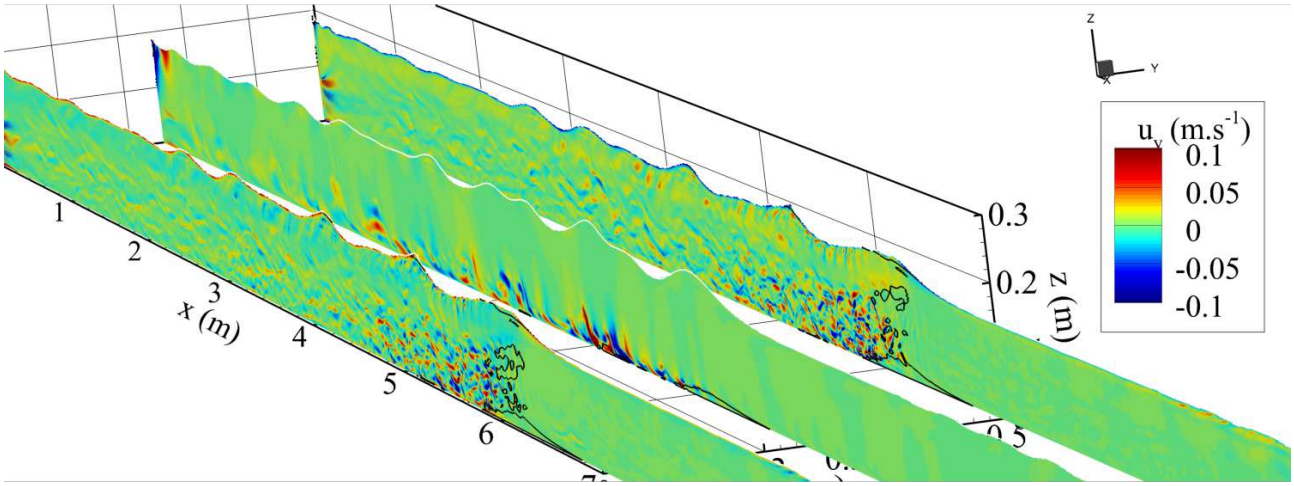

(b) Transversal component

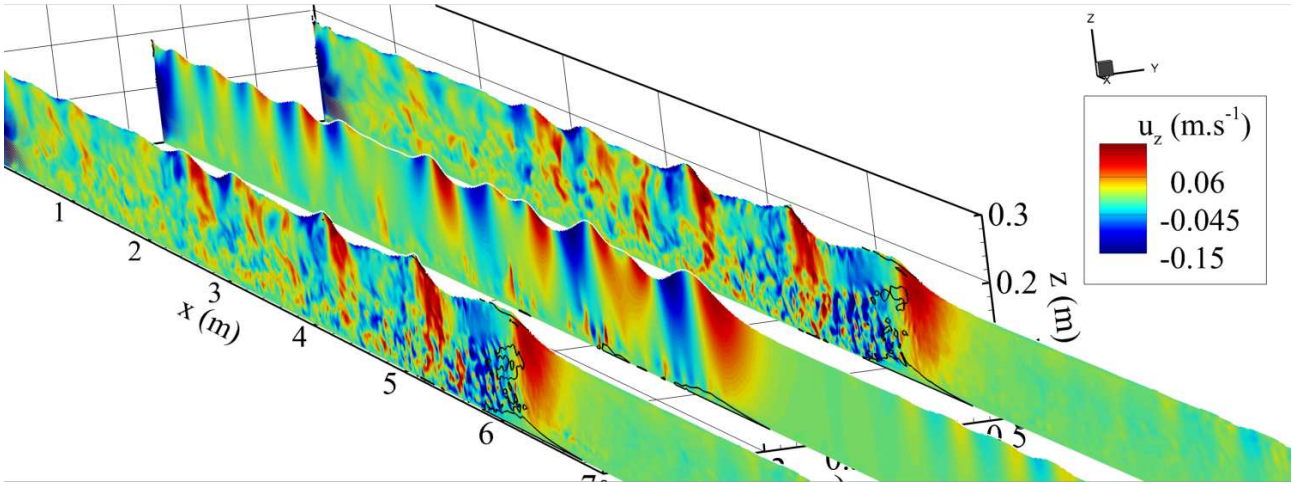

(c) Vertical component

Figure VI.19: Velocity fields in the undular bore of simulation ond3D. Bore propagation from left to right, bore at $x = 6$ m and $t = 10.46$ s. Vertical slices on the channel centreline and 5 mm from the sidewalls. The black line are isoline $u_x = 0$

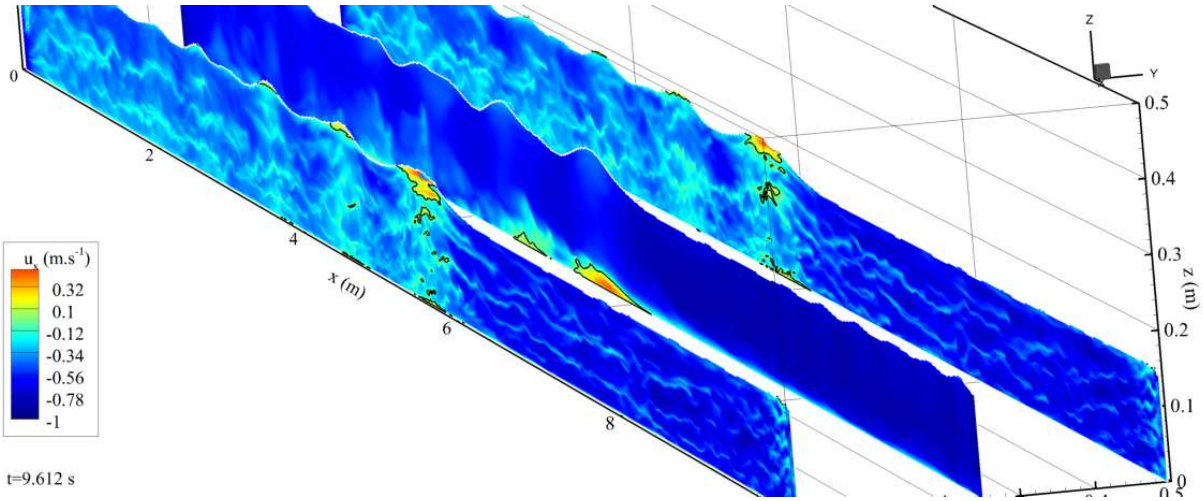

(a) Longitudinal component

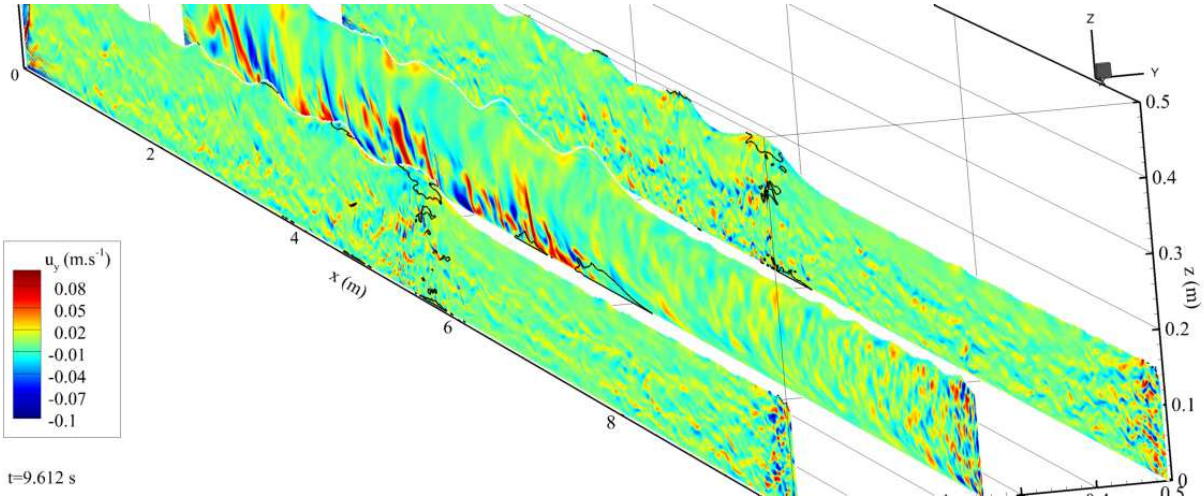

(b) Transversal component

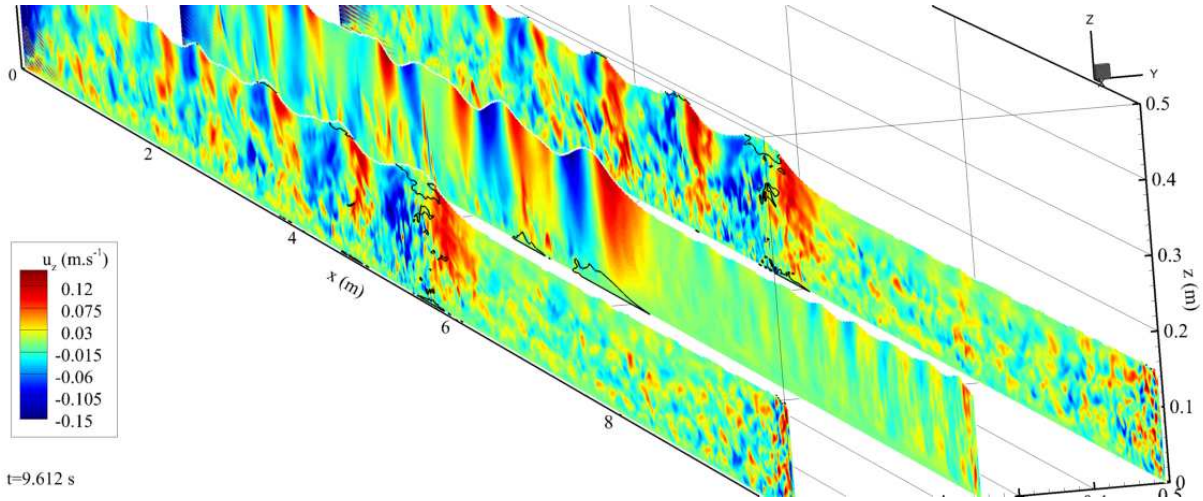

(c) Vertical component

Figure VI.20: Velocity fields in the undular bore of simulation ond3DSEM. Bore propagation from left to right, bore at $x = 5.5$ m and $t = 9.61$ s. Vertical slices on the channel centreline and 5 mm from the sidewalls. The black line are isoline $u_x = 0$

the secondary undulations. It also seemed that the initial turbulence had an effect on the bore celerity and appearance as mentioned earlier (Figure V.22 and Table V.8).

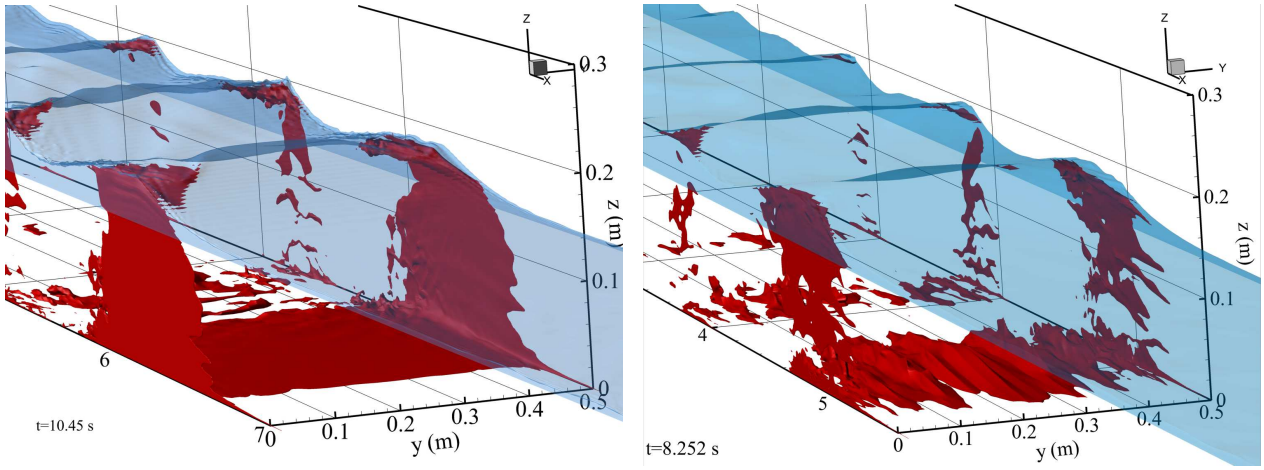

(a) Simulation ond3D, bore front at $x = 6$ m, $t = 10.46$ s

(b) Simulation ond3DSEM, bore front at $x = 5$ m

Figure VI.21: Velocity reversal beneath bores ond3D and ond3DSEM plotted with isocontour of $u_x = 0$ (in red) and free surface (in blue) plotted with transparency

VI.3.3 Discussion on bore effects and sensitivity to turbulent inflow conditions

VI.3.3.1 Simulations with a completely closed gate

For the simulations with a completely closed gate, the free surface evolution of the bore was mainly two dimensional with regular undulations along the entire channel width. The same two dimensional aspect of the free surface was observed during the experiments modelled by the simulation (Chanson, 2010a). The three dimensional simulations showed a free surface evolution on the channel centreline similar to the two dimensional simulation. But some effects of the undulations close to the wall (the small cross waves) could not be reproduced by the two dimensional simulation.

The flow evolution near the channel centreline was also globally similar to the two dimensional simulation rad2D13. Beneath crests, the unsteady flow velocity changed direction following the propagation of the bore and beneath trough, the flow velocity was partially orientated downstream. A separation in three zones along the vertical direction was observed in the water column beneath the wave crest as discussed in the previous section (VI.3.2.1). Nonetheless, the three dimensional simulations showed that the lateral walls also had significant effects on the flow. Small cross waves on the free surface appeared against the walls during the free surface

elevation as well as a strong flow reversal beneath the bore and secondary undulation crests (Figure VI.15). Beneath the trough, the longitudinal velocity which was partially orientated downstream, created some small recirculation zones. On a mobile bed, the strong shear on the bed and bank beneath the crest associated with recirculation structures would induce mixing and sediment resuspension. Close to the free surface, the strong flow reversal observed would help surfers to catch the bore.

The three dimensional simulations with and without initial turbulent steady flow (rad3D and rad3DSEM), showed some differences. Without initial turbulence, the simulation was mainly two dimensional except close to the wall. With an initially turbulent steady flow, the unsteady flow was three dimensional. The initial flow turbulence changed the maximal intensity of the flow reversal. For the case rad3DSEM, the flow reversal near the bed and away from the lateral walls reached up to 0.3 m.s^{-1} and only 0.21 m.s^{-1} for simulation rad3D (Figures VI.15).

Figure VI.22 present the isosurface of the Q-criterion with Q = 0.5 within the bore. A video of the Q-criterion evolution for simulation rad3DSEM is also presented in section D.3.3. The Q-criterion is the second invariant of the velocity gradient tensor (Hunt et al., 1988; Roth, 2000). It is defined as $Q = 1/2(\|\mathbf{\Omega}\|^2 - \|\mathbf{S}\|^2)$ where $\mathbf{\Omega}$ and $\mathbf{S}$ are the antisymmetric and symmetric component of $\nabla\mathbf{u}$ (also the vorticity and strain-rate tensors respectively). The quantity Q can be used to identify some coherent structures and vortices if $Q > 0$, i.e. regions where the vorticity dominates the strain (Hunt et al., 1988; Roth, 2000).

The bore passage for simulation rad3D did not seem to generate fluctuations. Moreover, for small values of the Q-criterion ($Q < 0.5$), few structures were observable during the bore passage (Figure VI.22a). Considering the velocity field of simulation rad3DSEM, some fluctuations of the steady flow seemed amplified after the bore passage (Figure VI.22b). By looking at the Q-criterion in simulation rad3DSEM, the coherent structures of the steady turbulent flow seemed to move following the free surface motion without appearance of more coherent structures beneath the bore front. Beneath the secondary undulations, the size of coherent structures increased and some structures appeared as the bore propagated (Figure VI.22b and movie in Appendix D.3.3).

VI.3.3.2 Simulations with a partially closed gate

For both three dimensional simulations with a partially closed gate, the bore free surface was three dimensional with appearance of cross waves (Figures VI.16 and VI.17). Chanson (2010b) also mentioned the appearance of cross waves during the physical experiment modelled by the numerical simulation.

The three dimensional simulations shared some similarities near the channel centreline with the two dimensional simulation. The longitudinal velocity decrease and increase beneath crests

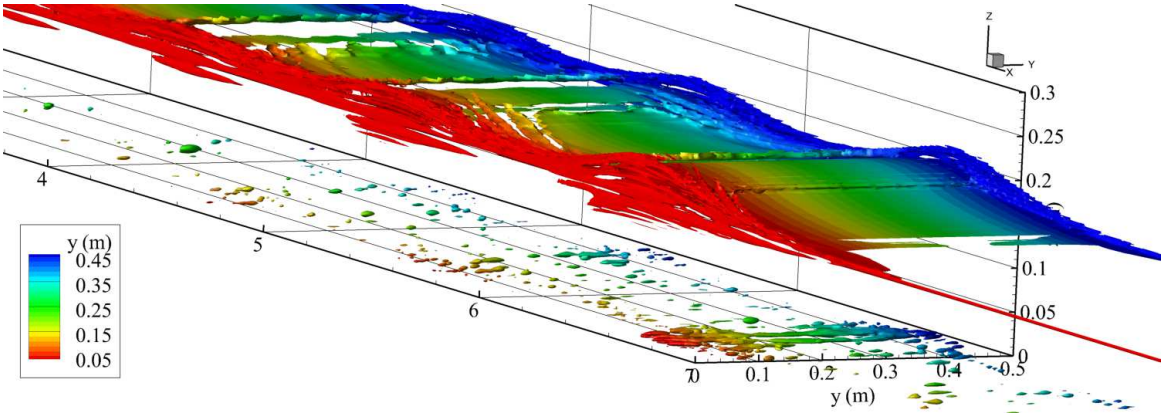

(a) Simulation rad3D, Q-criterion plotted with the free surface in the whole domain, bore front at $x = 7.8$ m, $t = 6.07$ s

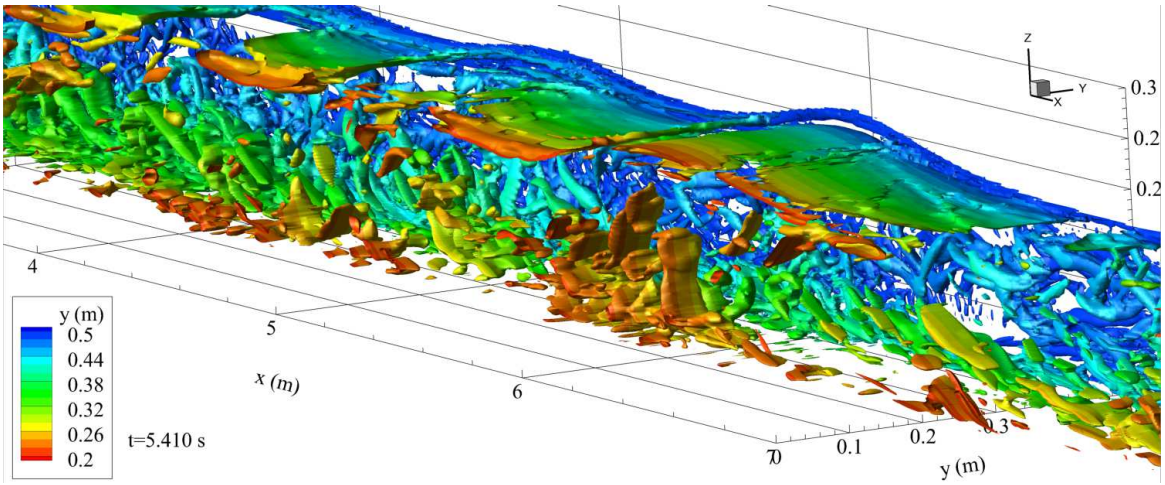

(b) Simulation rad3DSEM, criterion Q plotted for $y > 0.2$, bore front at $x = 6$ m, $t = 5.41$ s

Figure VI.22: Isosurfaces of the Q-criterion for Q = 0.5 beneath bores with colour mappings of the transversal distance

and troughs respectively. Moreover, a recirculation zone with a flow reversal was observed close to the bed below the bore crests. The recirculation zone was observed to create turbulent structures propagating upward in the water column. In the present experimental study, undular bores were also generated. The method of generation of bores was similar with a gate partially open, but over a rough bed. Velocity fluctuations generated from the reversal region on the bed were observed to propagate upward into the water column from the bed.

Recirculations were also observed against the channel sidewalls, also creating velocity fluctuations propagating toward the channel centreline. Some experiments were performed with measurement close to the sidewalls in undular bores (Koch and Chanson, 2009). Velocity reversals were observed beneath the bore crest on instantaneous measurements. Note that the

velocity reversals observed numerically were not observed by the modelled experiment (Chanson, 2010b). On the other hand, some flow reversal near the bed beneath undular bores were observed experimentally (Ryabenko, 1998).

The turbulent steady flow had a direct effect on the flow recirculation against the bed and the sidewalls. The recirculation zones were "deformed" by the turbulent flow changing the maximal values of the velocity reversal (Figures VI.21). For the simulation without the initial turbulent flow, the front of the flow reversal zone was nearly a line across the channel width. For the simulation with a turbulent flow, the front of the recirculation zone was complex and some separations of the zone occurred (Figures VI.21). Such a small three dimensional recirculation would be difficult to identify experimentally, particularly since the zone was sensitive to the flow turbulence.

Figure VI.23 illustrates the shape of coherent structures created in the water beneath the bore front using the Q-criterion with a value Q = 2. Figure VI.24 presents colour mappings of the Q-criterion for a slice of the domain on the channel centreline. A video of the Q-criterion evolution is also presented in section D.3.4. For the simulation ond3D, the recirculation appeared above the front of the recirculation zone taking the form of long tube orientated transversally to the flow (Figure VI.23a). At the end of the recirculation zone, the structures lost their "tubular" shapes and detached from the zone of velocity reversal. Then, the structures generated were advected downstream and upward into the flow, and slightly toward the channel centreline for the structures created against the sidewalls (Figure VI.24a). For the simulation ond3DSEM, the coherent structures were deformed by the initial turbulent flow and did not present a "tubular" aspect above the reversal zone (Figure VI.23b). But they followed a similar motion as seen in simulation ond3D. They tended to move higher in the flow (Figure VI.24b), probably due to the initial turbulence. Note that the coherent structures observed with the Q-criterion near the channel centreline (for approximately 0.20 m $< y <$ 0.30 m) appeared flattened in the transverse direction. This is believed to be an effect of the large transversal mesh size on the channel centreline.

For the two dimensional case, coherent structures were also observed to detach from the main recirculation beneath the bore front and a frequency of detachment was recorded. For the three dimensional simulations, the detachment occurred without organisation (Figure VI.23) and an accurate frequency of ejection could not be calculated. Nonetheless, the detachment of coherent structures occurred in a similar manner as observed for the two dimensional simulation ond2D17. The hypothesis of structures generated in a way similar to those behind a body into a flow with a high Reynolds number remains since turbulence appeared in the wake of the velocity reversal region (section VI.2.3). Note that for the three dimensional simulations, the structures generated in the wake of the recirculation region were associated with velocity fluctuations of

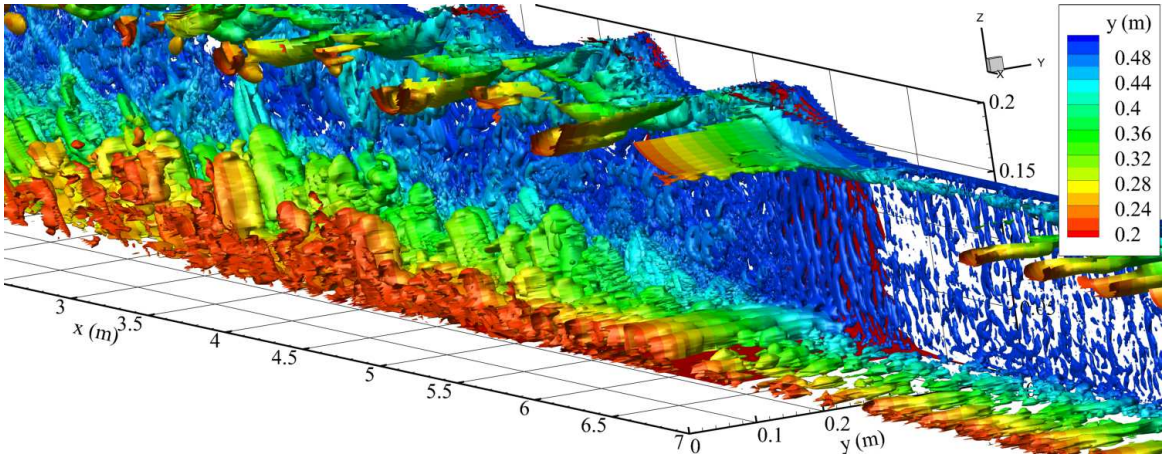

(a) Simulation ond3D, Q-criterion plotted for $y > 0.2$, bore front at $x = 5.7$ m, $t = 9.82$ s

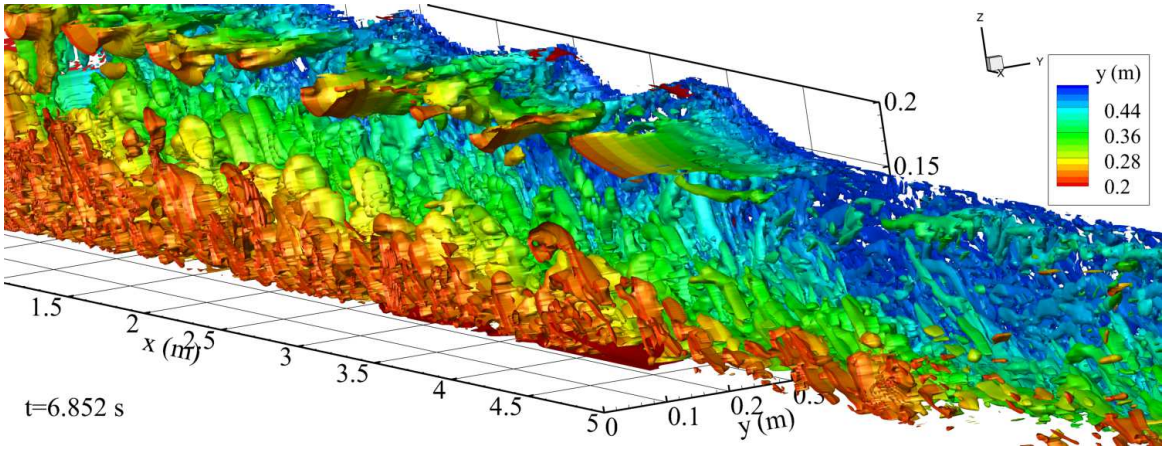

(b) Simulation ond3DSEM, criterion Q plotted for $y > 0.2$, bore front at $x = 4.5$ m, $t = 6.89$ s

Figure VI.23: Isosurfaces of the Q-criterion for Q = 2 beneath bores with colour mappings of the transversal distance and the isosurface of $u_x = 0$ in red

smaller intensity than for the simulation ond2D17 (Figure V.23). The structures in simulation ond2D17 were "forced" to appear and to exist only in a two dimensional space whereas the structures in simulations ond3D and ond3DSEM could develop in three dimensions.

VI.3.3.3 Effects of the gate opening and link with tidal bores

The sensitivity to the bore generation conditions was studied by using two different types of gate closure for a similar Froude number. It was observed that the flow properties were significantly different depending on the conditions of generation. For the gate completely closed, the flow between the gate and the door is supposed to be zero as explained by the theory (section II.3.3). For a bore generated with a gate partially opened, the water keeps flowing downstream

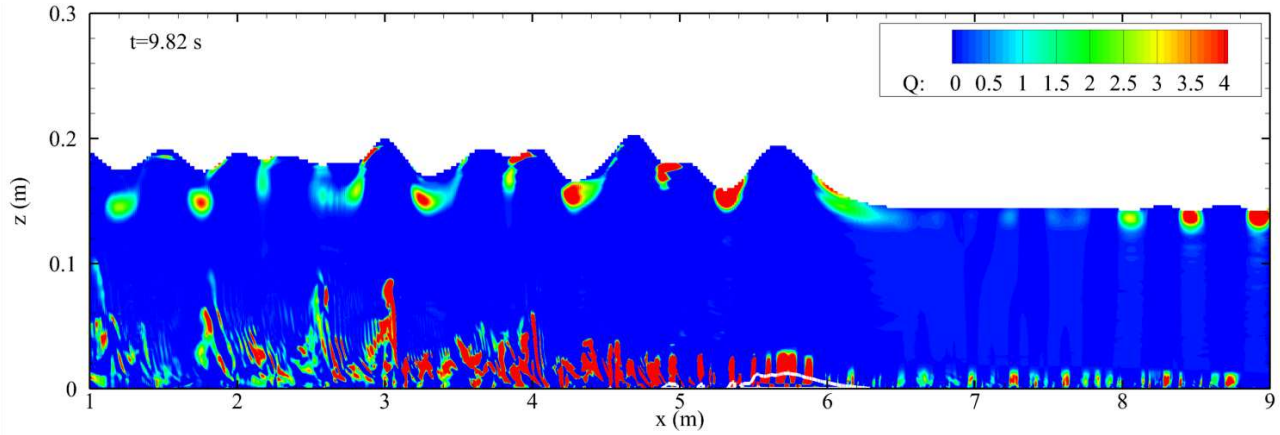

(a) Simulation ond3D, bore front at $x = 5.7$ m, $t = 9.82$ s

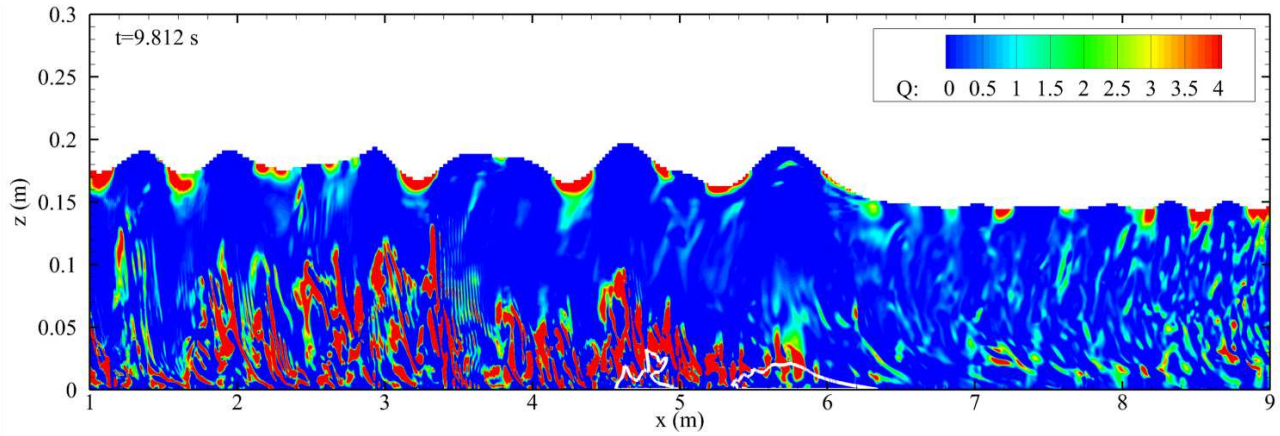

(b) Simulation ond3DSEM, bore front at $x = 5.7$ m, $t = 9.81$ s

Figure VI.24: Colour mapping of the Q-criterion for a slice of the domain on the channel centreline. The white line is the isoline of $u_x = 0$

after the bore generation. The first type of bore induced successive flow reversals below crests and troughs, and slightly changed the fluctuation intensity of the initially turbulent flow. The second type of bore created a flow reversal only close to the bed beneath crests. This reversal generated velocity fluctuations. In the case of prototype tidal bores, a complete flow reversal was generally observed in field studies. Therefore, only a limited parallel can be made between the positive surges generated by reflection against a gate and the phenomenon in rivers.
Nevertheless the flow within numerical bores shared one important feature: the strong flow reversal just above the bed (from 0.8 to 1.1 V_0). Similar observations were made on velocity data from field studies on tidal bore (personal communication with Lucille Furgerot and Dominique Mouazé, working on field studies for the ANR project MASCARET). The flow reversal just above the bed during the bore front could induce scour of the bed in rivers and estuaries. The strong shear just above the bed might be a particularity of positive surge propagating over

an opposite flow since it was not observed above positive surge propagating above a quiescent water (dam break case). For bore generated by reflection against a gate, it was observed that gravel could be pushed upstream by the flow reversal beneath breaking bores (Khezri and Chanson, 2012c). A flow reversal is also observed beneath breaking bores (Khezri and Chanson, 2012c; Koch and Chanson, 2009, present experimental study). Next to the bed, the flow reversal region is larger than for undular bore. Nonetheless, the strong shear generated by undular bores beneath bed and sidewalls would have a strong potential for mixing and sediment resuspension.

VI.4 Summary

Two dimensional and three dimensional simulations of undular bores were performed based on some experimental configurations (Chanson, 2010a,b). The three dimensional simulations reproduced both non turbulent and turbulent initially steady flow conditions.

The two configurations, one with a downstream gate fully closed and the other with a gate partially closed, were different in term flow evolution. In one hand, the simulations with a gate fully closed showed successive flow reversals beneath crests and troughs. On the other hand, the simulations with a partially closed gate showed velocity reversal zones close to the bed and sidewalls following the bore propagation. In both cases, strong shear was observed close to the bed and the sidewalls. For the case with a gate partially closed, coherent structures were observed in the wake of the velocity reversals. It was believed to be created in a similar way to the wake flow downstream of objects at high Reynolds number. The coherent structures propagated downstream following the flow motion and tended to move upward into the water column confirming the observation made in the experimental study (Chapter IV).

The comparison of two and three dimensional simulations showed that two dimensional simulations were insufficient to reproduce all bores features but could give some basic results concerning the global flow evolution.

The comparison of the simulation with and without an initial turbulent flows suggested that the initial turbulence had a limited effect on the free surface evolution, the bore celerity and the secondary undulation's shape for the investigated flow conditions. Whereas for the velocity, stronger fluctuations were observed for the flow using the synthetic turbulent method SEM as well as a different flow dynamic: for the case rad3D, the flow remained mainly two dimensional in the case of a non turbulent initial steady flow. The SEM was necessary to recreate realistic conditions of bore propagation.

VII

Conclusion

Positive surges are unsteady open channel flow phenomena corresponding to a sudden flood propagating as a wave train eventually with a breaking roller. Geophysical examples include tidal bores. Tidal bores appear when the leading edge of the tide surges into some estuaries and rivers under specific tide and bathymetric conditions. Tidal bores affect the estuary ecosystem because of the strong mixing and sudden change of flow conditions associated with their upstream propagation.

This thesis started in 2010 as part of two French projects to study tidal bores. The interest of physicists for tidal bores flourished in the late 1800 early 1900, with theoretical studies (Barré de Saint Venant, 1871; Brownlie, 1901; Comoy, 1881; Rayleigh, 1908) and visual observations (Booraem, 1902; Branner, 1884; Cornish, 1900; Gordon, 1924; Moore, 1893). Afterwards, the attention given to tidal bores progressively decreased (at least in France) until the 1990s when the media started to present news coverage and TV documentary on tidal bores. In China, the phenomenon remained more present due to a strong anchoring in folklore as a cultural heritage; Festivals happen every year to celebrate the propagation of the several meter high bore known as the Silver Dragon, in the Qiantang River. In the meantime, with the regain of public interest, scientific works became more available, some detailed field studies were published (Kjerfve and Ferreira, 1993; Navarre, 1995; Simpson et al., 2004; Wolanski et al., 2004) and laboratory modelling took place to reproduce positive surges for comparisons with

tidal bores (Chanson, 2010a,b; Chanson and Tan, 2010; Koch and Chanson, 2008, 2009) or for more general studies of positive surges (Bukreev, 2000; Hornung et al., 1995; Yeh and Mok, 1990). Following the publication of experimental data came the first preliminary numerical works (Furuyama and Chanson, 2010; Lubin et al., 2010a) solving the Navier-Stokes equations and showing encouraging results for two dimensional simulations. Other numerical work of interest were performed (Madsen et al., 2005; Peregrine, 1966) but limited to the modelling of the free surface evolution.

At the end of this PhD project, late 2013, another PhD study on laboratory model of tidal bores came to term by N. Khezri (Khezri and Chanson, 2012a, 2012b) focusing on the sediment motion induced by the bore passage. Early 2014, two thesis will come to a term with the work of L. Furgerot (Furgerot et al., 2013) studying the sediment processes in natural system and A. Berchet (Berchet et al., 2013) providing a numerical study of sediment transport during positive surges (physical and numerical model). The two last theses are part of the ANR project MASCARET. Some field investigation were also conducted in France in the Garonne River and the Bay of Mont Saint Michel (Chanson et al., 2011; Furgerot et al., 2013; Mouazé et al., 2010; Reungoat et al., 2012) and in China, with a study in the Qiantang River (Fan et al., 2012). Overall, those works provided some key outcome on the turbulence and sediment properties and sediment fluxes in rivers with tidal bores. Such data constitutes an important, yet incomplete, reference for study and comparison with model studies (physical and numerical).

VII.1 Result summary

In the previous context, the present work was orientated toward performing a complementary physical and numerical study. The experimental study was conducted in a relatively large channel with a fixed gravel bed. The steady flow properties were investigated using a Pitot tube and acoustic Doppler velocimeters (ADVs) at several locations. This provided a detailed characterisation of the steady flow, with the inspection of the boundary layer development, the boundary conditions as well as the bore generation processes. In the initially steady flow, the data showed the development of a turbulent boundary layer above the fixed gravel bed. The velocity profiles in the boundary layer followed a power law with an exponent $1/N$, with N varying between 4 and 5. The boundary shear stress was estimated using several methods. The bed roughness height was estimated as $k_s \approx 6$ mm close to the gravel median size $d_s = 5.7$ mm. The unsteady flow measurements were conducted based upon a Froude similitude. The free surface evolution was recorded using non intrusive sensors by ensemble averaging the measurements which was rarely done in previous study. Several configurations were tested to produce undular and breaking bores. In previous studies, only the fluctuations of the free surface for

breaking bores were detailed based on percentile differences (Docherty and Chanson, 2012). Herein, for undular bores, the fluctuations of the free surface were found to be small in comparison to breaking bores. This was due to the roller and bubble entrainment observed in breaking bores generating large fluctuations of the free surface elevation. Two initial steady flow conditions were selected to compare the effects of the Reynolds number for $Re_b = 1$ to 2×10^5. The analysis of the undulation characteristics, such as wave length and wave amplitude, seemed independent of the Reynolds number as well as the distance travelled by the bore, within the experimental flow condition.

The unsteady velocity measurements were performed for two different initially steady flow conditions and two types of bores: undular with and without a breaking roller. The velocity data were recorded at 200 Hz using ADVs, mostly at 6.13 m upstream of the gate. The longitudinal velocity evolution was characterised by a sudden deceleration beneath the bore front, followed by oscillations linked with the free surface undulations. For the breaking bores, a reversal of the ensemble averaged longitudinal velocity occurred beneath the bore front next to the bed and the secondary undulations, as observed in previous studies. In comparison with breaking bores, only some transient reversal occurred for the instantaneous velocity with undular bores. The transverse velocities exhibited large fluctuations beneath the bore front and wave train. The averaged vertical velocities were closely linked with the free surface evolution which was not detailed in previous studies. Beneath the bore front, the velocity fluctuations were larger close to the bed while they seemed to move upwards after the bore front passage. This was possible to observe after extrapolating colour mappings of the ensemble averaged data recorded at several depths, which was unique to this study. The velocity fluctuation data suggested an upward advection of macro-scale structures in the wake of the bore. Such structures would have some influence on the turbulent mixing in natural channels with movable bed with mud and sand.

The turbulent integral time and length scales were measured for the first time using two ADVs facing each other transversally to the flow, the steady and unsteady flow properties being investigated. The turbulent length scales were similar in steady and unsteady flows, with slightly larger values in the upper part of the water column during the unsteady flows (at $z/d_0 = 0.63$). The turbulent time scales were larger in the unsteady flow with a difference of the transversal integral turbulent time scale T_y up to 52% between the breaking and undular bores at $z/d_0 = 0.45$. This was believed to be linked with the flow deceleration slowing down the advection of turbulent structures passing through the ADVs.

The laboratory study was subjected to a few limitations. The intrusive effects of the ADV were investigated in Simon and Chanson (2013) and were shown to have an influence on the

flow. The measurements could not be performed below 5.8 mm from the bed and above the initial water depth because of the shape of the ADV head and because the ADV need to be immersed in water. The measurements of the turbulent integral scales were restricted by some interference appearing when the two ADVs were too close to each other. Finally, the measurements with ADV were only punctual measurements in space, thus limiting the analysis of the flow patterns. Nonetheless, this study presents a first attempt at measuring integral turbulent scales in positive surges and also offers a unique characterisation of the spatial evolution of the turbulence and the turbulent integral scales.

The numerical study aimed at modelling undular bores in a smooth channel to get the complete flow mapping of experimental bores. This represent the first numerical study of undular bores solving the Navier-Stokes equations for a two-phase flow. Here, the study was conducted in both two and three dimensions taking advantage of parallel computing. The Navier-Stokes equations were solved using large eddy simulation with a volume of fluid method to track the free surface. The steady flow turbulence was recreated by using a synthetic eddy method on the domain inlet. For the first time, undular bores were generated with and without an initially turbulent flow. The ability of numerical models at recreating turbulent steady flow conditions and at reproducing positive surges was tested and successfully compared to experimental data. The free surface evolution showed some characteristic bore features with the appearance of cross waves for the simulation realised with a bore Froude number of 1.26. The global evolution of bores was similar to experimental observations.
The unsteady velocity data showed a different evolution depending upon the bore generation. The simulations with a fully closed gate showed successive flow reversals beneath crests and troughs. The simulations with a partially closed gate showed velocity reversal zones close to the bed and sidewalls following the bore propagation. In both cases the flow reversal induced a strong shear next to the bed and the sidewalls beneath wave crests. Close to the bed, the intensity of flow reversal reached maximum values of up to 1.7 and 0.9 times the initial steady flow velocity for the case with a completely and partially closed gate respectively.
For the case with a gate partially closed, coherent structures were observed in the wake of the velocity reversals beneath the bore front close to the bed. It was believed to be similar to turbulent structures appearing in the wake of an object at high Reynolds number. For the two dimensional simulation, the Strouhal number based on the recirculation size was 0.14. In three dimensions, the flow generated complex structures. A characteristic Strouhal number could not be estimated due to the irregular appearance of the structure. The coherent structures were advected downstream following the flow motion and tended to move upward in the water column in agreement with the experimental observations.

The comparison of two and three dimensional simulations showed that the two dimensional simulations were insufficient to reproduce all the bores features, such as cross waves and coherent structures, but could give some basic results concerning the global flow patterns. Nonetheless, it stresses the importance of studying the flow in three dimensions. The comparison of the simulations with and without turbulence in the initial steady flow showed that the initial turbulence had a limited effect on the free surface evolution and the bore celerity, but could have a more significant effect on the velocity field. Indeed, the shape and intensity of the recirculation zones were affected by the turbulence in the steady flow.

Some limitations were observed with the numerical simulations. The case with a partially closed gate presented some difference with the experimental results as the initial steady flow conditions between experiment and numerical simulation were different. The numerical simulations were limited by the mesh size selected upon the available computing resources. In the initially steady flow, some limitations also appeared with non physical error next to the downstream boundary but disappeared once the bore was generated. Nevertheless, the numerical work presents a simultaneous characterisation of both the free surface and velocity, validated for each case with experimental data.

VII.2 Perspectives

The present study showed that positive surges propagating against steady flow induced large changes in the flow field. Tidal bores are particular cases of positive surges. They propagate in natural rivers and usually induce a complete flow reversal after their passage. It was seen that models of tidal bores generated numerically and experimentally did not induce a complete flow reversal after the bore propagation. Therefore the flow dynamics in the idealised model could be different to those in tidal bores in rivers. Nonetheless, both idealised model and tidal bore tended to induce a strong shear next to the bed and a similar free surface evolution. The findings might help understanding the mixing and scouring mechanisms within positive surges in moveable bed open channel, including the dispersion of fish eggs, pollutants, and sediments in rivers and estuaries. The findings could also be applied to help in the construction of river structures that can be damaged by tidal bore (Jiang et al., 2014) by predicting the interaction of the bore with the structures.
For a better understanding of tidal bore effects on estuaries and rivers, some limitations remain to be overcome. For experimental studies, the use of a non intrusive probe would give detailed flow evolution without interfering with the flow. Particle image velocimetry or similar techniques can record a more complete velocity field than ADV and can also give access to turbulent

scales. The use of ADV profiler could also give information on the turbulent scales; however the probe remains intrusive to the flow. The use of different techniques of measurements would also give more necessary and complementary information to configure and to validate the numerical simulations.

Sand and mud are common sediments in estuaries and rivers affected by tidal bores. Measurements with movable bed, like sand or mud, could be performed to see the effects of the bore. In both experimental and numerical studies, a strong shear was observed next to the bed beneath the bore front. Some studies were performed for moveable gravel bed beneath undular and breaking bores. The breaking bores were observed to induce gravel motion (Khezri and Chanson, 2012c). The interaction of the strong shear and flow reversal with a fine movable bed might give information on the sediment motion associated with the bore.

In river, there are no techniques that can measure the complete flow evolution in a large domain. Numerical simulations would be the only tool to give detailed data on the complete flow evolution in a portion of a river or an estuary. However, with numerical simulations, the size of the mesh induces limitations in term of computers properties (speed and storage) but also accuracy of the solution. For this study, the mesh size might need to be thinner for a better accuracy particularly in the transversal direction in order to follow the appearance and evolution of small turbulent structures. The domain should probably be discretised by a $5000 \times 500 \times 500$ grid mesh which makes it a 1.25×10^9 grid mesh with a transversal mesh size within 5 mm. Such a simulation is nowadays possible for modern super calculator.

Tidal bores are undular and breaking. Herein, the numerical study was focused on undular bores. Numerical studies of breaking bore would be interesting to observe the interaction of the bed turbulence with the turbulence created by the roller. A preliminary study was conducted (Simon et al., 2011a), but some limitation in the CFD code together with a lack of knowledge on experimental measurements needed to be overcome.

The experimental measurements conducted within this study were planned to be used for numerical study. However, a method modelling the gravel bed was not validated with the numerical code. A study using the experimental data for bores over a rough bed is planned to be realised as soon as an accurate method to model the bed is found. A method modelling the gravel bed using an equivalent porous media is being tested. The method still requires validation for simulation in three dimensions before exploitation.

Finally, those studies were motivated by the comprehension of tidal bores. Numerical simulations are planned to be used to model the geophysical phenomenon. Details of the complete flow conditions are missing in order to recreate the geophysical tidal bore flow conditions. Nevertheless, with some of the previous steps achieved, i.e. with validated methods to model rough bed and the sediments evolution with the flow, simulations with various sediments and irregular

bed roughness could be realised, making simulations of the complete processes taking place in full scale tidal bores a possibility.

References

Abadie, S. (2001). "Modélisation numérique du déferlement plongeant". French. In: *Revue Française de Génie Civil* 5.7, pp. 931–944.

Abbott, M. B. and G. S. Rodenhuis (1972). "A numerical simulation of the undular hydraulic jump". In: *Journal of Hydraulic Research* 10.3, pp. 239–257.

Abbott, M. R. and M. J. Lighthill (1956). "A theory of the propagation of bores in channels and rivers". In: *Mathematical Proceedings of the Cambridge Philosophical Society* 52.02, pp. 344–362.

Andersen, V. (1978). "Undular hydraulic jump". In: *Journal of the Hydraulics Division-Asce* 104.8, pp. 1185–1188.

Angot, P. (1989). "Contribution à l'étude des transferts thermiques dans des systèmes complexes : application aux composants électroniques". French. PhD thesis. Bordeaux, France: Université de Bordeaux I.

Angot, P., C.-H. Bruneau, and P. Fabrie (1999). "A penalization method to take into account obstacles in incompressible viscous flows". In: *Numerische Mathematik* 81.4, pp. 497–520.

Archer, A. W. (2013). "World's highest tides: Hypertidal coastal systems in North America, South America and Europe". In: *Sedimentary Geology* 284–285, pp. 1–25.

Arquis, E. and J.-P. Caltagirone (1984). "Sur les conditions hydrodynamiques au voisinage d'une interface milieu fluide-milieux poreux: application à la convection naturelle". French. In: *Comptes rendus de l'Académie des sciences. Série II b* 299, pp. 1–4.

Ascher, U. M. (1998). *Computer methods for ordinary differential equations and differential-algebraic equations*. Philadelphia, USA: Society for Industrial and Applied Mathematics.

Babinet, J. (1855). *Études et lectures sur les sciences d'observation et leurs applications pratiques*. French. Vol. 1. Paris, France: Mallet-Bachelier.

Bardina, J., J. Ferziger, and W. C. Reynolds (1980). "Improved subgrid-scale models for large-eddy simulation". In: *13th Fluid and PlasmaDynamics Conference*. Fluid Dynamics and Co-located Conferences. Snowmass, USA: American Institute of Aeronautics and Astronautics.

Barré de Saint Venant, A. (1871). "Théorie et équations générales du mouvement non permanent des eaux courantes". French. In: *Comptes rendus des séances de l'Academie des Sciences, Paris, france, Séance 17 Juillet 1871* 73, pp. 147–154.

Bartsch-Winkler, S. and D. K. Lynch (1988). *Catalog of worldwide tidal bore occurrences and characteristics*. USGS Numbered Series Ci no. 1022. U.S. Government Printing Office, p. 20.

Benet, F. and J. A. Cunge (1971). "Analysis of experiments on secondary undulations caused by surge waves in trapezoidal channels". In: *Journal of Hydraulic Research* 9.1, pp. 11–33.

Benjamin, T. B. and M. J. Lighthill (1954). "On cnoidal waves and bores". In: *Proceedings of the Royal Society A: Mathematical, Physical and Engineering Sciences* 224.1159, pp. 448–460.

Benson, D. J. (2002). "Volume of fluid interface reconstruction methods for multi-material problems". In: *Applied Mechanics Reviews* 55.2, p. 151.

Berchet, A., A. Beaudoin, A. Huberson, G. Rousseaux, B. Simon, and P. Lubin (2013). "Une vision naïve du transport sédimentaire induit par un mascaret ondulant". French. In: *21ème Congrés Français de Mécanique*. Bordeaux, France: AFM, Maison de la Mécanique, 39/41 rue Louis Blanc - 92400 Courbevoie.

Bonneton, P., J. Van de Loock, J.-P. Parisot, N. Bonneton, A. Sottolichio, G. Detandt, B. Castelle, V. Marieu, and N. Pochon (2011). "On the occurrence of tidal bores - The Garonne River case". In: vol. SI 64. Journal of Coastal Research. Poland, pp. 1462–1466.

Booraem, J. V. V. (1902). "Note on the tidal bore". In: *Bulletin of the American Geographical Society* 34.2, pp. 146–149.

Bradshaw, P. (1971). *An introduction to turbulence and its measurement*. Oxford, UK: Pergamon Press.

Branner, J. C. (1884). "The 'Pororoca,' or bore, of the Amazon". In: *Science* 4.95, pp. 488–492.

Breil, J. (2001). "Modélisation du remplissage en propergol de moteur à propulsion solide". French. PhD thesis. Bordeaux, France: Université de Bordeaux I.

British Standards (1951). *Flow measurement: BS 1042: 1943: Incorp. amendments issued March 1946, September 1948 and October 1951*. London: British Standards Institution.

Brownlie, A. (1901). "The solution of the problem of the tidal bore". In: *Bulletin of the American Geographical Society* 33.4, pp. 318–324.

Bukreev, V. (2000). "Undular bore in the counterflow". In: *Doklady Physics* 45.8, pp. 422–424.

Caplain, B. and D. Reungoat (2013). "Étude expérimentale de la turbulence de grille sur le transport sédimentaire". In: *21ème Congrés Français de Mécanique*. Bordeaux, France: AFM, Maison de la Mécanique, 39/41 rue Louis Blanc - 92400 Courbevoie.

Caputo, J.-G. and Y. A. Stepanyants (1999). "Bore formation, evolution and disintegration into solitons in shallow inhomogeneous channels". In: *Nonlin. Processes Geophys.* 10.4/5, pp. 407–424.

Chanson, H. (2001). "Flow field in a tidal bore: a physical model". In: *Proc. 29th IAHR Congress*. Beijing, China: Guifen Li, pp. 365–373.

Chanson, H. (2004a). *Environmental hydraulics of open channel flows: an introduction*. 2nd. Oxford, UK: Elsevier Butterworth-Heinemann.

Chanson, H. (2004b). *The hydraulics of open channel flow: an introduction ; basic principles, sediment motion, hydraulic modelling, design of hydraulic structures*. 2nd. London, UK: Butterworth Heinemann.

Chanson, H. (2004c). "The tidal bore of the Sélune river, Mont Saint Michel Bay, France". In: *Shore and Beach* 72.4, pp. 14–16.

Chanson, H. (2005). "Physical modelling of the flow field in an undular tidal bore". In: *Journal of hydraulic research* 43.3, pp. 234–244.

Chanson, H. (2008). *Turbulence in positive surges and tidal bores. Effects of bed roughness and adverse bed slopes*. Department Technical Report CH68/08. Brisbane, Australia: School of Civil Engineering, The University of Queensland, p. 121.

Chanson, H. (2009a). *An experimental study of tidal bore propagation: The impact of bridge piers and channel construction*. Hydraulic Model Report CH74/09. Brisbane, Australia: School of Civil Engineering, The University of Queensland, p. 110.

Chanson, H. (2009b). *Applied hydrodynamics: an introduction to ideal and real fluid flows*. Leiden: CRC.

Chanson, H. (2010a). "Undular tidal bores: basic theory and free-surface characteristics". In: *J. Hydraul. Eng.* 136.11, pp. 940–944.

Chanson, H. (2010b). "Unsteady turbulence in tidal bores: effects of bed roughness". In: *Journal of Waterway, Port, Coastal, and Ocean Engineering* 136.5, pp. 247–256.

Chanson, H. (2011a). *Tidal bores, aegir, eagre, mascaret, pororoca: theory and observations*. Singapore: World Scientific.

Chanson, H. (2011b). "Turbulent shear stresses in hydraulic jumps, bores and decelerating surges". In: *Earth Surface Processes and Landforms* 36.2, pp. 180–189.

Chanson, H. (2011c). "Undular tidal bores: effect of channel constriction and bridge piers". In: *Environmental Fluid Mechanics* 11.4, pp. 385–404.

Chanson, H. (2012). "Momentum considerations in hydraulic jumps and bores". In: *Journal of Irrigation and Drainage Engineering* 138.4, pp. 382–385.

Chanson, H. and G. Carosi (2007). "Turbulent time and length scale measurements in high-velocity open channel flows". In: *Experiments in Fluids* 42.3, pp. 385–401.

Chanson, H. and N. J. Docherty (2012). "Turbulent velocity measurements in open channel bores". In: *European Journal of Mechanics - B/Fluids* 32, pp. 52–58.

Chanson, H., P. Lubin, and S. Glockner (2012). "Unsteady turbulence in a shock: physical and numerical modelling in tidal bores and hydraulic jumps". In: *Turbulence: theory, types, and simulation*. Nova Science Publishers. Vol. 3. Hauppauge, N.Y: R.J. Marcuso, pp. 113–148.

Chanson, H., D. Reungoat, B. Simon, and P. Lubin (2011). "High-frequency turbulence and suspended sediment concentration measurements in the Garonne River tidal bore". In: *Estuarine, Coastal and Shelf Science* 95.2–3, pp. 298–306.

Chanson, H. and K.-K. Tan (2010). "Turbulent mixing of particles under tidal bores: an experimental analysis". In: *Journal of Hydraulic Research* 48.5, pp. 641–649.

Chanson, H. and Y. H. Toi (2013). "Breaking tidal bore: comparison between field data and laboratory experiments". In: *21ème Congrés Français de Mécanique*. Bordeaux, France.

Chanson, H., M. Trevethan, and C. Koch (2007). "Discussion of "Turbulence Measurements with Acoustic Doppler Velocimeters" by Carlos M. García, Mariano I. Cantero, Yarko Niño, and Marcelo H. García". In: *Journal of Hydraulic Engineering* 133.11, pp. 1283–1286.

Chassaing, P. (2000). *Turbulence en mécanique des fluides. Analyse du phénomène en vue de sa modélisation à l'usage de l'ingénieur*. French. Polytech de l'INP. Toulouse, France: Cépaduès éditions.

Chen, S.-L., J.-y. Chen, and G.-c. Gu (2003). "The tidal bore on the north branch of Changjiang Estuary and its effects on the estuary". Chinese. In: *Journal of East China Normal University (Natural Science Edition)* 1.

Chugh, R. S. (1961). "Tides in Hooghly River". In: *International Association of Scientific Hydrology. Bulletin* 6.2, pp. 10–26.

Comoy, G. E. (1881). *Étude pratique sur les marées fluviales et notamment sur le Mascaret*. French. Paris, France: Gauthier-Villars.

Cornish, V. (1900). "The Severn Bore". In: *Nature* 62.1597, pp. 126–127.

Cornish, V. (1934). "On tidal bores which assume the form of a group of short waves". In: *Geophysical Journal International* 3.5, pp. 183–190.

Cousteix, J. (1989). *Turbulence et couche limite*. French. Toulouse: Cepadues-éditions.

Cunge, J. A. (2003). "Undular bores and secondary waves - Experiments and hybrid finite volume modelling". In: *Journal of Hydraulic Research* 41.5, pp. 557–559.

Darcy, H. and H. Bazin (1865). *Recherches hydrauliques, 1er et 2ème parties*. French. Paris: Imprimerie Impériales, Dunod.

Deardorff, J. W. (1970). "A numerical study of three-dimensional turbulent channel flow at large Reynolds numbers". In: *Journal of Fluid Mechanics* 41.02, pp. 453–480.

Devkota, B. and J. Imberger (2009). "Lagrangian Modeling of Weakly Nonlinear Nonhydrostatic Shallow Water Waves in Open Channels". In: *Journal of Hydraulic Engineering* 135.11, pp. 926–934.

Docherty, N. J. and H. Chanson (2010). *Characterisation of unsteady turbulence in breaking tidal bores including the effects of bed roughness*. Department Technical Report ch7610. Brisbane, Australia: School of Civil Engineering, The University of Queensland, p. 112.

Docherty, N. J. and H. Chanson (2012). "Physical modeling of unsteady turbulence in breaking tidal bores". In: *Journal of Hydraulic Engineering* 138.5, pp. 412–419.

Donnelly, C. and H. Chanson (2005). "Environmental impact of undular tidal bores in tropical rivers". In: *Environmental Fluid Mechanics* 5.5, pp. 481–494.

Dyer, K. R. (1997). *Estuaries: a physical introduction*. 2nd ed. Chichester ; New York: John Wiley.

Ehrenstein, U. and F. Gallaire (2008). "Two-dimensional global low-frequency oscillations in a separating boundary-layer flow". In: *Journal of Fluid Mechanics* 614, p. 315.

Ezer, T., R. Hobbs, and L.-Y. Oey (2008). "On the movement of beluga whales in Cook Inlet, Alaska: simulations of tidal and environmental impacts using a hydrodynamic inundation model". In: *Oceanography* 21.4, pp. 186–195.

Falgout, R., J. Jones, and U. Yang (2006). "The design and implementation of hypre, a library of parallel high performance preconditioners". In: *Numerical solution of partial differential equations on parallel computers*. Vol. 51. Lecture notes in computational science and engineering. Springer Berlin Heidelberg, pages.

Fan, D., G. Cai, S. Shang, Y. Wu, Y. Zhang, and L. Gao (2012). "Sedimentation processes and sedimentary characteristics of tidal bores along the north bank of the Qiantang Estuary". In: *Chinese Science Bulletin* 57.13, pp. 1578–1589.

Favre, A. J. (1965). "Review on Space-Time Correlations in Turbulent Fluids". In: *Journal of Applied Mechanics* 32.2, pp. 241–257.

Favre, A. J., J. J. Gaviglio, and R. Dumas (1957). "Space-time double correlations and spectra in a turbulent boundary layer". In: *Journal of Fluid Mechanics* 2.04, pp. 313–342.

Favre, H. (1935). *Étude théorique et expérimentale des ondes de translation dans les canaux découverts*. French. Publications du Laboratoire de recherches hydrauliques, annexé à l'École polytechnique fédérale de Zurich. Paris: Dunod.

Furgerot, L., D. Mouazé, B. Tessier, and J. Brun-Cottan (2012). "Tidal bore: Eulerian velocities and suspended sediment concentration measurements". In: *River Flow 2012*. Vol. 1. Costa-Rica: Rafael Murillo Muñoz, CRC Press, pp. 399–406.

Furgerot, L., D. Mouazé, B. Tessier, L. Perez, and S. Haquin (2013). "Suspended sediment concentration in relation to the passage of a tidal bore (See River Estuary, Mont Saint

Michel Bay, NW France)". In: *7th International Conference on Coastal Dynamics*. Arcachon, France.

Furuyama, S.-I. and H. Chanson (2008). *A numerical study of open channel flow hydrodynamics and turbulence of the tidal bore and dam-break flows*. Hydraulic Model Series CH66/08. Australia: School of Civil Engineering, The University of Queensland, p. 88.

Furuyama, S.-I. and H. Chanson (2010). "A numerical study of a tidal bore flow". In: *Coastal Engineering Journal* 52.3, pp. 215–234.

Gastaldo, R. A. (2012). "Taphonomic controls on the distribution of palynomorphs in tidally influenced coastal deltaic settings". In: *PALAIOS* 27.11, pp. 798–810.

Goda, K. (1979). "A multistep technique with implicit difference schemes for calculating two- or three-dimensional cavity flows". In: *Journal of Computational Physics* 30.1, pp. 76–95.

Gordon, J. H. (1924). "Tidal bore at mouth of Colorado River December 8 to 10, 1923". In: *Monthly Weather Review* 52.2, pp. 98–99.

Goring, D. G. and V. I. Nikora (2002). "Despiking acoustic Doppler velocimeter data". In: *Journal of Hydraulic Engineering* 128.1, pp. 117–126.

Grujić, Z. and H. Kalisch (2009). "A bound on oscillations in an unsteady undular bore". In: *Applicable Analysis* 88.12, pp. 1701–1712.

Gualtieri, C. and H. Chanson (2012). "Experimental study of a positive surge. Part 1: basic flow patterns and wave attenuation". In: *Environmental Fluid Mechanics* 12.2, pp. 145–159.

Hafsia, Z., M. B. Hadj, H. Lamloumi, and K. Maalel (2009). "Internal inlet for wave generation and absorption treatment". In: *Coastal Engineering* 56.9, pp. 951–959.

Helluy, P. et al. (2005). "Numerical simulations of wave breaking". In: *ESAIM: Mathematical Modelling and Numerical Analysis* 39.03, pp. 591–607.

Henderson, F. M. (1966). *Open channel flow*. London, UK: Collier-Macmillan.

Hirt, C. and B. Nichols (1981). "Volume of fluid (VOF) method for the dynamics of free boundaries". In: *Journal of Computational Physics* 39.1, pp. 201–225.

Hirt, C. and J. Shannon (1968). "Free-surface stress conditions for incompressible-flow calculations". In: *Journal of Computational Physics* 2.4, pp. 403–411.

Holthuijsen, L. H. (2007). *Waves in oceanic and coastal waters*. Cambridge University Press.

Hornung, H. G., C. Willert, and S. Turner (1995). "The flow field downstream of a hydraulic jump". In: *Journal of Fluid Mechanics* 287, pp. 299–316.

Hunt, J. C. R., A. A. Wray, and P. Moin (1988). *Eddies, streams, and convergence zones in turbulent flows*. Center for Turbulence Research Report CTR-S88. Stanford Univ., CA., pp. 193–208.

Jánosi, I. M., D. Jan, K. G. Szabó, and T. Tél (2004). "Turbulent drag reduction in dam-break flows". In: *Experiments in Fluids* 37.2, pp. 219–229.

Jarrin, N. (2008). "Synthetic inflow boundary conditions for the numerical simulation of turbulence". PhD thesis. Manchester, UK: School of Mechanical, Aerospace and Civil Engineering, The University of Manchester.

Jarrin, N., S. Benhamadouche, D. Laurence, and R. Prosser (2006). "A synthetic-eddy method for generating inflow conditions for large-eddy simulations". In: *International Journal of Heat and Fluid Flow* 27.4, pp. 585–593.

Jarrin, N., R. Prosser, J.-C. Uribe, S. Benhamadouche, and D. Laurence (2009). "Reconstruction of turbulent fluctuations for hybrid RANS/LES simulations using a Synthetic-Eddy Method". In: *The Seventh International Symposium on Engineering Turbulence Modelling and Measurements, ETMM7* 30.3, pp. 435–442.

Jiang, H., L. Wang, L. Li, and Z. Guo (2014). "Safety evaluation of an ancient masonry seawall structure with modified DDA method". In: *Computers and Geotechnics* 55, pp. 277–289.

Kataoka, I. (1986). "Local instant formulation of two-phase flow". In: *International Journal of Multiphase Flow* 12.5, pp. 745–758.

Keating, A., U. Piomelli, E. Balaras, and H.-J. Kaltenbach (2004). "A priori and a posteriori tests of inflow conditions for large-eddy simulation". In: *Physics of Fluids* 16.12, p. 4696.

Kempf, A. M. (2008). "LES validation from experiments". In: *Flow, Turbulence and Combustion* 80.3, pp. 351–373.

Keulegan, G. H. and G. W. Patterson (1940). *Mathematical Theory of Irrotational Translation Waves*. Vol. 24. Washington, U.S.: National Bureau of Standards.

Khadra, K. (1994). "Méthodes adaptatives de raffinement local multigrille : applications aux équations de Navier-Stokes et de l'énergie". French. PhD thesis. Bordeaux, France: Université de Bordeaux I.

Khadra, K., P. Angot, S. Parneix, and J.-P. Caltagirone (2000). "Fictitious domain approach for numerical modelling of Navier–Stokes equations". In: *International Journal for Numerical Methods in Fluids* 34.8, pp. 651–684.

Khezri, N. and H. Chanson (2012a). "Inception of bed load motion beneath a bore". In: *Geomorphology* 153–154, pp. 39–47.

Khezri, N. and H. Chanson (2012b). "Sediment inception under breaking tidal bores". In: *Mechanics Research Communications* 41, pp. 49–53.

Khezri, N. and H. Chanson (2012c). "Undular and breaking bores on fixed and movable gravel beds". In: *Journal of Hydraulic Research* 50.4, pp. 353–363.

Kjerfve, B. and H. O. Ferreira (1993). "Tidal bores: first ever measurements". In: *Ciência e Cultura* 45.2, pp. 135–138.

Koch, C. and H. Chanson (2005). *An experimental study of tidal bores and positive surges: hydrodynamics and turbulence of the bore front*. Department Technical Report CH56/05. Brisbane, Australia: Dept. of Civil Engineering, The University of Queensland, p. 170.

Koch, C. and H. Chanson (2008). "Turbulent mixing beneath an undular bore front". In: *Journal of Coastal Research*, pp. 999–1007.

Koch, C. and H. Chanson (2009). "Turbulence measurements in positive surges and bores". In: *Journal of Hydraulic Research, IAHR* 47.1, pp. 29–40.

La Condamine, C. M. de (1778). *Relation abrégée d'un voyage fait dans l'intérieur de l'Amérique méridionale depuis la côte de la mer du Sud jusqu'aux côtes du Brésil et de la Guyane, en descendant la rivière des Amazones*. French. Paris, France: chez Jean-Edme Dufour & Philippe Roux.

Labourasse, E., D. Lacanette, A. Toutant, P. Lubin, S. Vincent, O. Lebaigue, J.-P. Caltagirone, and P. Sagaut (2007). "Towards large eddy simulation of isothermal two-phase flows: Governing equations and a priori tests". In: *International Journal of Multiphase Flow* 33.1, pp. 1–39.

Laut, L. L. M., D. E. d. S. Ferreira, V. F. Santos, A. G. Figueiredo Jr, M. d. A. Carvalho, and O. F. Machado (2010). "Foraminifera, thecamoebians and palynomorphs as hydrodynamic indicators in Araguari Estuary, Amazonian Coast, Amapá State - Brazil". In: *Anuário do Instituto de Geociências* 33, pp. 52–65.

Le Méhauté, B. (1976). *An introduction to hydrodynamics and water waves*. New York: Springer-Verlag.

Lemoine, R. (1948). "Sur les ondes positives de translation dans les canaux et sur le ressaut ondulé de faible amplitude". French. In: *La Houille Blanche* 2, pp. 183–185.

Lewis, A. W. (1972). "Field studies of a tidal bore in the River Dee". M.Sc. thesis. Bangor, UK: Marine Science Laboratories, University College of North Wales.

Liggett, J. A. (1994). *Fluid mechanics*. New York: McGraw-Hill.

Lu, C., J. Qiu, and R. Wang (2009). "Weighted essential non-oscillatory schemes for tidal bore on unstructured meshes". In: *International Journal for Numerical Methods in Fluids* 59.6, pp. 611–630.

Lubin, P., H. Chanson, and S. Glockner (2010a). "Large eddy simulation of turbulence generated by a weak breaking tidal bore". In: *Environmental Fluid Mechanics* 10.5, pp. 587–602.

Lubin, P., S. Glockner, and H. Chanson (2010b). "Numerical simulation of a weak breaking tidal bore". In: *Mechanics Research Communications* 37.1, pp. 119–121.

Lubin, P., S. Vincent, S. Abadie, and J.-P. Caltagirone (2006). "Three-dimensional large eddy simulation of air entrainment under plunging breaking waves". In: *Coastal Engineering* 53.8, pp. 631–655.

Lynch, D. K. (1982). "Tidal bores". In: *Scientific American* 247.4, pp. 146–156.

Madsen, P., H. Simonsen, and C.-H. Pan (2005). "Numerical simulation of tidal bores and hydraulic jumps". In: *Coastal Engineering* 52.5, pp. 409–433.

Marche, C., P. Beauchemin, and A. E. Kayloubi (1995). "Étude numérique et expérimentale des ondes secondaires de Favre consécutives à la rupture d'un barrage". French. In: *Canadian Journal of Civil Engineering* 22.4, pp. 793–801.

Marquillie, M. and U. Ehrenstein (2003). "On the onset of nonlinear oscillations in a separating boundary-layer flow". In: *Journal of Fluid Mechanics* 490, pp. 169–188.

Martinius, A. W. and S. Gowland (2011). "Tide-influenced fluvial bedforms and tidal bore deposits (Late Jurassic Lourinhã Formation, Lusitanian Basin, Western Portugal)". In: *Sedimentology* 58.1, pp. 285–324.

Mazumder, N. C. and S. Bose (1995). "Formation and propagation of tidal bore". In: *Journal of Waterway, Port, Coastal, and Ocean Engineering* 121.3, pp. 167–175.

McLelland, S. J. and A. P. Nicholas (2000). "A new method for evaluating errors in high-frequency ADV measurements". In: *Hydrological Processes* 14.2, pp. 351–366.

Microsonic (2004). *Instruction Manual: mic+ Ultrasonic Sensors with one analogue output.*

Mitchell, S. B. (2010). "Positive surge in trapezoidal and circular channels". In: *Proceedings of the ICE - Water Management* 163.4, pp. 199–205.

Montes, J. S. and H. Chanson (1998). "Characteristics of undular hydraulic jumps: Experiments and analysis". In: *Journal of Hydraulic Engineering* 124.2, pp. 192–205.

Moore, W. U. (1888). *Report on the bore of Tsien-Tang-Kiang.* English. London: Hydrographic Office, Admiralty.

Moore, W. U. (1893). *Further report on the bore of Tsien-Tang-Kiang.* London: Hydrographic Office, Admiralty.

Mouazé, D., H. Chanson, and B. Simon (2010). *Field measurements in the tidal bore of the Sélune River in the bay of Mont Saint Michel (September 2010).* Department Technical Report CH81/10. Brisbane, Australia: School of Civil Engineering, The University of Queensland, p. 72.

Musset, R. (1955). "Le mascaret sur la Seine". French. In: *Supplément aux Annales de Normandie* 2, pp. 22–25.

Navarre, P. (1995). "Aspects physiques du caracteres ondulatoire du macaret en Dordogne". French. D.E.A. Thesis. Université de Bordeaux, France.

Nezu, I. (2005). "Open-channel flow turbulence and its research prospect in the 21st century". In: *Journal of Hydraulic Engineering* 131.4, pp. 229–246.

Nezu, I. and H. Nakagawa (1993). *Turbulence in open-channel flows.* Rotterdam; Brookfield: Balkema.

Nortek AS (2009). *Vectrino velocimeter: User guide 2009*.

Pacheco, P. S. (1997). *Parallel programming with MPI*. San Francisco, USA: Morgan Kaufmann Publishers.

Pamiès, M., P.-É. Weiss, E. Garnier, S. Deck, and P. Sagaut (2009). "Generation of synthetic turbulent inflow data for large eddy simulation of spatially evolving wall-bounded flows". In: *Physics of Fluids* 21.4, p. 045103.

Pan, C.-H. and H. Lu (2011). "2D numerical simulation of tidal bore on Qiantang River using KVFS scheme". In: *Coastal Engineering Proceedings* 32.1.

Paramore, L. M. and R. A. Rulifson (2001). "Dorsal coloration as an indicator of different life history patterns for striped bass within a single watershed of Atlantic Canada". In: *Transactions of the American Fisheries Society* 130.4, pp. 663–674.

Patankar, S. V. (1980). *Numerical heat transfer and fluid flow*. Washington; New York: Hemisphere Pub. Corp. ; McGraw-Hill.

Peregrine, D. H. (1966). "Calculations of the development of an undular bore". In: *Journal of Fluid Mechanics* 25.02, pp. 321–330.

Piquet, J. (1999). *Turbulent flows: models and physics*. Berlin, New York: Springer-Verlag.

Poletto, R., A. Revell, T. Craft, and N. Ashton (2012). "Embedded DDES of 2D Hump Flow". In: *Progress in Hybrid RANS-LES Modelling*. Ed. by S. Fu, W. Haase, S.-H. Peng, and D. Schwamborn. Vol. 117. Notes on Numerical Fluid Mechanics and Multidisciplinary Design. Springer Berlin Heidelberg, pp. 169–179.

Post, F. H., B. Vrolijk, H. Hauser, R. S. Laramee, and H. Doleisch (2003). "The State of the Art in Flow Visualisation: Feature Extraction and Tracking". In: *Computer Graphics Forum* 22.4, pp. 775–792.

Poux, A., S. Glockner, E. Ahusborde, and M. Azaïez (2012). "Open boundary conditions for the velocity-correction scheme of the Navier–Stokes equations". In: *Computers & Fluids* 70, pp. 29–43.

Poux, A., S. Glockner, and M. Azaïez (2011). "Improvements on open and traction boundary conditions for Navier–Stokes time-splitting methods". In: *Journal of Computational Physics* 230.10, pp. 4011–4027.

Prandtl, L. (1925). "Bericht über Untersuchungen zur ausgebildeten Turbulenz". In: *Z. Angew. Math. Mech.* 5.2, pp. 136–139.

Precht, E., F. Janssen, and M. Huettel (2006). "Near-bottom performance of the Acoustic Doppler Velocimeter (ADV) – a comparative study". In: *Aquatic Ecology* 40.4, pp. 481–492.

Rayleigh, L. (1908). "Note on tidal bores". In: *Proceedings of the Royal Society A: Mathematical, Physical and Engineering Sciences* 81.549, pp. 448–449.

Reichstetter, M. (2011). "Hydraulic Modelling of Unsteady Open Channel Flow: Physical and Analytical Validation of Numerical Models of Positive and Negative Surges". MPhil Thesis. Brisbane, Australia: School of Civil Engineering, The University of Queensland.

Reungoat, D., H. Chanson, and B. Caplain (2012). *Field measurements in the tidal bore of the Garonne River at Arcins (June 2012)*. Hydraulic Model Report CH89/12. Brisbane, Australia: School of Civil Engineering, The University of Queensland, p. 121.

Roth, M. (2000). "Automatic extraction of vortex core lines and other line-type features for scientific visualization". In: *Selected readings in vision and graphics Vol. 9*. Hartung-Gorre Verlag. Diss. Technische Wissenschaften ETH Zürich, Nr.13673, p. 204.

Rulifson, R. A. and K. A. Tull (1999). "Striped bass spawning in a tidal bore river: The Shubenacadie Estuary, Atlantic Canada". In: *Transactions of the American Fisheries Society* 128.4, pp. 613–624.

Ryabenko, A. (1998). "Representation of a wave jump and group of translation waves as a combination of a solitary wave and knoidal waves". In: *Hydrotechnical Construction* 32.5, pp. 246–252.

Saad, Y. and M. H. Schultz (1986). "GMRES: A generalized minimal residual algorithm for solving nonsymmetric linear systems". In: *SIAM Journal on Scientific and Statistical Computing* 7.3, pp. 856–869.

Sagaut, P. (2006). *Large eddy simulation for incompressible flows: an introduction*. 3rd. Berlin, Heidelberg, New York: Springer-Verlag Berlin and Heidelberg.

Schlichting, H. (1979). *Boundary-layer theory*. 7th ed. New York: McGraw-Hill.

Simon, B. and H. Chanson (2013). *Turbulence measurements in tidal bore-like positive surges over a rough bed*. Hydraulic Model Report CH90/12. Brisbane, Australia: School of Civil Engineering, The University of Queensland, p. 176.

Simon, B., P. Lubin, S. Glockner, and H. Chanson (2011a). "Three-dimensional numerical simulation of the hydrodynamics generated by a weak breaking tidal bore". In: *34th IAHR World Congress, 33rd Hydrology and Water Resources Symposium and 10th Conference on Hydraulics in Water Engineering*. Brisbane, Australia: Eric Valentine, Colin Apelt, James Ball, Hubert Chanson, Ron Cox, Robert Ettema, George Kuczera, Martin Lambert, Bruce Melville and Jane Sargison, pp. 1133–1140.

Simon, B., P. Lubin, D. Reungoat, and H. Chanson (2011b). "Turbulence measurements in the Garonne River tidal bore: First observations". In: *34th IAHR World Congress, 33rd Hydrology and Water Resources Symposium and 10th Conference on Hydraulics in Water Engineering*. Brisbane, Australia: Eric Valentine, Colin Apelt, James Ball, Hubert Chanson, Ron Cox, Robert Ettema, George Kuczera, Martin Lambert, Bruce Melville and Jane Sargison, pp. 1141–1148.

Simpson, J. H., N. R. Fisher, and P. Wiles (2004). "Reynolds stress and TKE production in an estuary with a tidal bore". In: *Estuarine, Coastal and Shelf Science* 60.4, pp. 619–627.

Smagorinsky, J. (1963). "General circulation experiments with the primitive equations". In: *Monthly Weather Review* 91.3, pp. 99–164.

Soares Frazao, S. and Y. Zech (2002). "Undular bores and secondary waves -Experiments and hybrid finite-volume modelling". In: *Journal of Hydraulic Research* 40.1, pp. 33–43.

Stoker, J. J. (1957). *Water waves: The mathematical theory with applications*. New York: Interscience Publisher, Inc.

Sturtevant, B. (1965). "Implications of experiments on the weak undular bore". In: *Physics of Fluids* 8.6, pp. 1052–1055.

Su, M. D., X. Xu, J. L. Zhu, and Y. C. Hon (2001). "Numerical simulation of tidal bore in Hangzhou Gulf and Qiantangjiang". In: *International Journal for Numerical Methods in Fluids* 36.2, pp. 205–247.

Süli, E. (2003). *An introduction to numerical analysis*. Cambridge ; New York: Cambridge University Press.

Tessier, B. and J. H. J. Terwindt (1994). "Un exemple de déformations synsédimentaires en milieu intertidal: l'effet du mascaret". French. In: *Comptes rendus de l'Académie des sciences. Série 2. Sciences de la terre et des planétes* 319.2, pp. 217–223.

Timmermans, L. J. P., P. D. Minev, and F. N. Van De Vosse (1996). "An approximate projection scheme for incompressible flow using spectral elements". In: *International Journal for Numerical Methods in Fluids* 22.7, pp. 673–688.

Treske, A. (1994). "Undular bores (Favre-waves) in open channels - Experimental studies". In: *Journal of Hydraulic Research* 32.3, pp. 355–370.

Uncles, R., J. Stephens, and D. Law (2006). "Turbidity maximum in the macrotidal, highly turbid Humber Estuary, UK: Flocs, fluid mud, stationary suspensions and tidal bores". In: *Estuarine, Coastal and Shelf Science* 67.1–2, pp. 30–52.

Van Der Vorst, H. A. (1992). "Bi-CGSTAB: A fast and smoothly converging variant of Bi-CG for the solution of nonsymmetric linear systems". In: *SIAM Journal on Scientific and Statistical Computing* 13.2, pp. 631–644.

Van Driest, E. R. (1956). "On turbulent flow near a wall". In: *Journal of the Aeronautical Sciences (Institute of the Aeronautical Sciences)* 23.11, pp. 1007–1011.

Vincent, S. (1999). "Modélisation d'écoulements incompressibles de fluides non-miscibles". French. PhD thesis. Bordeaux, France: Université de Bordeaux I.

Vincent, S. and J.-P. Caltagirone (2000). "A One-cell local multigrid method for solving unsteady incompressible multiphase flows". In: *Journal of Computational Physics* 163.1, pp. 172–215.

Voulgaris, G. and J. H. Trowbridge (1998). "Evaluation of the acoustic Doppler velocimeter (ADV) for turbulence measurements". In: *J. Atmos. Oceanic Technol.* 15.1, pp. 272–289.

Wahl, T. L. (2003). "Discussion of "Despiking acoustic Doppler velocimeter data" by Derek G. Goring and Vladimir I. Nikora". In: *Journal of Hydraulic Engineering* 129.6, pp. 484–487.

Wang, C., K. Ji, B. Yang, S. Wang, L. Wu, and A. Li (2009). "Physically based simulation of tidal bore". In: China: IEEE, pp. 100–104.

Wesseling, P. (1992). *An introduction to multigrid methods*. Chichester; New York: John Wiley & Sons Australia.

Wilkinson, D. and M. Banner (1977). "Undular bores". In: Adelaide, Australia: Australasian Fluid Mechanics Conference, pp. 369–373.

Williamson, C. H. K. (1996). "Vortex Dynamics in the Cylinder Wake". In: *Annual Review of Fluid Mechanics* 28.1, pp. 477–539.

Wolanski, E., K. Moore, S. Spagnol, N. D'Adamo, and C. Pattiaratchi (2001). "Rapid, human-induced siltation of the macro-tidal Ord River estuary, Western Australia". In: *Estuarine, Coastal and Shelf Science* 53.5, pp. 717–732.

Wolanski, E., D. Williams, S. Spagnol, and H. Chanson (2004). "Undular tidal bore dynamics in the Daly Estuary, Northern Australia". In: *Estuarine, Coastal and Shelf Science* 60.4, pp. 629–636.

Yee, H. C. (1987). *Upwind and symmetric shock-capturing schemes*. Technical Report N-87-24145; NASA-TM-89464; A-87236; NAS-1.15:89464. Moffett Field, CA, USA: NASA. Ames Research Center, p. 130.

Yeh, H. H. and K.-M. Mok (1990). "On turbulence in bores". In: *Physics of Fluids A: Fluid Dynamics* 2.5, pp. 821–828.

Youngs, D. L. (1982). "Time-dependent multi material flow with large fluid distortion". In: *Numerical methods for fluid dynamics*. Conference series (Institute of Mathematics and Its Applications). London, New York: K. W. Morton, M. J. Baines, Academic Press.

A

Ensemble averaged free surface data of bores

A.1 Presentation

The experiments on positive surges over the gravel bed were all repeated 25 times to perform an ensemble average of the instantaneous free-surface data. Between each repetition of a bore, the steady flow conditions were left unchanged for 5 minutes to achieve the same initial condition. A series of acoustic displacement meters (ADMs) were used to record the evolution of the free surface at several longitudinal locations.

The present appendix regroups a number of dimensionless graphs presenting the time evolution of the free surface measured at $x = 6.13$ m where x is the distance from the downstream gate, d_0 is the initial water depth at $x = 6.13$ m, Q is the water discharge and Fr is the bore Froude number. Each graph includes the superimposition of the free surface data of the 25 runs, the ensemble averaged median water depth d_{median}, the difference between the 3^{rd} and 1^{st} ($d_{75} - d_{25}$), the difference between 90% and 10% percentiles ($d_{90} - d_{10}$) and the difference between maximum and minimum water elevation observations ($d_{\max} - d_{\min}$). The detailed bore conditions were given in Table IV.3.

A.2 Data sets

A.2.1 Water discharge: $Q = 0.036$ m^3.s^{-1}

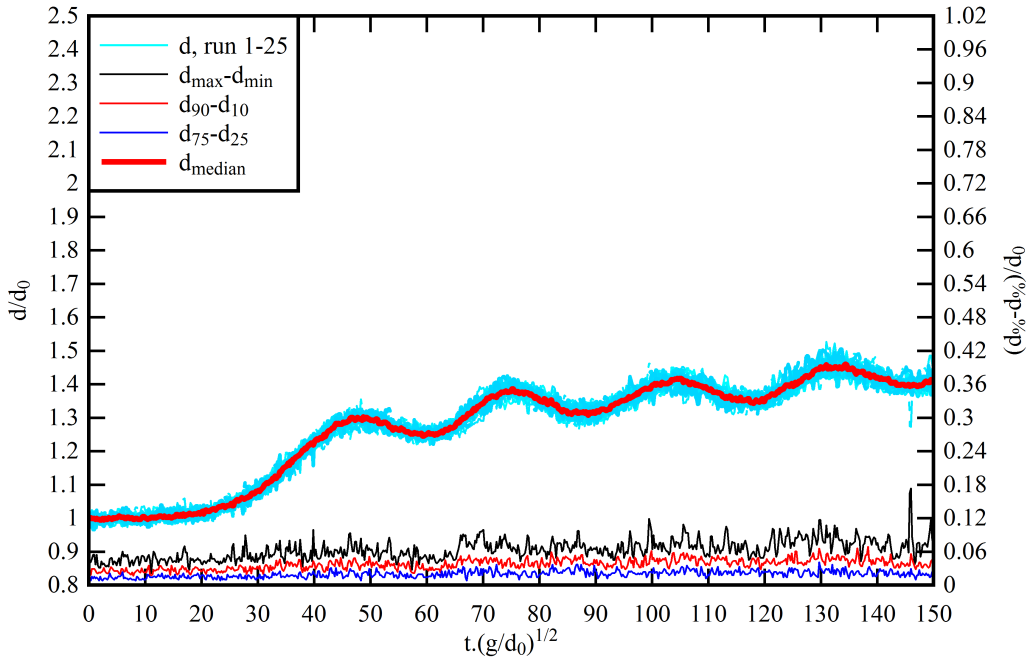

Figure A.1: Ensemble averaged free surface data for an undular bore. Flow conditions: $Fr = 1.14$, $Q = 0.036$ m^3.s^{-1}, $d_0 = 0.088$ m, $h_g = 57$ mm

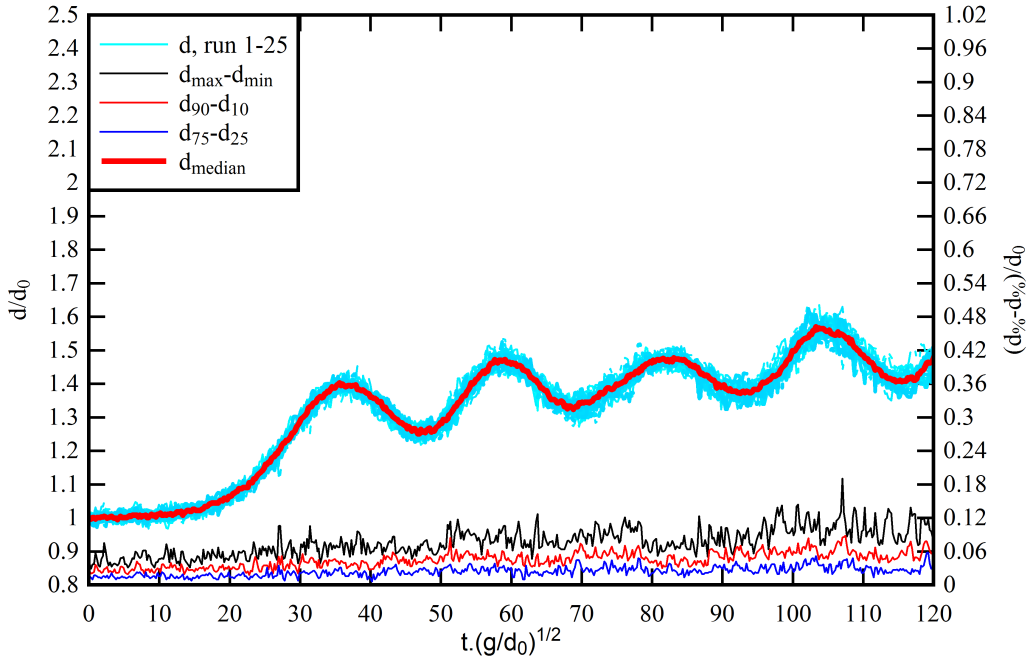

Figure A.2: Ensemble averaged free surface data for an undular bore. Flow conditions: $Fr = 1.18$, $Q = 0.036$ m^3.s^{-1}, $d_0 = 0.089$ m, $h_g = 51$ mm

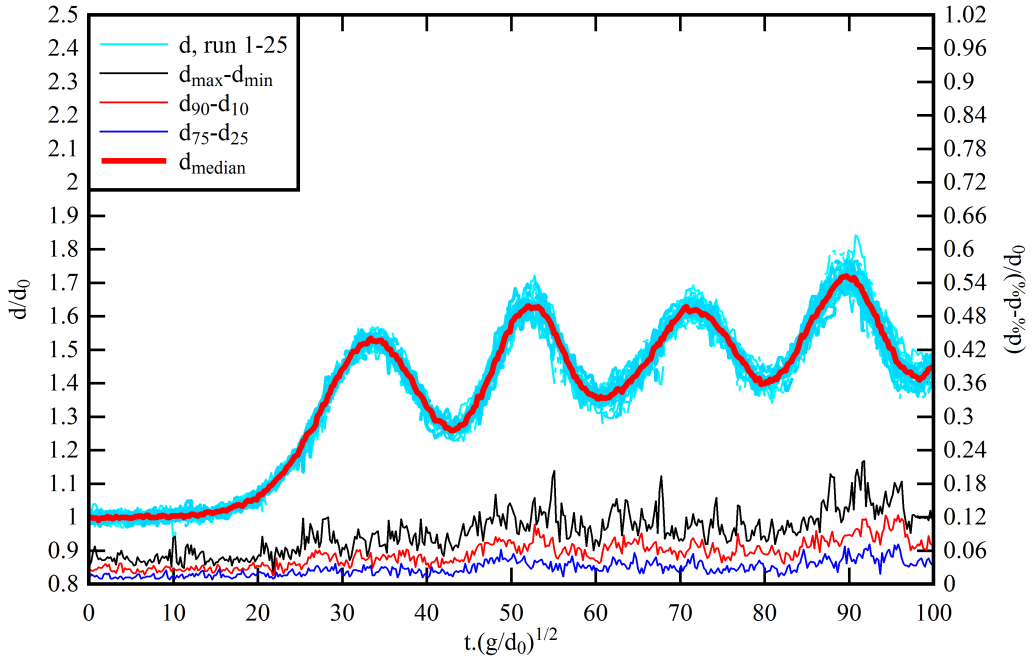

Figure A.3: Ensemble averaged free surface data for an undular bore. Flow conditions: $Fr = 1.26$, $Q = 0.036$ m^3.s^{-1}, $d_0 = 0.088$ m, $h_g = 43$ mm

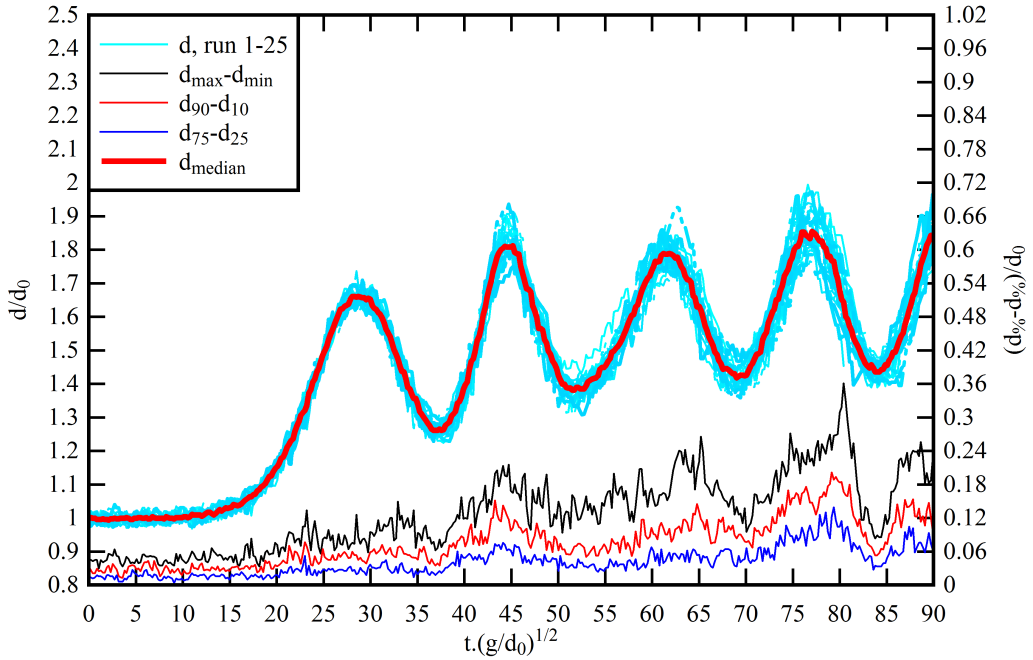

Figure A.4: Ensemble averaged free surface data for an undular bore. Flow conditions: $Fr = 1.32$, $Q = 0.036$ m^3.s^{-1}, $d_0 = 0.088$ m, $h_g = 36$ mm

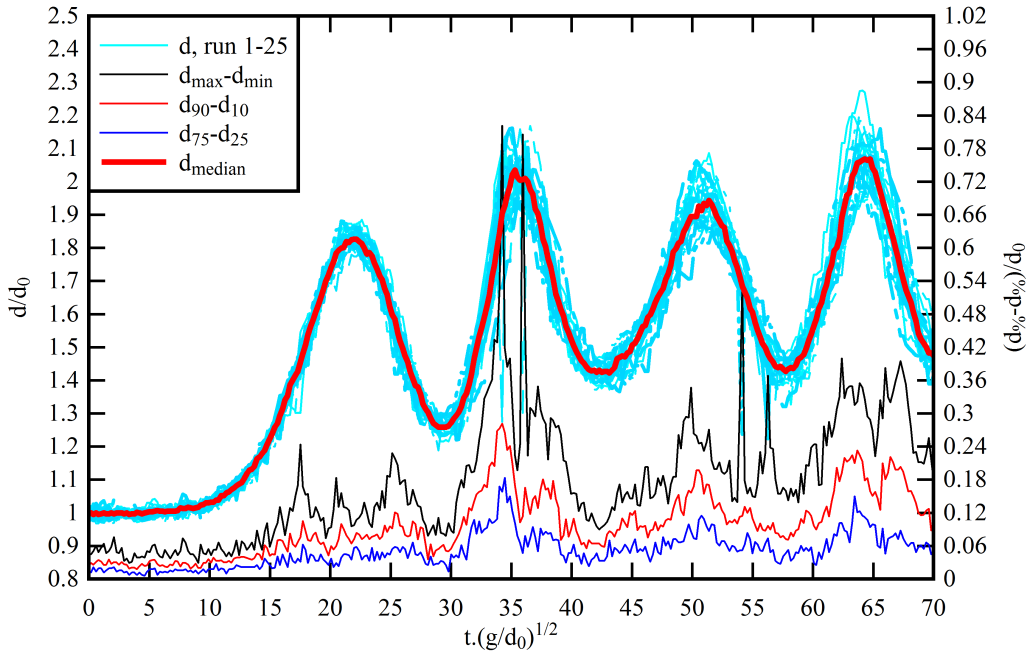

Figure A.5: Ensemble averaged free surface data for an undular bore. Flow conditions: $Fr = 1.40$, $Q = 0.036$ m^3.s^{-1}, $d_0 = 0.087$ m, $h_g = 27$ mm

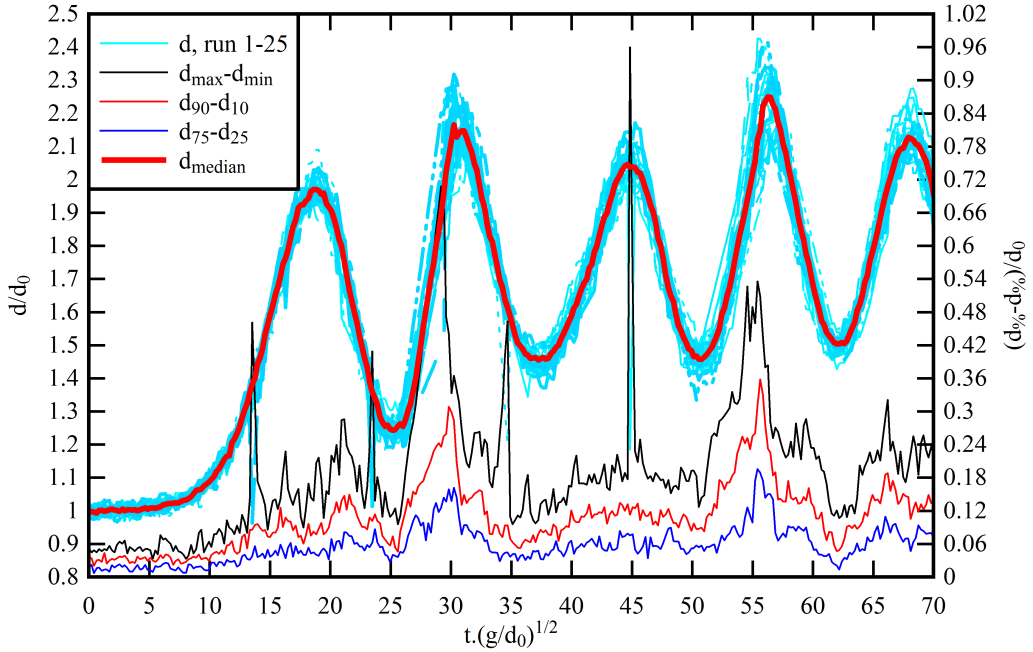

Figure A.6: Ensemble averaged free surface data for an undular bore. Flow conditions: $Fr = 1.45$, $Q = 0.036$ m^3.s^{-1}, $d_0 = 0.088$ m, $h_g = 21$ mm

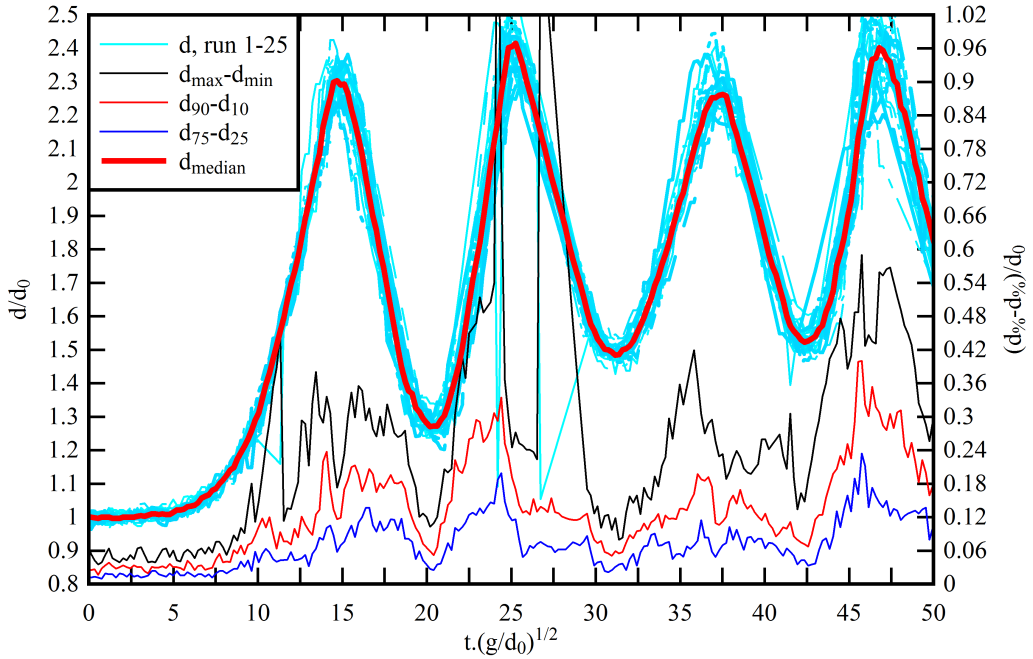

Figure A.7: Ensemble averaged free surface data for a breaking bore. Flow conditions: $Fr = 1.50$, $Q = 0.036$ m^3.s^{-1}, $d_0 = 0.088$ m, $h_g = 9$ mm

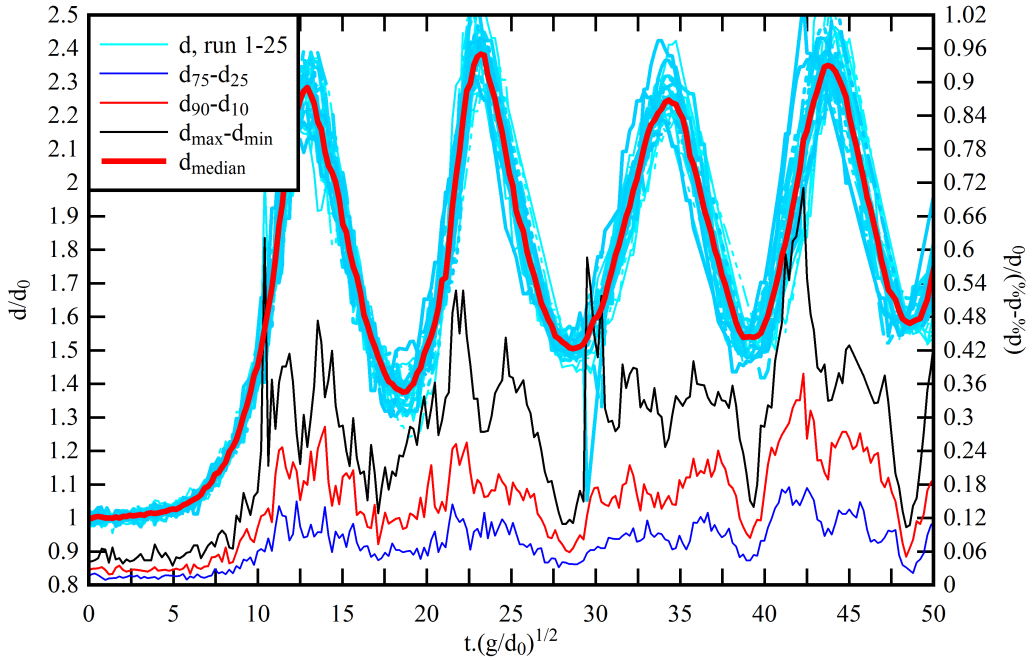

Figure A.8: Ensemble averaged free surface data for a breaking bore. Flow conditions: $Fr = 1.50$, $Q = 0.036$ m^3.s^{-1}, $d_0 = 0.089$ m, $h_g = 3$ mm

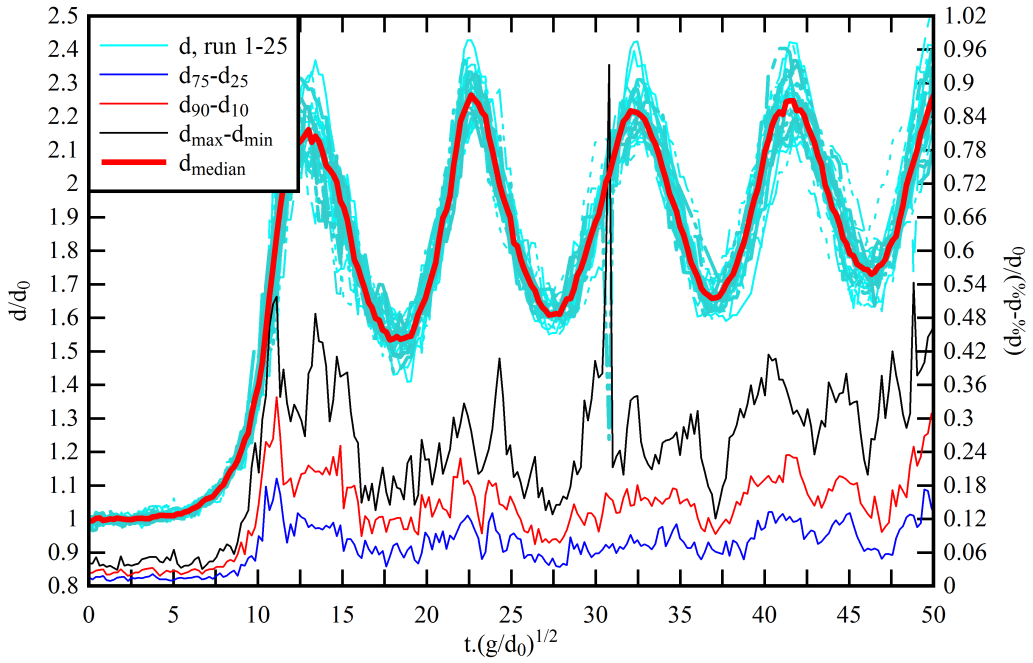

Figure A.9: Ensemble averaged free surface data for a breaking bore. Flow conditions: $Fr = 1.56$, $Q = 0.036$ m^3.s^{-1}, $d_0 = 0.088$ m, $h_g = 0$ mm

A.2.2 Water discharge: $Q = 0.055$ m^3.s^{-1}

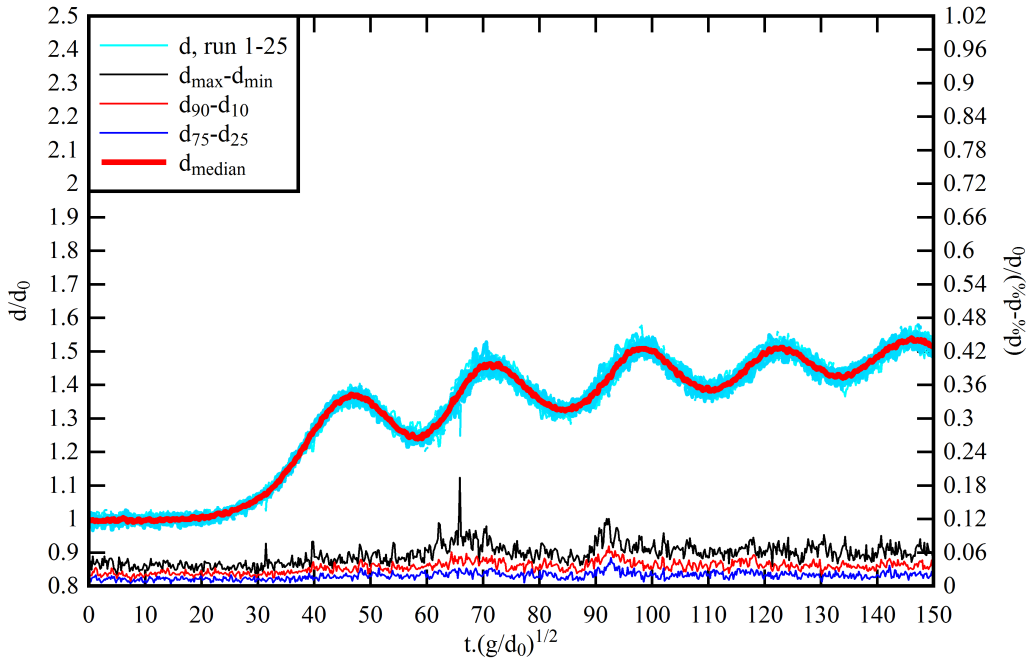

Figure A.10: Ensemble averaged free surface data for an undular bore. Flow conditions: $Fr = 1.21$, $Q = 0.055$ m^3.s^{-1}, $d_0 = 0.112$ m, $h_g = 79$ mm

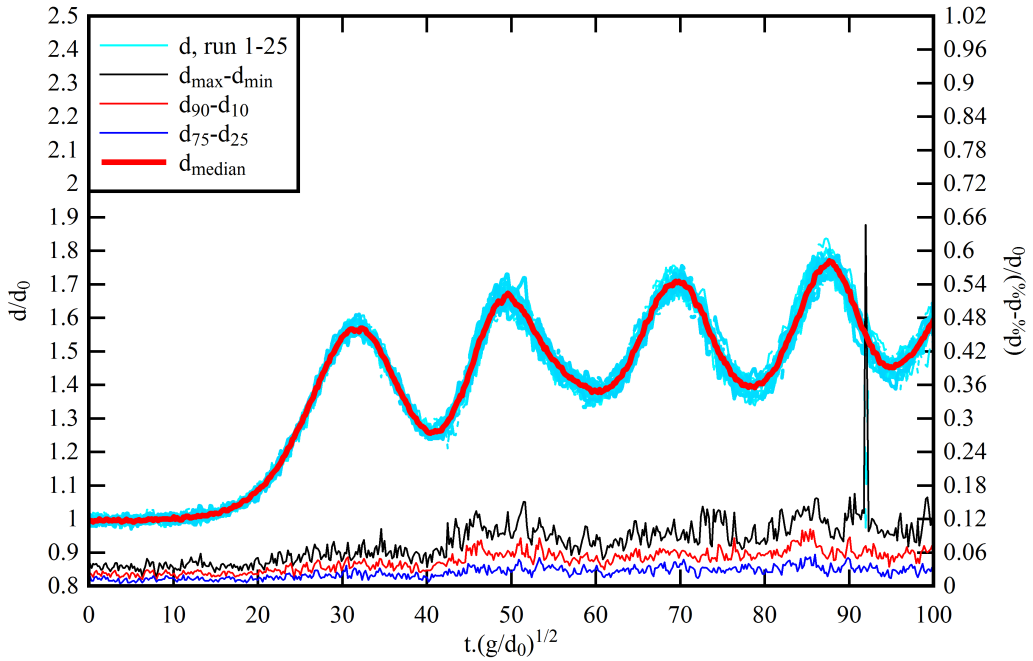

Figure A.11: Ensemble averaged free surface data for an undular bore. Flow conditions: $Fr = 1.31$, $Q = 0.055$ m^3.s^{-1}, $d_0 = 0.112$ m, $h_g = 65$ mm

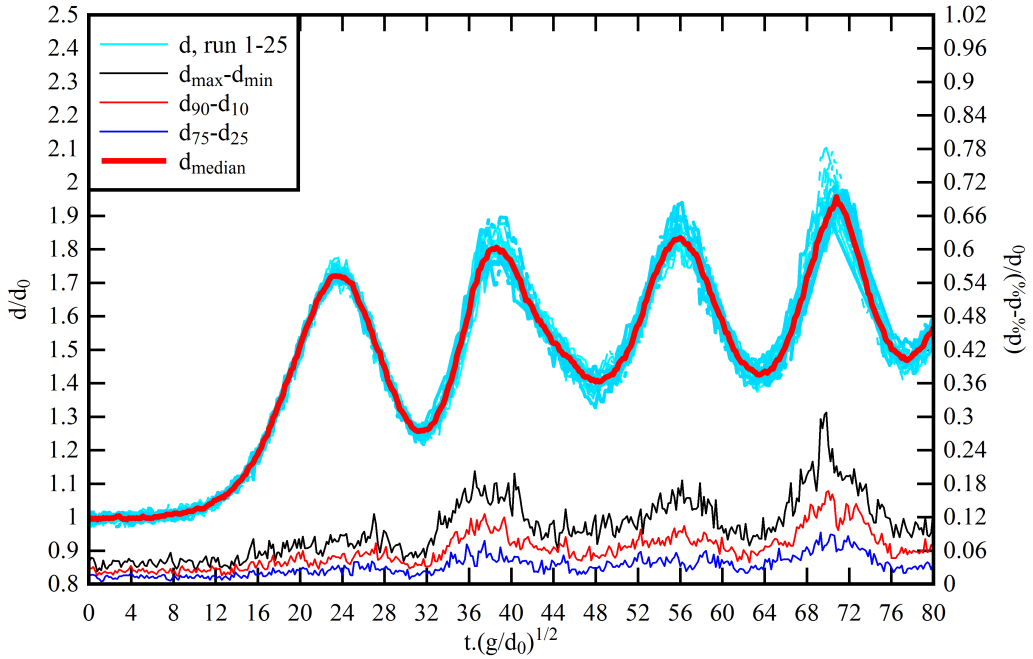

Figure A.12: Ensemble averaged free surface data for an undular bore. Flow conditions: $Fr = 1.37$, $Q = 0.055$ m^3.s^{-1}, $d_0 = 0.112$ m, $h_g = 55$ mm

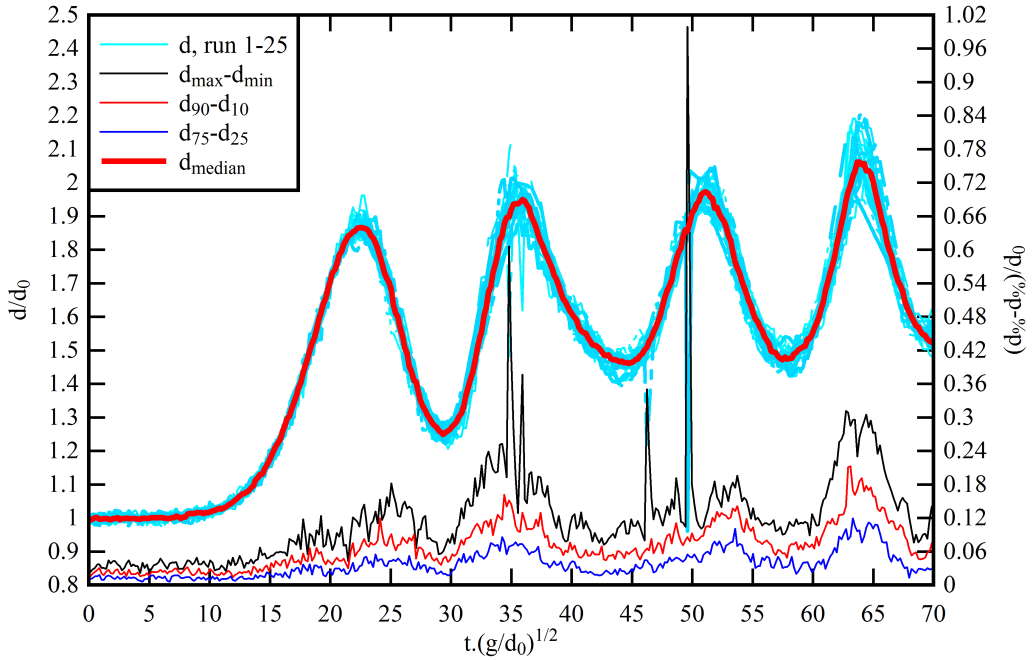

Figure A.13: Ensemble averaged free surface data for an undular bore. Flow conditions: $Fr = 1.43$, $Q = 0.055$ m^3.s^{-1}, $d_0 = 0.112$ m, $h_g = 44$ mm

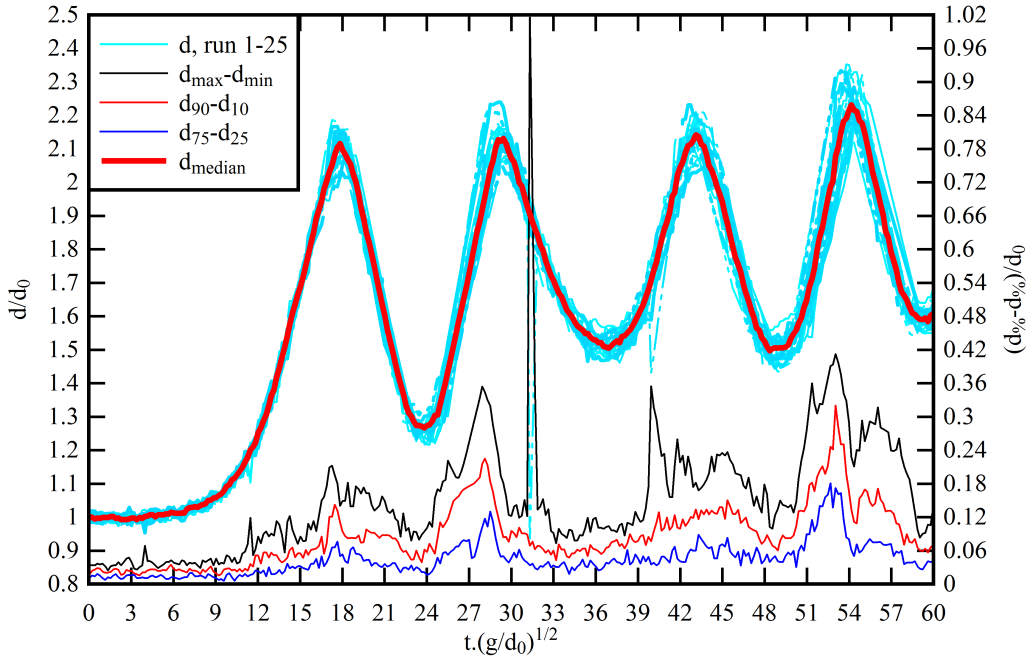

Figure A.14: Ensemble averaged free surface data for an undular bore. Flow conditions: $Fr = 1.48$, $Q = 0.055$ m^3.s^{-1}, $d_0 = 0.112$ m, $h_g = 31$ mm

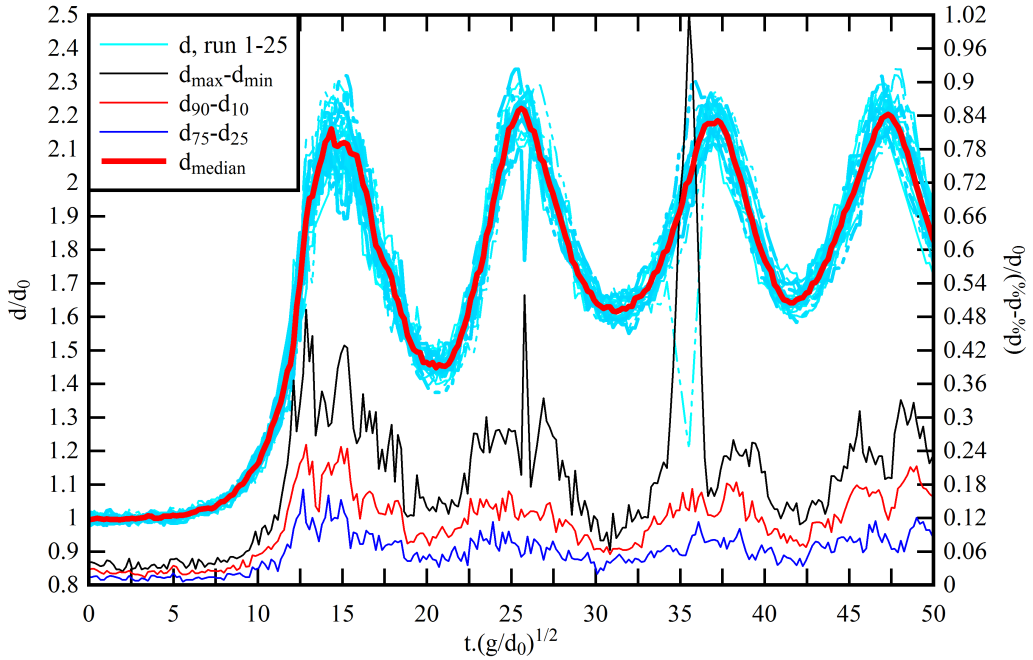

Figure A.15: Ensemble averaged free surface data for a breaking bore. Flow conditions: $Fr = 1.56$, $Q = 0.055$ m^3.s^{-1}, $d_0 = 0.112$ m, $h_g = 21$ mm

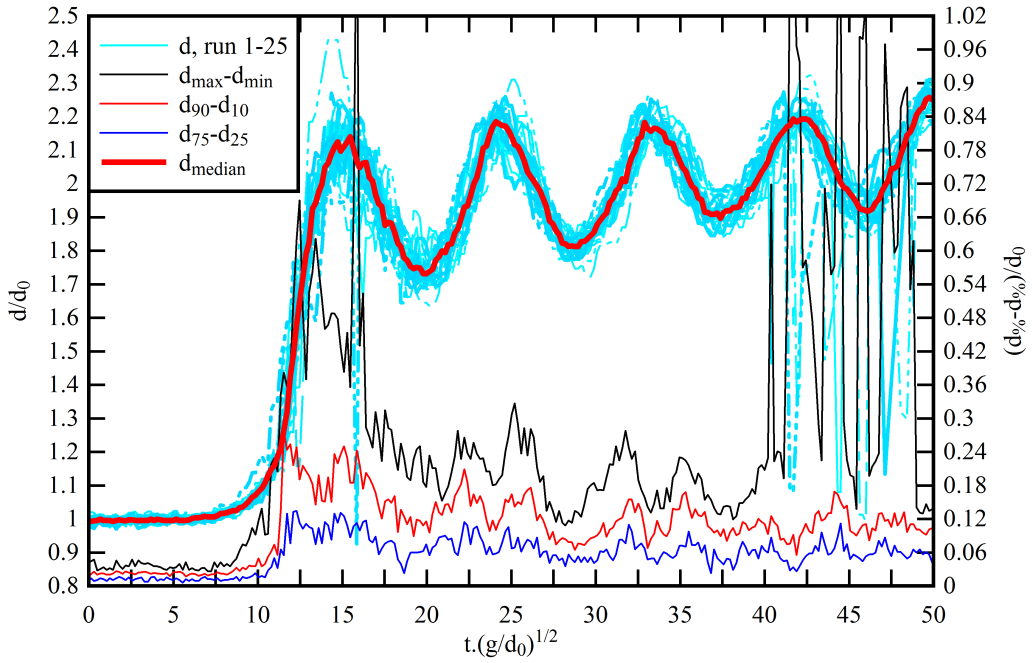

Figure A.16: Ensemble averaged free surface data for a breaking bore. Flow conditions: $Fr = 1.66$, $Q = 0.055$ m^3.s^{-1}, $d_0 = 0.112$ m, $h_g = 0$ mm

B

Ensemble averaged velocity data in bores

B.1 Presentation

In undular positive surges with and without breaking, several series of 25 instantaneous velocity measurements were repeated at several elevations z above a gravel bed for two discharges Q (Table IV.4). The instantaneous velocity components were recorded with a Nortek^{TM} acoustic Doppler velocimeter (ADV) located on the channel centreline at $x = 6.13$ m upstream the downstream gate. The initial flow conditions d_0 and V_0 were respectively the initial water depth and initial flow velocity at $x = 6.15$ m. Fr is the bore Froude number and U_b is the bore velocity.

The bores were repeated every 5 minutes, to ensure that the initial flow conditions were well-defined and unchanged between each run. An ensemble median of the velocity time series was performed for each vertical elevation. The data were synchronised on the bore passage. The results of the measurements are presented below. The colour mappings were constructed by linear interpolation of data between measurements at different elevations.

B.2 Data sets

B.2.1 Ensemble averaged velocity colour maps

Figures on the next pages.

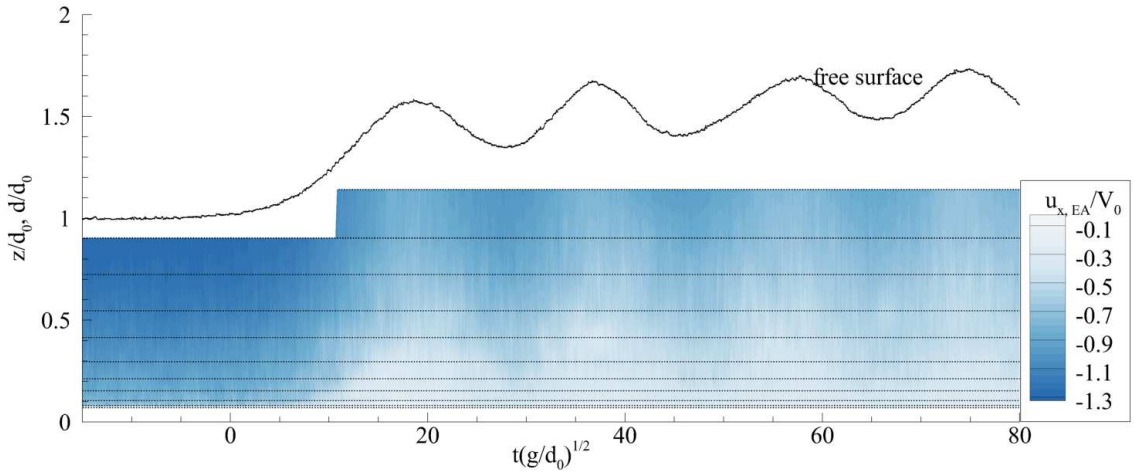

(a) Longitudinal velocity

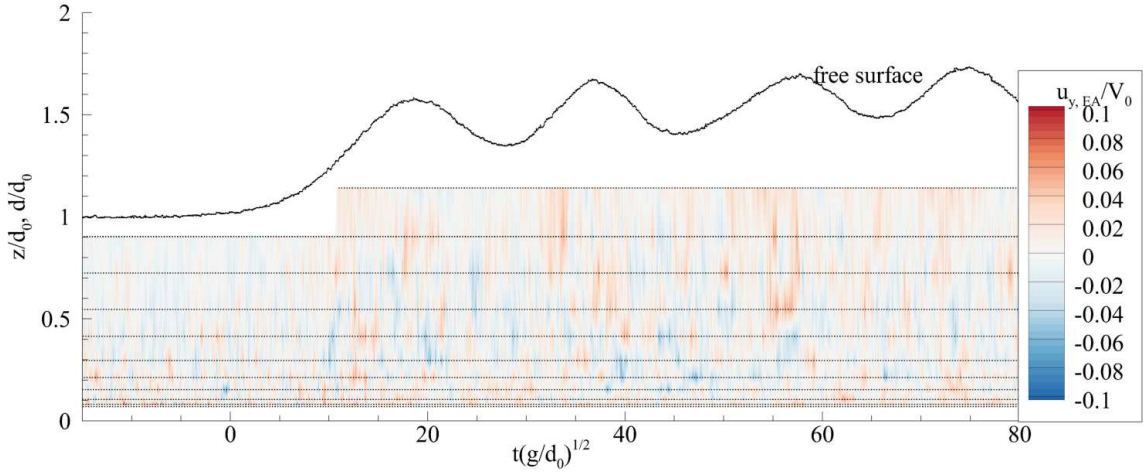

(b) Transversal velocity

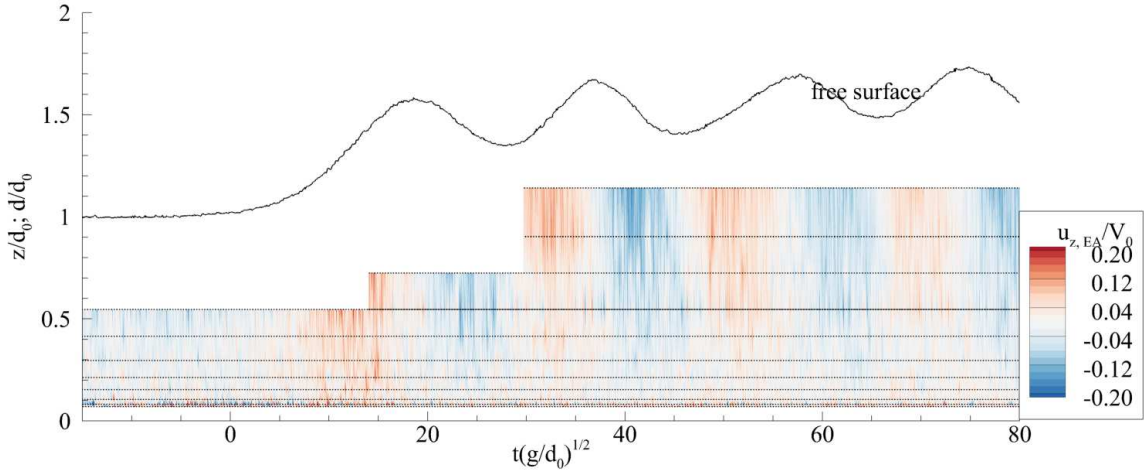

(c) Vertical velocity

Figure B.1: Dimensionless ensemble averaged velocity colour mapping and ensemble averaged water depth in undular bores. Flow conditions: $Q = 0.036$ m^3.s^{-1}, $Fr = 1.33$, $x = 6.13$ m, $h_g = 43$ mm

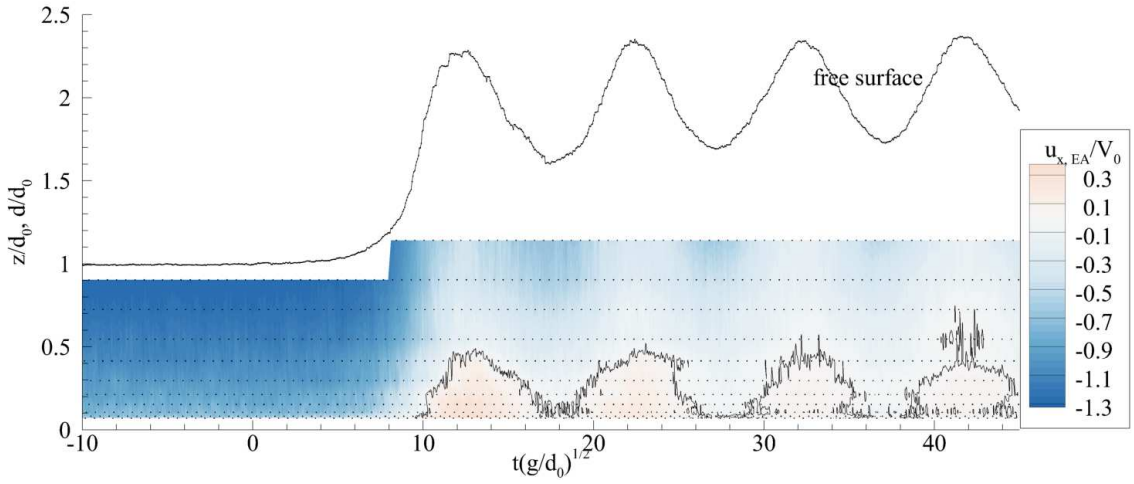

(a) Longitudinal velocity

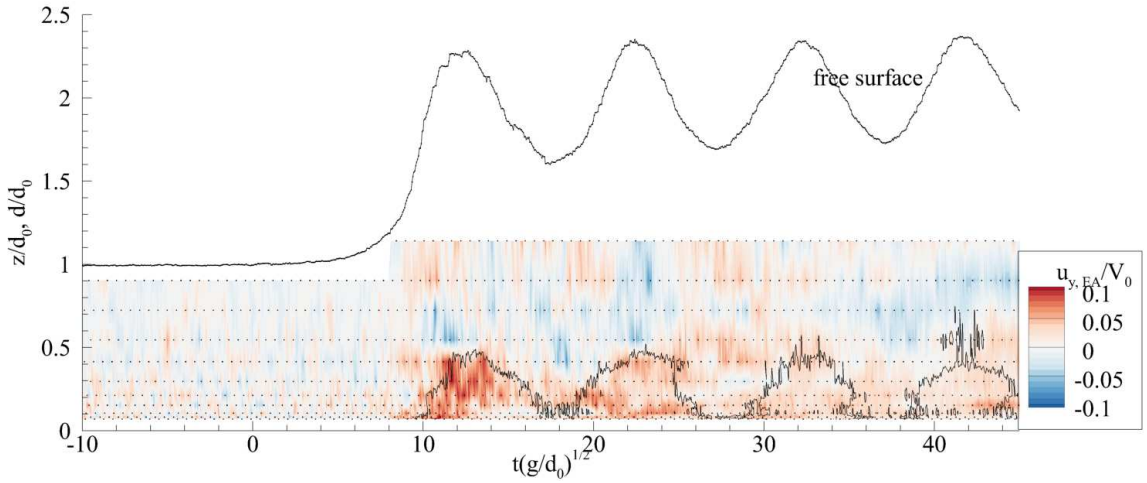

(b) Transversal velocity

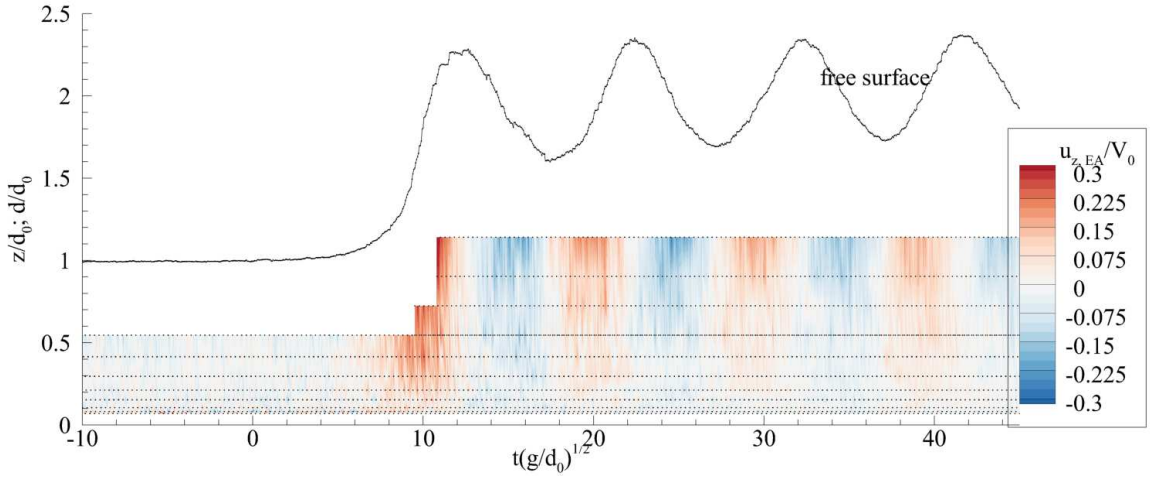

(c) Vertical velocity

Figure B.2: Dimensionless ensemble averaged velocity colour mapping and ensemble averaged water depth in breaking bores. Flow conditions: $Q = 0.036$ m^3.s^{-1}, $Fr = 1.60$, $x = 6.13$ m, $h_g = 0$ mm

B.2.2 Colours maps of the difference between third and first velocity quartiles

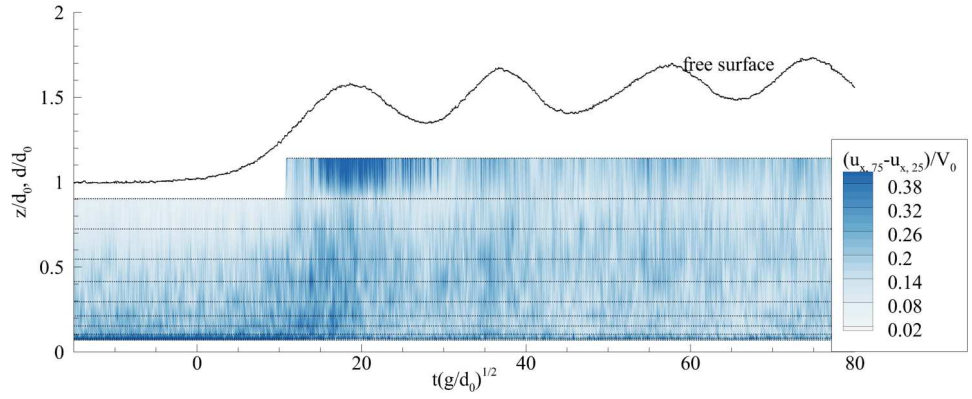

(a) Longitudinal velocity

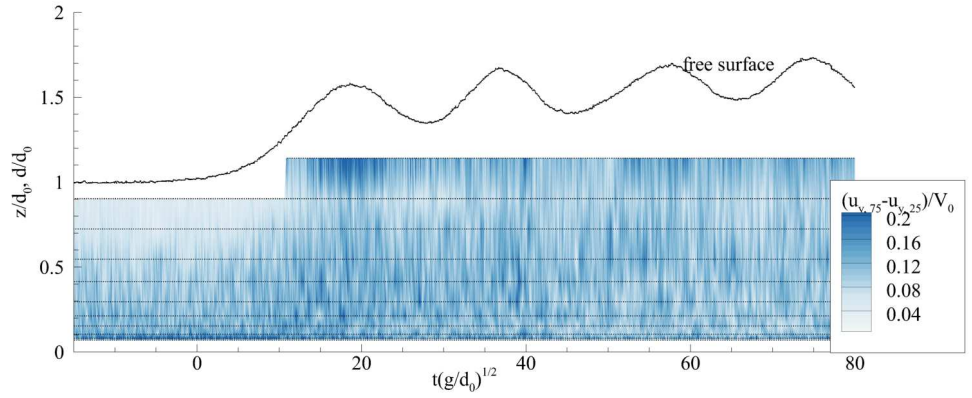

(b) Transversal velocity

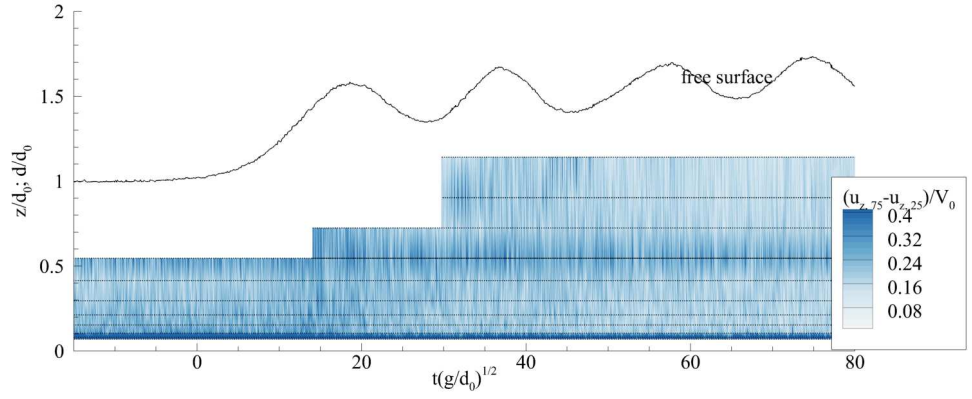

(c) Vertical velocity

Figure B.3: Dimensionless difference between the first and third quartiles ($u_{i,75} - u_{i,25}$) and ensemble averaged water depth in undular bores. Flow conditions: $Q = 0.036$ m^3.s^{-1}, $Fr = 1.33$, $x = 6.13$ m, $h_g = 43$ mm

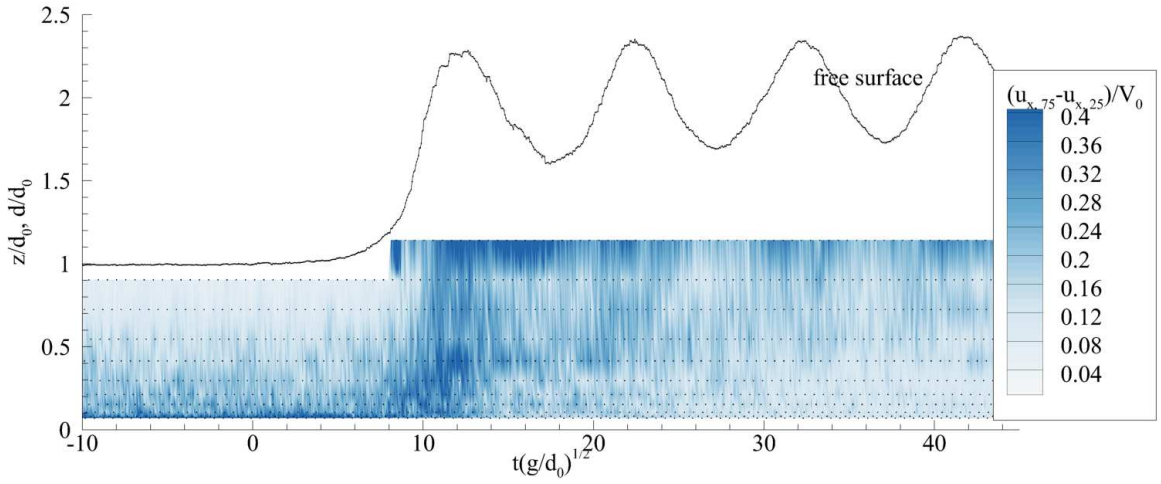

(a) Longitudinal velocity

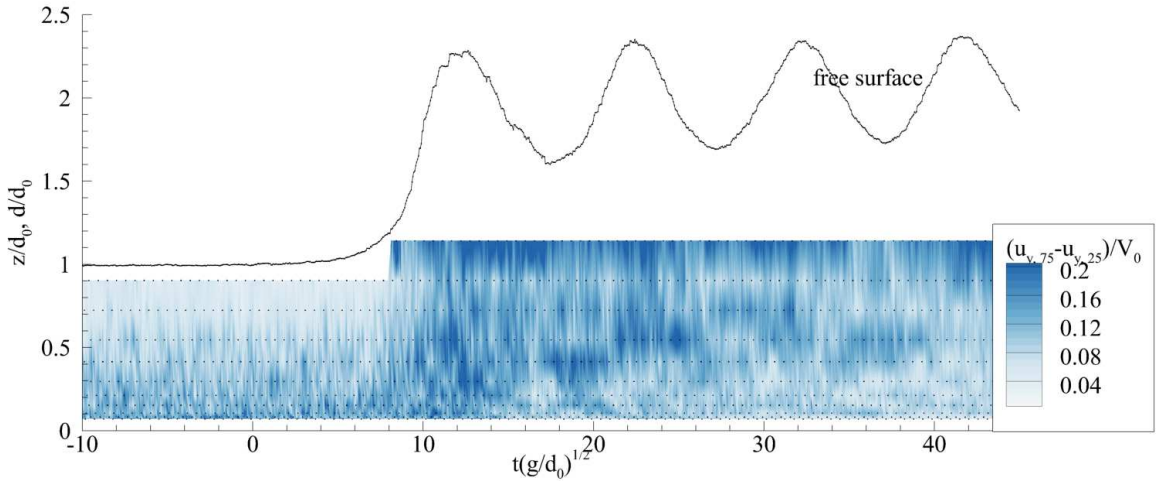

(b) Transversal velocity

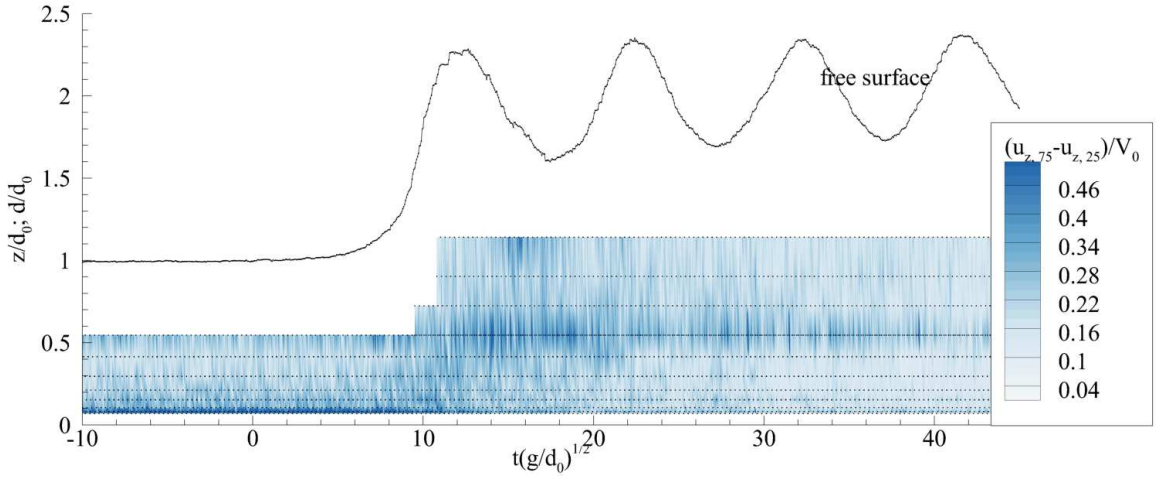

(c) Vertical velocity

Figure B.4: Dimensionless difference between the first and third quartiles ($u_{i,75} - u_{i,25}$) and ensemble averaged water depth in breaking bores. Flow conditions: $Q = 0.036$ m^3.s^{-1}, $Fr = 1.60$, $x = 6.13$ m, $h_g = 0$ mm

B.2.3 Turbulent stress colour maps

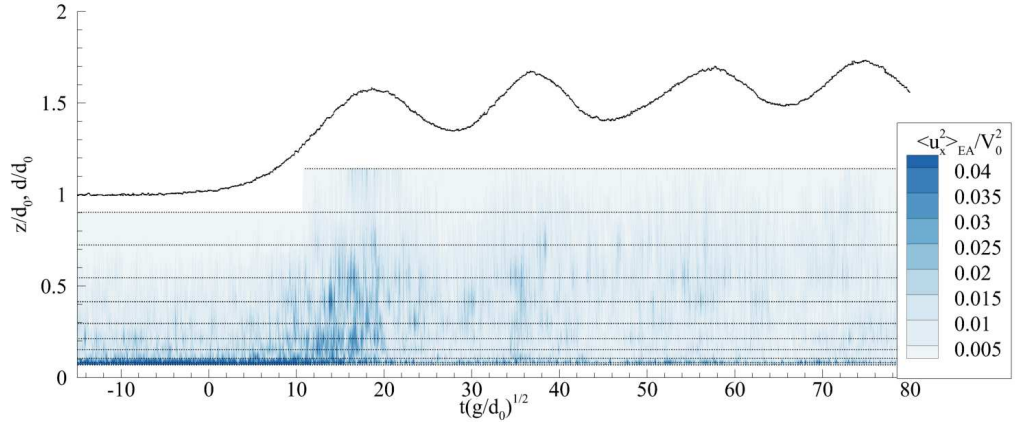

(a) Longitudinal velocity

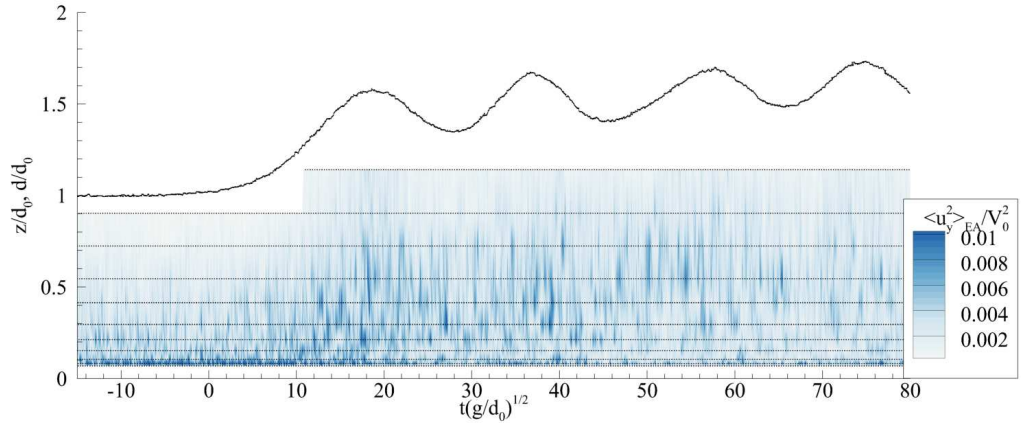

(b) Transversal velocity

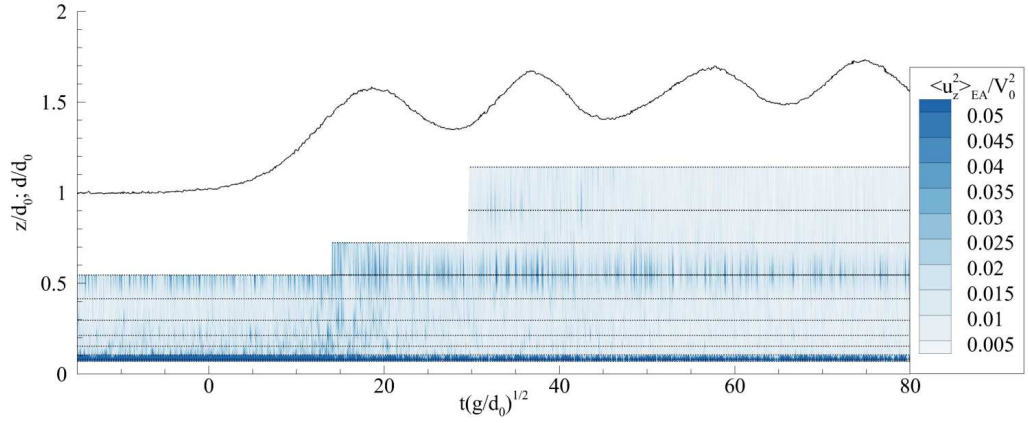

(c) Vertical velocity

Figure B.5: Colour mapping of ensemble-averaged turbulent normal stresses in undular bores with ensemble averaged water depth. Flow conditions: $Q = 0.036$ m^3.s^{-1}, $Fr = 1.33$, $x = 6.13$ m, $h_g = 43$ mm

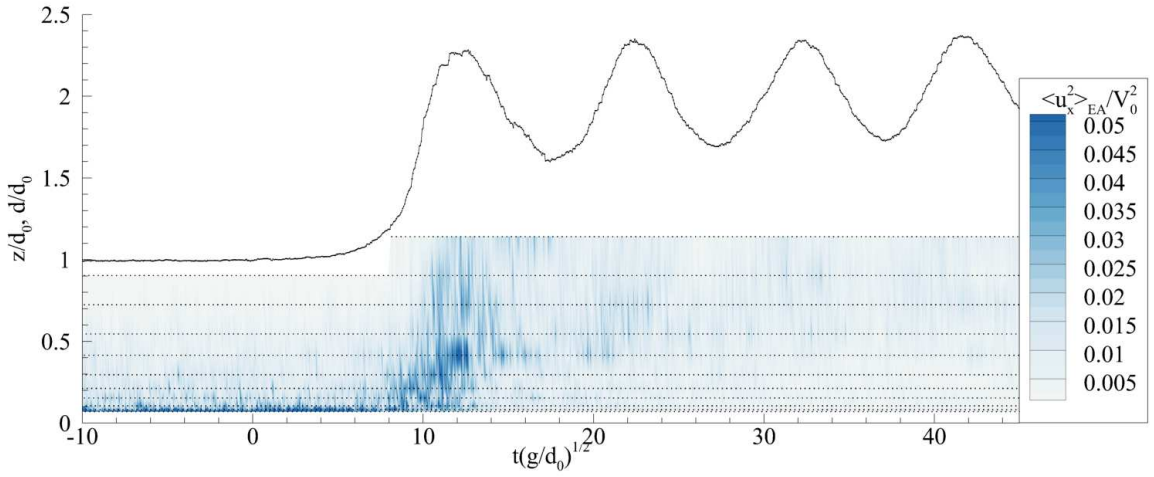

(a) Longitudinal velocity

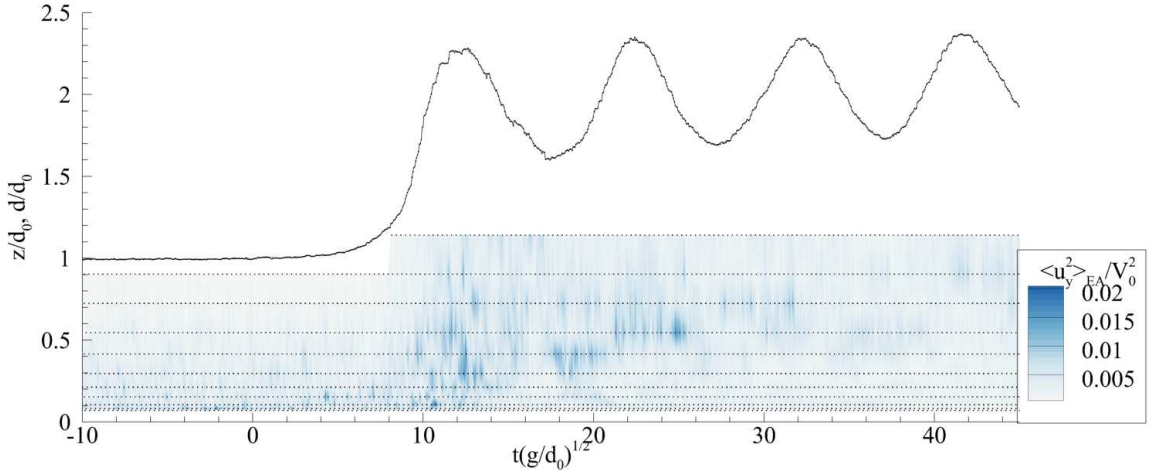

(b) Transversal velocity

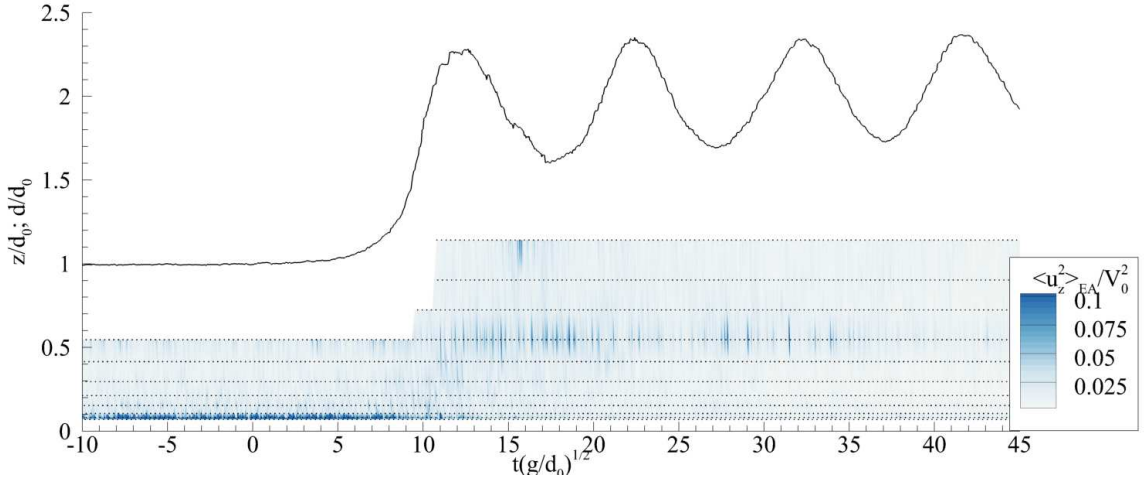

(c) Vertical velocity

Figure B.6: Colour mapping of ensemble-averaged turbulent normal stresses in breaking bores with ensemble averaged water depth. Flow conditions: $Q = 0.036$ m^3.s^{-1}, $Fr = 1.60$, $x = 6.13$ m, $h_g = 0$ mm

C

Velocity data comparison between experiments and numerical simulations

C.1 Presentation

The data of the two and three dimensional numerical simulations were compared with the experimental data of Chanson (2010a,b). The basic flow configuration are presented in Table C.1. Herein, x is the longitudinal distance from the gate, y is the horizontal distance from the left sidewall looking upstream and z is the vertical distance from the bed. h_g is the gate opening after closure, V_0 is the initial flow velocity positive downstream and d_0 is the initial water depth at the location of sampling (either $x = 6.15$ m or $x = 7.15$ m). The complete configurations of the simulations are presented in sections V.4 and V.5. Figures C.1 to C.8 present the time evolution of the velocity measured at several vertical elevations for the experiments (Chanson, 2010a,b) and the simulations (Table C.1).

Table C.1: Initial configuration of the simulations, bores basic characteristics of the simulation and corresponding experiments

Simulation	d_0 m	V_0 m.s^{-1}	h_g m	Inflow condition	Bore type	Experiments
rad2D13	0.165	0.23	0	V_0	Undular	(Chanson, 2010a) 090427
rad3D				V_0		
rad3DSEM				SEM		
ond2D17	0.1385	0.83	0.1	V_0	Undular	(Chanson, 2010b) 080422
ond3D				V_0		
ond3DSEM				SEM		

C.2 Data sets

C.2.1 Bore generated by a completely closed gate

Figures are presented on the next page.

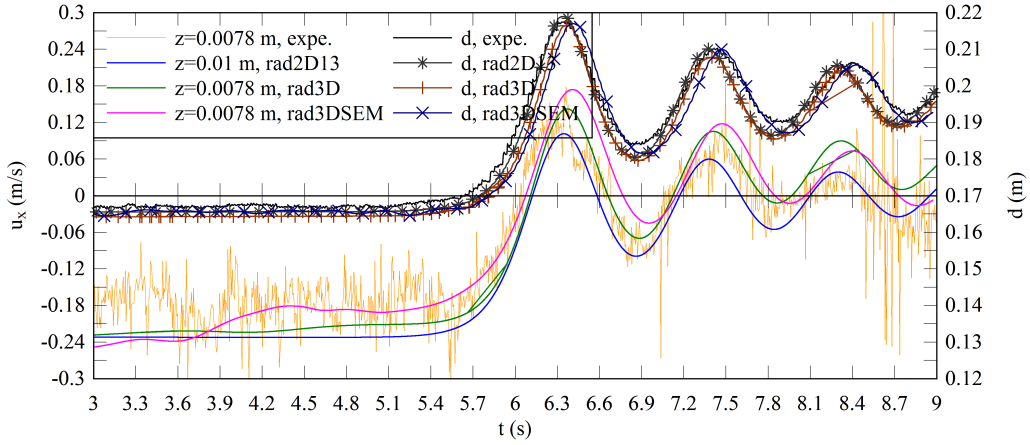

(a) Longitudinal component

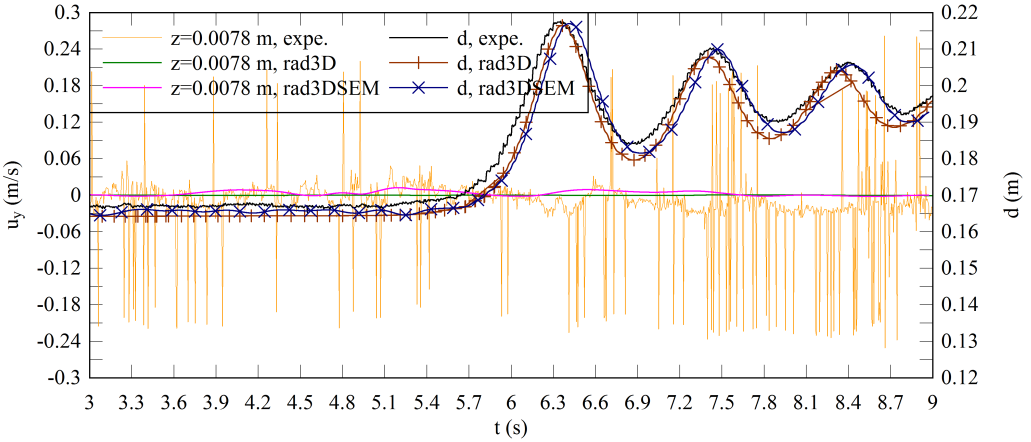

(b) Transversal component

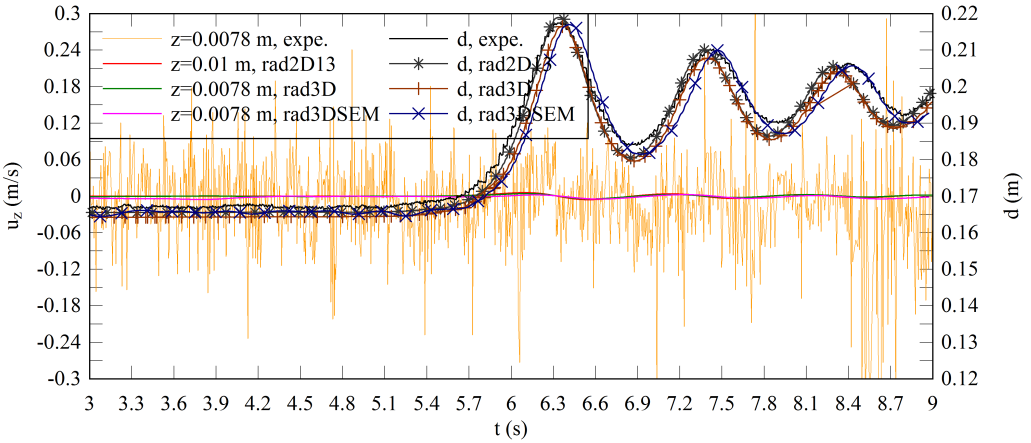

(c) Vertical component

Figure C.1: Time evolutions of the velocity at $z/d_0 = 0.047$ and the free surface evolution at $x = 7.15$ m for rad2D13, rad3D and rad3DSEM. Comparison between numerical simulations and experiments (Chanson, 2010a)

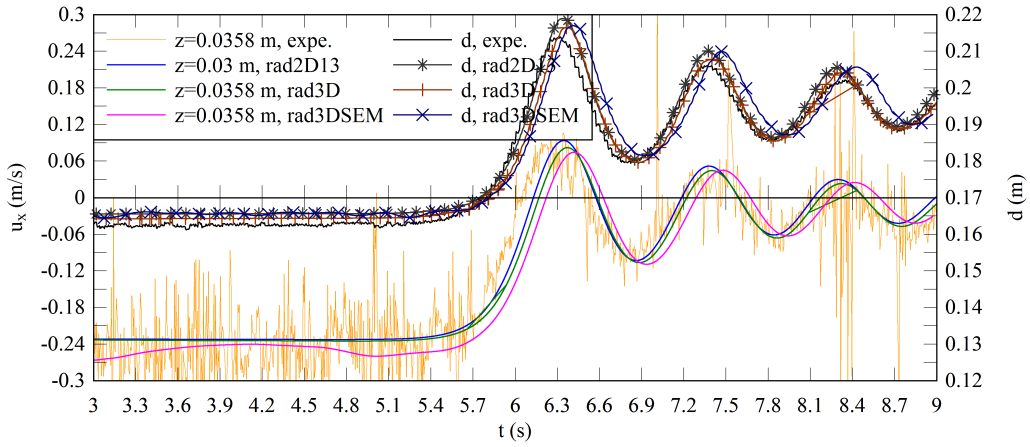

(a) Longitudinal component

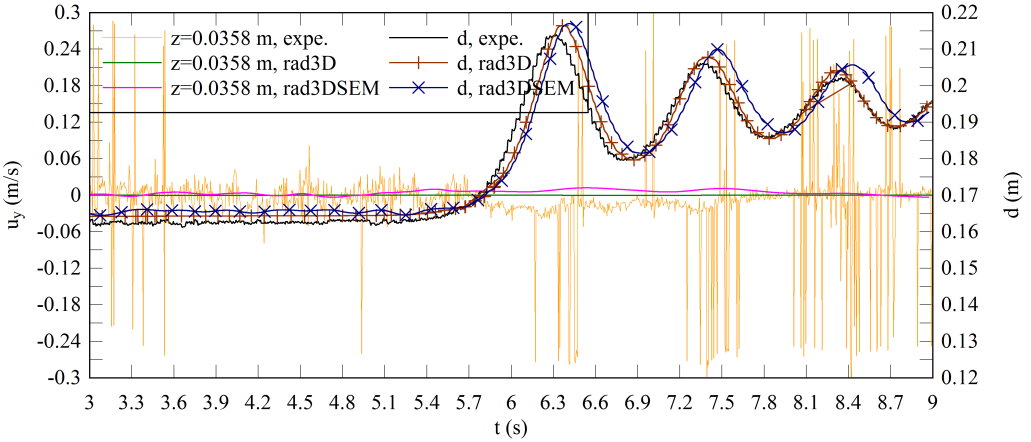

(b) Transversal component

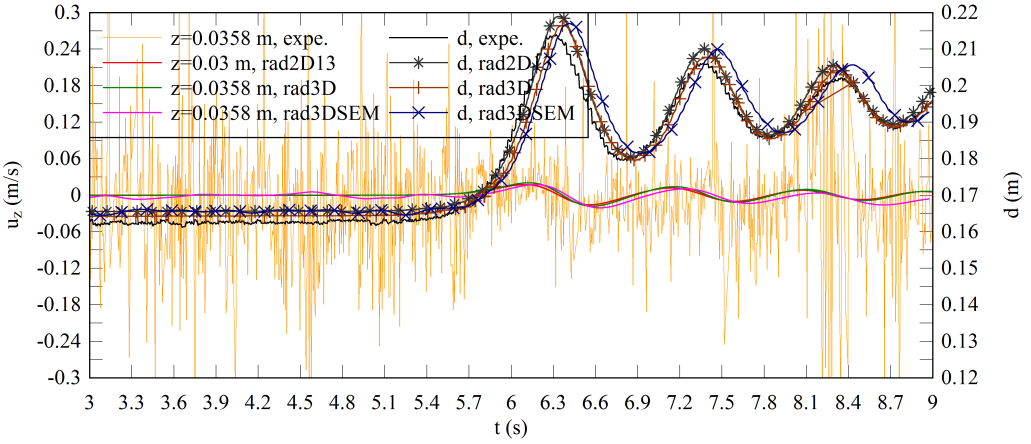

(c) Vertical component

Figure C.2: Time evolutions of the velocity at $z/d_0 = 0.22$ and the free surface evolution at $x = 7.15$ m for rad2D13, rad3D and rad3DSEM. Comparison between numerical simulations and experiments (Chanson, 2010a)

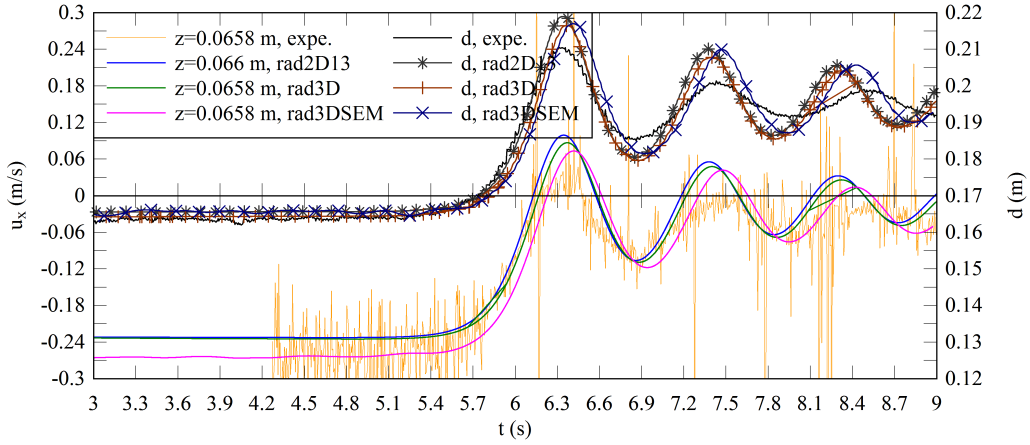

(a) Longitudinal component

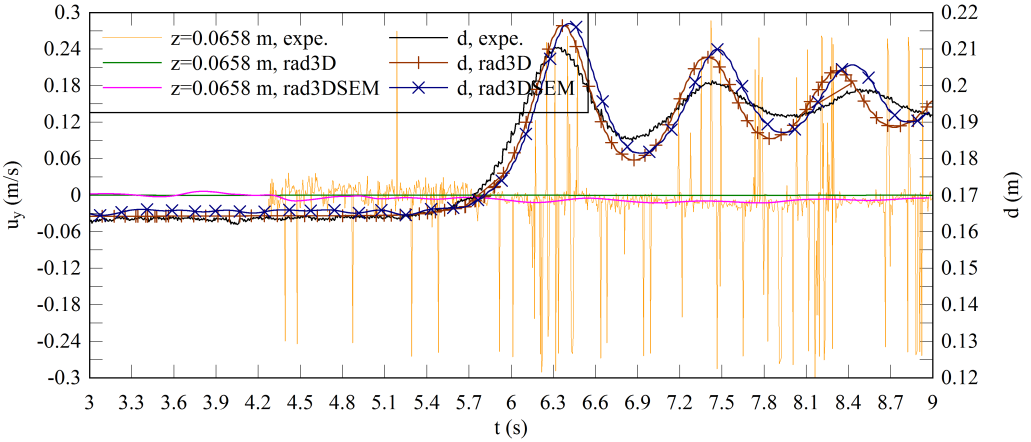

(b) Transversal component

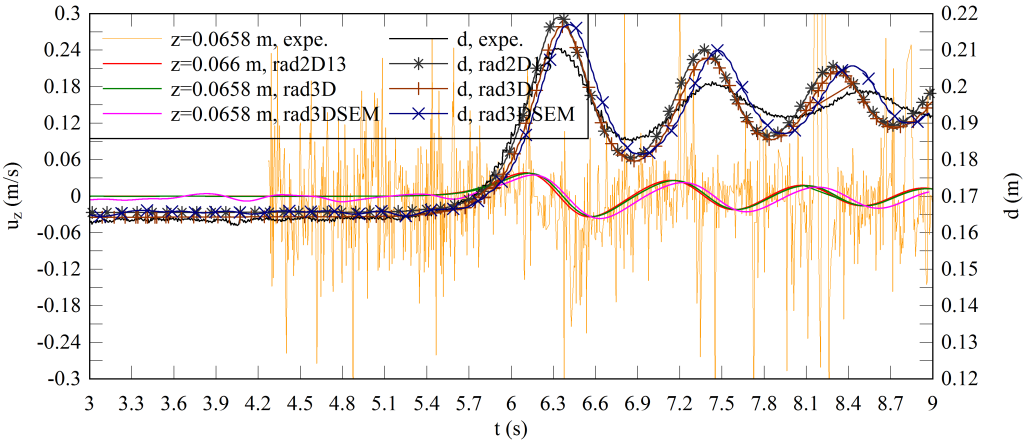

(c) Vertical component

Figure C.3: Time evolutions of the velocity at $z/d_0 = 0.40$ and the free surface evolution at $x = 7.15$ m for rad2D13, rad3D and rad3DSEM. Comparison between numerical simulations and experiments (Chanson, 2010a)

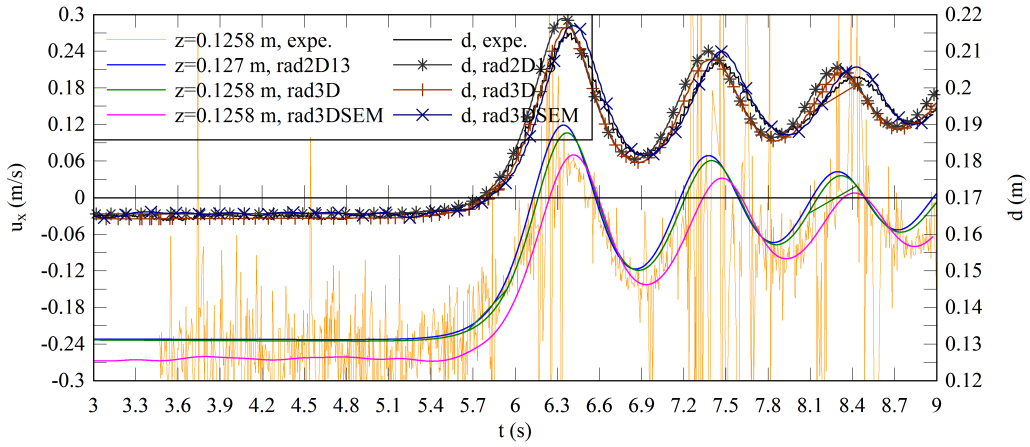

(a) Longitudinal component

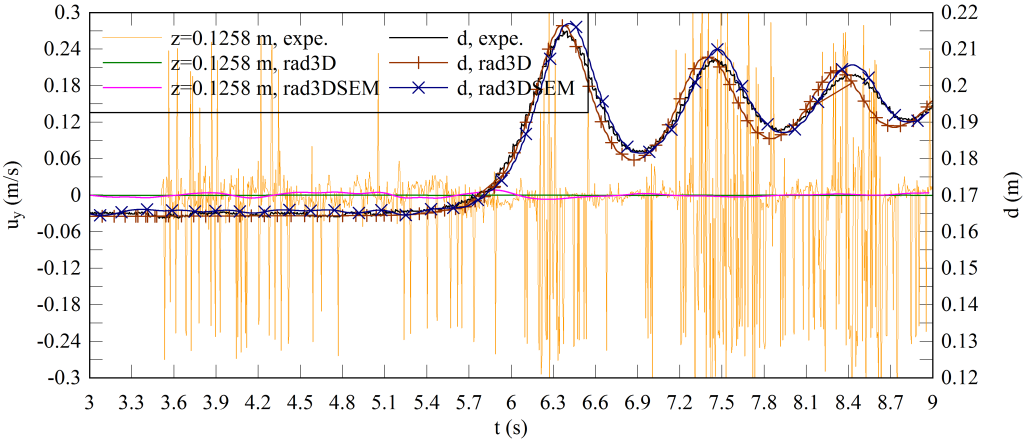

(b) Transversal component

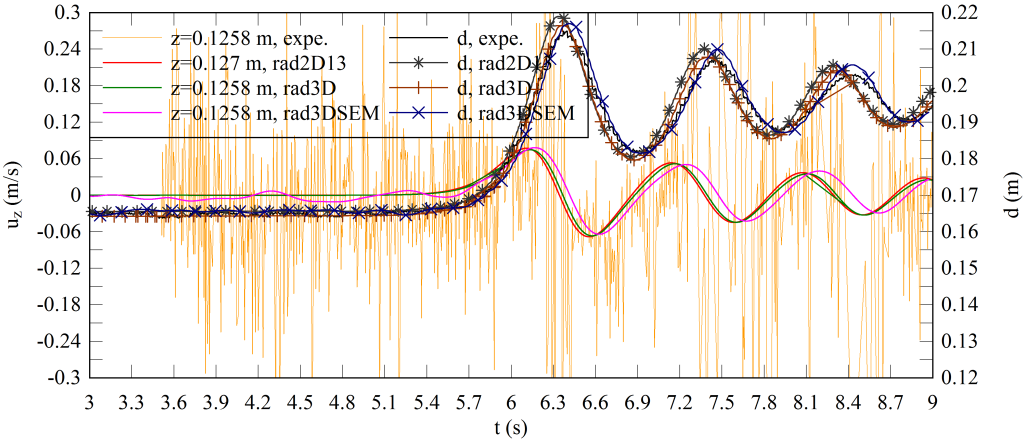

(c) Vertical component

Figure C.4: Time evolutions of the velocity at $z/d_0 = 0.77$ and the free surface evolution at $x = 7.15$ m for rad2D13, rad3D and rad3DSEM. Comparison between numerical simulations and experiments (Chanson, 2010a)

C.2.2 Bore generated by a partially closed gate

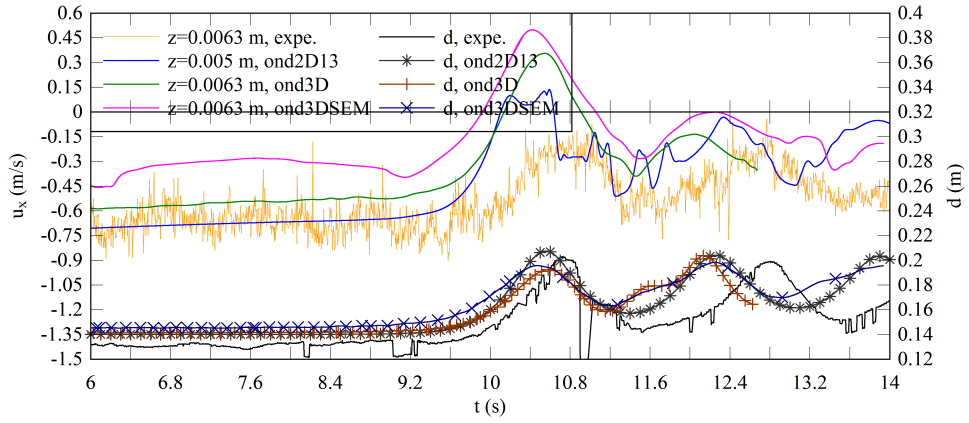

(a) Longitudinal component

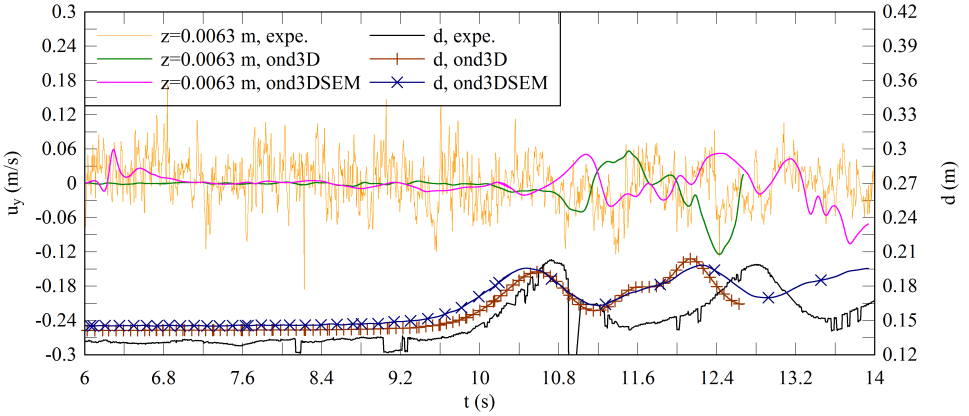

(b) Transversal component

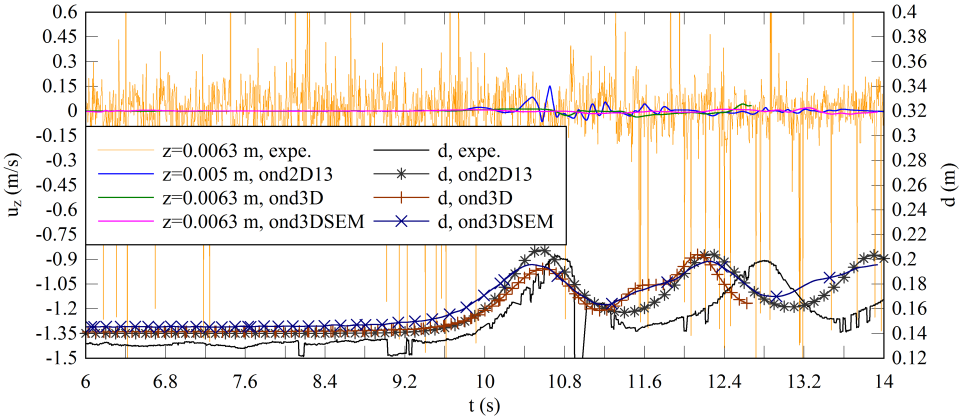

(c) Vertical component

Figure C.5: Time evolutions of the velocity at $z/d_0 = 0.05$ and the free surface evolution at $x = 6.15$ m for ond2D17, ond3D and ond3DSEM. Comparison between numerical simulations and experiments (Chanson, 2010b)

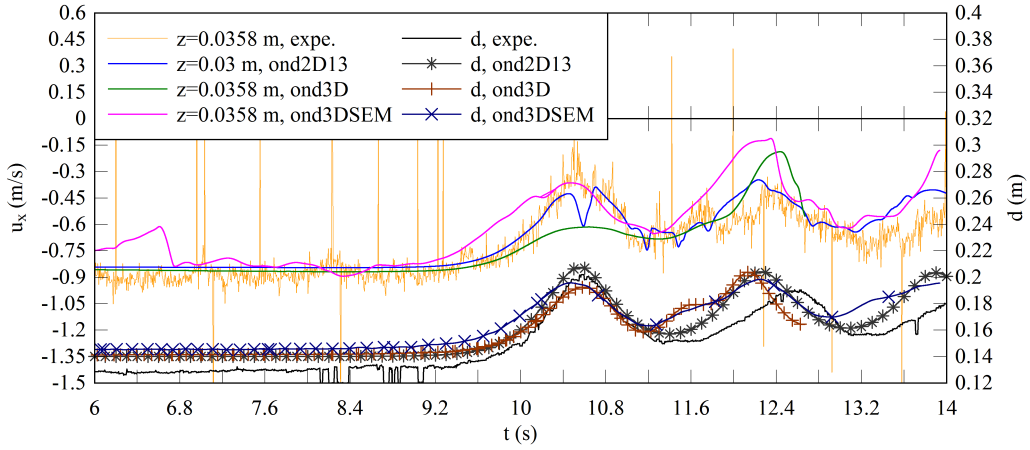

(a) Longitudinal component

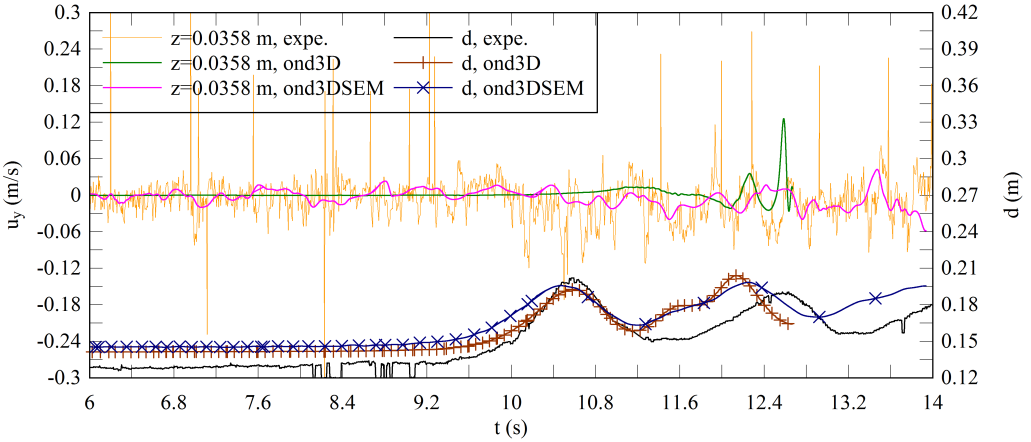

(b) Transversal component

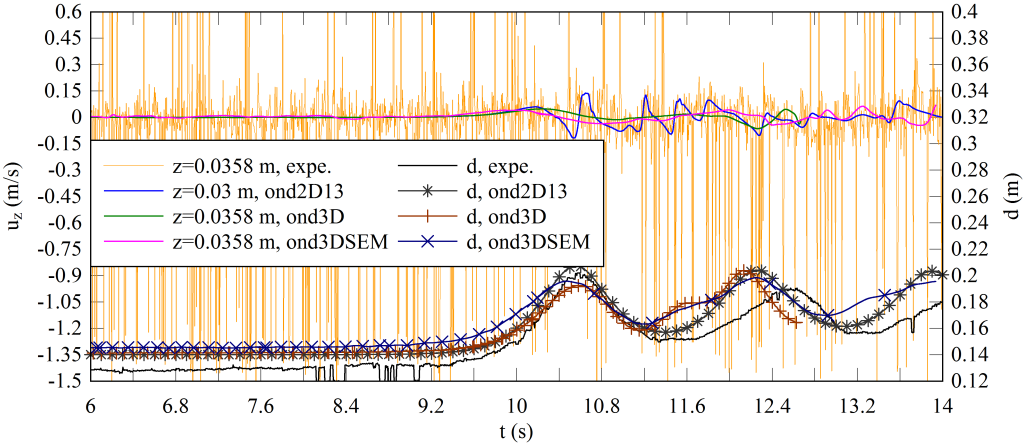

(c) Vertical component

Figure C.6: Time evolutions of the velocity at $z/d_0 = 0.26$ and the free surface evolution at $x = 6.15$ m for ond2D17, ond3D and ond3DSEM. Comparison between numerical simulations and experiments (Chanson, 2010b)

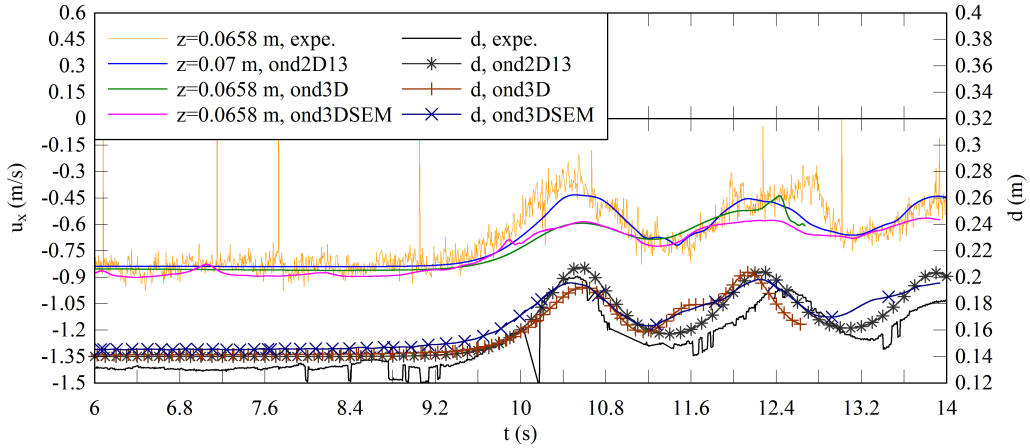

(a) Longitudinal component

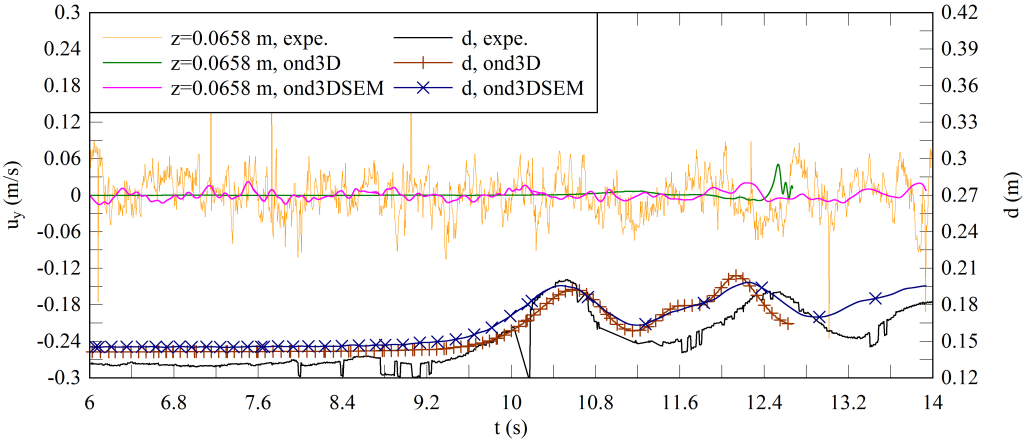

(b) Transversal component

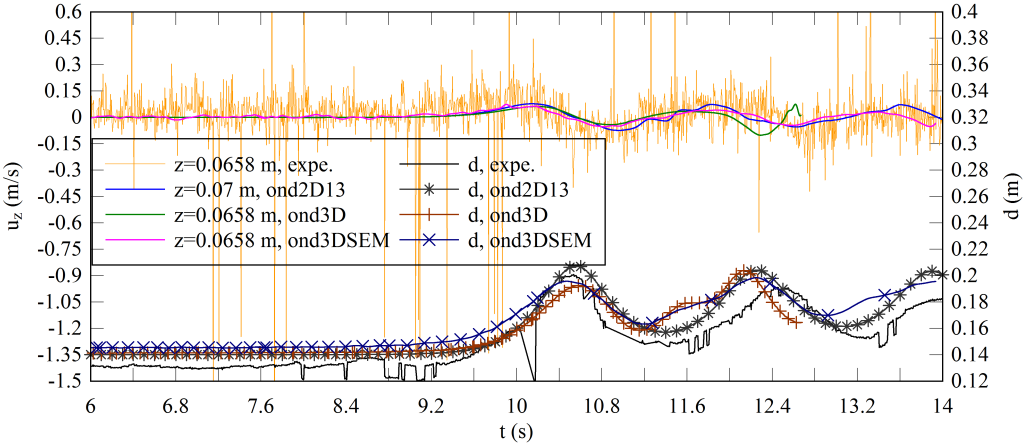

(c) Vertical component

Figure C.7: Time evolutions of the velocity at $z/d_0 = 0.48$ and the free surface evolution at $x = 6.15$ m for ond2D17, ond3D and ond3DSEM. Comparison between numerical simulations and experiments (Chanson, 2010b)

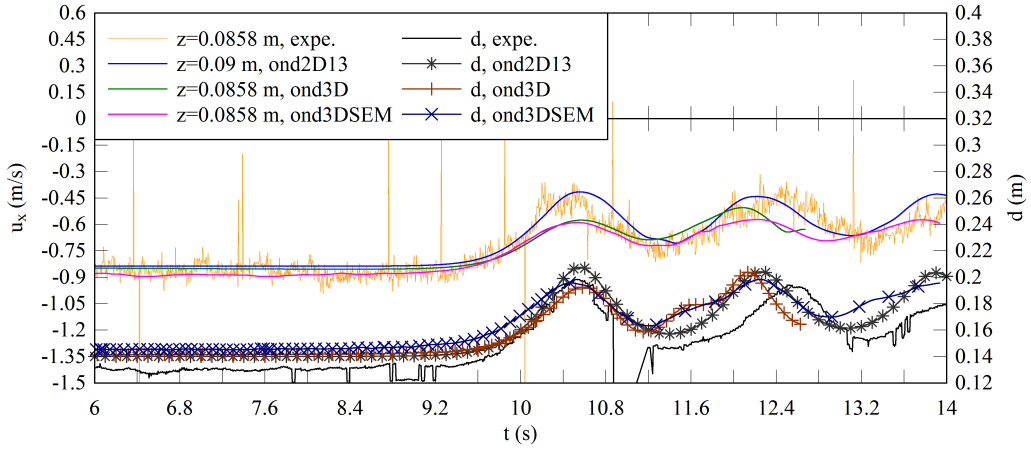

(a) Longitudinal component

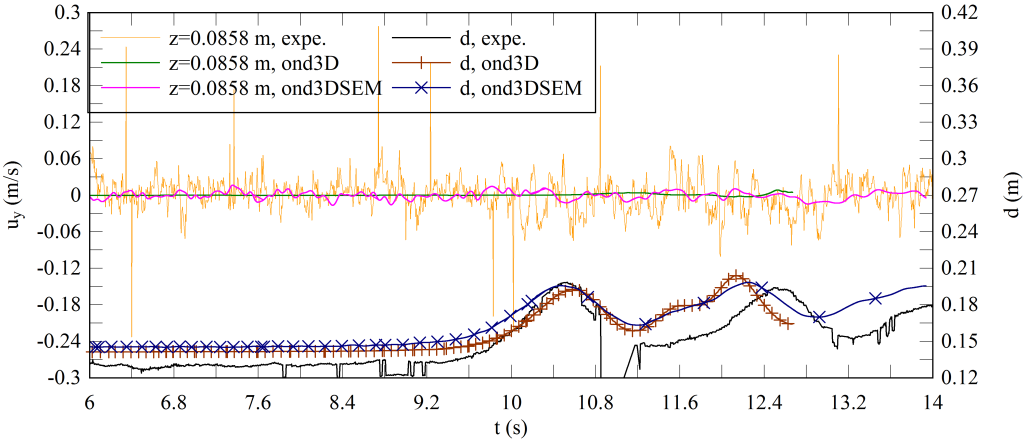

(b) Transversal component

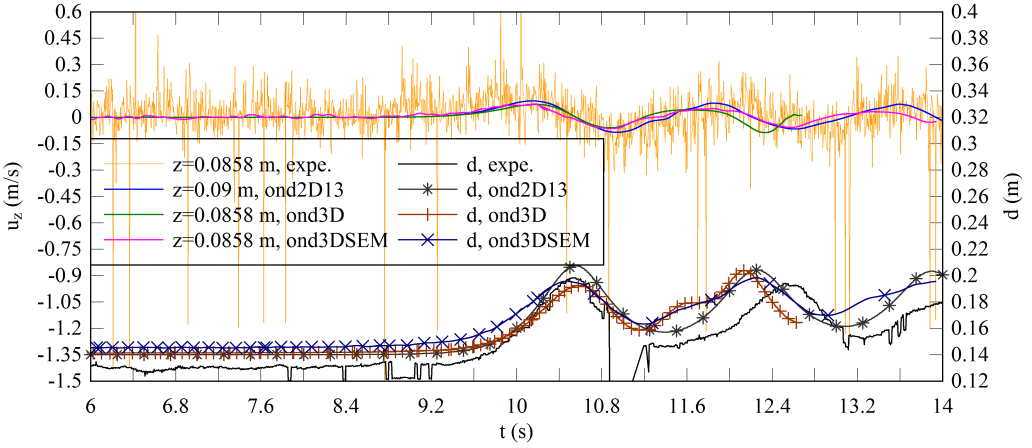

(c) Vertical component

Figure C.8: Time evolutions of the velocity at $z/d_0 = 0.62$ and the free surface evolution at $x = 6.15$ m for ond2D17, ond3D and ond3DSEM. Comparison between numerical simulations and experiments (Chanson, 2010b)

D

Videos of experiments and numerical simulations

D.1 Presentation

A series of videos were taken during the experiments and others were created using the numerical data. The movie files are deposited with the digital record of the publication at the institutional open access repository of the University of Queensland: http://espace.library.uq.edu.au/. They are listed as part of the PhD thesis manuscript deposit at http://espace.library.uq.edu.au/list/author_id/91159/. The list of the videos is detailed in sections D.2 and D.3, including the filenames, the file format and a description of the video together with some basic flow conditions for the bore. Herein, d_0, V_0 and h_g are respectively the initial water depth, the steady flow velocity and the opening after gate closure. C is the phase function from the volume of fluid modelling and Q is the Q-criterion used to visualise coherent structures.

D.2 Videos of experiments

D.2.1 Undular bore propagating in a channel covered by a fixed gravel bed

Filename: 1_undular_V0_083_hg_43.avi

Format: MPEG-4, 30 fps, 1280×720 px
Duration: 21 s
Description: Undular bore propagating upstream with cross-waves in a channel with a fixed gravel bed. View looking downstream approximately 6 m from the gate as the bore propagates upstream. Video playing at real time speed.
Flow configuration: $d_0 = 0.084$ m, $V_0 = 0.87$ m.s^{-1}, $h_g = 0.043$ m, $Fr = 1.33$

D.2.2 Breaking bore propagating in a channel covered by a fixed gravel bed

Filename: 2_breaking_V0_083_hg_0.avi
Format: MPEG-4, 30 fps, 1280×720 px
Duration: 15 s
Description: Breaking bore propagating upstream with secondary undulations in a channel with a fixed gravel bed. View looking downstream approximately 6 m from the gate as the bore propagates upstream. Note the air entrainment associated with the roller. Video playing at real time speed.
Flow configuration: $d_0 = 0.084$ m, $V_0 = 0.87$ m.s^{-1}, $h_g = 0$, $Fr = 1.60$

D.3 Videos of numerical simulations

D.3.1 Two dimensional undular bore generated with a completely closed gate

Filename: 3_ux_rad2D13.mp4
Format: MPEG-4, 29 fps, 1920×1080 px
Duration: 16 s
Description: Propagation of an undular bore from left to right generated by a completely closed gate located at $x = 0$. The video shows colour mapping of the longitudinal velocity in the water. Some velocity streamlines are represented by line with arrows. The isoline $u_x = 0$ is added to the colour mapping (black line). The physical time of the simulation is given by t in the video. Note that the time steps were calculated dynamically for each iteration.
Flow configuration: $d_0 = 0.165$ m, $V_0 = 0.23$ m.s^{-1}, $h_g = 0$, simulation rad2D13

D.3.2 Two dimensional undular bore generated with a partially closed gate

Filename: 4_vorticity_ond2D17.mp4
Format: MPEG-4, 29 fps, 1920×1080 px
Duration: 73 s
Description: Propagation of an undular bore from left to right generated by a partially closed gate located at $x = 0$. The video shows colour mapping of the vorticity in the water. Some velocity streamlines are represented by green lines with arrows. The isoline $u_x = 0$ is added to the colour mapping (black line). The physical time of the simulation is given by t in the video. Note that the time steps were calculated dynamically for each iteration.
Flow configuration: $d_0 = 0.1385$ m, $V_0 = 0.83$ m.s^{-1}, $h_g = 0.10$ m, simulation ond2D17

D.3.3 Three dimensional structures beneath undular bore generated with a completely closed gate and a turbulent steady flow

Filename: 5_critQ_rad3DSEM.mp4
Format: MPEG-4, 29 fps, 1920×1080 px
Duration: 41 s
Description: Propagation of an undular bore from left to right generated by a completely closed gate located at $x = 0$. The video shows the bore free surface in the whole domain and the evolution of coherent structure in the water clipped beneath $y < 0.15$ m. The isosurface of the free surface is plotted at $C = 0.5$ in blue with 70% of translucency of the surface. Coherent structures are visualised with the Q-criterion using a isosurface Q = 1.5, additionally the isosurface of Q is coloured with the longitudinal velocity u_x. The physical time of the simulation is given by t in the video with $t = 0$ at gate closure. Note that the time steps were calculated dynamically for each iteration.
Flow configuration: $d_0 = 0.165$ m, $V_0 = 0.23$ m.s^{-1}, $h_g = 0$, using turbulent inflow condition, simulation rad3DSEM

D.3.4 Three dimensional structures beneath undular bore generated with a partially closed gate and a turbulent steady flow

Filename: 6_critQ_ond3DSEM.mp4
Format: MPEG-4, 29 fps, 1920×1080 px
Duration: 82 s

Description: Propagation of an undular bore from left to right generated by a partially closed gate located at $x = 0$. The video shows the bore free surface in the whole domain, the zone of velocity reversal in the water and the evolution of coherent structure in the water clipped beneath $y < 0.20$ m. The isosurface of the free surface is plotted at $C = 0.5$ in blue with 70% of translucency of the surface. The velocity reversal is shown with the isosurface $u_x = 0$ plotted in yellow. Coherent structures are visualised with the Q-criterion using a isosurface Q = 4, additionally the isosurface of Q is coloured with the longitudinal velocity u_x. The physical time of the simulation is given by t in the video with $t = 0$ at gate closure. Note that the time steps were calculated dynamically for each iteration.
Flow configuration: $d_0 = 0.1385$ m, $V_0 = 0.83$ m.s^{-1}, $h_g = 0.10$ m, using turbulent inflow condition, simulation ond3DSEM

D.3.5 Free surface evolution for an undular bore generated with a partially closed gate and a turbulent steady flow

Filename: 7_ond3DSEM_freeSurface.mp4
Format: MPEG-4, 29 fps, 1920×1080 px
Duration: 49 s
Description: Undular bore propagating upstream with cross-waves initiated on the channel sidewalls. View looking downstream as the bore propagates upstream. The isosurface of the free surface is plotted at $C = 0.5$ with a colour mapping of the water elevation. The physical time of the simulation is given by t in the video with $t = 0$ at gate closure. Note that the time steps were calculated dynamically for each iteration. Figure D.1 describes some details of the free surface.
Flow configuration: $d_0 = 0.1385$ m, $V_0 = 0.83$ m.s^{-1}, $h_g = 0.10$ m, using turbulent inflow condition, simulation ond3DSEM

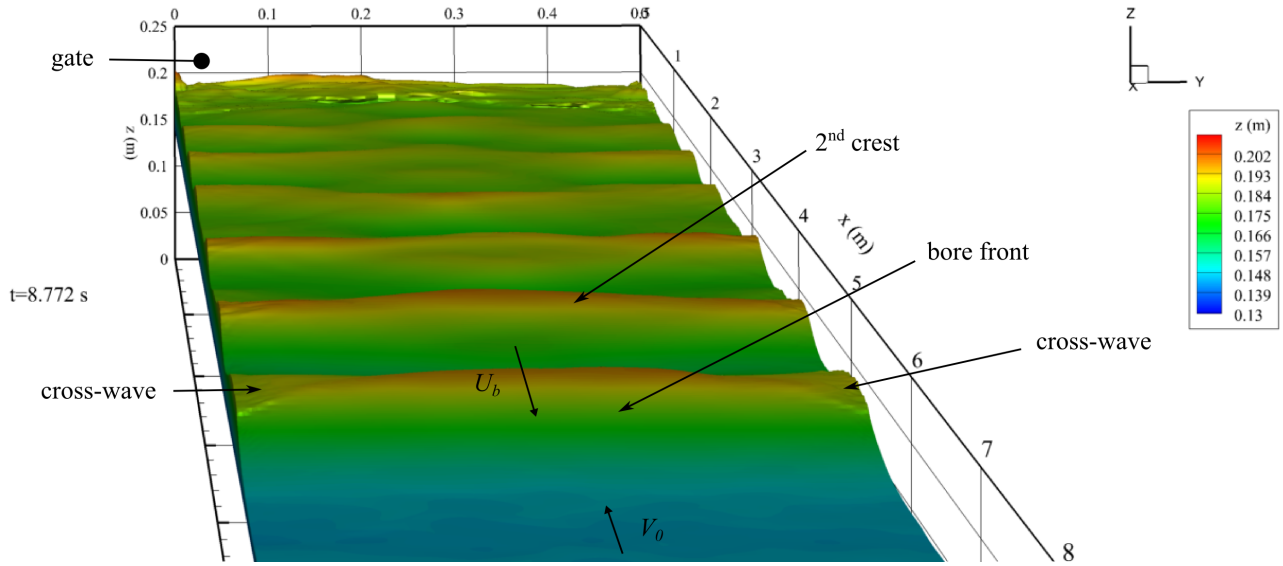

Figure D.1: Description of some details of unsteady flow presented in the video